SSI-DT79145047

Development of virtual accessibility evaluation system by combining digital human models with 3-dimensional as-is environment models

Tsubasa Maruyama

Graduate School of Information Science Technology

Hokkaido University

A thesis submitted for the degree of Doctor of Philosophy

Feb. 15th, 2017

Abstract

Owing to our rapidly aging society, accessibility evaluation is increasing in importance to enhance the ease and safety of access to indoor and outdoor environments for the elderly and disabled. Accessibility must be assessed not only from the general standard aspect, but also from physical and cognitive aspects for users of different ages, genders, and abilities. Examples of the former are dimensional criteria such as corridor width and slope angle, which can be evaluated only by taking account of the shape of the environment. The latter examples indicate more human-centered criteria, such as tripping risk and ease of wayfinding, which can be evaluated by taking account of the interaction between human physical and cognitive behaviors and the environments. On the other hand, human behavior simulation has been progressing recently in the areas of crowd behavior analysis and emergency evaluation planning. In human behavior simulation, the activities of pedestrian models can be predicted in the simplified 2D indoor and outdoor environment models. Human behavior simulation can evaluate the accessibility criteria in emergencies such as the evacuation time and crowd density. However, the evaluation of accessibility criteria in daily life situation such as the tripping risk and the ease of way wayfinding is basically impossible, since the movements of pedestrian model and the environment model are simplified to the particle movements and the as-planned environment model, respectively. Therefore, the pedestrian model cannot generate the detailed 3-dimensional articulated walking movements of various people, and the environment model does not represent the as-is situation of the 3-dimensional environment in the previous human behavior simulation.

Therefore, the objective of this study is to develop a novel virtual accessibility evaluation system based on human behavior simulation, which is more accurate and reliable than previous one, by combining a digital human model (DHM) with 3D “as-is” environment models. The system makes it possible to evaluate the human-centered accessibility criteria such as the tripping risk and the ease of wayfinding in an integrative framework, from the aspects of both physical and cognitive behaviors of various people of different ages, genders, and body dimensions.

This thesis mainly includes the following topics:

(1) 3D as-is environment modeling from laser-scanned point clouds: an automatic and efficient algorithm of 3D as-is environment modeling from laser-scanned point clouds was developed. The 3D as-is environment model for the human behavior simulation consists of the down-sampled points with normal vectors, the set of walk surface points, the navigation graph, and the tread boundary. The effectiveness and efficiency of the algorithm were validated in the point clouds of indoor, outdoor, and urban environments. In addition, accuracy of the 3D as-is

environment model was further validated by a comparison of the dimensions between the model and the real environment.

(2) Autonomous walking simulation of DHM: an algorithm of autonomous walking simulation of the DHM was developed. The walking simulation was realized by three processes: preference-based path selection, optimization-based motion planning, and motion-capture (MoCap)-based adaptive walking motion generation. The effectiveness and efficiency of the walking simulation were validated in the 3D as-is environment models of indoor, outdoor, and urban environments. In addition, the simulated walking motion of the DHM was validated by a comparison of the joint angles and toe clearance of the DHM with those in the MoCap data on actual human walking.

(3) Tripping risk evaluation based on autonomous walking simulation: an algorithm of tripping risk evaluation was developed. The evaluation consists of the tripping-hazard map generation from the laser-scanned point clouds, quantitative tripping risk evaluation based on the autonomous walking simulation combined with Monte Carlo simulation. The effectiveness and efficiency of the algorithm were validated in the point clouds of virtual indoor and real outdoor environments. In addition, the tripping risk evaluation result was further validated by a comparison of the risk from the simulation with the risk measured from younger participants in a walking experiment.

(4) Ease of wayfinding evaluation based on vision-based wayfinding simulation: an algorithm of the ease of wayfinding evaluation based on vision-based wayfinding simulation of the DHM was developed. As the criteria representing the ease of wayfinding, the disorientation place was automatically detected by taking account of the signage location, visibility, legibility, and continuity. For the wayfinding simulation, the textured 3D as-is environment models were further created by structure-from-motion in addition to the point clouds-based 3D as-is environment models. The vision-based wayfinding simulation of the DHM was realized by four processes: the signage perception based on imitated visual perception, state transition-based decision making, signage-based motion planning, and MoCap-based adaptive walking motion generation. The effectiveness and efficiency of the algorithm were validated in two types of indoor environments. In addition, the ease of wayfinding evaluation results were validated by a comparison of the simulated wayfinding behavior of the DHM with those of younger participants measured in a wayfinding experiment.

Contents

Development of virtual accessibility evaluation system by combining digital human models with 3-dimensional as-is environment models i

Abstract iii

List of Figures xi

List of Tables xvii

Chapter 1 Introduction 1

1.1 Background ····· 1

1.1.1 Importance of accessibility evaluation and its requirements ····· 1

1.1.2 Current accessibility evaluation based on human behavior simulation and their issues ····· 3

1.1.3 Current ergonomics evaluation utilizing digital human model and their issues ····· 6

1.1.4 Current 3D as-is environment modeling technologies and their issues ····· 7

1.1.5 Summary of issues of current accessibility evaluation studies ····· 10

1.2 Objective of this study ····· 11

1.3 Overview and Features of this study ····· 12

1.4 Organization of this thesis ····· 16

Chapter 2 3D As-is Environment Modeling from Laser-scanned Point Clouds 19

2.1 Background ····· 19

2.2 Related work on 3D environment modeling ····· 20

2.2.1 Environment modeling in current human behavior simulation ····· 20

2.2.2 As-is environment modeling from 3D laser-scanned point clouds ····· 22

2.2.3 As-is environment modeling utilizing Structure-from-Motion ····· 23

2.2.4 Summary of features of current 3D environment modeling studies and as-is environment modeling approach in this study ····· 25

2.3 Objective and overview ····· 26
2.4 Methods of 3D as-is environment modeling from laser-scanned point clouds ····· 28
2.4.1 Creating down-sampled point clouds with normal vectors ····· 28
2.4.2 Extracting set of walk surface points ····· 30
2.4.3 Navigation graph construction ····· 32
2.4.3.1 Navigation graph construction from laser-scanned point clouds ····· 32
2.4.3.2 Stair structure construction ····· 35
2.4.4 Tread boundaries extraction ····· 36
2.5 Results and validations of 3D as-is environment modeling ····· 37
2.5.1 Laser-scanner, point clouds, and modeling parameters used in experiments ··· 37
2.5.2 As-is environment modeling results in indoor environments ····· 38
2.5.3 As-is environment modeling results in outdoor environment ····· 40
2.5.4 As-is environment modeling results in urban environment ····· 41
2.5.5 Efficiency and accuracy validations of as-is environment modeling ····· 44
2.5.5.1 Efficiency of as-is environment modeling ····· 44
2.5.5.2 Accuracy validations of as-is environment modeling ····· 44
2.6 Summary ····· 46
Chapter 3 Autonomous Walking Simulation of Digital Human Model 49
3.1 Background and requirements ····· 49
3.2 Related work on autonomous human walking simulation ····· 50
3.2.1 Pedestrian model in current human behavior simulation ····· 50
3.2.2 Digital human modeling for walking simulation ····· 52
3.2.3 Summary of features of current walking simulation studies and walking simulation approach in this study ····· 57
3.3 Objective and overview ····· 58
3.4 Methods of autonomous walking simulation ····· 61
3.4.1 Digital human model and MoCap data used in simulation ····· 61

3.4.2 Preference-based path selection ····· 63
3.4.3 Optimization-based motion planning ····· 64
3.4.3.1 Overview ····· 64
3.4.3.2 Initial walking trajectory and path boundary generation ····· 64
3.4.3.3 Walking trajectory optimization ····· 66
3.4.4 MoCap-based adaptive walking motion generation ····· 68
3.4.4.1 Overview ····· 68
3.4.4.2 Estimating next footprint ····· 68
3.4.4.3 Pre-generation of virtual flat walking motion ····· 70
3.4.4.4 Adapting joint position trajectories ····· 74
3.4.4.5 Elevation angle interpolation ····· 75
3.4.4.6 Foot collision avoidance on stairs ····· 76
3.4.4.7 Walking motion generation ····· 77
3.5 Results and validations of autonomous walking simulation ····· 79
3.5.1 Results of autonomous walking simulation in indoor environments ····· 79
3.5.2 Results of autonomous walking simulation in outdoor environment ····· 86
3.5.3 Results of autonomous walking simulation in large-scale urban environment ····· 89
3.5.4 Efficiency and accuracy validations of autonomous walking simulation ····· 93
3.5.4.1 Efficiency of autonomous walking simulation ····· 93
3.5.4.2 Validation of joint angles of digital human model by comparison with motion-capture data ····· 94
3.5.4.3 Validation of toe position of digital human model by comparison with MoCap data ····· 96
3.6 Summary ····· 97
Chapter 4 Tripping Risk Evaluation based on Autonomous Walking Simulation 99
4.1 Background and requirements ····· 99
4.2 Related work on falls prevention ····· 101

4.2.1 Strategies for current falls prevention ····· 101
4.2.2 Human behavior simulation ····· 104
4.2.3 Tripping risk evaluation approach in this study ····· 105
4.3 Objective and overview ····· 105
4.4 Methods of tripping risk evaluation ····· 108
4.4.1 Tripping-hazard map generation ····· 108
4.4.2 Quantitative evaluation of tripping risk ····· 110
4.4.2.1 Overview ····· 110
4.4.2.2 Resampling the walking simulation parameters ····· 114
4.4.2.3 Detecting the tripping event of the DHM during the walking simulation ····· 115
4.5 Results and validations of tripping risk evaluation ····· 116
4.5.1 Overview ····· 116
4.5.2 Results of tripping risk evaluation in virtual indoor environment ····· 116
4.5.2.1 Point clouds of virtual indoor environment ····· 116
4.5.2.2 Tripping-hazard map generation results ····· 117
4.5.2.3 Quantitative tripping risk evaluation results ····· 118
4.5.3 Results of tripping risk evaluation in real outdoor environment ····· 118
4.5.3.1 Point clouds of real outdoor environment ····· 118
4.5.3.2 Tripping-hazard map generation results ····· 119
4.5.3.3 Quantitative tripping risk evaluation results ····· 119
4.5.4 Efficiency of tripping risk evaluation system ····· 123
4.5.5 Experimental validation of tripping risk evaluation results by comparison with tripping risk measured from actual human ····· 124
4.5.5.1 Overview ····· 124
4.5.5.2 On-site measurement of tripping risk of actual human ····· 124
4.5.5.3 Validation results of tripping risk evaluation system ····· 126
4.5.5.4 Discussions ····· 127

4.6 Summary……128

Chapter 5 Ease of Wayfinding Evaluation based on Vision-based Wayfinding Simulation 131

5.1 Background and requirements……131

5.2 Related work on ease of wayfinding evaluation studies……134

5.2.1 Ease of wayfinding evaluation based on field tests……134

5.2.2 Ease of wayfinding evaluation based on current human behavior simulation……136

5.2.3 Summary of issues of current ease of wayfinding evaluation studies and approach in this study……138

5.3 Objective and overview……139

5.4 Textured 3D as-is environment modeling based on structure-from-motion……143

5.4.1 Overview……143

5.4.2 Signage and interior geometry modeling……144

5.4.3 Signage information assigning……146

5.5 Methods of vision-based wayfinding simulation……149

5.5.1 Overview……149

5.5.2 Signage perception based on imitated visual perception……151

5.5.3 State transition-based decision making……153

5.5.4 Signage-based motion planning……154

5.6 Results and validations of ease of wayfinding evaluation……156

5.6.1 Results of textured 3D as-is environment modeling……156

5.6.2 Results of ease of wayfinding evaluation using vision-based wayfinding simulation……160

5.6.2.1 Results of ease of wayfinding evaluation in one-floor indoor environment……160

5.6.2.2 Results of ease of wayfinding evaluation in two-story indoor environment……163

5.6.2.3 Efficiency of vision-based wayfinding simulation……172

5.6.3 Experimental validation of simulated wayfinding behavior by comparison with wayfinding behavior of real human ····· 172

5.6.3.1 Overview ····· 172

5.6.3.2 Measurement of wayfinding behavior of younger participants ····· 173

5.6.3.3 Comparison of wayfinding behavior between simulation and real human ····· 173

5.7 Summary ····· 180

Chapter 6 Conclusions and future works **182**

Appendix **186**

Appendix A: Estimation of rise and tread width from tread boundaries ····· 186

Appendix B: Approach for finding suitable weight coefficients in optimization-based motion planning ····· 188

Appendix C: Preliminary experiment for measuring human motion on various walking terrains ····· 191

Appendix D: Method of extending 2D VCA to 3D VCA ····· 195

Appendix E: Virtual eyesight simulator ····· 198

References **201**

Acknowledgement **207**

Publication list **209**

List of Figures

Fig. 1.1 Examples of accessibility recommendations in ISO guideline 1

Fig. 1.2 Human-centered accessibility criteria 2

Fig. 1.3 Examples of current human behavior simulation studies 5

Fig. 1.4 Overview and features of 3D laser-scanning technologies 8

Fig. 1.5 Accessibility evaluation based on laser-scanned point clouds 8

Fig. 1.6 Overview and features of structure-from-motion (SfM) 9

Fig. 1.7 Approaches of this study 12

Fig. 1.8 Overview of this study and structures of chapters in this thesis 14

Fig. 2.1 Environment models used in current human behavior simulation 21

Fig. 2.2 As-is environment modeling from laser-scanned point clouds 23

Fig. 2.3 Environment reconstruction utilizing SfM 24

Fig. 2.4 Overview of 3D as-is environment modeling from laser-scanned point clouds 27

Fig. 2.5 Down-sampling using voxel grid 29

Fig. 2.6 Noise removal using SOR filter 29

Fig. 2.7 Removed outliers using Euclidian clustering filter 30

Fig. 2.8 Extracting set of walk surface points 31

Fig. 2.9 Structure of the navigation graph 32

Fig. 2.10 Set of graph nodes generation 33

Fig. 2.11 Set of graph edges generation 34

Fig. 2.12 Stair structure construction 34

Fig. 2.13 Tread boundaries extraction 37

Fig. 2.14 Results of as-is environment modeling in one-floor indoor environment 39

Fig. 2.15 Results of as-is environment modeling in two-story indoor environment 40

Fig. 2.16 Results of as-is environment modeling in outdoor environment 41

Fig. 2.17 Results of as-is environment modeling in urban environment 42
Fig. 2.18 Selected graph nodes for path clearance validation 45
Fig. 2.19 Definition of rise and tread width of stairs 46
Fig. 2.20 Selected stairs for stairs dimensions validation 46
Fig. 3.1 Requirements for walking simulation of DHM 50
Fig. 3.2 Pedestrian model in current human behavior simulation studies 51
Fig. 3.3 Walking simulation based on MoCap data 53
Fig. 3.4 Physics-based walking simulation 55
Fig. 3.5 Physics-based walking simulation with key-frame specification 56
Fig. 3.6 Overview of autonomous walking simulation of DHM 59
Fig. 3.7 Walking behavior of DHM in the point clouds-based 3D as-is environment model 60
Fig. 3.8 Link mechanism of our DHM 61
Fig. 3.9 Processing flow of autonomous walking simulation 62
Fig. 3.10 Overview of preference-based path selection 63
Fig. 3.11 Overviews of initial walking trajectory and path boundary generation 65
Fig. 3.12 Internal and external energies 67
Fig. 3.13 Updating next subgoal position and locomotion vector 69
Fig. 3.14 Next footprint estimation 69
Fig. 3.15 Overview of pre-generation of virtual flat walking motion 71
Fig. 3.16 Target posture generation 71
Fig. 3.17 Interpolating stance leg motion 72
Fig. 3.18 Generating swing leg motion 73
Fig. 3.19 Adapting joint position trajectories 75
Fig. 3.20 Elevation angle interpolation 76
Fig. 3.21 Foot collision avoidance on stairs 77
Fig. 3.22 Generating walking motion 78
Fig. 3.23 Joint angle definition in this study 78

Fig. 3.24 Results of preference-based path selection 80
Fig. 3.25 Autonomous walking simulation in one-floor indoor environment 81
Fig. 3.26 Autonomous walking simulation on stairs 83
Fig. 3.27 Comparison of simulated walking motion of DHM using different MoCap data 84
Fig. 3.28 Comparison of simulated walking motion of DHM using different strides 85
Fig. 3.29 Autonomous walking simulation in two-story indoor environment 87
Fig. 3.30 Autonomous walking simulation in outdoor environment 88
Fig. 3.31 Preference-based path selection in large-scale urban environment 90
Fig. 3.32 Autonomous walking simulation in urban environment 91
Fig. 3.33 Autonomous walking simulation in urban environment including stairs 92
Fig. 3.34 Comparisons of joint angles of DHM with those of younger subjects 94
Fig. 3.35 Comparisons of joint angles of DHM with real human in 6-deg slope 95
Fig. 3.36 Difference in MTC between simulated walking motion and original MoCap data 97
Fig. 4.1 Comparison of falling place between visual inspection and hearing survey 100
Fig. 4.2 Difference of toe clearance distribution between younger and older people 101
Fig. 4.3 Reducing MTC variability by improving human gait 102
Fig. 4.4 Accessibility diagnosis from mobile laser-scanning data 103
Fig. 4.5 Real-time falls and near-miss falls detection 104
Fig. 4.6 Overview of the tripping risk evaluation 106
Fig. 4.7 Basic concept of tripping risk evaluation 107
Fig. 4.8 Overview of tripping-hazard map generation 109
Fig. 4.9 Overview of autonomous walking simulation combined with Monte Carlo simulation 111
Fig. 4.10 Walking stride and offset value of ankle height 112
Fig. 4.11 Making the DHM start walking 112
Fig. 4.12 Toe clearance estimation 115

Fig. 4.13 Tripping risk evaluation results in virtual indoor environment 117

Fig. 4.14 Tripping-hazard map generation results in outdoor environment 120

Fig. 4.15 Tripping-hazard map generation results in the outdoor environment..... 121

Fig. 4.16 Tripping risk evaluation results in outdoor environment 122

Fig. 4.17 Walking motion of the DHM on interested region 122

Fig. 4.18 On-site tripping risk measurement 125

Fig. 4.19 Comparison of tripping risk between simulation and measurements from actual human 126

Fig. 4.20 Comparison of toe position between link model of DHM and subjects of MoCap data 126

Fig. 5.1 Relation among information used for wayfinding [Hiiro 93] 132

Fig. 5.2 Virtual field tests 135

Fig. 5.3 Ease of wayfinding evaluation based on wayfinding simulation in 3D as-planned indoor environment 137

Fig. 5.4 Overview of the wayfinding simulation 141

Fig. 5.5 Overview of textured as-is environment modeling 144

Fig. 5.6 Overview of interior geometry construction utilizing SfM 145

Fig. 5.7 Overview of signage information assigning..... 147

Fig. 5.8 Comparison of 2D VCA with proposed 3D VCA 148

Fig. 5.9 Overview of vision-based wayfinding simulation..... 150

Fig. 5.10 Overview of each process of vision-based wayfinding simulation 151

Fig. 5.11 Visibility estimation of signage 152

Fig. 5.12 Legibility estimation of signage information 152

Fig. 5.13 State transition-based decision making 153

Fig. 5.14 Signage-based motion planning 155

Fig. 5.15 Textured as-is environment model of one-floor indoor environment 157

Fig. 5.16 Textured as-is environment model of two-story indoor environment by SfM 158

Fig. 5.17 Ease of wayfinding evaluation in one-floor indoor environment

with one signage 160

Fig. 5.18 Ease of wayfinding evaluation in one-floor indoor environment with new signage 162

Fig. 5.19 Signage locations and wayfinding evaluation conditions in two-story as-is environment model 165

Fig. 5.20 Ease of wayfinding evaluation in two-story indoor environment with three signage 166

Fig. 5.21 Adding a new signage into two-story as-is environment model 168

Fig. 5.22 Ease of wayfinding evaluation in two-story indoor environment with new signage 169

Fig. 5.23 Difference in wayfinding simulation results between eye heights 171

Fig. 5.24 Measurement of wayfinding behavior of younger participant 174

Fig. 5.25 Wayfinding behavior of DHM in two-story indoor environment 176

Fig. 5.26 Wayfinding behavior of participants Y1-Y3 in two-story indoor environment 177

Fig. 5.27 Wayfinding behavior of participants Y4-Y6 in two-story indoor environment 178

Fig. 5.28 Eyesight of the DHM at a disorientation place 180

Fig. A.1 Estimation of stairs dimensions from tread boundaries 186

Fig. B.1 Comparison of walking trajectory between DHM and younger participants around corner 189

Fig. B.2 Overview of vision-based localization system 189

Fig. B.3 Comparison of walking trajectory between DHM and younger participant in corridors 190

Fig. C.1 Overview of walking measurement experiment 191

Fig. C.2 Difference in pelvis and ankle height between walking motion on flat terrain and 6-deg slope 193

Fig. C.3 Comparison of ankle heights between walking on flat terrains and walking on stairs 194

Fig. D.1 Comparison of 2D VCA with proposed 3D VCA 195

Fig. D.2 Extension of 2D VCA to 3D VCA 196

Fig. D.3 MTF of human eyes 197

Fig. E.1 Overview of virtual eyesight simulator 199

Fig. E.2 Results of virtual eyesight simulator 200

List of Tables

Table 1.1 Environment and pedestrian model representations in current human behavior simulation studies 5

Table 1.2 Features of current as-is environment modeling technologies 10

Table 2.1 Essential environmental information for human behavior simulation 19

Table 2.2 Features of current environment modeling technologies 25

Table 2.3 Components of point clouds-based 3D as-is environment model 28

Table 2.4 Properties of laser-scanned point clouds used for as-is environment modeling 37

Table 2.5 Strategies and setting of environment modeling parameters 38

Table 2.6 Elapsed time of 3D as-is environment modeling from laser-scanned point clouds 43

Table 2.7 Comparison of estimated path clearance with measurements 45

Table 2.8 Comparison of stair dimensions between as-is environment model and real environment 46

Table 3.1 Features of current walking simulation 57

Table 3.2 Elapsed time of autonomous walking simulation 93

Table 3.3 Age and body height of selected subjects, and difference in MTC between simulated walking motion and original MoCap data 97

Table 4.1 Resampling strategy and setting of walking simulation parameters 114

Table 4.2 Age and body height of participants in measurement experiment 125

Table 5.1 Information used for wayfinding 132

Table 5.2 Classification of visual signage 133

Table 5.3 Summary of issues of current ease of wayfinding evaluation studies 140

Table 5.4 Attributes of signage information 146

Table 5.5 Elapsed time of textured as-is environment modeling 156

Table 5.6 Elapsed time of vision-based wayfinding simulation 172

Table 5.7 Wayfinding events of participants Y1-Y3..... 179

Table 5.8 Wayfinding events of participants Y4-Y6..... 179

Table C.1 Estimated joint velocities and ankle height..... 193

Chapter 1 Introduction

1.1 Background

1.1.1 Importance of accessibility evaluation and its requirements

The World Health Organization (WHO) reported that the number of people over 60 years age is estimated to grow to almost two billion by 2050 in the world [WHO 07]. Therefore, owing to our rapidly aging society, accessibility evaluation is increasing in importance to enhance the ease and safety of access to indoor and outdoor environments for the elderly and disabled. In the International Organization for Standardization (ISO) 21542, "accessibility" is defined as "provision of buildings or parts of buildings for people, regardless of disability, age or gender, to be able to gain access to them, into them, to use them and exit from them" [ISO 21542, 11]. In accordance with the ISO guideline, for example, living environments such as hospitals and nursing homes need to be designed or improved to ensure the ease and safety of access for the users. In the ISO guideline, concepts of accessibility, design considerations, and requirements, and recommendations for the elements in built environments have been specified. Examples of accessibility recommendations in the guideline standard are shown in Fig. 1.1. As shown in the figure, in the guideline, dimensional recommendations such as the maximum height of barrier in entrances, and the stairs dimensions have been specified.

On the other hand, as recommended in ISO/IEC Guide 71 [ISO/IEC 14], accessibility must be assessed not only from the general standard aspect specified in the ISO guideline [ISO 21542, 11]

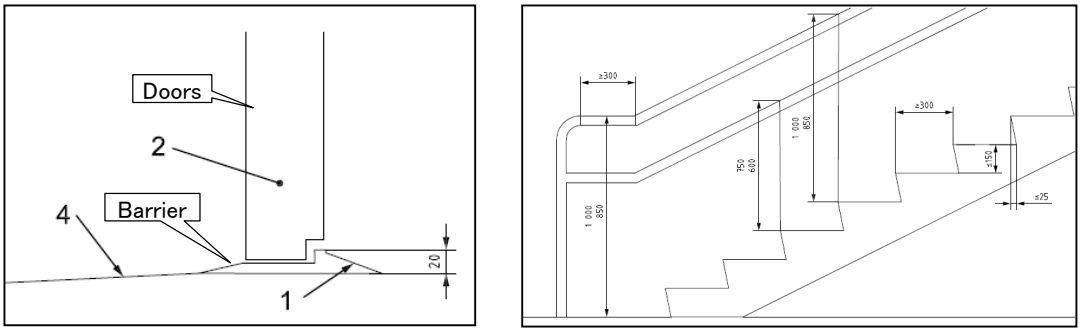

(a) Maximum barrier height in entrances (b) Recommended stairs dimensions

Fig. 1.1 Examples of accessibility recommendations in ISO guideline [ISO 21542, 11]

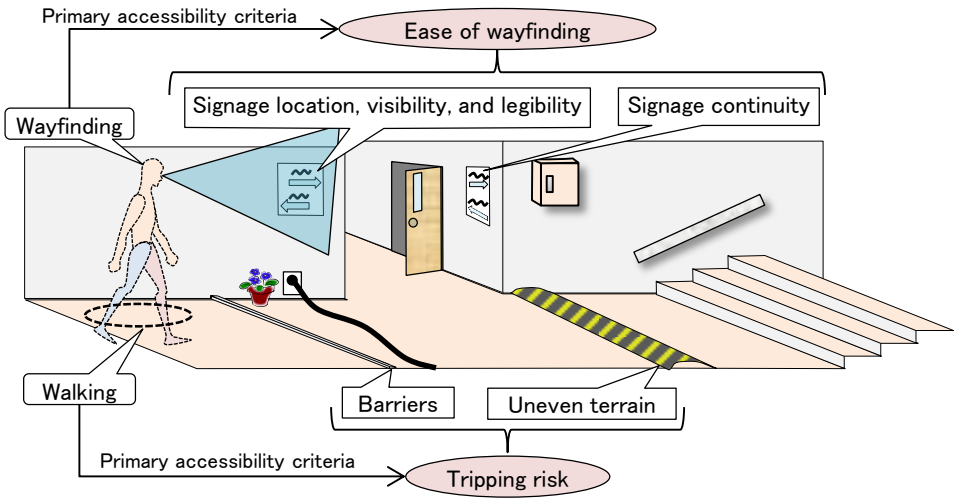

Fig. 1.2 Human-centered accessibility criteria

but also from physical and cognitive aspects for users of different ages, genders, and abilities [ISO/IEC 14]. As shown in Fig. 1.1, examples of the former are dimensional criteria such as barrier height and tread width, which can be evaluated only by taking account of the shape of the environment. On the other hand, as shown in Fig. 1.2, the latter examples indicate more human-centered criteria, such as a tripping risk and ease of wayfinding, which can be evaluated by considering physical and cognitive behaviors of various people of different ages, genders, body dimensions, and abilities. In general, walking and wayfinding behaviors are the essential and basic ones of all people in a given environment. Therefore, among several accessibility criteria, evaluating human-centered accessibility criteria related to the walking and wayfinding behaviors of the user is indispensable.

For the human-centered accessibility evaluation from the aspect of human physical behavior (i.e., walking), evaluating the tripping risk as primary accessibility criteria is important, since falls injuries are the leading cause of unintentional death in older people, as reported by WHO [WHO 07]. On the other hand, for the evaluation from the aspect of human cognitive behavior (i.e., wayfinding), evaluating the ease of wayfinding stemming from signage location, visibility, legibility and continuity as primary accessibility criteria is important, since the signage greatly contributes to wayfinding behavior of people in unfamiliar environments [Hölscher 07]. Therefore, as shown in Fig. 1.2, for the reliable accessibility evaluation, both tripping risk and ease of wayfinding need to be evaluated by taking account of the interaction between the environment and physical and cognitive behaviors of various people.

On the other hand, accessibility of “as-is” environments must be evaluated instead of “as-planned” environments. In contrast to as-planned environments, as-is environments exhibit the following characteristics:

– They do not ignore extra objects placed in environments after completion of building

construction (e.g., furniture, dustbins, fire extinguisher, and signage).

- They include small barriers and obstacles on the floor that have been ignored in the CAD data of building information model (BIM)
- They include uneven outdoor walking terrains that have been neglected to model in the CAD data of BIM

The presence of extra objects, small barriers and obstacles, signage, and uneven outdoor terrains strongly affects the accessibility of the environment. For example, the tripping risk greatly increases on the small barriers and uneven terrains, and the signage visibility significantly decreases if obstacles are placed between the signage and the user. Therefore, evaluating accessibility criteria based on really existing elements in environments is indispensable for reliable accessibility evaluation.

From the above reasons, the requirements for accessibility evaluation can be summarized as follows:

- Accessibility must be evaluated in terms of physical and cognitive friendliness for users of different ages, genders, body dimensions, and abilities.
- The tripping risk must be evaluated in consideration both of environmental hazards and of physical behaviors of various people.
- The ease of wayfinding such as signage visibility must be evaluated in consideration both of signage system and of cognitive behaviors of various people.
- Accessibility must be evaluated in as-is environments including small barriers and obstacles, signage, and uneven outdoor terrains.

1.1.2 Current accessibility evaluation based on human behavior simulation and their issues

Human behavior simulation has been progressing recently in the areas of crowd behavior analysis and emergency evacuation planning [Duives 13]. In the human behavior simulation, as shown in Fig. 1.3 (a), first, the activities of pedestrian models are predicted in the as-planned environment models. Then, the accessibility criteria such as crowd density and evacuation time are evaluated, by analyzing the simulated behaviors of pedestrian models.

As shown in Fig. 1.3 and Table 1.1, according to the representation of environment and pedestrian models, the previous human behavior simulations can be classified into four categories: (1) traditional 2D crowd simulation, (2) 3D evacuation simulation, (3) 2D wayfinding simulation, and (4) 3D wayfinding simulation.

As shown in Fig. 1.3, in the simulation (1) such as [Helbing 00], [Duives 13], the evacuation time and crowd density are estimated by predicting the 2D movements of the pedestrian model in a

simplified 2D as-planned environment model. In the simulation (2) such as [Kakizaki 12], the evacuation time and crowd density are estimated by predicting the 3D walking motion of the digital human model in a simplified 3D as-planned environment model, while considering the detailed 3D articulated movements such as ascending stairs and conveying the injured. In the simulation (3) such as [Hajibabai 07], the evacuation time is estimated by predicting the 2D wayfinding behavior of the pedestrian model based on the arranged signage in a simplified 2D as-planned environment. In the simulation (4) such as [Becker-Asano 14], [Brunnhuber 12], the ease of wayfinding such as the success rate of the navigation depending on the arranged signage is estimated by predicting the 3D wayfinding behavior of the pedestrian model in an as-planned 3D environment model.

These human behavior simulations have been utilized for evaluating the accessibility criteria specifically in emergencies. Therefore, the human behavior simulation technologies are potentially utilized for evaluating the human-centered accessibility criteria in daily life situation such as tripping risk and ease of wayfinding.

However, as shown in Table 1.1, in these previous human behavior simulation studies, the environment models represent only “as-planned” situations instead of “as-is” environments. This is because that making ideal and detailed as-is environment model including small barriers, signage, and uneven terrains using the 3D CAD software technically impossible, since the 3D CAD models are generally comprised of a set of solid primitives. If we make the as-is environment model for the human behavior simulation using the 3D CAD software, the 3D as-is environment model needs to be manually created with detailed modeling and measurement works. However, this is labor-intensive and tedious, and the constructed environment model is sometimes inaccurate. Therefore, manually making the 3D as-is environment model for the human behavior simulation is basically impractical.

From the aspect of the physical behavior of the pedestrian model, the previous human behavior simulation cannot evaluate the human-centered accessibility criteria in daily life situation such as the tripping risk. As described in the previous section, the tripping risk needs to be evaluated by taking account of the interaction between the environment and walking behavior of various people. Therefore, to evaluate the tripping risk by the human behavior simulation, the detailed articulated walking movements need to be generated, while considering the gait difference among individuals including the elderly. However, as shown in Table 1.1, in the previous simulations (1), (3), and (4), the pedestrian model cannot generate the 3D articulated walking movements similar to real human. In the simulation (2) proposed by Kakizaki et al. [Kakizaki 12], the pedestrian model can generate the articulated walking movement. However, the generated movements do not change in various groups of people such as the elderly, children, males, and females, so it is impossible to evaluate the human-centered accessibility criteria by taking account of the gait difference among individuals.

Furthermore, as described in the previous section, the ease of wayfinding needs to be evaluated in consideration both of signage system and wayfinding behavior of various people. As shown in Table 1.1, several algorithms for decision making based on visually perceived signage are proposed

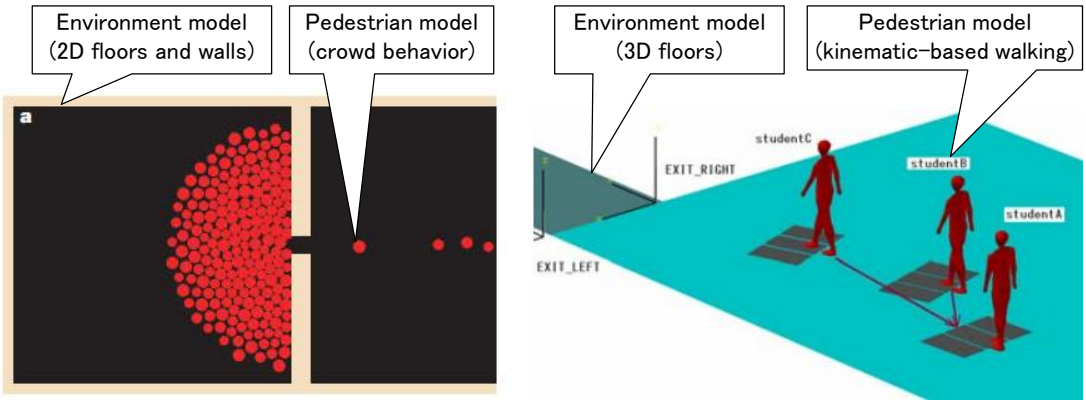

(a) Traditional 2D crowd simulation [Helbing 00] (b) 3D evacuation simulation [Kakizaki 12]

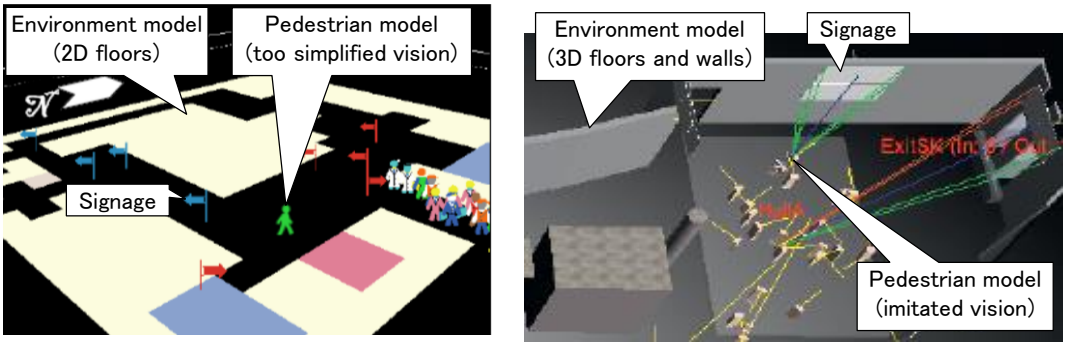

(c) 2D wayfinding simulation [Hajibabai 07] (d) 3D wayfinding simulation [Becker-Asano 14]

Fig. 1.3 Examples of current human behavior simulation studies

Table 1.1 Environment and pedestrian model representations in current human behavior simulation studies

	Environment model	Physical behavior of pedestrian model	Cognitive behavior of pedestrian model
(1) Traditional 2D crowd simulation [Helbing 00], [Duives 13]	Simplified 2D as-planned environment model	— Crowd behavior — Approximation to particle movements	— N/A
(2) 3D evacuation simulation [Kakizaki 12]	Simplified 3D as-planned environment model	— Crowd behavior — Articulated walking movements	— N/A
(3) 2D wayfinding simulation [Hajibabai 07]	Simplified 2D as-planned environment model	— Transition between rooms and corridors	— Decision making based on too simplified signage perception
(4) 3D wayfinding simulation [Becker-Asano 14], [Brunnhuber 12]	3D as-planned environment model	— Crowd behavior — Approximation to particle movements	— Decision making based on signage perception

in the previous wayfinding simulation (4). However, in the simulation (4), the 3D as-planned environment model is used in the simulation instead of the 3D as-is environment model. In addition, in the simulation (4), the physical behavior of the pedestrian model is also simplified to the 2D particle movements, as same as those in the simulations (1) and (3).

From the above reasons, in the previous human behavior simulation studies, it is impossible to

reliably evaluate the human-centered accessibility criteria in daily life situation such as the tripping risk and ease of wayfinding, from the aspects both of the environment models and the pedestrian models. Therefore, to realize the human-centered accessibility evaluation based on the human behavior simulation, the simulation needs to be improved to satisfy the following requirements:

- The environment model must represent the detailed 3D as-is situation of the environment without any labor-intensive and tedious modeling works.
- The pedestrian model can generate the detailed articulated walking movements of various people of different ages, genders, body dimensions, and abilities.
- The pedestrian model can simulate the human wayfinding behavior based on the visually perceived signage in the as-is environment model.
- The human behavior simulation can evaluate the human-centered accessibility criteria such as the tripping risk and ease of wayfinding, by taking account of the interaction between the as-is environment and the simulated physical and cognitive behaviors of various people.

1.1.3 Current ergonomics evaluation utilizing digital human model and their issues

For the human-centered accessibility evaluation, digital human model (DHM) technologies can be potentially utilized. As reviewed by Mochimaru et al. [Mochimaru 10], recently, many commercial DHM technologies such as Jack [SIEMENS] and RAMSIS [HUMAN SOLUTIONS ASSYST AVM] has been developed and utilized for ergonomics evaluation mainly in automotive design and manufacturing fields. For examples, Chang et al. [Chang 10] proposed an ergonomics evaluation system of predicting the physical load of a worker during assembly task in automotive factory based on the DHM, where the motion of the DHM was copied from the measurements of a worker's motion. In addition, Saito et al. [Saito 10] and Hareesh et al. [Hareesh 10] developed an ergonomics evaluation system for residential equipment, by predicting the affordable voluntary contraction of various people using the DHM, where the posture of the DHM was predicted by inverse-kinematics (IK)-based approach with a set of user-specified constrains such as foot or hand contact positions.

Therefore, these DHMs are potentially utilized for evaluating the human-centered accessibility criteria based on their predicted motions. However, the motion of the DHM needs to be specified by some semi-automatic methods such as IK-based approach [Saito 10] and optimization-based approach [Xiang 10], or copied from motion-capture (MoCap) data on real human. In the semi-automatic methods such as [Saito 10] and [Xiang 10], to make the DHM autonomously walk in a given environment model, several constraints such as the walking path, pelvis trajectories, and footprints need to be specified manually. This work becomes labor-intensive and tedious work as the environment becomes more large-scale. On the other hand, duplicating the DHM's motion from

the MoCap data on the pedestrian behaviors in a given environment is costly and basically impossible, since the long-time and exhaustive data collection are required in the real environment with various subjects of different ages, genders, and body dimensions. In addition, in order to make the DHM mimic the wayfinding behavior of real human, the detailed human measurements such as the eye tracking and think-aloud need to be conducted.

Therefore, for the accessibility evaluation, physical and cognitive behaviors of the DHM, such as walking route selection, articulated walking movements, and signage-based wayfinding behavior, need to be simulated in a given as-is environment. In addition, the DHM's behaviors need to be generated by taking account of the difference in human behaviors among individuals.

1.1.4 Current 3D as-is environment modeling technologies and their issues

As shown in Fig. 1.4 (a), recently, it has been becoming possible to easily acquire massive 3D point clouds of large-scale environments, with the progress of laser-scanning technologies. The acquired point clouds represent the detailed shape of the environment, and used in various fields, such as civil engineering, construction, city planning, and plant management. For example, the distance accuracy of a 3D laser-scanner, FARO Focus3D S120 [FARO], is ± 2 mm at 25 m. Therefore, as shown in Fig. 1.4 (b), small barriers and uneven outdoor terrains can be well captured as 3D point clouds, which are the indispensable elements for the tripping risk evaluation. Therefore, 3D laser-scanning technologies are potentially utilized for evaluating the human-centered accessibility criteria.

Recently, Andres et.al [Andres 13] proposed an accessibility evaluation system using mobile laser-scanning technology. In their study, first, the environment can be captured as the accurate and massive 3D point clouds by mobile laser scanner. Then, as shown in Fig. 1.5, the accessible and inaccessible walking route were automatically extracted as the criteria of urban accessibility, based on the ground and obstacles extracted from the point clouds. However, in their algorithm, the environmental hazards such as small barriers and uneven terrains were not considered and extracted, and the tripping risk did not evaluated.

As one insoluble problem of laser-scanned point clouds, as shown in Figs. 1.4 (b) and (c), they do not have the surface primitive such as triangular mesh, so the point clouds have a poor visibility. Therefore, utilizing only the laser-scanned point clouds is insufficient for the ease of wayfinding evaluation including the signage visibility and legibility evaluation.

On the other hand, as shown in Fig. 1.6, recently, structure-from-motion (SfM) is actively used for making 3D textured as-is environment model from a set of photographs. As an example, Furukawa et al. [Furukawa 09] proposed an excellent algorithm of reconstructing the interiors of building utilizing the SfM. As shown in Fig. 1.6 (b), in SfM, first, feature points are extracted from each photograph. Then, as shown in Fig. 1.6 (c), positions and orientations of each camera are

(a) 3D laser-scanning

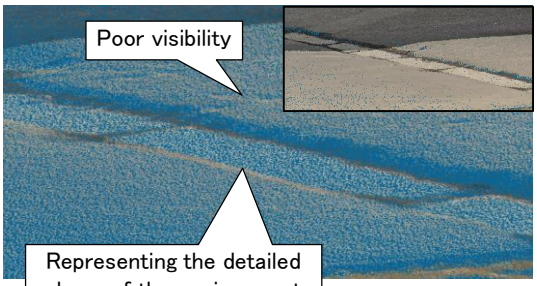

(b) Point clouds of outdoor terrains

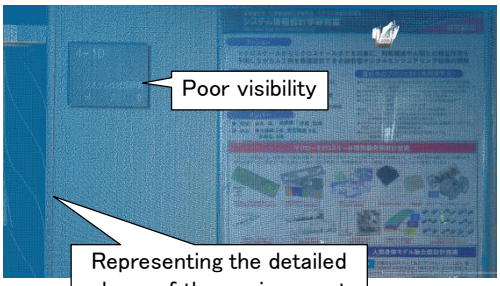

(c) Point clouds of walls and signage

Fig. 1.4 Overview and features of 3D laser-scanning technologies

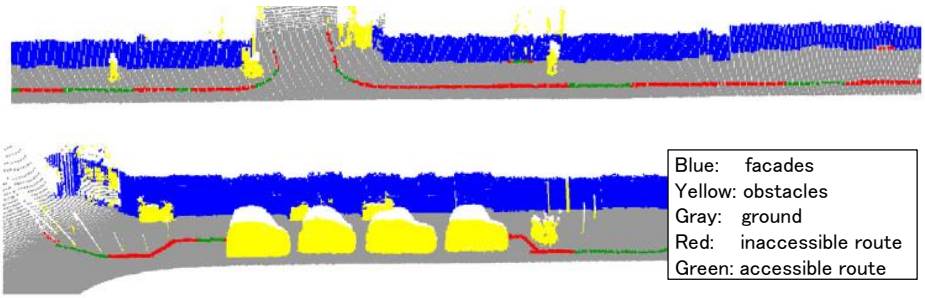

Fig. 1.5 Accessibility evaluation based on laser-scanned point clouds [Andres 13]

estimated based on the correspondences between extracted feature points by bundle adjustment process [Micheletti 15]. Finally, 3D mesh model with textures are created by multi-view stereo matching algorithm (i.e., dense matching) [Zhang 12]. By utilizing the SfM, as shown in Fig. 1.6 (d), visual signage can be modeled as 3D mesh model with textures. Therefore, there is a high potential of applying the SfM to the ease of wayfinding evaluation.

However, as one insoluble problem of SfM, the modeling accuracy of the SfM is significantly less than those of the laser-scanning due to the natures of bundle adjustment and dense matching. As shown in Fig. 1.6 (e), for example, the SfM sometimes makes the bumpy 3D mesh model on the flat floors. Therefore, SfM is basically inapplicable to the tripping risk evaluation.

From the above reasons, features of current 3D as-is environment modeling technologies can be

summarized as shown in Table 1.2. As shown in Table 1.2, due to the features of laser-scanning and SfM, it is insufficient to evaluate accessibility criteria including both tripping risk and ease of wayfinding only by using either laser-scanning or SfM. In addition, for human-centered accessibility evaluation, the interaction between as-is environment and human walking and wayfinding behaviors needs to be considered.

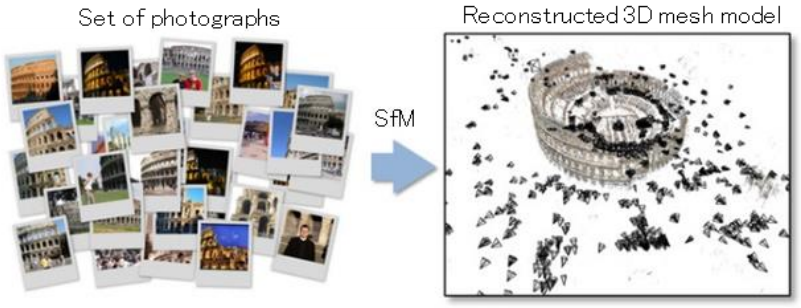

(a) Structure-from-motion [Agarwal 11]

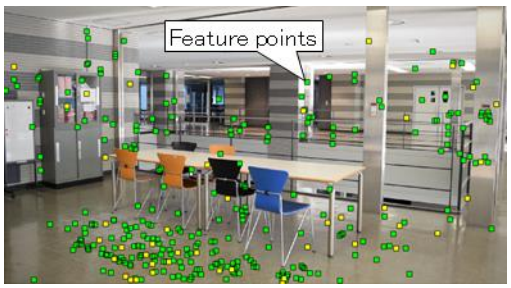

(b) Extracted feature points

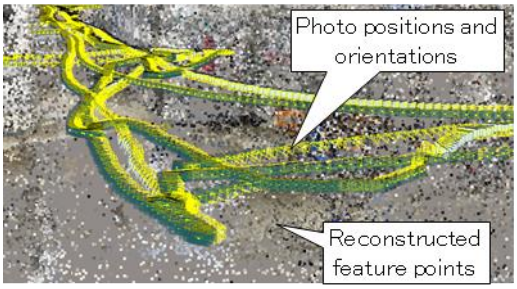

(c) Estimated camera positions and orientations

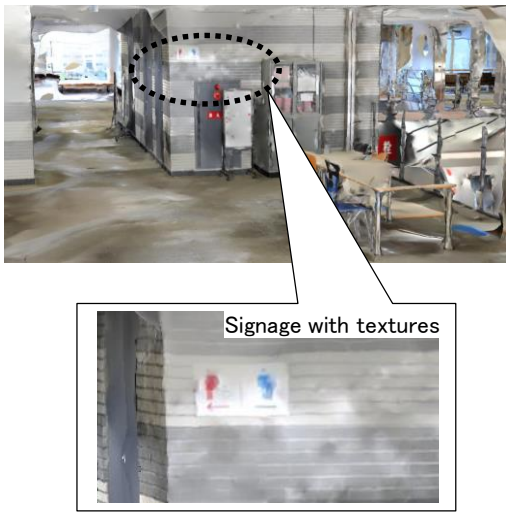

(d) Reconstructed 3D mesh model with textures

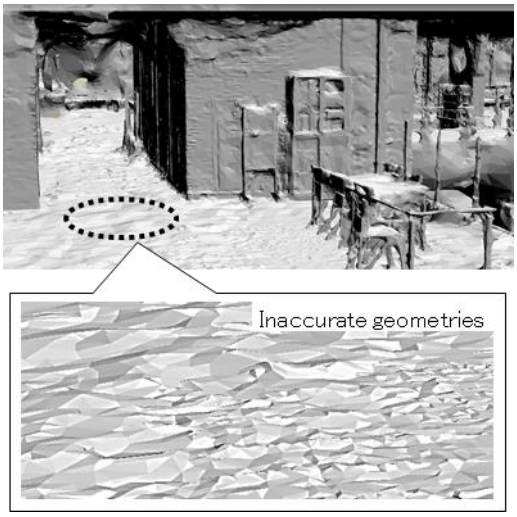

(e) Reconstructed 3D mesh model without textures

Fig. 1.6 Overview and features of structure-from-motion (SfM)

Table 1.2 Features of current as-is environment modeling technologies

	3D laser-scanning	Structure-from-motion (SfM)
Acquired data	— 3D point clouds	— 3D triangular mesh model with textures
Features of acquired data	— Representing the detailed shape the actual environment — Poor visibility	— having surface primitives with high-quality textures — Do not necessarily reproduce the actual shape of environment
Features from accessibility evaluation aspect	— Suitable for tripping risk evaluation — Insufficient for ease of wayfinding evaluation	— Suitable for ease of wayfinding evaluation — Insufficient for tripping risk evaluation

1.1.5 Summary of issues of current accessibility evaluation studies

Based on the discussions given in 1.1.2‐1.1.4, the issues when applying the current human behavior simulation, DHM, and as-is environment modeling technologies to the human-centered accessibility evaluation are summarized as follows:

(a) In the human behavior simulations, their pedestrian models cannot reproduce the detailed articulated walking movements and wayfinding behaviors in consideration of the difference among individuals.

(b) In the human behavior simulations, their environment models do not accurately represent as-is situation of the environments to be examined.

(c) Most of the human behaviors at the level of 3D articulated walking movements and of 3D visual perception-based decision making are modeled as the particle movements on a 2D space under mutual interactions, so that the human-centered accessibility criteria cannot be evaluated.

(d) The walking and wayfinding behaviors of DHMs cannot be simulated in the as-is environments without user-specified constrains such as walking path and footprints.

(e) The human-centered accessibility criteria cannot be evaluated based only on the as-is environment modeling technologies, since human physical and cognitive behaviors are not considered in the evaluation.

(f) Only using 3D laser-scanned point clouds is insufficient for evaluating the ease of wayfinding, since the point clouds do not have surface primitive with textures, and have a poor visibility.

(g) Only using SfM is insufficient for evaluating the tripping risk, since the geometric accuracy of the SfM is not enough to model small barriers and uneven terrains.

(h) The human-centered accessibility criteria including both the tripping risk and the ease of wayfinding cannot be evaluated in a single framework at the same time, from the aspects both of physical and cognitive behaviors of various people.

Therefore, this study aims to solve these issues for the reliable human-centered accessibility evaluation.

1.2 Objective of this study

Considering the background in the last section, the objective of this study is to develop a novel virtual accessibility evaluation system based on human behavior simulation, which is more accurate and reliable than previous one, by combining a DHM with as-is environment models. The system makes it possible to evaluate the human-centered accessibility criteria such as the tripping risk and the ease of wayfinding in an integrative framework, from the aspects of both physical and cognitive behaviors of various people of different ages, genders, and body dimensions.

Fig. 1.7 briefly illustrates the approaches for the issues summarized in 1.1.5. In Fig. 1.7, (a)-(g) represent the issues in 1.1.5. Details are given below.

(1) Approach for the issues (f) and (g)

As shown in Fig. 1.7, the issues (f) and (g) can be solved by building the accurate and detailed 3D as-is environment model both from laser-scanning and from SfM. Combing the laser-scanning with SfM makes it possible to construct the 3D as-is environment model which is applicable to the human centered accessibility evaluation including both tripping risk and ease of wayfinding evaluation.

(2) Approach for (b) and (e)

The issues of (b) and (e) can be solved by introducing the detailed 3D as-is environment model into the human behavior simulation. For this purpose, the 3D as-is environment model including the semantic information utilized by human behavior simulation such as navigation information, small barriers, and visual signage, is constructed based on both laser-scanning and SfM.

(3) Approach for (a) and (b)

The issues of (a) and (d) can be solved by generating the realistic and detailed articulated walking movements, and simulating wayfinding behavior of DHM in consideration of differences in human behaviors among individuals. As shown in Fig. 1.7, the walking and wayfinding behaviors of DHM are simulated based on MoCap data on actual human walking motion, and imitated visual perception, respectively. By combing DHM with 3D as-is environment models, the accurate and reliable human behavior simulation is realized for the human-centered accessibility evaluation.

(4) Approach for (c) and (h)

Finally, the issues (c) and (h) can be solved by combing the above solutions, i.e., evaluating the human-centered accessibility criteria such as the tripping risk and the ease of wayfinding based on the stochastic analysis of the simulated walking and wayfinding behaviors of DHM. The reliable accessibility evaluation from the aspects both of human physical and cognitive behaviors is

achieved by the accurate and reliable human behavior simulation.

The proposed virtual accessibility evaluation system in this study was established based on these approaches.

1.3 Overview and Features of this study

Fig. 1.8 shows an overview of the proposed virtual accessibility evaluation system. As shown in Fig. 1.8, the core part of this study is human behavior simulation, which mainly consists of autonomous walking simulation of the DHM (A2), and vision-based wayfinding simulation of the DHM (A4). The autonomous walking simulation is mainly used for the human-centered accessibility evaluation from physical aspects, i.e., tripping risk evaluation, while the vision-based wayfinding simulation is used for the evaluation from cognitive aspects, i.e., ease of wayfinding evaluation.

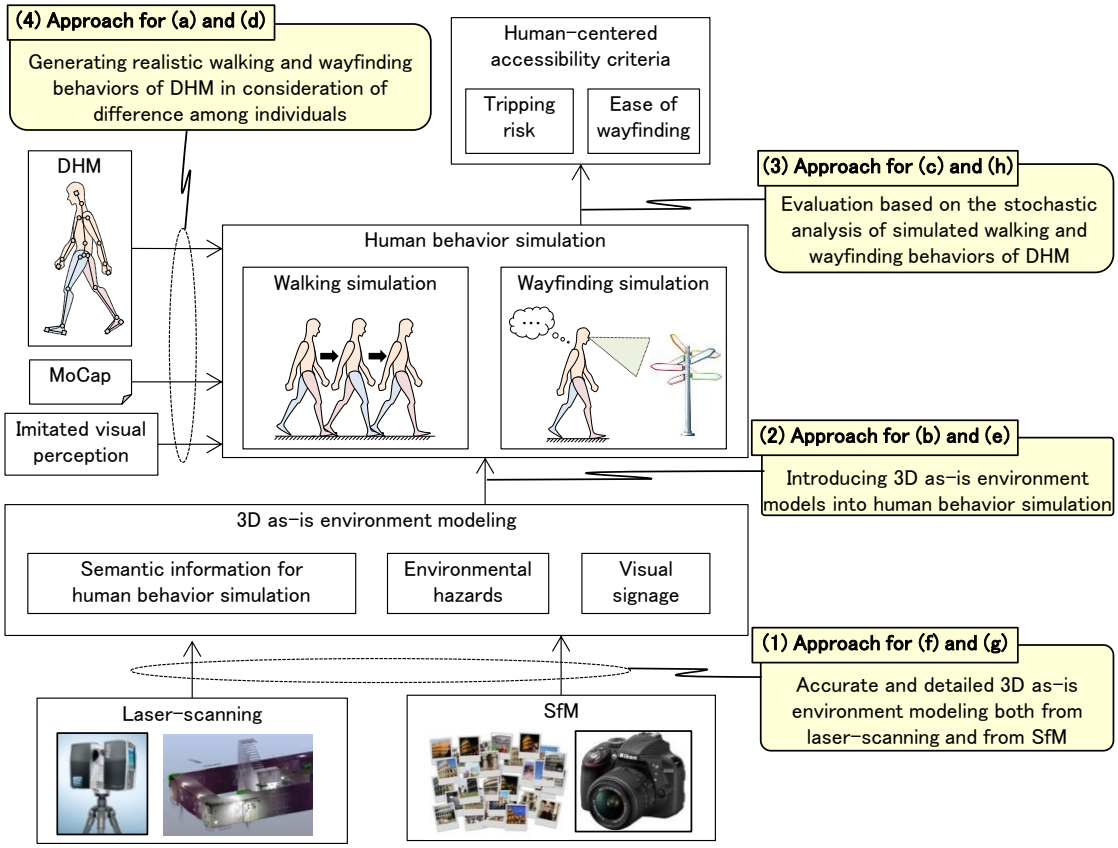

Fig. 1.7 Approaches of this study

In this study, the tripping risk is evaluated as the human-centered accessibility criteria from human physical aspect. Therefore, the following subsystems (A1)–(A3) are first developed mainly for the tripping risk evaluation.

(A1) As-is environment modeling from laser-scanned point clouds

In the proposed system, as shown in the part (A1) in Fig. 1.8, first, point clouds-based 3D as-is environment model is automatically generated from the laser-scanned point clouds. This model contains the semantic information, which is utilized by the human behavior simulation, such as the down-sampled points with normal vectors Q, the set of walk surface points W_S, the navigation graph G_N, and the tread boundary $B_{m,n}$. Q represents the entire shape of the environment, and W_S represents the walkable surfaces in the environment such as the floors and staircase treads. In addition, G_N represents the environmental pathways.

(A2) Autonomous walking simulation

As shown in the part (A2) in Fig. 1.8, an autonomous walking simulation of the DHM is performed in the point clouds-based as-is environment model. The walking simulation can be realized by three processes: the preference-based path selection, optimization-based motion planning, and MoCap-based adaptive walking motion generation. In the MoCap-based adaptive walking motion generation, the detailed articulated walking movements are generated based on a single reference MoCap data for flat walking, to reproduce the walking motion of various people such as the elderly, children, males and females. This MoCap data for flat walking is obtained from the gait DB [Kobayashi 13] provided by the national research institute, digital human research center (DHRC), where the data of 139 subjects ranging in age from 13 to 73 are contained.

(A3) Tripping risk evaluation

As shown in the part (A3) in Fig. 1.8, the tripping risk can be evaluated by taking account of the interaction between the point clouds-based as-is environment model and the simulated walking motion of the DHM. In the tripping risk evaluation, first, the possible tripping-hazard regions, i.e., the regions on which high possibility of tripping are expected, are automatically detected from the as-is environment model. After that, the autonomous walking simulation is performed with Monte Carlo simulation on the detected region, in order to quantitatively evaluate the tripping risk on the region in consideration of the differences in human gait among individuals. As a result, our system can detect the possible tripping-hazard regions exhaustively, and quantitatively evaluate the tripping risks on the regions varied in individuals.

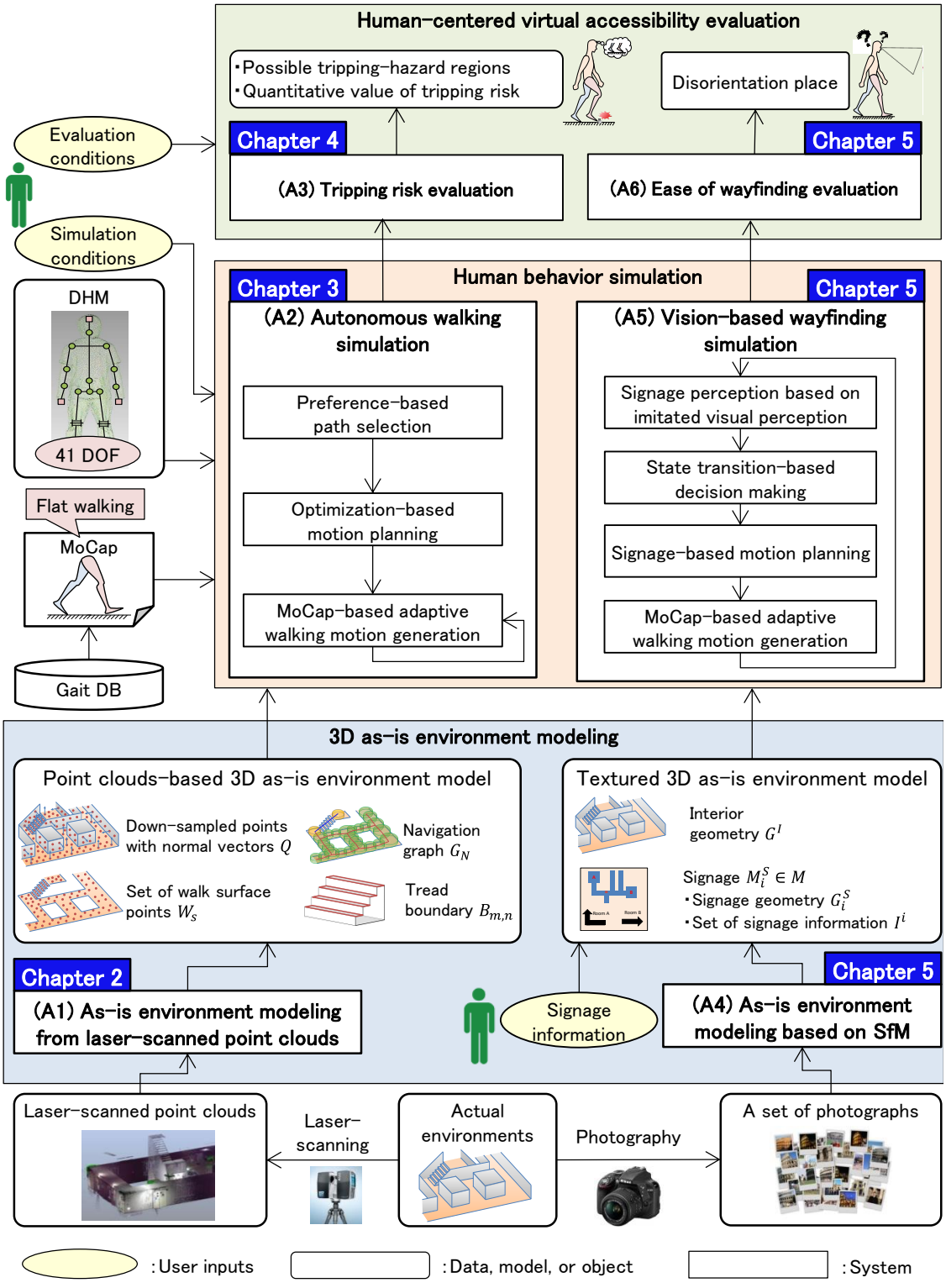

Fig. 1.8 Overview of this study and structures of chapters in this thesis

In this study, in addition to evaluating the tripping risk as the human-centered accessibility criteria from human physical aspect, the ease of wayfinding is further evaluated as the criteria from human cognitive aspect. Therefore, the following subsystems (A4)–(A6) are further developed.

(A4) As-is environment modeling based on SfM

As shown in the part (A4) in Fig. 1.8, the textured 3D as-is environment model is further generated based on the SfM, in addition to the point clouds-based as-is environment model. The model consists of the interior geometry G^I, and the set of signage M, where each signage $M_i^S \in M$ includes the signage geometry G_i^S and set of signage information I^i. The signage information $\boldsymbol{I}_k^i \in I^i$ can be assigned by the user, which includes its navigation and legibility information.

(A5) Vision-based wayfinding simulation

As shown in the part (A5) in Fig. 1.8, the vision-based wayfinding simulation of the DHM is performed in the point clouds-based 3D as-is environment model and the textured 3D as-is environment model. The wayfinding simulation can be realized by four processes: signage perception based on imitated visual perception, state transition-based decision making, signage-based motion planning, and MoCap-based adaptive walking motion generation. In the wayfinding simulation, the DHM automatically select its walking path according to the signage location, visibility, legibility, and continuity.

(A6) Ease of wayfinding evaluation

Finally, as shown in the part (A6) in Fig. 1.6, the ease of wayfinding can be evaluated based on the vision-based wayfinding simulation result in the 3D as-is environment model. In this study, as the ease of wayfinding evaluation, the disorientation place is automatically detected by taking account of the interaction between the as-is environment model and the simulated wayfinding behavior of the DHM, where the DHM cannot find any signage indicating its destination on the detected disorientation place.

By developing and integrating the subsystems (A1)–(A6), this study realizes the virtual accessibility evaluation system from the aspects both of physical and cognitive behaviors of various people of different ages, genders, and body dimensions.

In contrast to the previous accessibility evaluation studies intended in 1.1.2–1.1.4, our system makes it possible to evaluate the human-centered accessibility criteria such as tripping risk and ease

of wayfinding based on the simulated walking and wayfinding behavior of the DHM in the as-is environment model. The features of the proposed system can be summarized as follows:

- Our system can automatically construct the large-scale 3D as-is environment models regardless of indoor or outdoor environments by utilizing both laser-scanning and SfM.
- The system enables a DHM to autonomously walk in the point clouds-based as-is environment model, while reproducing its articulated walking movements similar to the MoCap data of a person with specified age, gender, and body dimensions.
- The system can exhaustively and quantitatively evaluate the tripping risk in the environment by taking account of the interaction between the as-is environment model and the simulated walking motion of DHM. It can clarify the difference in the tripping risk among individuals, e.g., the difference in the tripping risk between younger and older people.
- The system enables a DHM to simulate the human wayfinding behavior based on the imitated visual perception by taking account of the signage location, visibility, legibility, and continuity.
- As the ease of wayfinding evaluation, the system can detect disorientation places in the environment, where the DHM cannot find its walkway due to the inappropriate signage location, visibility, legibility, and continuity.
- The system realizes an advanced reliable human-centered accessibility evaluation technologies, by combining and improving the technologies such as human behavior simulation, digital human modeling, and as-is environment modeling.

1.4 Organization of this thesis

As shown in Fig. 1.8, this thesis is divided into 6 chapters including this chapter. The organization of this thesis is as follows.

In Chapter 2, as shown in the part (A1) in Fig. 1.6, an algorithm of as-is environment modeling from laser-scanned point clouds is introduced. In addition, the effectiveness, efficiency and accuracy of the as-is environment modeling are validated using the point clouds of indoor, outdoor, and urban environments.

In Chapter 3, as shown in the part (A2) in Fig. 1.6, an algorithm of the autonomous walking simulation of the DHM is introduced. The effectiveness and efficiency of the walking simulation are validated in the 3D as-is environment models. In addition, the accuracy of the walking simulation is further validated by a comparison of the walking motion between the DHM and the MoCap data on actual human motion.

In Chapter 4, as shown in the part (A3) in Fig. 1.6, an algorithm of the tripping risk evaluation

based on the autonomous walking simulation is introduced. The effectiveness and efficiency of the algorithm are validated in the point clouds of virtual indoor and real outdoor environments. In addition, the tripping risk evaluation result is further validated by comparing the simulated risk with the risk measured from younger people in a walking experiment.

In Chapter 5, as shown in the parts (A4)–(A6) in Fig. 1.6, the algorithms of the as-is environment modeling based on the SfM, the vision-based wayfinding simulation of the DHM, and the ease of wayfinding evaluation are introduced. The effectiveness and efficiency of the algorithm are validated in two types of indoor environments. In addition, the ease of wayfinding evaluation results are validated by comparing the simulated wayfinding behavior of the DHM with the wayfinding behavior measured from younger people in a wayfinding experiment.

Finally, in Chapter 6, the overall conclusions of the former chapters, and remaining issues and future works are summarized.

Chapter 2 3D As-is Environment Modeling from Laser-scanned Point Clouds

2.1 Background

As discussed in Chapter 1, for the reliable human-centered accessibility evaluation based on human behavior simulation, detailed as-is environment models must be constructed. In addition, the as-is environment models must have the environmental information utilized for the human behavior simulation consisting of the autonomous walking simulation and the vision-based wayfinding simulation. Table 2.1 shows the essential environmental information for the human behavior simulation. As shown in Table 2.1, the basic environmental information including walkable surfaces, pathway structure, and stairs must be modeled for the human behavior simulation. In addition, the detailed shape of the environment including environmental hazards such as small barriers and uneven walking terrains must be modeled for the human-centered accessibility evaluation from the physical aspect, i.e., tripping risk evaluation. Furthermore, the visual appearance of signage must be modeled for the human-centered accessibility evaluation from the cognitive aspect, i.e., ease of wayfinding evaluation. The information needs to be modeled as a part of "as-is" environmental model instead of as-planned environment model.

As mentioned in the ISO guideline [ISO 21542, 11], the accessibility needs to be ensured in both indoor and outdoor environments. Therefore, the 3D as-is environment models must be constructed regardless of indoor or outdoor environments.

Table 2.1 Essential environmental information for human behavior simulation

Environmental information		Drawing	Purposes	Modeling elements
Basic environmental information	Walkable surfaces	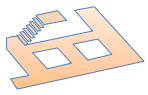	— For identifying walkable surfaces — For determining footprints of DHM	— Floors — Slopes — Staircase treads — Uneven terrains
	Pathway structure	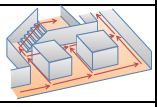	— For navigating DHM along pathways	— Width of the pathways — Connection between the pathways
	Stairs	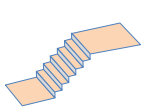	— For making DHM walk on stairs	— Start and end position of the stairs — Nosing of the treads — Dimensions of the stairs such as the rise, run, and tread width
Detailed shape	Environmental hazards	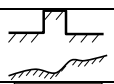	— For the tripping risk evaluation	— Small barriers — Uneven terrains
Visual appearance	Visual signage	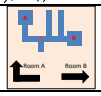	— For navigating DHM based on signage — For the ease of wayfinding evaluation	— Visual signage including its legibility and navigation information

As reviewed by Duives et al. [Duives 13], in the current human behavior simulation studies, simplified as-planned environment models are manually created, and used for the simulation. However, manually creating the detailed as-is environment model is basically impossible, since the labor-intensive and detailed modeling and measurement works are required. Therefore, an automatic and accurate as-is environment modeling technology needs to be developed for the human behavior simulation.

To solve the problem, recent as-is environmental modeling technologies such as laser-scanning and SfM can be potentially utilized. By utilizing laser-scanning and SfM, environments can be acquired as 3D point clouds, and textured 3D mesh model, respectively. In general, laser-scanned point clouds consist of a set of point having the attribute of its 3D position (x, y, z), color $(\mathrm{R}, \mathrm{G}, \mathrm{B})$, and intensity. On the other hand, textured 3D mesh model generated by SfM contains a set of the surface primitive such as triangular mesh with textures. However, these data only represent the detailed geometries and textures of the environment. Therefore, for the human behavior simulation, the environmental information shown in Table 2.1 needs to be extracted and modeled automatically from the laser-scanned point clouds or the textured 3D mesh model.

Considering the above discussions, the requirements for as-is environment modeling can be summarized as follows:

(a) Basic environmental information including walkable surfaces, pathway structure, and stairs must be modeled as a part of the 3D as-is environment models.

(b) Detailed shape such as small barriers and uneven walking terrains must be modeled as a part of the 3D as-is environment models.

(c) Visual appearance of signage must be modeled as a part of the 3D as-is environment models.

(d) The 3D as-is environment models must be constructed regardless of indoor or outdoor environments.

(e) The 3D as-is environment models must be created automatically.

In this chapter, we aim to develop an as-is environment modeling algorithm satisfying these requirements.

2.2 Related work on 3D environment modeling

2.2.1 Environment modeling in current human behavior simulation

In the current human behavior simulation studies [Duives 13], the environment modeling method is closely related to the method of controlling the pedestrian model. Helbing et al. [Helbing 00] proposed a crowd simulation based on social force model. In their study, the pedestrian model is

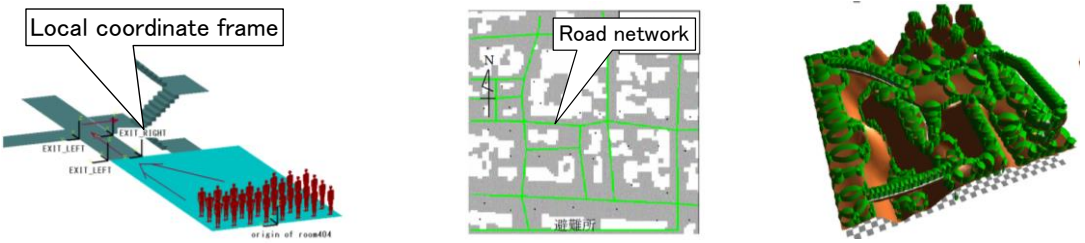

(a) 3D as-planned environment model [Kakizaki 12]

(b) Road network extracted from point clouds of ALS [Ueno 07]

(b) Navigation graph [Pettre 05]

Fig. 2.1 Environment models used in current human behavior simulation

moved based on the social force from the other pedestrian models and surrounding walls in a 2D as-planned environment model. Therefore, their environment model was manually created as a set of boundary lines of the floors. As reviewed by Duives et al. [Duives 13], several human behavior simulations used such simplified 2D as-planned environment models, which were created manually.

On the other hand, Kakizaki et al. [Kakizaki 12] proposed an evaluation-planning simulator that realized kinematics-based walking simulation of the DHMs in a 3D as-planned environment model. In their study, the environment model consists of a set of 3D surfaces representing the floors and the stair treads. However, their environment model was created manually, so the environment model necessarily represent the as-is environment. In addition, as shown in Fig. 2.1 (a), the local coordinate frame need to be assigned to each facility model such as rooms and corridors, for navigating the DHM between the facilities. This is labor-intensive and tedious work as the environment becomes more large-scale.

As described above, in most of the human behavior simulation studies such as [Duives 13] and [Kakizaki 12], simplified as-planned environment models are manually created, and used for the simulation. Therefore, in these studies, satisfying the requirement (b) and (e) in Section 2.1 is basically impossible.

On the other hand, several studies were conducted on making the environment models automatically for human behavior simulation. As shown in Fig. 2.1 (b), Ueno et al. [Ueno 07] proposed an algorithm of making an as-is road network model from 3D point clouds acquired by air-bone laser-scanning (ALS). In their algorithm, a road network of urban environments was automatically extracted from the point clouds for shelter simulation. Therefore, the extracted road network represents the as-is situation of the environment. However, their algorithm focuses only on extracting the broad road utilized for the shelter simulation, and extracting narrow walkway utilized in daily life situation was neglected. In addition, as shown in Fig. 2.1 (b), modeling detailed shape of the environment such as uneven terrains and small barriers was also neglected in their study. Furthermore, due to the nature of their algorithm, it has no applicability to the as-is environment modeling of indoor environment. Therefore, their study cannot satisfy the requirements (a)–(d) in

Section 2.1.

On the other hand, as shown in Fig. 2.1 (c), in the simulation by Pettre et al. [Pettre 05], a navigation graph representing free spaces and environmental connectivity can be generated automatically from a 3D mesh model of an environment. In their study, the walking path of each pedestrian model is automatically selected by specifying start and goal points on the navigation graph. Then, each pedestrian model is commanded to walk automatically along the selected path. Their algorithm is potentially utilized for the as-is environment modeling in this study. However, in their study, there is no discussion as to whether the 3D mesh model was as-is or as-planned. In addition, they used a simple-shaped 3D mesh model, which is too rough to capture the detailed shape and structure of as-is indoor and outdoor environments. Furthermore, modeling stairs were neglected in their study. Therefore, in these studies, satisfying the requirements (a)–(c) in Section 2.1 is basically impossible.

2.2.2 As-is environment modeling from 3D laser-scanned point clouds

3D as-is environment modeling from massive laser-scanned point clouds has been actively studied. As shown in Fig. 2.2, the goal of these studies was to automatically reconstruct indoor environments [Oesau 14] and extract semantic objects such as floors, walls and ceilings [Nüchter 08], [Xiong 13], household goods [Rusu 13], and a constructive solid geometry (CSG) model of environments [Xiao 14] from massive laser-scanned point clouds. Existing algorithms and related techniques have been reviewed in the literature [Tang 10]. These studies can construct the as-is environment model automatically, and are potentially utilized for the as-is environment modeling in this study. However, these studies focus on general object recognition for environmental modeling, and do not necessarily aim for human behavior simulation. Therefore, modeling pathways and stairs were neglected in these studies.

On the other hand, as shown in Figs. 2.2 (a), (c), and (d), several studies such as [Oesau 14], [Xiong 13], and [Xiao 14] aim to make simplified solid or wireframe model of the environment, while approximating small barriers and uneven terrains to the completely flat surfaces. However, the lack of modeling and recognition greatly affects the results of both human behavior simulation and accessibility evaluation. For example, if the small barriers were not modeled as a part of the environment model, the tripping risk evaluation results become different from the actual one. In addition, these algorithms were designed to well reconstruct walled indoor environments, and inapplicable to reconstruction of outdoor environments.

On the other hand, as shown in Fig. 2.2 (b), in the algorithm of Nüchter et al. [Nüchter 08], the original 3D laser-scanned point clouds were also used as a part of the as-is environment model, and small barriers and uneven terrains were not approximated inappropriately. Such semantic labeling of the point clouds can be considered as a suitable approach for the human-centered accessibility

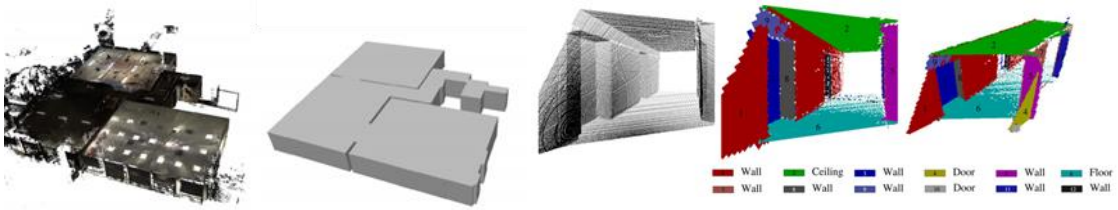

(a) Building reconstruction (b) Semantic labeling of point clouds

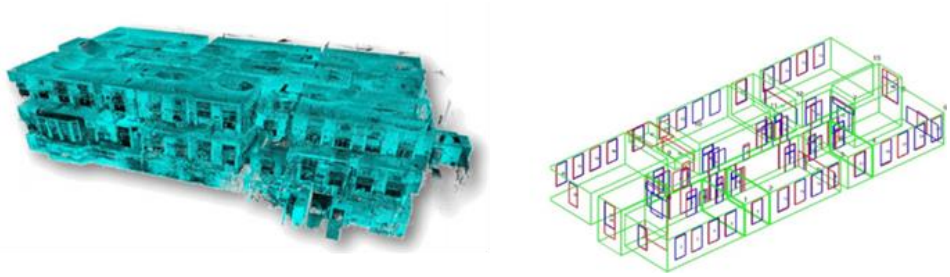

(c) Recognition of semantic objects [Xiong 13]

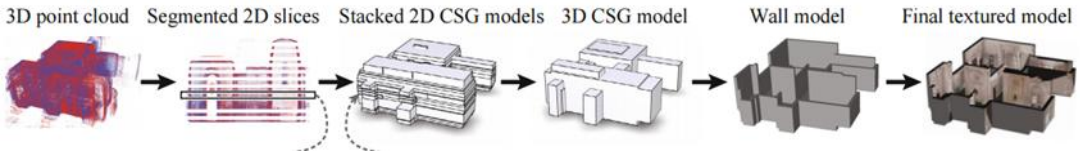

(d) CSG model construction [Xiao 14]

Fig. 2.2 As-is environment modeling from laser-scanned point clouds

evaluation. However, in the algorithm, the structures of environmental pathways and stairs were neglected to recognize.

As discussed in 1.1.4, one insoluble problem of laser-scanning is that the acquired point clouds do not have the surface primitive such as triangular mesh, so the point clouds have a poor visibility. Therefore, modeling visual appearance of signage as a part of the as-is environment model is basically impossible only using laser-scanned point clouds.

As discussed above, the studies for as-is environment modeling from laser-scanned point clouds cannot satisfy the all requirements (a)–(d) in Section 2.1 at the same time.

2.2.3 As-is environment modeling utilizing Structure-from-Motion

In contrast to laser-scanning technologies, SfM is actively used for making textured 3D as-is environment model from a set of photograph [Furukawa 09]. In addition, some consumer software is available for SfM, such as ContextCapture [Bentley] and Photoscan [Agisoft]. In SfM, the textured 3D as-is environment models can be automatically generated by two processes: bundle adjustment [Micheletti 15] and dense matching [Zhang 12]. In the former process, relative position

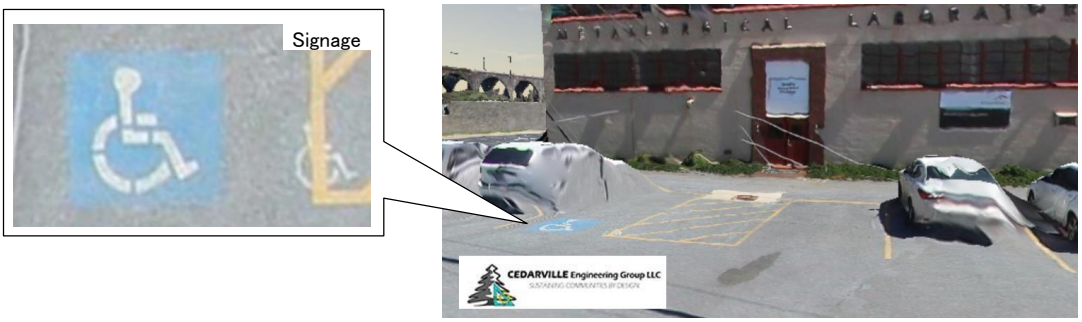

(a) Textured 3D mesh model [Bentley]

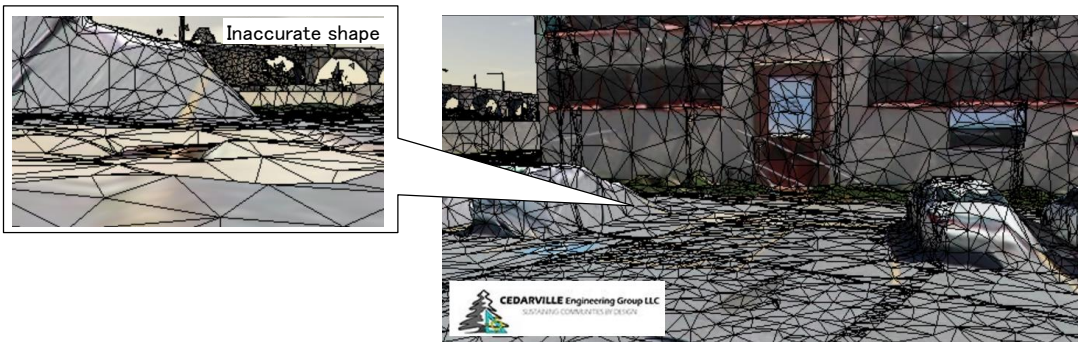

(b) Textured 3D mesh model [Bentley] (rendered with edges)

Fig. 2.3 Environment reconstruction utilizing SfM

and orientation of photographs are estimated based on the relation between the feature points extracted from each photograph, while minimizing the reprojection error of the feature points [Micheletti 15]. After that, in the latter process, 3D triangular meshes with textures are created using the multi-view stereo matching [Zhang 12]. The generated 3D textured as-is environment model has been utilized for several purposes such as the landform monitoring [Micheletti 15], since the model contains the high-quality textures.

Therefore, by utilizing SfM, as shown in Fig. 2.3 (a), visual appearance of signage can be modeled as a textured 3D mesh model. As recommended by Burunnhuber et al. [Burunnhuber 12], using realistic and textured 3D environment models enable the simulation user to easily understand the results of the human behavior simulation.

However, as shown in Fig. 2.3 (b), one insoluble problem of SfM is that the modeling accuracy of SfM is significantly less than those of laser-scanning due to the natures of bundle adjustment and dense matching. Therefore, SfM is basically inapplicable to the human-centered accessibility evaluation from physical aspect, i.e., the tripping risk evaluation.

As discussed above, SfM is suitable for introducing visual appearance of signage into the as-is environment model, and can satisfy the requirement (c) in Section 2.1. However, due to its modeling accuracy, it is impossible to satisfy the other requirements based only on SfM.

Table 2.2 Features of current environment modeling technologies

	(a) Basic environmental information	(b) Detailed shape	(c) Visual appearance	(b) Environmental independency	(e) Automatic modeling
Manual modeling in human behavior simulation [Duives 13]	✔ — Available	× — As-planned and too simplified	✔ — Available	✔ — Both for indoor and outdoor environments	× — Manual
Road network construction in human behavior simulation [Ueno 07]	× — Cannot model small pathways and stairs	× — Too simplified	× — N/A	× — Only for road network	✔ — Automatic
Navigation graph construction in human behavior simulation [Pettre 05]	× — Cannot model stairs	× — Too simplified	× — N/A	✔ — Both for indoor and outdoor environments	✔ — Automatic
Environment reconstruction from laser-scanned point clouds [Tang 10]	× — Cannot model pathways and stairs	× — Approximated	× — Poor visibility	× — Cannot be applied to outdoor environments	✔ — Automatic
Semantic labeling of laser-scanned point clouds [Nüchter 08]	× — Cannot model pathways and stairs	✔ — Accurate	× — Poor visibility	× — Unclear	✔ — Automatic
Environment reconstruction utilizing SfM [Furukawa 09]	× — N/A	× — Inaccurate	✔ — High quality textures	✔ — Both for indoor and outdoor environments	✔ — Automatic

Meaning of the mark: ✔: Sufficient ×: Insufficient

2.2.4 Summary of features of current 3D environment modeling studies and as-is environment modeling approach in this study

Based on the discussions given in 2.2.1–2.2.3, the features of the current environment modeling technologies are summarized in Table 2.2. In the table, (a)–(e) represent the requirements in Section 2.1. As shown in the table, the current environment modeling technologies cannot satisfy all of the requirements, and are insufficient for the as-is environment modeling for the human behavior simulation aiming to the human-centered accessibility evaluation.

Considering the features in Table 2.2, it is a suitable approach by utilizing both laser-scanning and SfM, to satisfy the requirements (b) and (c) at the same time. In addition, in the study of navigation graph construction in human behavior simulation [Pettre 05], the basic environmental information without stairs can be automatically constructed for both indoor and outdoor environment.

Therefore, in this study, we aim to realize the as-is environment modeling satisfying all of the requirements (a)–(e) by combining these studies. Considering the features of laser scanning and SfM, it is reasonable approach to dived the as-is environment modeling process into two steps: (1) extracting the basic environmental information from the laser-scanned point clouds, (2) modeling visual appearance of signage based on SfM. In addition, to represent the detailed shape of the

environment, the modeling algorithm needs to designed to keep the laser-scanned point clouds as a part of the as-is environment model. To realize the former step (1), point clouds-based as-is environment modeling algorithm needs to be newly developed, while the latter step (2) could be realized by utilizing SfM without complex modeling algorithms. Therefore, in this chapter, we only focus on realizing the point clouds-based as-is environment modeling algorithm, and the SfM-based modeling algorithm are introduced in Chapter 5.

2.3 Objective and overview

As discussed in the last section, the objective of this chapter is to develop an algorithm of as-is environment modeling from laser-scanned point clouds, which is suitable for the human behavior simulation aiming to the human-centered accessibility evaluation. The point clouds-based 3D as-is environment model includes the environmental information such as walkable surfaces, pathway structure, stairs, and detailed shape of the environments. On the other hand, an algorithm of constructing textured 3D as-is environment model including visual appearance of signage based on SfM is introduced in Chapter 5, since the algorithm closely relates to the vision-based wayfinding simulation and ease of wayfinding evaluation.

Fig. 2.4 shows an overview of the propose point clouds-based as-is environment modeling, and the relations to the other chapters in this thesis. As shown in Fig. 2.4, the point clouds-based 3D as-is environment model is utilized both for the autonomous walking simulation and for the vision-based wayfinding simulation, while the textured 3D as-is environment model is utilized only for the vision-based wayfinding simulation.

Table 2.3 shows components of the point clouds-based 3D as-is environment model. In this study, as shown in Fig. 2.4 and Table 2.3, down-sampled points with normal vectors $Q = \{(\boldsymbol{q}_i, \boldsymbol{n}_i)\}$, set of walk surface points $W_S = \{W_i\}$, navigation graph G_N, and tread boundaries $B_{m,n}$ can be automatically generated as a part of the point clouds-based 3D as-is environment model. Q represents the entire shape of the environments, and W_S represents the walkable surfaces in the environment such as the floors and staircase treads. In addition, G_N represents the environmental pathways, and $B_{m,n}$ represents the boundary lines of the nth stairstep in the mth stairs.

Note that modeling the objects with significant low-reflectance such as windows and glasses is not covered in this study, since it is impossible to capture them by the laser scanner as 3D point clouds in principle.

The rest of this chapter is organized as follows. First, the algorithms of the as-is environment modeling from laser-scanned point clouds are described in Section 2.4. After that, the modeling and validation results using the point clouds of indoor, outdoor, and urban environments are shown in Section 2.5. Finally, the summary of this chapter is described in Section 2.6.

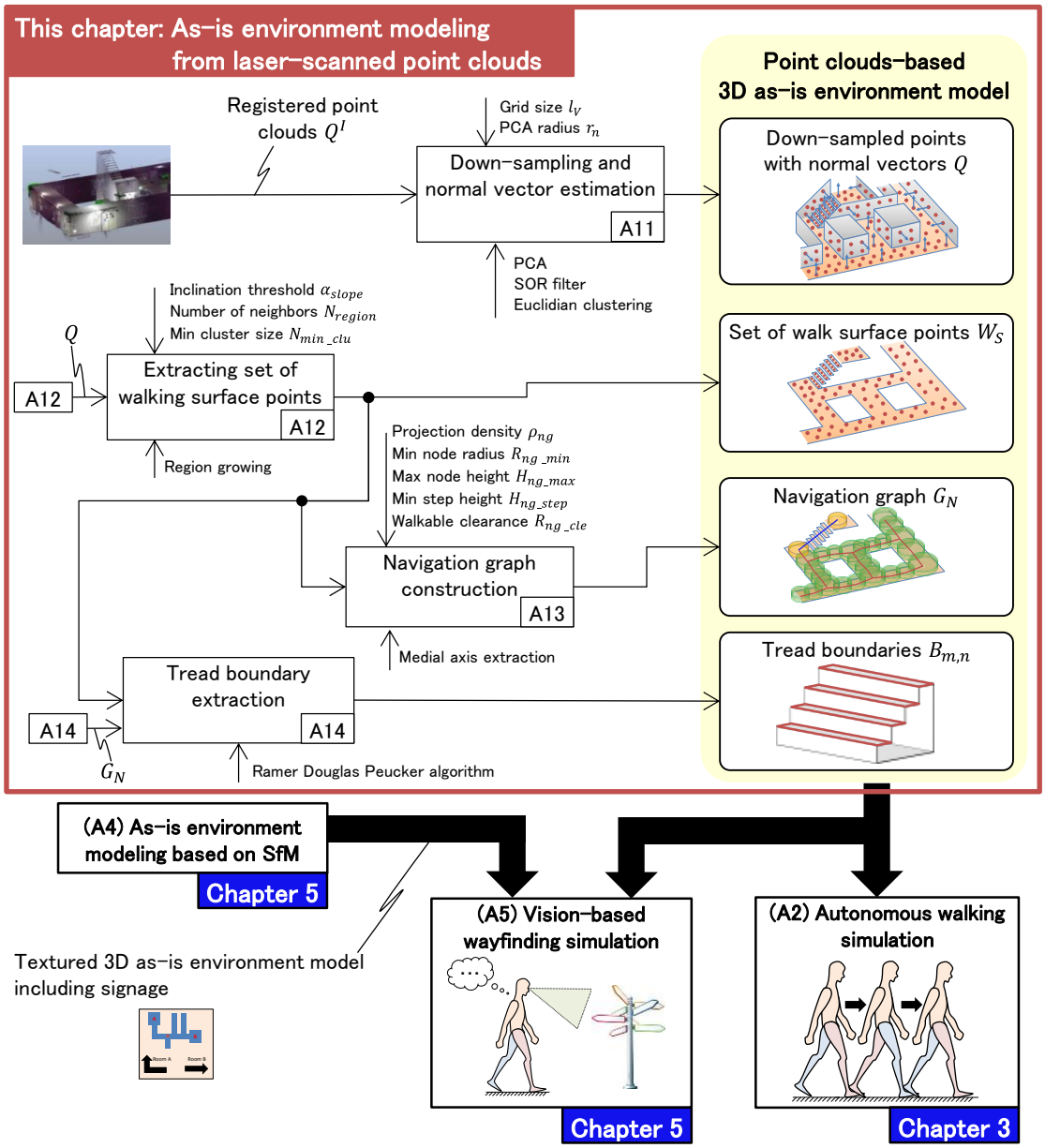

Fig. 2.4 Overview of 3D as-is environment modeling from laser-scanned point clouds

Table 2.3 Components of point clouds-based 3D as-is environment model

Components	Drawing	Purposes	Modeling elements
down-sampled points with normal vectors $Q = \{(\boldsymbol{q}_i, \boldsymbol{n}_i)\}$	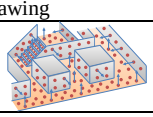	— For representing the entire environment	— Entire environment
Set of walk surface points W_S	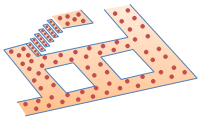	— For identifying the walkable surfaces — For determining the footprints of the DHM — For navigating the DHM	— Floors — slopes — Staircase treads — Uneven terrains — Environmental hazards including small barriers
Navigation graph G_N	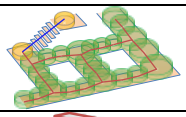	— For navigating the DHM — For making the DHM walk on the stairs	— Connection between the pathways — Start and end position of the stairs
Tread boundaries $B_{m,n}$	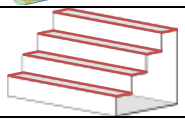	— For making the DHM walk on the stairs	— Nosing of stair treads — Dimensions of stairs such as rise and run

2.4 Methods of 3D as-is environment modeling from laser-scanned point clouds

2.4.1 Creating down-sampled point clouds with normal vectors

In this study, as shown in Fig. 2.4, the 3D as-is environment model is constructed from registered point clouds of an environment. Therefore, before the environment modeling, multiple laser-scanned point clouds are first merged to make one registered point cloud $Q^I = \{\boldsymbol{q}_i^I\}$. In general, Q^I consists of massive and noisy point clouds. Therefore, first, Q^I is down-sampled. After that, noisy points and outliers are removed from the down-sampled points. Details are given below.

(1) Down-sampling using voxel grid filtering

First, Q^I is down-sampled using a voxel grid filtering [Rusu 13]. As shown in Fig. 2.5, a voxel grid is assigned to the entire point clouds, where the length l_V of a side of each voxel is specified by the user according to the desired density of the point clouds. Then, a set of points $Q^{x,y,z} = \{\boldsymbol{q}_i^I\}$ included in a voxel $V^S(x, y, z)$ are extracted from Q^I, where x, y, and z represent the indices of each voxel with respect to the coordinate system of Q^I. Finally, a down-sampled point $\boldsymbol{q}_i$ is calculated as the centroid of the points $\boldsymbol{q}_i^I \in Q^{x,y,z}$, and inserted into a set of down-sampled points Q^D. By performing these processes to all voxels, the set of down-sampled point Q^D is completely obtained from Q^I.

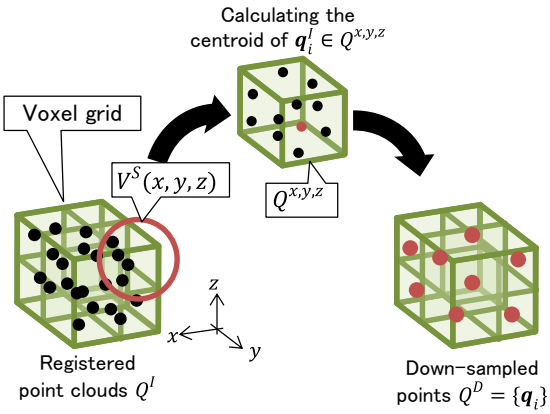

Fig. 2.5 Down-sampling using voxel grid

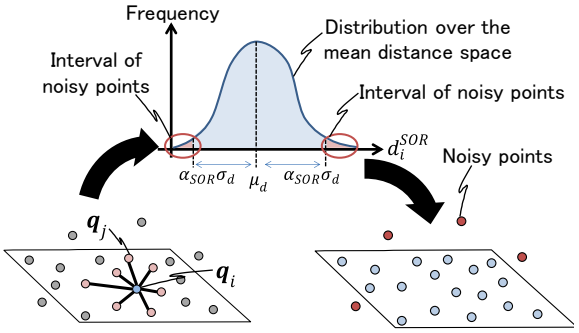

Fig. 2.6 Noise removal using SOR filter

(2) Removing noisy points using SOR filter

After the down-sampling, noisy points are removed from the down-sampled points $Q^D = \{\boldsymbol{q}_i\}$. In this study, the noisy points are removed by applying the statistical outlier removal (SOR) filter [Rusu 13] to Q^D. As shown in Fig. 2.6, in the SOR filtering, first, for each point $\boldsymbol{q}_i \in Q^D$, its k-nearest neighboring points $K_i = \{\boldsymbol{q}_j\}$ are extracted using k-dimensional-tree (kd-tree) constructed from Q^D. Then, the mean distance d_i^{SOR} between $\boldsymbol{q}_i$ and $K_i = \{\boldsymbol{q}_j\}$ is calculated by the following equation (2.1).

$$d_i^{SOR} = \frac{\sum_{j=0}^{k-1}(\|\boldsymbol{q}_i - \boldsymbol{q}_j\|)}{k} \tag{2.1}$$

where the number of nearest points k is specified as $k = 26$ so as to obtain the surrounding point of $\boldsymbol{q}_i$. Then, as shown in Fig. 2.6, the noisy points are removed based on a distribution of d_i^{SOR} for Q^D. In particular, if the point $\boldsymbol{q}_i$ satisfies the following conditions, $\boldsymbol{q}_i$ is removed as the noisy point.

$$d_i^{SOR} < \mu_d - \alpha_{SOR}\sigma_d \text{ , OR } d_i^{SOR} > \mu_d + \alpha_{SOR}\sigma_d \tag{2.2}$$

where μ_d, σ_d, and α_{SOR} represent the mean and standard deviation of the mean distance distribution, and user-specified threshold value representing the predicted ratio of noisy points to Q^D, respectively. α_{SOR} can be determined in accordance with laser-scanning conditions, such as capability of laser-scanner. In this study, α_{SOR} is specified as $\alpha_{SOR} = 2.5$, under the assumption that 1-5 % noisy points are generally included in Q^D.

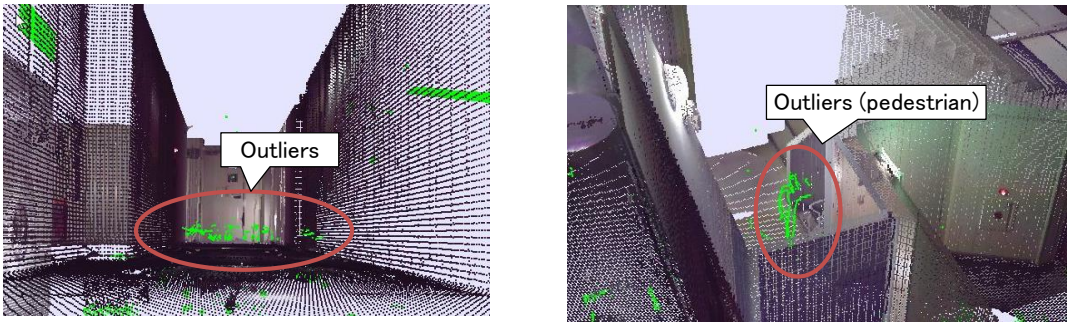

Fig. 2.7 Removed outliers using Euclidian clustering filter

(3) Removing outliers based on Euclidian clustering filter

After that, in addition to the SOR filter, Euclidian clustering filter [Rusu 13] is further applied to Q^D. In the algorithm, Q^D is first divided into a set of clusters by Euclidian clustering algorithm. Then, assuming that point clouds representing the environments are included in a maximum cluster having the maximum number of points, the point clouds included in the other clusters are removed from Q^D as the outliers. As a result of the Euclidian clustering filter, as shown in Fig. 2.7, the outliers such as the points over the floors and ones representing the pedestrian can be removed.

Finally, normal vectors at the down-sampled points Q^D are estimated using principal component analysis (PCA) on the local neighboring points with a user-specified radius r_n. These point clouds with normal vectors $Q = \{(\boldsymbol{q}_i, \boldsymbol{n}_i)\}$ $(\boldsymbol{q}_i \in Q^D)$ are used as a part of the 3D as-is environment model. The parameter setting strategies of l_V and r_n are introduced in Section 2.5.

2.4.2 Extracting set of walk surface points

After the down-sampling and noise removal, the set of walk surface points $W_S = \{W_i\}$ representing walkable surfaces such as floors and stairsteps is automatically extracted from the down-sampled points Q.

As shown in Fig. 2.8 (a), first, if an angle between a normal vector $\boldsymbol{n}_j$ at a point $\boldsymbol{q}_j$ and a vertical vector $\boldsymbol{v} = [0,0,+1]$ is smaller than the user-specified threshold α_{slope}, then the point is added into a set of horizontal points $Q_H = \{\boldsymbol{q}_j\}$ located on a horizontal plane.

After that, as shown in Fig. 2.8 (b)–(d), the horizontal points Q_H are clustered into a set of walk surface points $W = \{W_k \subseteq Q_H\}$ using a region-growing algorithm based on a k-nearest search as follows.

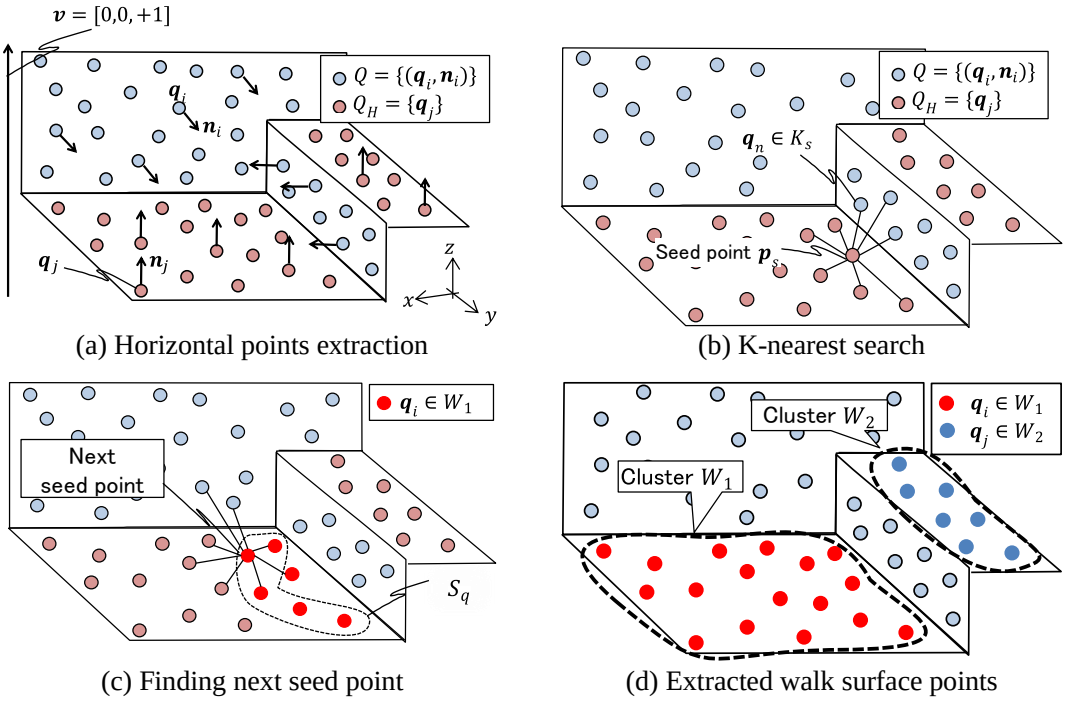

Fig. 2.8 Extracting set of walk surface points

(1) As shown in Fig. 2.8 (b), a seed point $\boldsymbol{q}_s$ randomly selected from Q_H is added into a seed-queue S_q and a current cluster W_i.

(2) The seed point $\boldsymbol{q}_s \in S_q$ is removed from S_q, and its k-nearest neighbors $K_s = \{\boldsymbol{q}_n\}$ are extracted using kd-tree of Q, where the number of nearest points to be extracted is specified as the user-specified value N_{region}.

(3) As shown in Fig. 2.8 (c), if any neighboring point $\boldsymbol{q}_n \in K_s$ satisfy the two conditions, $\boldsymbol{q}_n \in Q_H$, and $\|\boldsymbol{q}_s - \boldsymbol{q}_n\| \leq d_t$, at the same time, then $\boldsymbol{q}_n$ is added into W_i and S_q.

(4) Steps (2) and (3) are repeated until S_q becomes empty.

(5) If the number of points included in W_i is larger than the user-specified threshold N_{min_clu}, then W_i is added into a set of walk surface points W_S.

(6) Steps (1)-(5) are repeated until Q_H becomes empty.

In the step (3), the first condition, i.e., $\boldsymbol{q}_n \in Q_H$, is used to avoid the under segmentation problem. The second one, i.e., $\|\boldsymbol{q}_s - \boldsymbol{q}_n\| \leq d_t$, is used to avoid extracting the point clouds which are too sparse to make DHM walk on the point clouds. By combing the k-nearest search with these conditions, the algorithm can exhaustively extract each floors and stair-treads as the walk surface points W_k without relying on the density of Q.

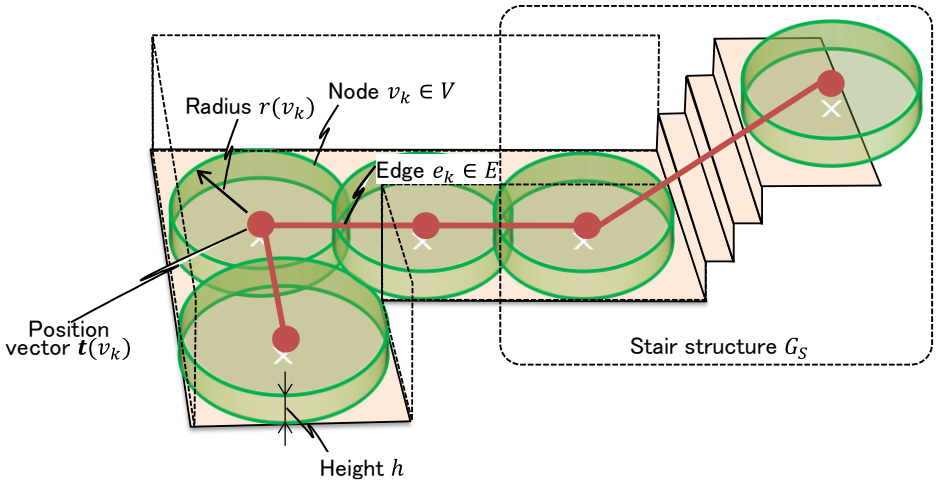

Fig. 2.9 Structure of the navigation graph

As the results of these processes, as shown in Fig. 2.8 (d), the set of the walk surface points $W_S = \{W_i\}$ are extracted, and it is treated as a part of the 3D as-is environment model. The parameter setting strategies of α_{slope}, N_{region}, and N_{min_clu} is introduced in Section 2.5.

2.4.3 Navigation graph construction

2.4.3.1 Navigation graph construction from laser-scanned point clouds

After extracting the set of walk surface points W_S, a navigation graph representing the environmental pathway structure is automatically constructed on $W_i \subseteq W_S$. In this study, to construct navigation graphs from laser-scanned point clouds including stairs, we extend the algorithm of Pettre et al. [Pettre 05], which constructs navigation graphs from a simple-shaped 3D mesh model.

As shown in Fig. 2.9, the navigation graph $G_N = \langle V, E, c, \boldsymbol{t}, G_S \rangle$ comprises a set of graph nodes V and set of edges E. Each node $v_k \in V$ represents free space of the environment. It has a position vector $\boldsymbol{t}(v_k)$ and an attribute of a cylinder $c(v_k)$, whose radius $r(v_k)$ and height h represent the distance to the wall and the walkable step height, respectively. Each edge e_k represents connectivity of the environment, and is generated between two adjacent nodes with a common region. In addition, G_S is a stair structure representing pathway structure on stairs. Construction algorithm of G_N is given below.

(1) Medial axis extraction

First, as shown in Fig. 2.10, a set of walk surface image $I_W = \{I_i\}$ is generated by projecting the

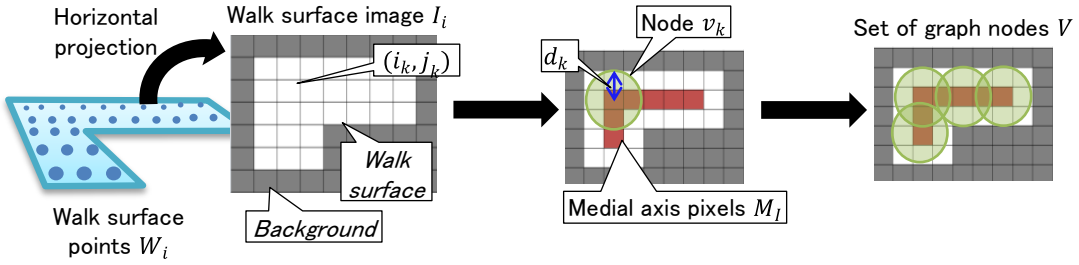

Fig. 2.10 Set of graph nodes generation

walk surface points W_i onto a horizontal plane. $I_i \in I_W$ consists of the walk surface pixels on which one or multiple walk surface points are projected, and the background pixels on which any walk surface points are not projected. In this process, the projection density ρ_{ng} [m/pix] is specified by the user depending on the density of Q. Then, a set of medial axis pixels $M_I = \{(i_k, j_k)\}$, and a corresponding set of distances $D_I = \{d_k\}$ are extracted from I_i, where d_k represents the distance between (i_k, j_k) and its nearest background pixel.

(2) Generating a set of graph nodes V

Next, a graph node v_k having a position vector $\boldsymbol{t}(v_k)$ and an attribute of a cylinder $c(v_k)$ is generated on the medial axis pixel $(i_u, j_u) \in M_I$, and added into the set of graph node V. $\boldsymbol{t}(v_k)$ and $c(v_k)$ is calculated by the equations,

$$\begin{aligned} \boldsymbol{t}(v_k) &= \boldsymbol{f}_I\left(\arg\max_{(i,j)\in M_I} m(i,j)\right) \\ c(v_k) &= [r(v_k), h] \end{aligned} \tag{2.3}$$

where $\boldsymbol{f}_I(i,j)$, $r(v_k)$, and h represent the 3D position vector of the walk surface point $\boldsymbol{q}_k \in W_i$ projected onto the pixel (i,j), the radius of the cylinder, and the height of the cylinder, respectively. If the multiple walk surface points were projected onto (i,j), these centroid is treated as $\boldsymbol{f}_I(i,j)$. In this study, $r(v_k)$ and h are specified as $r(v_k) = d_u$ and $h = H_{ng\_max}$, respectively, where H_{ng_max} represents the user-specified threshold. Note that if $r(v_k)$ is smaller than the user-specified threshold R_{ng_max}, v_k is not added into V. Finally, (i_u, j_u) is removed from M_I, and this process is repeated until $M_I = \emptyset$.

(3) Generating a set of graph edges E

After generating V, as shown in Fig. 2.11, if the two adjacent nodes v_1 and v_2 satisfy the following equation (2.4), a graph edge e_k is generated to make a connection between v_1 and v_2, and inserted into the set of graph edge E.

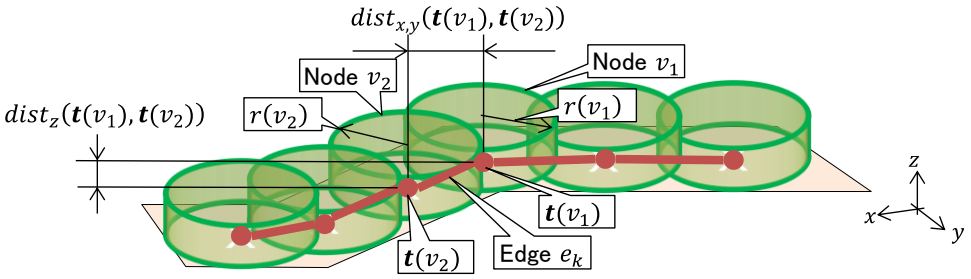

Fig. 2.11 Set of graph edges generation

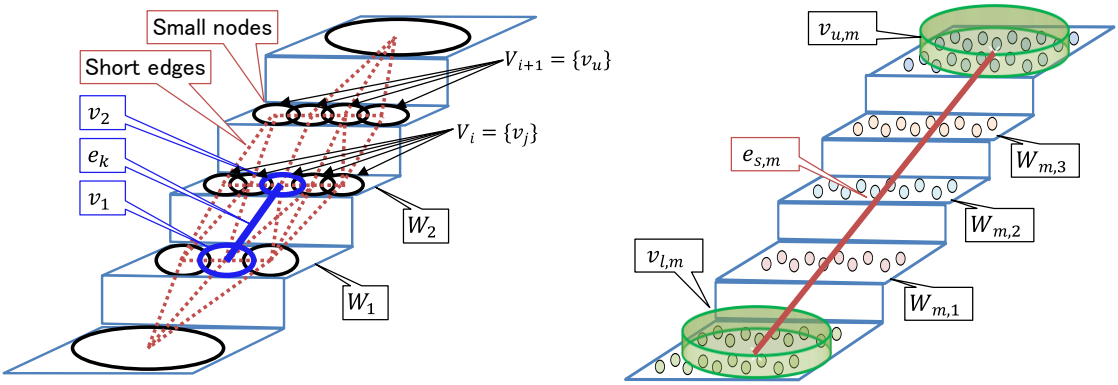

(a) Navigation graph G_N on stairs, and construction algorithm of G_S

(b) Stair structure G_S

Fig. 2.12 Stair structure construction

$$dist_{x,y}(\boldsymbol{t}(v_1), \boldsymbol{t}(v_2)) \leq r(v_1) + r(v_2)$$
$$dist_z(\boldsymbol{t}(v_1), \boldsymbol{t}(v_2)) \leq H_{ng\_max} \quad (2.4)$$

where $dist_{x,y}(\boldsymbol{t}(v_1), \boldsymbol{t}(v_2))$, $dist_z(\boldsymbol{t}(v_1), \boldsymbol{t}(v_2))$, and H_{ng_max} represent the horizontal and vertical distance between $\boldsymbol{t}(v_1)$ and $\boldsymbol{t}(v_2)$, and a user-specified threshold value, respectively.

Finally, by applying these processes (1)–(3) to all of the walk surface points $W_i \subset W_S$, the navigation graph $G_N = \langle V, E, c, \boldsymbol{t}, G_S \rangle$ is obtained without the stair structure G_S. As shown in Fig. 2.12 (a), the navigation graph on the stairs initially contains a complex graph structure including a lot of small nodes and short edges. It does not reproduce the actual pathway structure on the stairs. Therefore, a stair structure G_S is further generated, and inserted into G_N, by improving G_N constructed on the stairs. Details are given in the following subsection.

2.4.3.2 Stair structure construction

As shown in Fig. 2.12 (b), a stair structure $G_S = \langle v_{u,m}, v_{l,m}, e_{s,m}, W_{m,n} \rangle$ is further generated on the stairs as a part of the navigation graph G_N. In G_S, an upper stair node $v_{u,m}$, lower stair node $v_{l,m}$, and stair edge $e_{s,m}$, represent a graph node on the highest or lowest part of mth stairs, and a graph edge connecting between $v_{u,m}$ and $v_{l,m}$. In addition, $W_{m,n}$ represents the walk surface points existing on a stair tread of nth stairstep in mth stairs.

As shown in Fig. 2.12 (a), G_S is constructed by the following processes.

(1) If a vertical distance between incident two nodes $v_1 \in V$ and $v_2 \in V$ is larger than the user-specified threshold H_{ng_step}, i.e., $dist_z(\boldsymbol{t}(v_1), \boldsymbol{t}(v_2)) \geq H_{ng\_step}$, then an edge e_k is extracted from E as the edge connecting multilevel walk surfaces, where e_k represents a graph edge generated between v_1 and v_2.

(2) The walk surface points $W_1 \subseteq W_S$ and $W_2 \subseteq W_S$ are extracted, where the v_1 and v_2 are generated on W_1 and W_2, respectively.

(3) A set of graph nodes $V_i = \{v_j\}$ are extracted from V, where v_j is a graph node generated on W_2.

(4) A set of graph nodes $V_{i+1} = \{v_u\}$ and its corresponding walk surface points W_{i+1} are extracted, where v_u is a graph node which is connected with $v_j \in V_i$, and is not included in V_i. Then, W_{i+1} and V_{i+1} are stored into W_{stair} and V_{stair}, respectively.

(5) Step (4) is repeated until the following equation (2.5) is satisfied.

$$A_{i+1} > \alpha_{stair} A_i \tag{2.5}$$

where A_i, A_{i+1}, and $\alpha_{stair} > 1$ represent the pseudo area of W_1 and W_2, and the user-specified area ratio, respectively. In this study, α_{stair} is specified as a higher value, i.e., $\alpha_{stair} = 2.5$, under the assumption that approximately 40% area of the stair tread is captured as 3D point clouds. If V_{i+N} satisfy the equation (2.5) after the N times iteration of step (4), the nearest graph node $v_p \in V_{i+N}$ to v_1 is extracted from V_{i+N}. If the Z-component of $\boldsymbol{t}(v_p)$ is larger than $\boldsymbol{t}(v_1)$, v_p is inserted into G_S as the upper node $v_{u,m}$; otherwise v_p is inserted into G_S as the lower node $v_{l,m}$.

(6) Steps (3)-(5) are again performed after replacing W_2 with W_1. As the result, both $v_{u,m}$ and $v_{l,m}$ are obtained.

(7) The stair edge $e_{s,m}$ is generated between $v_{u,m}$ and $v_{l,m}$, and inserted into G_S.

(8) The walk surface points W_j stored in W_{stair} is sorted by the Z-component of its

centroid in ascending order, and inserted into G_S as $W_{m,n}$.

(9) All graph nodes included in V_{stair} is removed from V.

(10) Steps (1)–(9) are repeated for every two adjacent nodes included in V.

Finally, stair structure $G_S = \langle v_{u,m}, v_{l,m}, e_{s,m}, W_{m,n} \rangle$ is completely generated for every stairs in a given environment, and it is treated as a part of navigation graph. After the construction of G_S, if the radius of cylinder attributes of a graph node $v_k \in V$ is less than the user-specified threshold R_{ng_cle}, i.e., $r(v_k) \leq R_{ng\_cle}$, v_k is removed from V, where R_{ng_cle} needs to be specified as the half of walkable clearance, e.g., half of shoulder width of people. This reduction needs to be performed after the stair structure construction, since the radius of the cylinder attributes of graph node on the stairs tread is generally less than the half of walkable clearance before the stair structure construction as shown in Fig. 2.12 (a).

The parameter setting strategies of ρ_{ng}, R_{ng_min}, H_{ng_max}, H_{ng_step}, and R_{ng_cle} are introduced in Section 2.5.

2.4.4 Tread boundaries extraction

Finally, tread boundaries $B_{m,n}$ are estimated from the walk surface points $W_i \subset W_S$, which are utilized for estimating suitable footprints of the DHM and avoiding swing foot collisions with treads when the DHM walks on stairs. $B_{m,n}$ represents the boundary lines of nth stairstep in mth stair.

In this study, the tread boundaries are estimated from W_i extracted by the region-growing algorithm based on the normal vectors of each point, as described in 2.4.2. These normal vectors were estimated by PCA. However, the normal vector at a point located near the actual boundary of a stair tread is often tilted toward the neighboring region due to the nature of PCA. As a result, the extracted walk surface points W_i of the stair tread will often miss the point clouds on the actual tread boundaries. Therefore, in this study, the point clouds on the actual tread boundary of stairs are first extracted at high speed and with high precision using a neighboring search algorithm. The actual tread boundary is then estimated using these points. Details are given below.

As shown in Fig. 2.13, first, a convex hull $H_{m,n}$ is generated from the walk surface points $W_{m,n}$, where $W_{m,n}$ represents the walk surface points of the nth stairstep in the mth stair included in G_S. In the figure, $\boldsymbol{q}_k$ represents the kth vertex of $H_{m,n}$. Then, a set of neighboring points K_H of $\boldsymbol{q}_k$ is extracted from Q using its kd-tree to exactly extract the entire set of points of the nth stairstep. These points $\boldsymbol{p}_u \in K_H$ are inserted into $W_{m,n}$. Finally, as shown in Fig. 2.13, the tread boundary $B_{m,n}$ is constructed as a convex hull of $W_{m,n}$. In this study, the Ramer Douglas Peucker algorithm [Ramer 72] is applied to $B_{m,n}$ in order to reduce the number of vertices in $B_{m,n}$.

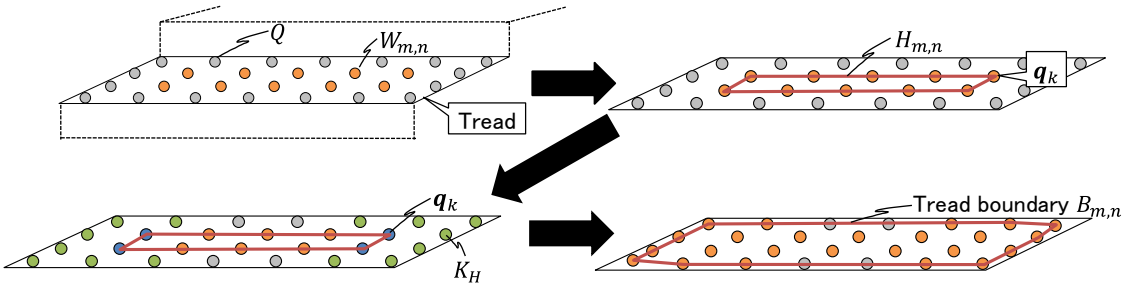

Fig. 2.13 Tread boundaries extraction

Table 2.4 Properties of laser-scanned point clouds used for as-is environment modeling

	(a) One-floor indoor environment	(b) Two-story indoor environment	(c) Outdoor environment	(d) Urban environment
Picture				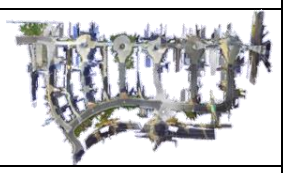
Scale [m]	W18 × D10 × H2	W38 × D34 × H7	W35 × D36 × H10	W220 × D100 × H11
Included elements	— Corridors — Corners — Stairs	— Corridors — Corners — Halls — Stairs — Caracoles	— Paved walkways — Slopes	— Roadways — Paved walkway — Stairs — Rotaries
Laser-scanner	FARO Focus 3D S120 (±2 mm at 25 m)	FARO Focus 3D S120 (±2 mm at 25 m)	RIEGL VZ-1000 (±8 mm at 100 m)	FARO Focus 3D X330 (±2 mm at 25 m)
# scans	20	48	7	46
# points	7,058,731	346,457,626	41,067,944	617,105,730
# down-sampled point	1,043,386	9,287,847	2,530,737	35,968,315

The extracted tread boundaries $B_{m,n}$ are treated as a part of the 3D as-is environment model.

2.5 Results and validations of 3D as-is environment modeling

2.5.1 Laser-scanner, point clouds, and modeling parameters used in experiments

We tested our as-is environment modeling algorithm using the point clouds acquired from the four types of environments: one-floor indoor environment, two-story indoor environment, outdoor environment, and urban environment. Table 2.4 shows the properties of these point clouds.

In this study, the original laser-scanned point clouds were down-sampled so that the density of the points corresponded to 1,000 points/m^2, which is sufficient for the modeling and human behavior simulation. Therefore, the grid size l_V of each voxel in 2.4.1 was specified as 0.03 m.

Table 2.5 Strategies and setting of environment modeling parameters

Parameter	Process	Setting	Strategy or reason
PCA radius r_n	Down-sampling and normal vector estimation	$r_n = 0.08$ m	To estimate normal vectors from sufficient number of point clouds (in general, more than 20 points), r_n is specified as 0.08 m.
Inclination threshold α_{slope}	Extracting set of walking surface points	$\alpha_{slope} = 30$ deg	To extract the walk surface points exhaustively, α_{slope} is specified as a value larger than existing maximum road gradient (14 deg in Tokyo [NILIM]).
Number of neighbors N_{region}		$N_{region} = 12$ points	To certainly obtain 8 neighbors of a given point, N_{region} is specified as a value larger than 8.
Min cluster size N_{min_clu}		$N_{min\_clu} = 150$ points	To avoid the lack of the recognition of stair treads, N_{min_clu} is specified as a larger value than 130 points, under the assumption that the area of a stair tread is larger than approximately 0.13 m^2 (e.g., W0.7 × D0.18).
Projection density ρ_{ng}	Navigation graph construction	$\rho_{ng} = 10$ pix/m	To make sure that each pixel includes one or multiple walk surface points.
Min node radiusR_{ng_min}		$R_{ng\_min} = 0.04$ m	To make multiple graph nodes on a stair tread, R_{ng_min} is specified as a half of 0.08 m under the assumption that the run of stair treads is generally larger than 0.08 m.
Max node height H_{ng_max}		$H_{ng\_max} = 0.2$ m	To connect the graph node between adjacent stair treads, H_{ng_max} is specified as a half of 0.4 m, under the assumption that the rise of the stairs is generally smaller than 0.4 m.
Walkable clearance R_{ng_cle}		$R_{ng\_cle} = 0.2$ m	To keep the pathway connection, R_{ng_cle} is specified as a value smaller than the minimum shoulder width 0.33 m [AIST 05].
Min step height H_{ng_step}		$H_{ng\_step} = 0.1$ m	To exhaustively recognize the stair treads, H_{ng_step} is specified as 0.1 m under the assumption that the rise of the stairs is generally larger than 0.1 m.

On the other hand, some modeling parameters, r_n, α_{slope}, N_{region}, N_{min_clu}, ρ_{ng}, R_{ng_min}, H_{ng_max}, and H_{ng_step} needed to be specified for as-is environment modeling. In this study, each parameter was initially specified as shown in Table 2.5 in the case of the down-sampled point clouds Q was denser than 1,000 points/m^2. If a suitable as-is environment model could not obtained from the given point clouds, these parameters needed to be changed according to the modeling results. In case that Q is sparser than 1,000 points/m^2, these parameters need to be changed according to the point density of Q.

In the following subsection, modeling parameters were specified as the values in Table 2.5. However, for the one-floor indoor environment, ρ_{ng} was specified as $\rho_{ng} = 20$ pix/m, since the environment contains corridors separated by a thin wall. For the urban environment, α_{slope} was specified as $\alpha_{slope} = 20$ deg, not to extract the roofs as the walk surface points.

2.5.2 As-is environment modeling results in indoor environments

Results of the as-is environment modeling in the two types of the indoor environments are shown in Fig. 2.14 and Fig. 2.15. Fig. 2.14 is the modeling result from the laser-scanned point clouds of the one-floor indoor environment, and Fig. 2.15 is one of the two-story indoor environment. As shown in Fig. 2.14 (b) and Fig. 2.15 (b), the walkable surfaces such as the floors, walls, and stair treads could be successfully extracted as the walk surface points. Moreover, as shown in Figs. 2.14 (c), the free spaces and these relations in the environments, i.e., pathway

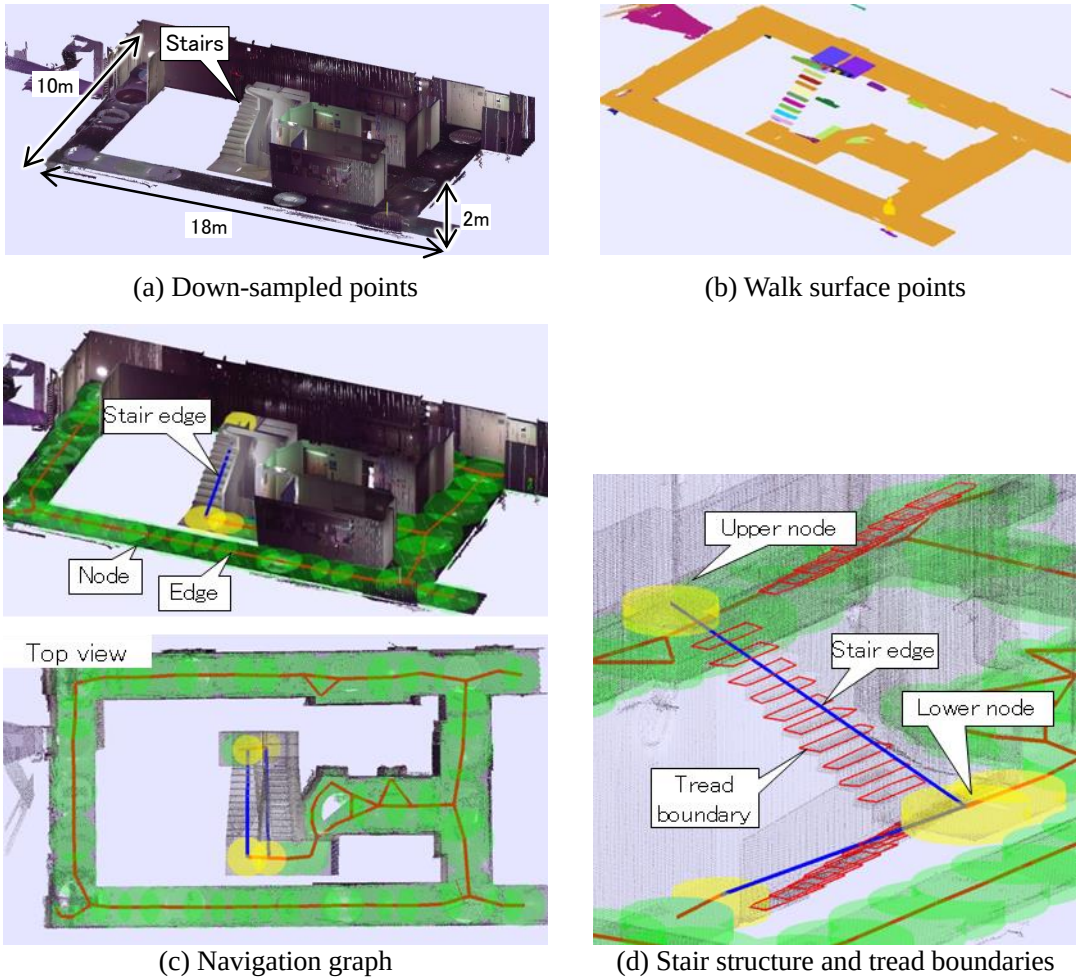

(a) Down-sampled points (b) Walk surface points

(c) Navigation graph (d) Stair structure and tread boundaries

Fig. 2.14 Results of as-is environment modeling in one-floor indoor environment

structure, could be successfully modeled as the navigation graph. In addition, as shown in Fig. 2.14 (d), the pathway of the stairs and the boundary lines of each tread could be reproduced as the stair structure and the tread boundaries, respectively. On the other hand, as shown in Fig 2.15 (c), the navigation graph including stair structure could be successfully constructed even from the point clouds of the two-story indoor, where each floor is connected by the stair structure generated on the caracole and staircases. In addition, as shown in Figs. 2.15 (d) and (e), the tread boundaries could be generated even on the caracole and staircases.

These 3D as-is environment models were automatically generated from the laser-scanned point clouds. Therefore, it was confirmed that the proposed as-is environment modeling algorithm made it possible to automatically construct the 3D as-is environment models from point clouds of indoor environments.

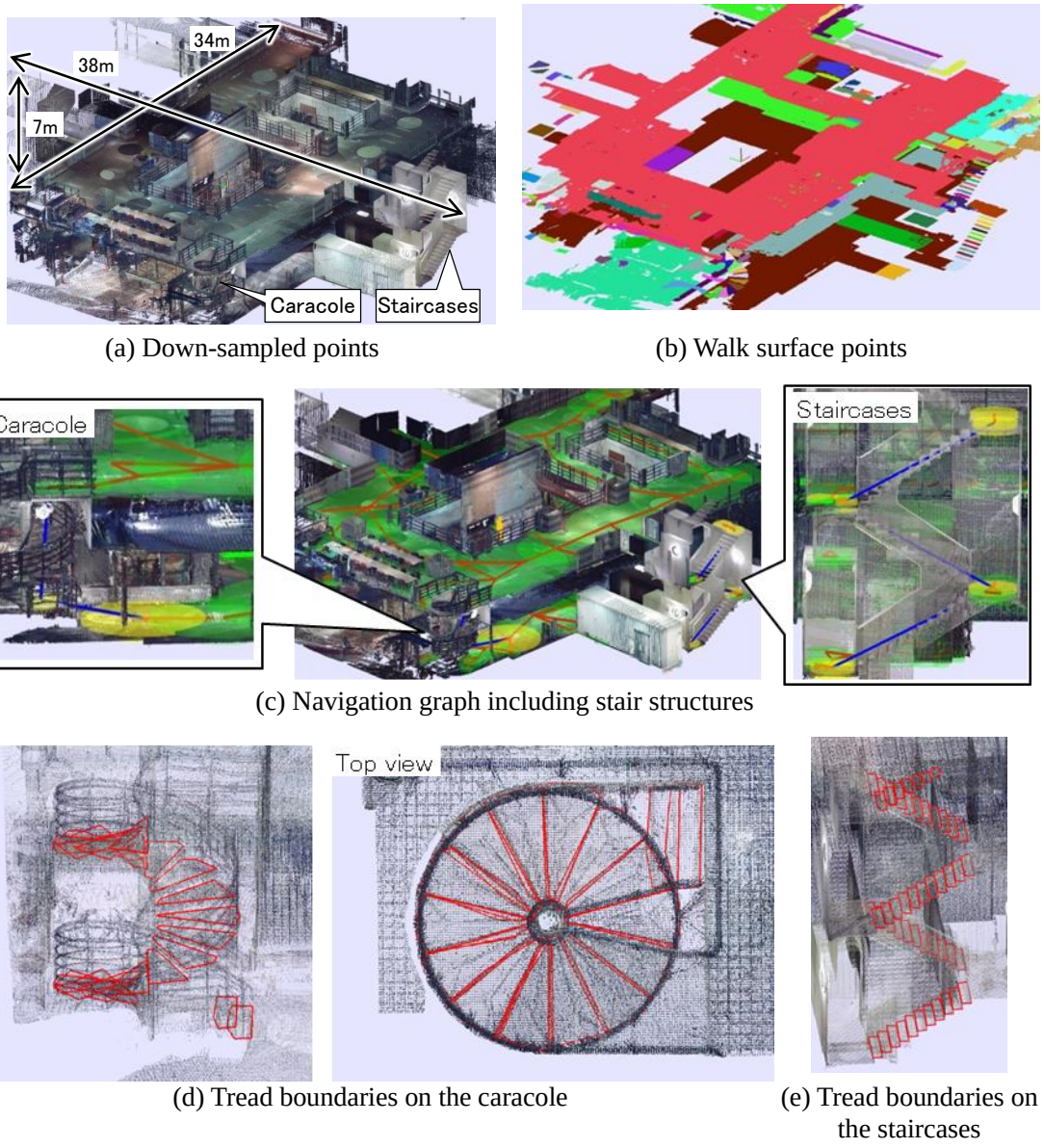

(a) Down-sampled points (b) Walk surface points

(c) Navigation graph including stair structures

(d) Tread boundaries on the caracole (e) Tread boundaries on the staircases

Fig. 2.15 Results of as-is environment modeling in two-story indoor environment

2.5.3 As-is environment modeling results in outdoor environment

Results of the as-is environment modeling in the outdoor environment are shown in Fig. 2.16. As shown in Figs. 2.16 (b), (c) and (d), the walk surface points, the navigation graph including the stair structure and the tread boundaries could be successfully generated even from the point clouds of the outdoor environment. In addition, as shown in Fig. 2.16 (e), the navigation graph could be generated even on the consecutive slopes without the un-scanned regions.

Therefore, it was confirmed that the proposed 3D as-is environment modeling algorithm made it possible to automatically construct the 3D as-is environment models even from the point clouds of

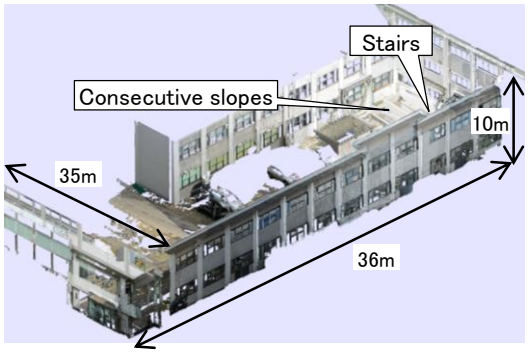

(a) Down-sampled points

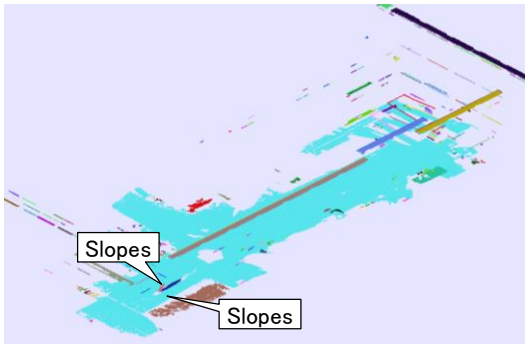

(b) Walk surface points

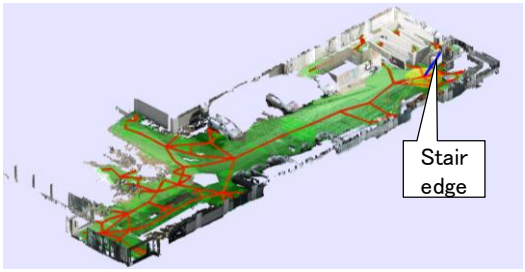

(c) Navigation graph including stair structure

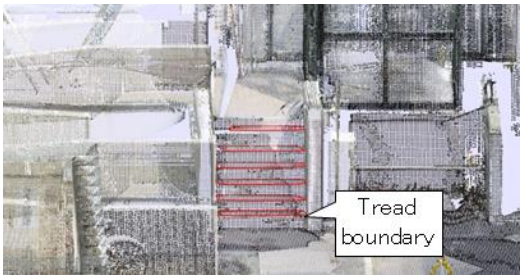

(d) Tread boundaries

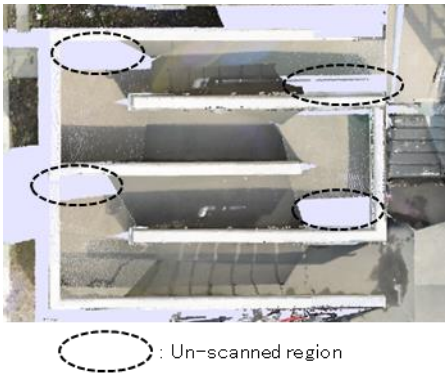

(e) Consecutive slopes

(f) Navigation graph on consecutive slopes

Fig. 2.16 Results of as-is environment modeling in outdoor environment

the outdoor environment. Furthermore, considering the modeling results shown in 2.5.2 and 2.5.3, it was confirmed that the proposed algorithm could construct the 3D as-is environment model regardless of indoor and outdoor environments.

2.5.4 As-is environment modeling results in urban environment

Results of the as-is environment modeling in the urban environment are shown in Fig. 2.17. As shown in Figs. 2.17 (b), (c), the walk surface and the navigation graph could be successfully generated even from the point clouds of large-scale urban environments. In addition, as shown in Figs. 2.17 (d) and (e), the walk surface points and the navigation graph including the stair structure could be generated even on the stairs.

Therefore, it was confirmed that the proposed 3D as-is environment modeling algorithm could construct the 3D as-is environment models even from the point clouds of the large-scale urban environment. Furthermore, considering the modeling results shown in 2.5.2–2.5.4, it was confirmed that the proposed as-is environment modeling algorithm could automatically construct the as-is environment model from the point clouds of various environments such as one-floor and two-story indoor environments, outdoor environments, and large-scale urban environments. This showed the effectiveness of the proposed as-is environment modeling algorithm.

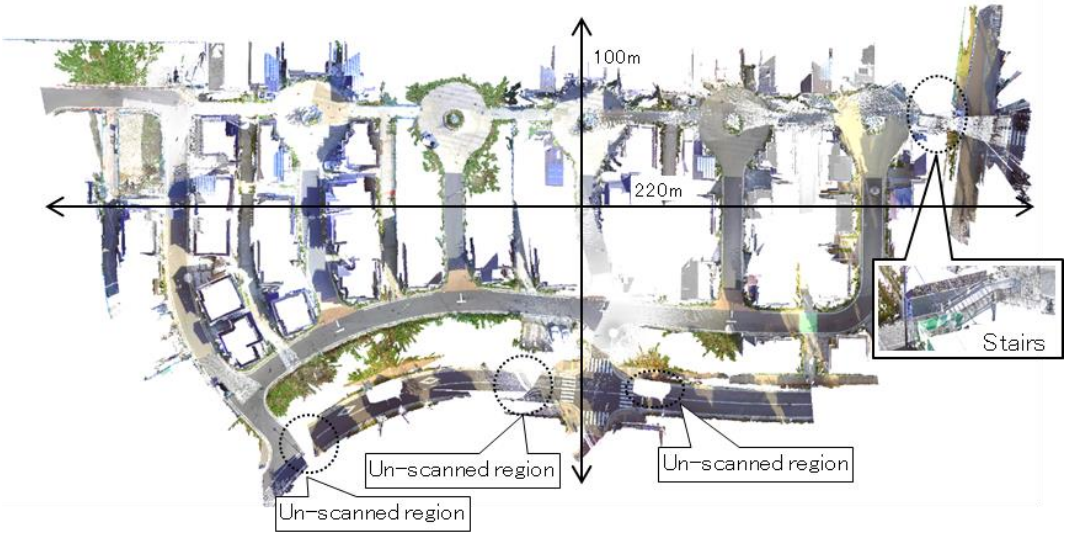

(a) Down-sampled points

(b) Walking surface points

Fig. 2.17 Results of as-is environment modeling in urban environment

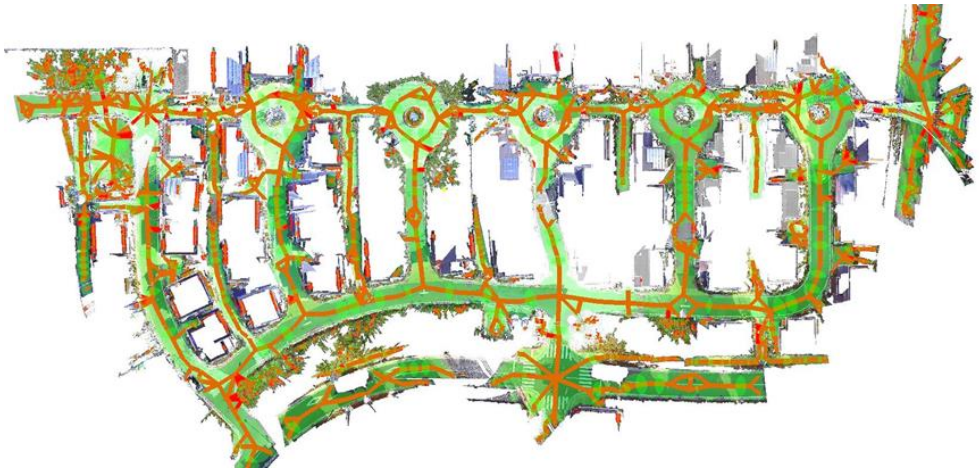

(c) Navigation graph

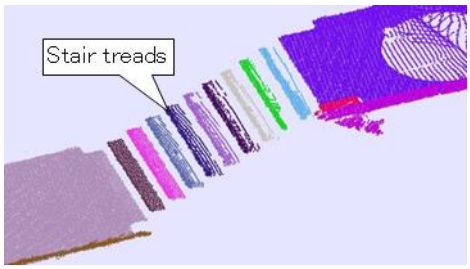

(d) Walk surface points on stairs

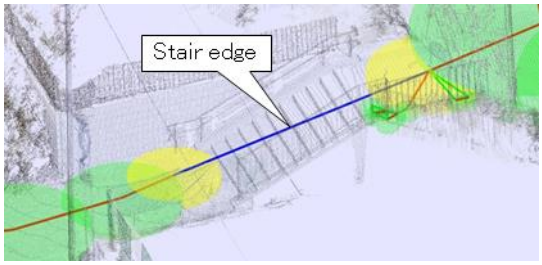

(e) Stair structure

Fig. 2.17 Results of as-is environment modeling in urban environment (cont.)

Table 2.6 Elapsed time of 3D as-is environment modeling from laser-scanned point clouds

(CPU: Intel Core i7 3.30GHz, RAM: 32GB, GPU: Quadro K4200)

	(a) One-floor indoor environment	(b) Two-story indoor environment	(c) Outdoor environment	(d) Urban environment
# points	7,058,731	346,457,626	41,067,944	617,105,730
# down-sampled point	1,043,386	9,287,847	2,530,737	35,968,315
Laser scanning	5 h	6 h	1.2 h	1 day
Point clouds registration	1 h	4 h	1 h	4−5 days
Down-sampling and noise removal	5 s	2.5 min	23 s	39 min
As-is environment modeling without the down-sampling and noise removal	1 s	80 s	12 s	6 min
Total time of as-is environment modeling	6 s	4 min	35 s	45 min

2.5.5 Efficiency and accuracy validations of as-is environment modeling

2.5.5.1 Efficiency of as-is environment modeling

Table 2.6 shows the elapsed time of the 3D as-is environment modeling from the laser-scanned point clouds. In our implementation, PCL (Point Cloud Library) [PCL] was partly used for the point clouds processing, and OpenGL [OpenGL] was used for rendering. As shown in Table 2.6, the total elapsed time of the as-is environment modeling was 6 s for the point clouds of one-floor indoor environment, and was 45 min for the point clouds of urban environment, which were significantly lower than the time required for manual modeling. Therefore, it was concluded that the proposed 3D as-is environment modeling algorithm could automatically construct the 3D as-is environment models in an efficient way. As shown in Table 2.6, the elapsed time of down-sampling and noise removal was dominant in the total time of as-is environment modeling. This was caused by the fact that the massive original laser-scanned point clouds were used in the down-sampling process. Therefore, to realize more efficient as-is environment modeling, the algorithm of the down-sampling needs to be improved.

2.5.5.2 Accuracy validations of as-is environment modeling

Finally, the proposed 3D as-is environment modeling algorithm was validated by a comparison of the dimensions between the resultant as-is environment model with the real environment. In particular, the dimensions of path clearance and of stairs were validated. Details are given below.

(a) Comparison of path clearance

In this study, first, the clearance of a corridor estimated from the as-is environment model was compared with the clearance measured from the corridor in real environment.

As shown in Fig. 2.18, first, a set of graph node $V_1 = \{v_1, \cdots v_N\}$ generated on a corridor was manually selected from the navigation graph G_N of the one-floor indoor environment in 2.5.3. Then, the path clearance pc_1 was estimated from V_1 using the equation:

$$pc_1 = \frac{\sum_{i=1}^{N} 2r(v_i)}{N} \tag{2.5}$$

where N represent the number of graph nodes included in V_1. In the case of Fig. 2.18, 9 graph nodes selected from the navigation graph, i.e., $N = 9$. On the other hand, the actual path clearance PC_1 was measured by a laser distance meter, Leica DISTO D3a (measuring accuracy: ± 1.0 mm) [Leica].

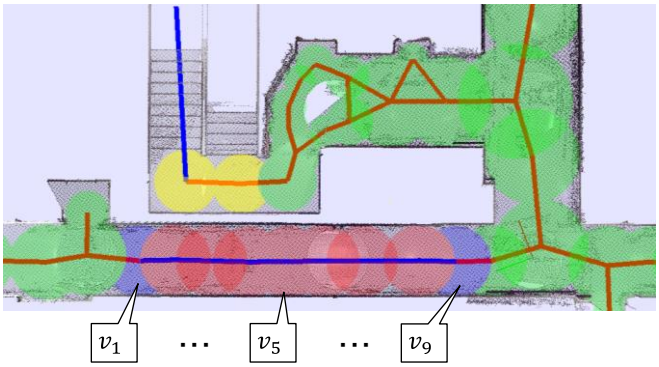

Fig. 2.18 Selected graph nodes for path clearance validation

Table 2.7 Comparison of estimated path clearance with measurements

	Estimated path clearance pc_1	Measured path clearance PC_1	Difference ($PC_1 - pc_1$)
Path clearance [m]	1.80	1.81	0.01

Table 2.7 shows the comparison results of path clearance. As shown in Table 2.7, the difference between pc_1 and PC_1 was achieved 0.01 m. Therefore, it was confirmed that the constructed 3D as-is environment model could reproduce the path clearance of real environment.

(b) Comparison of the dimensions of stairs

In this study, dimensions of stairs were compared between the as-is environment model and the real environment. In particular, as shown in Fig. 2.19, the rise, i.e., height between two adjacent stair treads, and the tread width estimated from the as-is environment model were compared with those measured from the real environment. As shown in Fig. 2.20, the three stairs included in the as-is environment model of one-floor building was used in the validation. The rise and tread with of stairs were estimated based on the tread boundaries of the stairs. Details of the estimation algorithm are described in Appendix A. On the other hand, the actual rise and tread width of these stairs were measured by a laser distance meter [Leica].

Table 2.8 shows the comparison results of stair dimensions. As shown in Table 2.8, the differences in the rise and tread width between the as-is environment model and the real environment were 0.003 m, and 0.015 m at a maximum, respectively. Therefore, it was confirmed that the constructed 3D as-is environment model could reproduce the dimensions of stairs of real environment.

Table 2.8 Comparison of stair dimensions between as-is environment model and real environment

	Rise [m]	Tread width [m]
Stairs 1	0.179	0.291
Stairs 2	0.182	0.305
Stairs 3	0.183	0.291
Measurements of real environment	0.180	0.290
Maximum difference	0.003 (stairs 3)	0.015 (stairs 2)

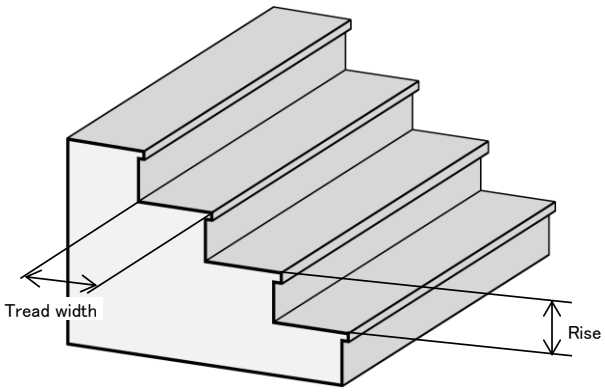

Fig. 2.19 Definition of rise and tread width of stairs

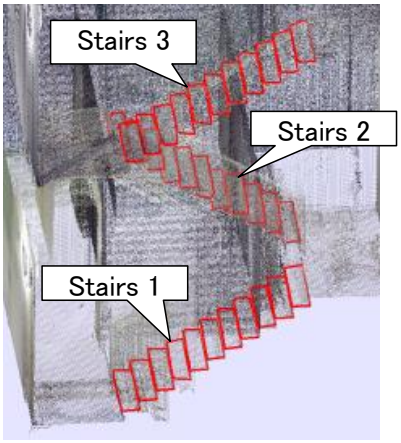

Fig. 2.20 Selected stairs for stairs dimensions validation

Considering the comparison results, it was concluded that the proposed as-is environment modeling algorithm could construct the accurate as-is environment model from the laser-scanned point clouds.

2.6 Summary

In this chapter, an algorithm of 3D as-is environment modeling from laser-scanned point clouds was developed. Our algorithm made it possible to construct the 3D as-is environment models automatically, which are suitable for human behavior simulation aiming to the human-centered accessibility evaluation. As environmental information for the human behavior simulation, a set of walk surface points, navigation graph, and stair structure were modeled as a part of the 3D as-is environment models. In addition, to represent the detailed shape of environment, the algorithm made it possible to make the 3D as-is environment models based on accurate laser-scanned point clouds.

In addition, our as-is environment modeling algorithm was validated with the multiple point clouds of indoor, outdoor, and urban environments. The results showed the effectiveness of the modeling algorithm regardless of indoor and outdoor environments. Moreover, it was confirmed that the modeling algorithm could efficiently construct the 3D as-is environment models in fully automatic way, e.g., the total elapsed time of the as-is environment modeling was 6 s for the point clouds of one-floor indoor environment.

In addition, modeling accuracy of our algorithm was further validated by a comparison of the dimensions between the as-is environment models and real indoor environments. As a result, the differences in path clearance, rise of stairs, and tread width of stairs between the as-is environment model and actual environment were 0.01 m, 0.003 m, and 0.015 m at a maximum, respectively. Therefore, it was further confirmed that the algorithm could make the accurate 3D as-is environment model from the laser-scanned point clouds.

Chapter 3 Autonomous Walking Simulation of Digital Human Model

3.1 Background and requirements

In the last chapter, an algorithm of 3D as-is environment modeling from laser-scanned point clouds was proposed and introduced. However, to evaluate the human-centered accessibility criteria such as tripping risk and ease of wayfinding, the human behavior simulation of the DHM needs to be performed in the as-is environment model, which consists of the autonomous walking simulation and the vision-based wayfinding simulation. Therefore, in this chapter, we aim to develop the autonomous walking simulation of the DHM, which is utilized for tripping risk evaluation.

As discussed in Chapter 1, accessibility must be evaluated in term of physical and cognitive friendliness for users of different ages, genders, and abilities. In addition, the tripping risk must be evaluated while considering both environmental hazards and physical behaviors of various people. Therefore, as shown in Fig. 3.1, the following three requirements need to be satisfied in the autonomous walking simulation of the DHM in terms of the requirements for accessibility evaluation.

(a) Walking autonomy: enabling a DHM to autonomously walk along walkways from an arbitrary start position to goal position, while making human-like walking trajectory.

(b) Gait reproducibility: enabling a DHM to reproduce articulated walking movements of various people of different ages, genders, and body dimensions.

(c) Environmental flexibility: enabling a DHM to autonomously walk on various walking terrains such as flat terrains, slopes, and stairs.

The first requirement needs to be satisfied to evaluate both tripping risk and ease of wayfinding, by taking account of the interaction between walking behavior and the environments under the realistic usage situation. The second one needs to be satisfied to evaluate the tripping risk, by taking account of the difference of walking motion among individuals. The last one needs to be satisfied for accessibility evaluation of complex and realistic environment including various walking terrains.

Therefore, in this chapter, we aim to develop an algorithm of autonomous walking simulation of DHM, which can satisfy the above requirements such as (a) walking autonomy, (b) gait reproducibility, and (c) environmental flexibility.

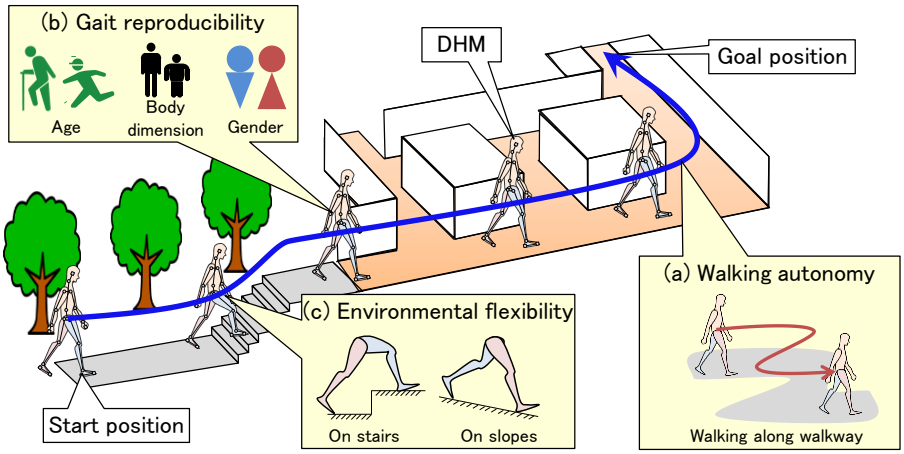

Fig. 3.1 Requirements for walking simulation of DHM

3.2 Related work on autonomous human walking simulation

3.2.1 Pedestrian model in current human behavior simulation

Currently, several walking simulation algorithms have been proposed in human behavior simulation and digital human modeling studies. Among them, the previous human behavior simulation studies were classified into: (1) general human behavior simulation, and (2) 3D human behavior simulation using DHM. The overviews and issues of these studies are given below.

(1) General human behavior simulation

In general human behavior simulation studies, methods of generating walking motion of pedestrian model is designed based on the purpose of the simulation. The simulation proposed by Helbing et al. [Helbing 00] aim to analyze and prevent the crowd accidents, so their pedestrian model is designed to mimic the crowd movements in the environments. In practice, the pedestrian model is moved based on the social force from the other pedestrian models and walls, to avoid collisions with walls and other pedestrians. Similarly, as shown in Fig. 3.2 (a), van den Berg et al. [van den Berg 08] proposed an algorithm of the local collision avoidance based on the reciprocal velocity obstacles (RVO). As shown in the figure, in their algorithm, the pedestrian model is moved to avoid the collisions with the other pedestrian models, while considering the reactive behavior of other pedestrians under the assumption that all pedestrian models make similar collision avoidance reasoning, i.e., RVO. However, generating the detailed articulated walking movements of the pedestrian models are neglected in their studies, since these algorithms focus on mimic the crowd movements. In addition, the movements of the pedestrian models are determined on-the-fly, so the

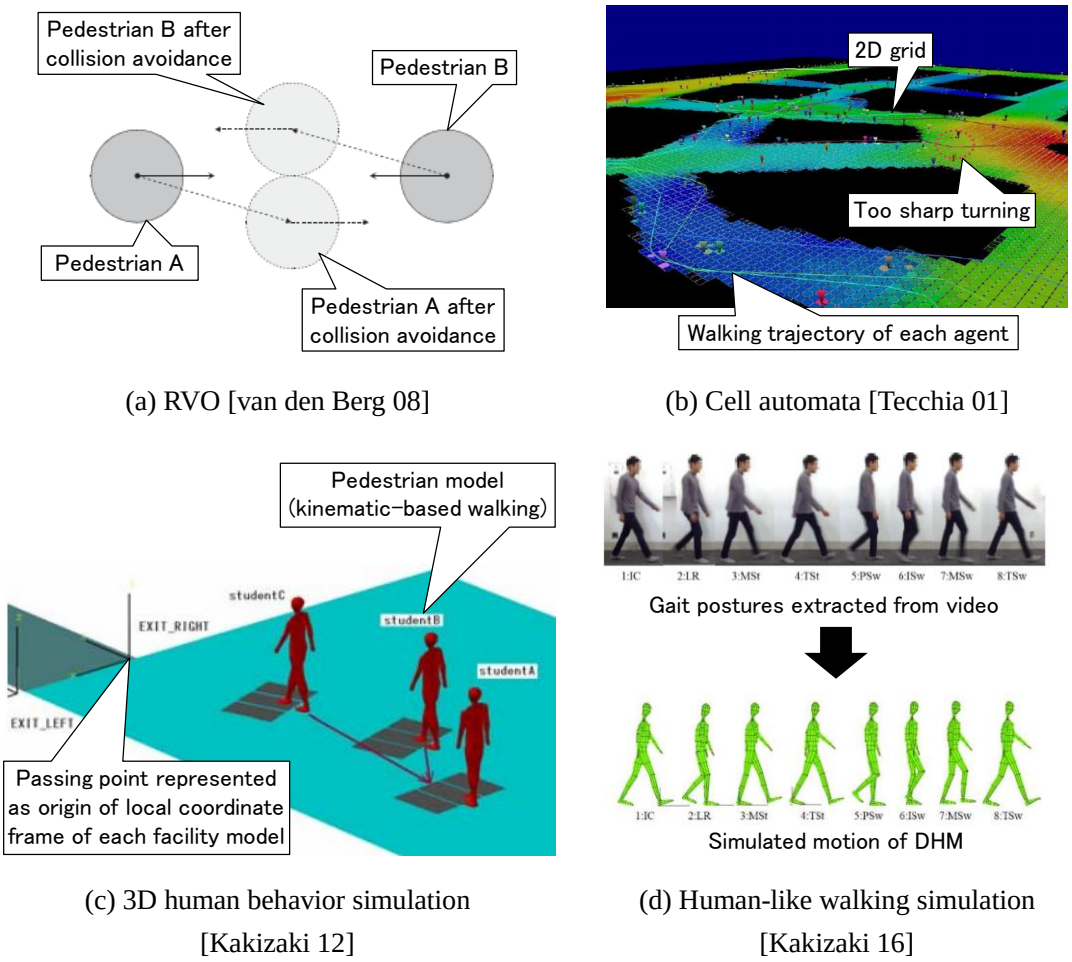

(a) RVO [van den Berg 08]

(b) Cell automata [Tecchia 01]

(c) 3D human behavior simulation [Kakizaki 12]

(d) Human-like walking simulation [Kakizaki 16]

Fig. 3.2 Pedestrian model in current human behavior simulation studies

resultant walking trajectory is not necessarily human-like, e.g., contacting with walls, making too sharp turning, or moving backward unnaturally. Therefore, the algorithm in these studies cannot satisfy the requirements (a)–(c) mentioned in the last section.

On the other hand, as shown in Fig. 3.2 (b), the algorithm of cellular automata, such as [Tecchia 01], is also widely used in human behavior simulation. In contrast to the social force model [Helbing 00], the walking trajectory of the pedestrian is preliminarily determined by searching over the 2D grid structure assigned on the environment. However, as shown in the figure, the resultant walking trajectory includes too sharp turning, so generating human-like walking trajectory is not always achieved. As reviewed by Duives et al. [Duives 13], several human behavior simulations used the algorithms similar to the social force model, RVO, or cellular automata for making the pedestrian models walk in the environment models.

Therefore, it is impossible to satisfy the requirements (a)—(c) in Section 3.1 based on the algorithm used in the general human behavior simulation.

(2) 3D human behavior simulation using DHM

On the other hand, as shown in Fig. 3.2 (c), recent advances in computer performance enabled the human behavior simulation based on the kinematics-based walking simulation of the DHM in a 3D as-planned environment model [Kakizaki 12]. In their algorithm, the articulated walking movements of the DHM can be generated by solving inverse kinematics (IK). In addition, as shown in Fig. 3.2 (d), in their recent study [Kakizaki 16], the algorithm of enabling the DHM to generate the human-like walking motion of various people based on the video of the flat walking of a subject is proposed for physiotherapy training. Therefore, by introducing the walking simulation algorithm proposed in [Kakizaki 16] into the 3D human behavior simulation framework [Kakizaki 12], it is supposed to be possible to generate human-like walking motion of various people in the 3D as-planned environment model.

However, to make the DHM walk on various walking terrains such as slopes, uneven terrains, and stairs, the walking motions of each subject on different walking terrains need to be recorded on video. It is generally difficult to capture the walking motion of various people of different ages, genders, and body dimensions on various walking terrains. Therefore, although their study can satisfy the requirement (b) and (c) at the same time, it is basically impractical, since the walking data collection in various environment for various people are required.

On the other hand, in terms of the requirement (a), i.e., walking autonomy, the evacuation route of each DHM needs to be specified manually. In particular, as shown in Fig. 3.2 (c), the user has to select the evaluation route as a set of passing points, where the passing point is represented as the origin of the local coordinate system of each facility model. This work becomes tedious and time-consuming, as the environment becomes large-scale and complex.

From the above reasons, although combing their studies [Kakizaki 12], [Kakizaki 16] makes it possible to satisfy the requirement (b) and (c) in Section 3.1, i.e., gait reproducibility and environmental flexibility, applying their studies to the human-centered accessibility evaluation is basically impractical. In addition, their study cannot satisfy the requirement (a) in Section 3.1, i.e., walking autonomy.

3.2.2 Digital human modeling for walking simulation

In the human behavior simulation studies, the pedestrian models are generally designed to mimic the crowd behavior in an as-planned environment. In contrast, in digital human modeling for walking simulation, many algorithms have been developed to generate human-like walking motion of various people in various walking terrains. The walking simulation studies were classified into: (3) MoCap-synthesis-based walking simulation, (4) MoCap-synthesis-based walking simulation with terrain adaptation, (5) Physics-based walking simulation, and (6) physics-based walking simulation with key-frame specification. The overviews and issues of these studies are described

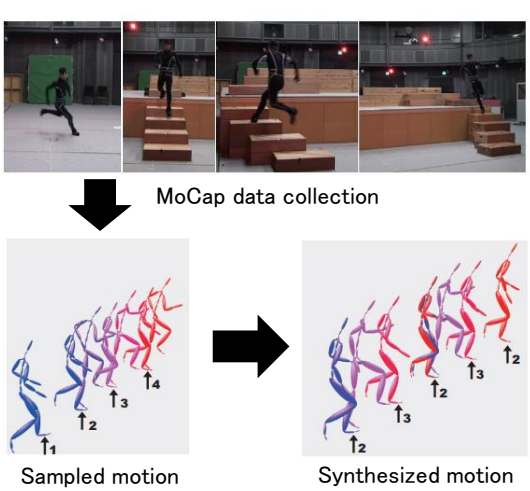

(a) MoCap-synthesis-based walking simulation [Mukai 11]

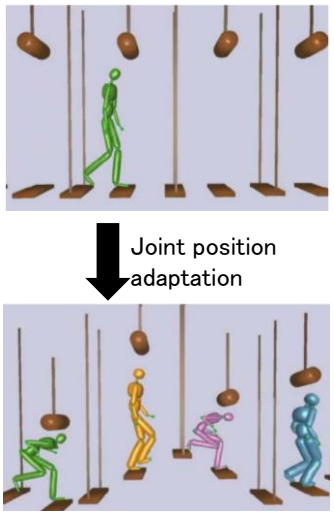

(b) MoCap-synthesis-based walking simulation with terrain adaptation [Rami 13]

Fig. 3.3 Walking simulation based on MoCap data

below.

(3) MoCap-synthesis-based walking simulation

Currently, several walking simulation algorithms have been proposed to generate human-like waking motions of DHM based on existing MoCap data set. A variety of human walking patterns can be synthesized using PCA [Troje 02]. Although such simulation systems can generate human-like walking motion of various people, they still require a large collection of MoCap data in advance. Therefore, many researchers tackle generating an arbitrary human motion from only a small number of existing MoCap data. Motion synthesis and editing [Min 10], motion rings [Mukai 11] (Fig. 3.3 (a)), and machine learning [Grochow 04] are typical examples. They require a small number of MoCap data to adapt the DHM's strides, turning angles, and footprints to its walking environment models. However, it is generally difficult to persuade elderly persons, who are the main targets of accessibility evaluation, to join prolonged MoCap data collection experiments shown in Fig. 3.3 (a).

Therefore, in the MoCap-synthesis-based walking simulation, the requirements (b) and (c) in Section 3.1, i.e., gait reproducibility and environmental flexibility, can be satisfied. However, it is basically impractical to use these simulations for accessibility evaluation purpose, since a set of MoCap data on various walking terrains are required for one subject including the elderly. In addition, in these simulation studies, the walking route of the DHM needs to be specified manually, so it is insufficient for satisfying the requirement (a) in Section 3.1, i.e., walking autonomy.

(4) MoCap-synthesis-based walking simulation with terrain adaptation

On the other hand, as shown in Fig. 3.3 (b), Rami et al. [Rami 13] proposed a MoCap-based walking simulation algorithm, which can generate the walking motion of the DHM even on non-flat walking terrain using a single reference MoCap data. In their algorithm, joint positions of the DHM relative to the walking surface can be flexibly adapted even to dynamically changing walking terrain. Therefore, as shown in Fig. 3.3 (b), in their study, the walking motion on non-flat terrain can be generated based only on the single reference MoCap data for flat walking. However, their algorithm cannot keep the length of each body segment of the DHM during the simulation, so the resultant motion is necessarily reproducing the real human motion. In addition, the motion of the DHM was not validated in their paper [Rami 13].

Therefore, we concluded that the MoCap-synthesis-based walking simulation with terrain adaptation [Rami 13] could not satisfy the requirement (b), i.e., gait reproducibility. In addition, in their simulation, it is impossible to change the walking trajectory in horizontal plane, i.e., turning, so it cannot satisfy the requirement (a), i.e., walking autonomy.

(5) Physics-based walking simulation

On the other hand, physics-based walking simulation algorithms have been proposed to generate human-like walking motions of DHM based on motion controllers (e.g., PD controller) and game-engines (i.e., physics simulator) [Yin 07], [Xiang 10]. In the physics-based walking simulation algorithms, as shown in Fig. 3.4 (a), the motion of the DHM is generated by applying torque to each joint estimated from the motion controller. Therefore, the motion controller parameters greatly affect the resultant walking motion. Wang et al. [Wang 9] proposed an algorithm of optimizing the controller parameters to minimize an objective function representing such as the smoothness of head motions, and efficiency and power of the motions. By optimizing the controller parameters, the human-like walking motion of DHM was automatically generated in their study. However, their optimization algorithm needs to be performed on each walking terrain, and require a lot of computational time even with parallel processing. In addition, as shown in Fig. 3.4 (b), it is difficult to reproduce the walking motion of various people using their optimization algorithm, since their algorithm was designed to mimic the general walking patterns of people of different body heights, so the gait difference among individuals was not considered in their study.

As shown in Fig. 3.4 (c), in the simulation of Wang et al. [Wang 12], the physics-based walking simulation is further combined with the human musculotendon models. Using the musculotendon models enables the DHM to generate human-like walking motion in a straight line and on flat ground. However, the possibility of generating human-like walking motion on various walking terrains was not discussed in the paper [Wang 12]. On the other hand, as shown in Figs. 3.4 (d) and (e), several physics-based walking simulations are proposed to enhance the robustness for various walking environments, such as slippery floor [Wang 10], [Yin 08], and complex stairs and slopes

[Mordatch 10]. However, in these studies, there is no discussion to reproduce human-like walking motion of various people using their algorithm.

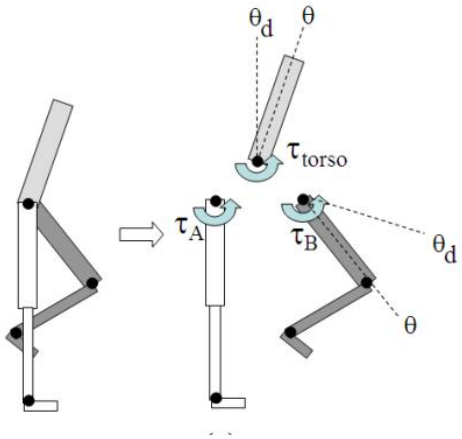

(a) SIMBICON [Yin 07]

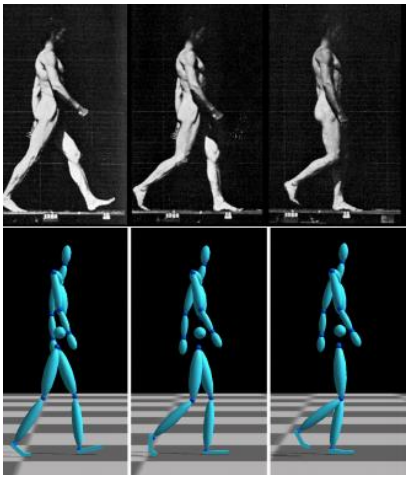

(b) Walking motion generated by optimized motion controller [Wang 9]

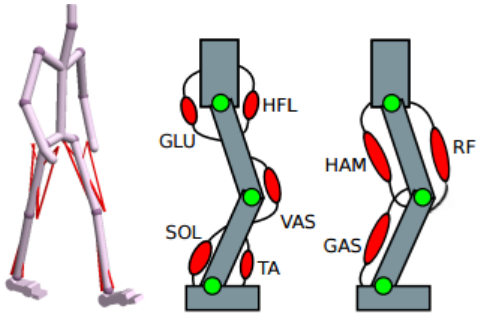

(c) Musculotendon models [Wang 12]

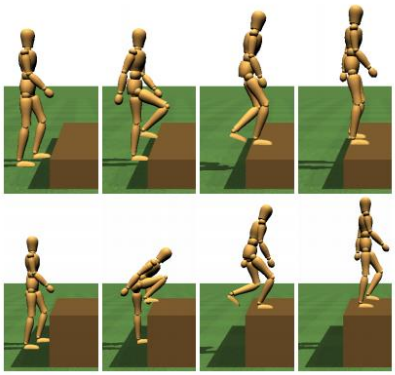

(d) Taking a large step up [Yin 08]

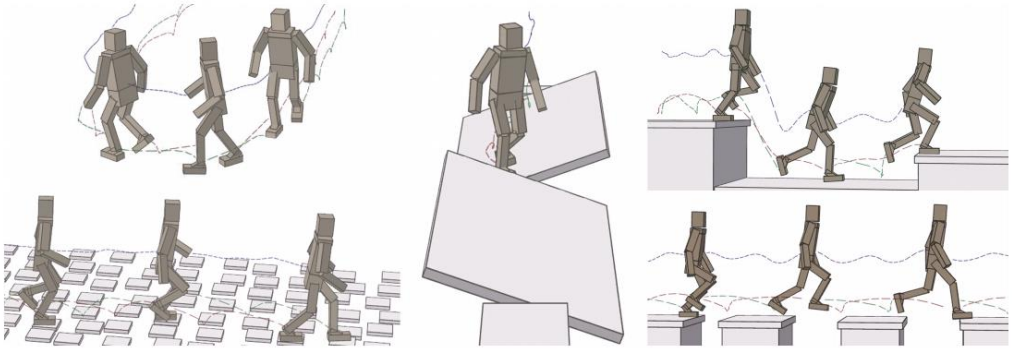

(e) Walking on various walking terrains [Mordatch 10]

Fig. 3.4 Physics-based walking simulation

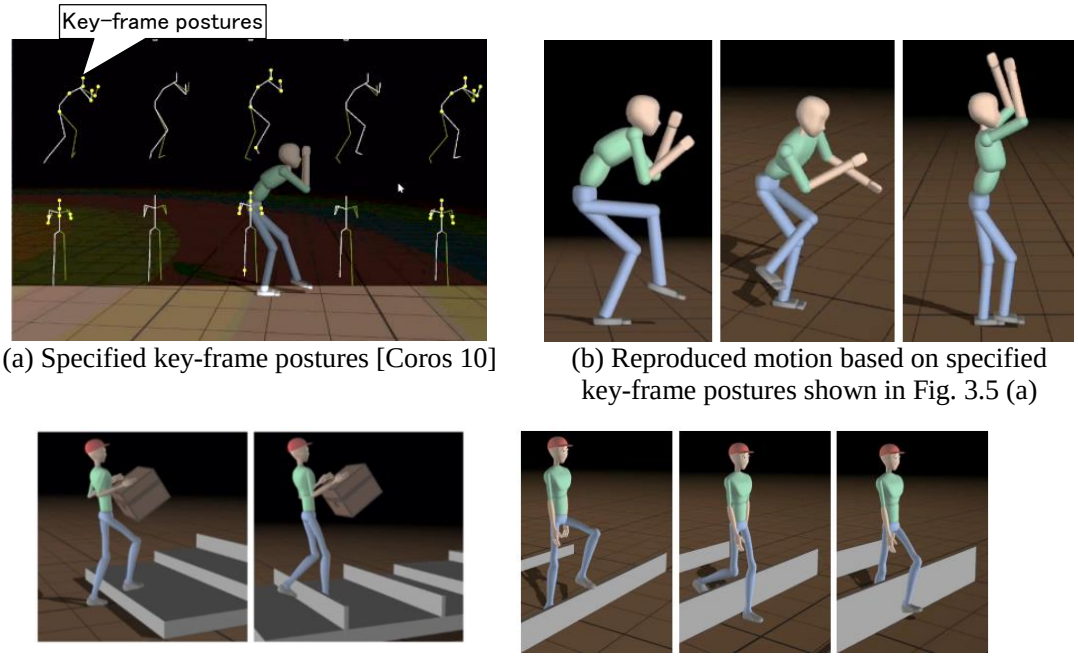

(a) Specified key-frame postures [Coros 10]

(b) Reproduced motion based on specified key-frame postures shown in Fig. 3.5 (a)

(c) Walking on various walking terrains

Fig. 3.5 Physics-based walking simulation with key-frame specification

Therefore, in the physics-based walking simulation, the requirement (c) in Section 3.1, i.e., environmental flexibility, can be satisfied by generating DHM's motion based on the motion controllers. However, these studies could be considered as insufficient approaches to satisfy the requirement (b) in Section 3.1, i.e., gait reproducibility. In addition, in these simulations, the walking route of the DHM needs to be specified manually, so it cannot satisfy the requirement (a), i.e., walking autonomy.

(6) Physics-based walking simulation with key-frame specification

On the other hand, as shown in Fig. 3.5, Coros et al. [Coros 10] proposed a physics-based walking simulation of DHM based on user-specified key frame postures. As shown in the figure, creating the motion controller based on the user-specified key-frame postures enables the DHM to generate walking motion on various walking terrains, while reproducing the specified key-frame postures. However, as reported in their paper [Coros 10], self-interaction between the stance and swing legs occurs in some situations, so it cannot necessarily reproduce the human-like walking motion of the DHM. In addition, the resultant motion was not validated in the paper [Coros 10].

Therefore, we concluded that the physics-based walking simulation with key-frame specification [Coros 10] could not satisfy the requirement (b) in Section 3.1, i.e., gait reproducibility. In addition, in their simulation, the walking route of the DHM needs to be specified manually, so it is insufficient for satisfying the requirement (a), i.e., walking autonomy.

3.2.3 Summary of features of current walking simulation studies and walking simulation approach in this study

Based on the discussions given in 3.2.1 and 3.2.2, the features of the current walking simulation studies when applying these studies to the human behavior simulation aiming to the human-centered accessibility evaluation are summarized in Table 3.1. As shown in Table 3.1, the current walking simulation studies cannot satisfy all of the requirements (a)–(c) at the same time.

As shown in Table 3.1, (2) 3D human behavior simulation using DHM, and (3) MoCap-synthesis-based walking simulation approaches are potentially utilized for satisfying the requirements (b) and (c) at the same time. However, these simulations require measurements of human walking motion such as MoCap and video, on various walking terrains for a subject. On the other hand, (4) MoCap-synthesis-based walking simulation with terrain adaptation can generate walking motion of DHM on various walking terrains based only on the single reference MoCap data. However, as discussed in 3.2.2, in this simulation, the resultant motion cannot necessarily reproduce the real human motion. Furthermore, the motion of the DHM was not validated in their paper [Rami 13]. Moreover, to satisfy the requirement (a), the walking simulation algorithms (2)–(6) need to be combined with the algorithms of the general human behavior simulation such as [Duives 13].

Table 3.1 Features of current walking simulation

	(a) Walking autonomy	(b) Gait reproducibility	(c) Environmental flexibility	Feasibility
(1) General human behavior simulation [Duives 13], etc.	✔ — Walking route can be automatically determined	× — Cannot generate articulated walking movements	✔ — Can make pedestrian models walk on various walking terrains	
(2) 3D human behavior simulation using DHM [Kakizaki 14], [Kakizaki 16]	× — Walking route needs to be specified manually	✔ — Can generate human-like articulated movements of various people	✔ — Can make DHMs walk on various walking terrains	× — Many walking measurement data on various terrains are needed
(3) MoCap-synthesis-based walking simulation [Mukai 11], etc.	× — Walking route needs to be specified manually	✔ — Can generate human-like articulated movements of various people	✔ — Can make DHMs walk on various walking terrains	× — Many MoCap data on various terrains are needed
(4) MoCap-synthesis-based walking simulation with terrain adaptation [Rami 13]	× — Cannot change walking trajectory	× — Cannot reproduce human-like walking motion	✔ — Can make DHMs walk on various walking terrains	✔ — Single MoCap data for flat walking are needed
(5) Physics-based simulation [Yin 07], etc.	× — Walking route needs to be specified manually	× — Cannot reproduce human-like walking motion of various people	✔ — Can make DHMs walk on various walking terrains	✔ — Any MoCap data are not required
(6) Physics-based simulation with key-frame specification [Coros 10]	× — Walking route needs to be specified manually	× — Cannot necessarily reproduce human-like walking motion	✔ — Can make DHMs walk on various walking terrains	✔ — Only key-frame postures are needed
Meaning of the mark: ✔: Sufficient ×: Insufficient				

In contrast to the previous walking simulation algorithms, in this study, we aim to develop the autonomous walking simulation of the DHM, which can satisfy the requirements (a)—(c) as follows.

- To satisfy the requirement (a), i.e., walking autonomy, the walking path and walking trajectory of a DHM are generated based on the point clouds-based 3D as-is environment models.
- To satisfy the requirement (b), i.e., gait reproducibility, the walking motions of a DHM are generated based only on a single reference MoCap data for flat walking.
- To satisfy the requirement (c), i.e., environmental flexibility, the walking motions of a DHM on flat terrains are adapted to various walking terrains such as slopes and stairs, by modifying its joint positions based on the changes in the terrain height.

To satisfy the requirement (b) and (c) at the same time, in this study, the flat walking motion of the DHM is adapted to the different walking terrains based on the analysis of measurements of real human walking motion on various walking terrains including slopes and stairs.

3.3 Objective and overview

As discussed in the last section, the objective of this chapter is to develop an algorithm of autonomous walking simulation of the DHM in the 3D as-is environment models, which can satisfy the requirements such as the walking autonomy, gait reproducibility, and environmental flexibility.

Fig. 3.6 and Fig. 3.7 show overviews of the proposed autonomous walking simulation. As shown in the figures, the walking simulation is performed in the point clouds-based 3D as-is environment model in accordance with the user-specified walking simulation conditions such as the start position $\boldsymbol{p}_s$, goal position $\boldsymbol{p}_g$, walking stride w', subject s_i, and path preference $\boldsymbol{P}_P$. In accordance with the conditions, the DHM is set to autonomously walk along a walking path V^P, while reproducing the articulated walking movements of MoCap data of s_i, where V^P represents the walking path from $\boldsymbol{p}_s$ to $\boldsymbol{p}_g$, and is automatically selected based on $\boldsymbol{P}_P$.

As shown in Fig. 3.6 and Fig. 3.7, the autonomous walking simulation is realized by the following processes.

(1) Preference-based path selection

First of all, the walking path V^P of the DHM is automatically selected by searching over the navigation graph G_N based on the user-specified path preference $\boldsymbol{P}_P$. Details are described in 3.4.2.

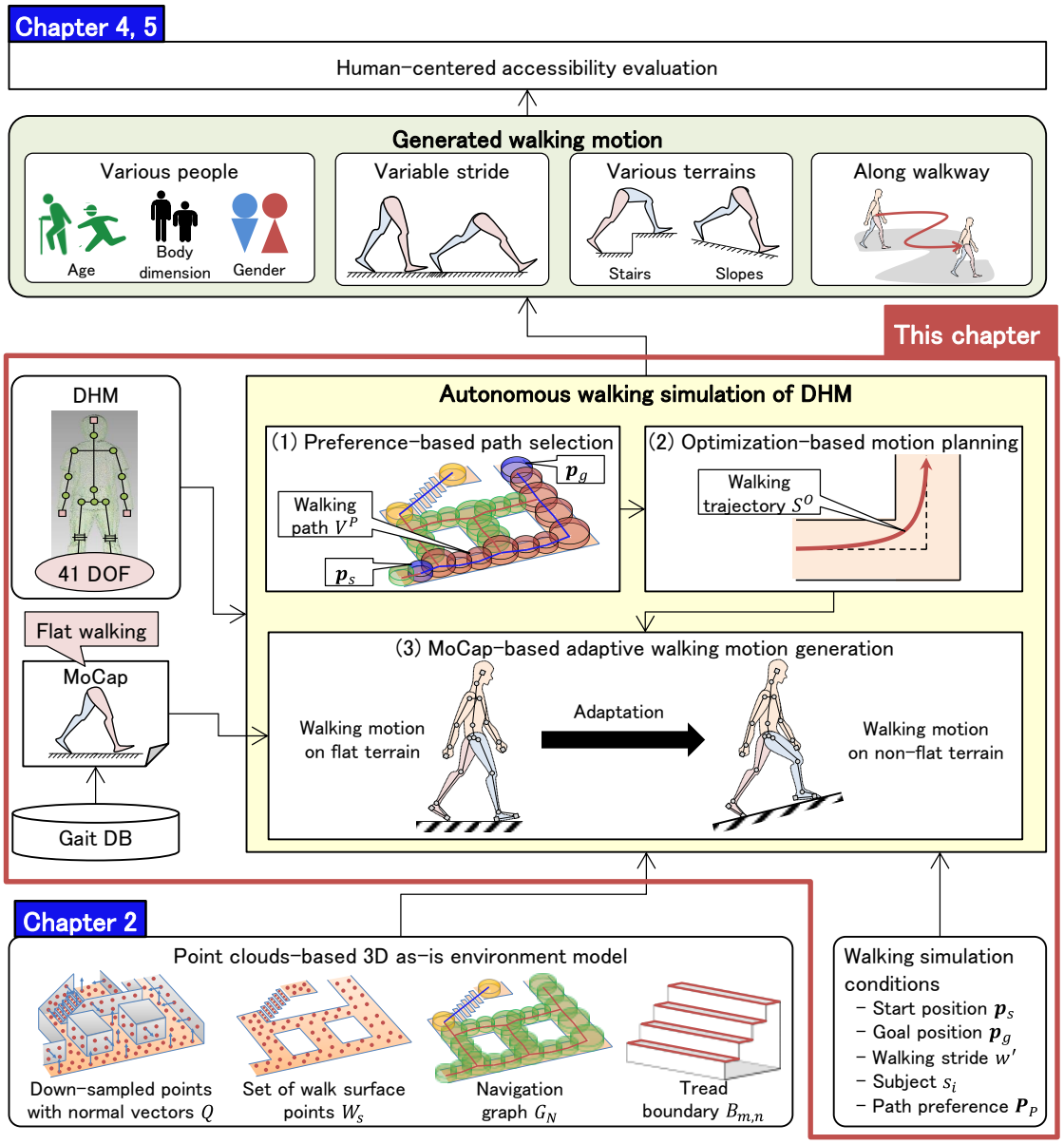

Fig. 3.6 Overview of autonomous walking simulation of DHM

(2) Optimization-based motion planning

Then, a walking trajectory $S^O = \{t_i\}$ of the DHM is automatically generated from V^P, where t_i represent the discretized pelvis position of the DHM at each walking step. The trajectory can be determined based on an optimization algorithm, which makes the trajectory S^O more smooth and natural, while avoiding contact with the walls. Details are described in 3.4.3.

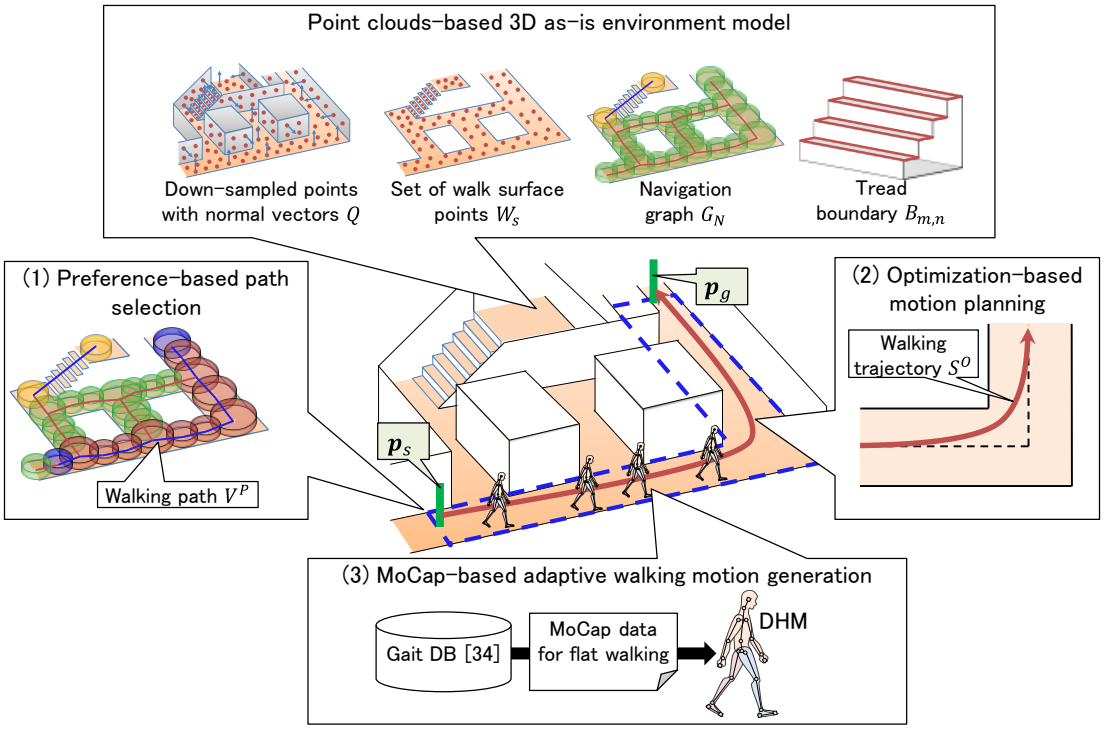

Fig. 3.7 Walking behavior of DHM in the point clouds-based 3D as-is environment model

(3) MoCap-based adaptive walking motion generation

Finally, the articulated walking movements of the DHM along the trajectory S^O are generated based on the single reference MoCap data for flat walking. In the algorithm, first, an one-step flat walking motion of the DHM is generated based on the single reference MoCap data for flat walking of the subject s_i. Then, the flat walking motion of the DHM is adapted to the actual walking terrains, by changing the pelvis and swing ankle positions based on the changes in the terrain height per step. Details are described in 3.4.4.

As shown in Fig. 3.6, as a result of the autonomous walking simulation of the DHM, the walking motion of various people of different ages, genders and body dimensions, with variable stride are obtained in various walking terrains such as the flat terrains, slopes, and stairs, while making the DHM autonomously walk along the walkway. The waking simulation results are used both for the tripping risk evaluation in Chapter 4, and for the ease of wayfinding evaluation in Chapter 5.

In contrast to the current walking simulation studies described in the last section, our autonomous walking simulation algorithm,

– generates the human-like walking motion even on non-flat walking terrain such as slopes and stairs, using only the single reference MoCap data for flat walking,

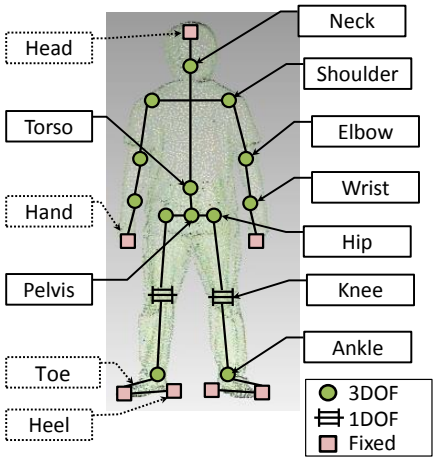

Fig. 3.8 Link mechanism of our DHM

- adapts the strides, turning angles, and footprints of the DHM to different as-is environment models including corridors, slopes, and stairs, even on non-flat terrain,
- provides fast and autonomous walking simulation directly in the point cloud-based 3D as-is environment models,
- is validated by a comparison of walking motion between the simulation and MoCap data on flat and non-flat walking terrains,
- provides a small difference in joint angles between the DHM and MoCap data.

The rest of this chapter is organized as follows. First, the algorithms of the autonomous walking simulation of the DHM are described in Section 3.4. After that, the simulation and validation results in the point clouds of indoor, outdoor, and urban environments are shown in Section 3.5. Finally, the summary of this chapter is described in Section 3.6.

3.4 Methods of autonomous walking simulation

3.4.1 Digital human model and MoCap data used in simulation

The autonomous walking simulation of the DHM is performed directly in the point clouds-based 3D as-is environment models, which were generated in Chapter 2. As shown in Fig. 3.6, a single reference MoCap data for flat walking of subject s_i are used in the proposed simulation to reproduce the motion of s_i during the simulation. This MoCap data is selected from the gait database (DB) containing the data of 139 subjects ranging in age from 13 to 72, which is measured and provided by DHRC [Kobayashi 13]. In addition, as shown in Fig. 3.8, our DHM has 41 degrees of freedom (DOF) in total, and has the same body dimensions as the subject s_i in the gait DB. The

link mechanism of the DHM was constructed based on the joint definition of MoCap data in the gait DB.

Fig. 3.9 shows a processing flow of the autonomous walking simulation of the DHM. Details of each process in Fig. 3.9 are described in the following subsections.

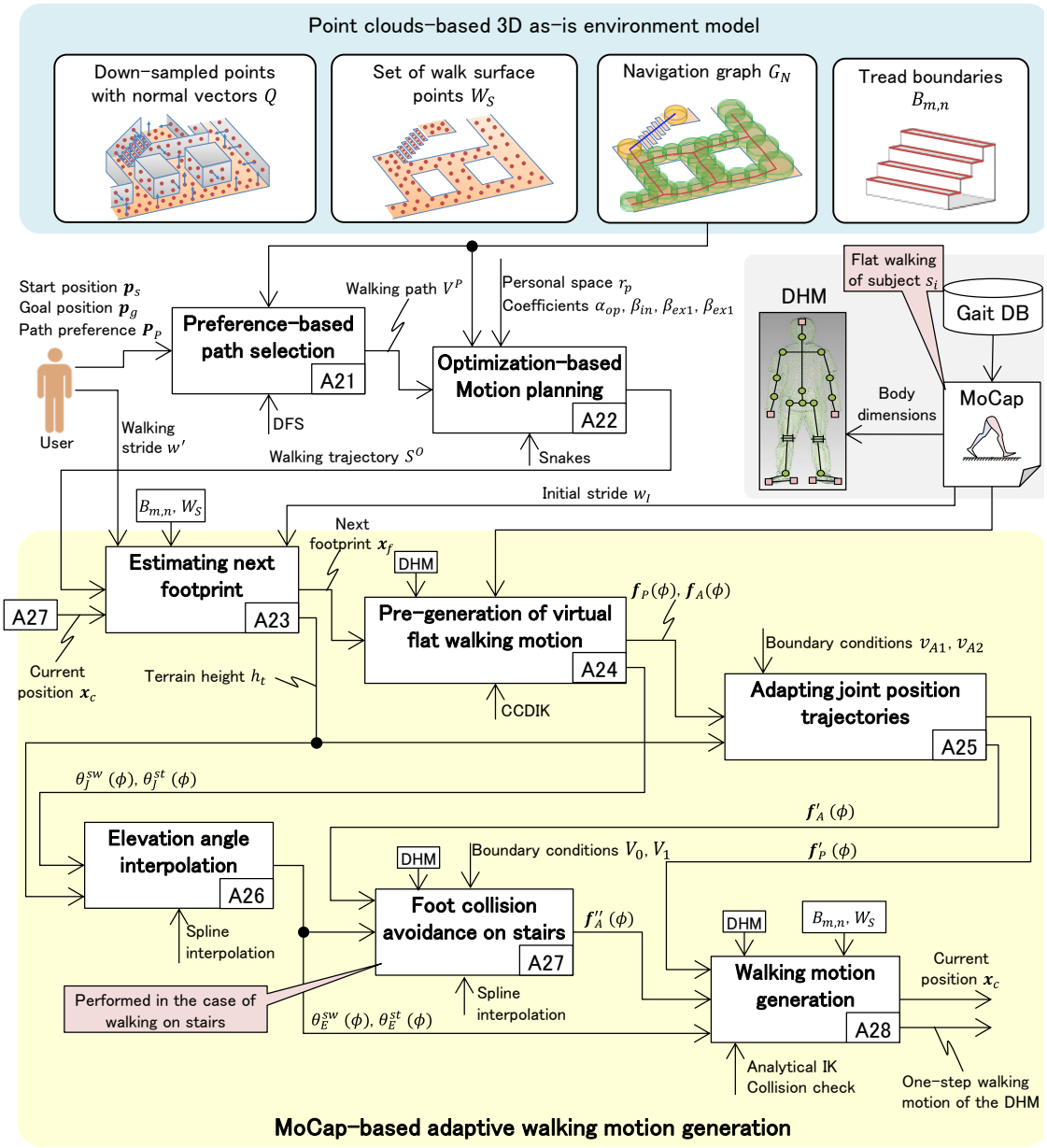

Fig. 3.9 Processing flow of autonomous walking simulation

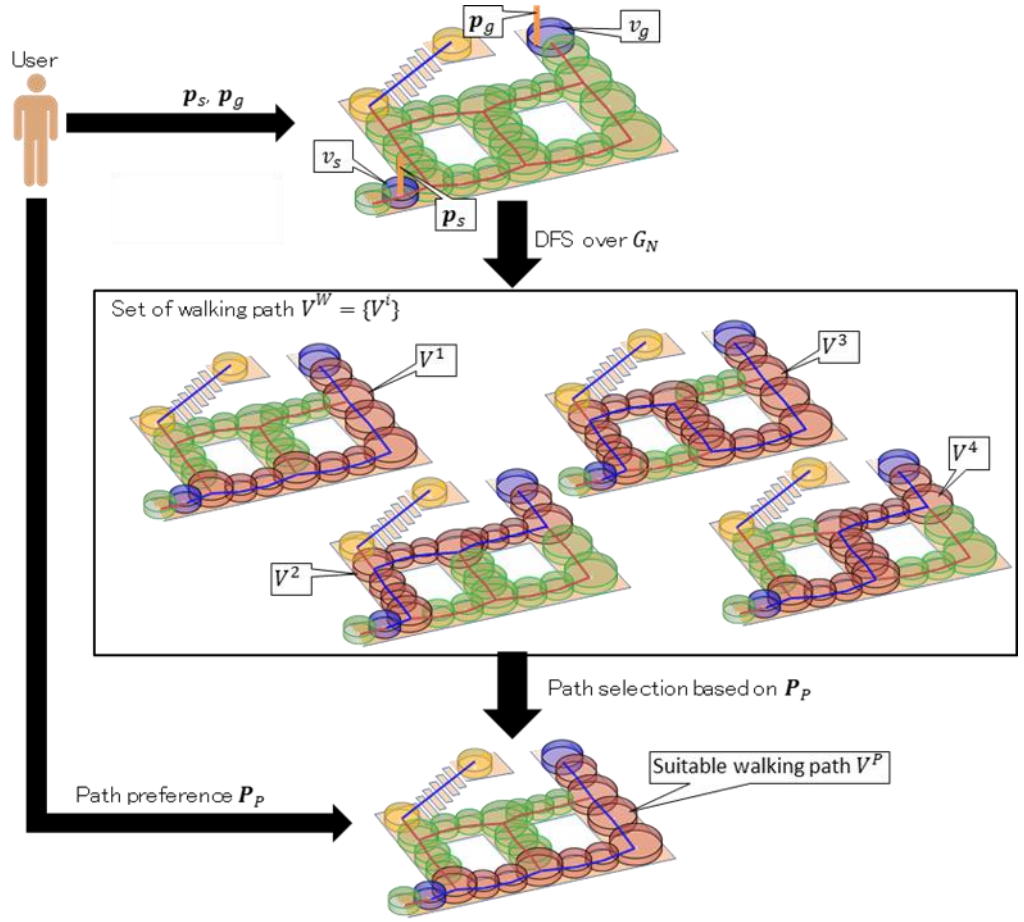

Fig. 3.10 Overview of preference-based path selection

3.4.2 Preference-based path selection

As shown in the part (A21) in Fig. 3.9, at the beginning of the autonomous walking simulation, the walking path V^P of the DHM is automatically selected from the navigation graph G_N.

Fig. 3.10 shows an overview of the preference-based path selection. As shown in Fig. 3.10, first, the user is asked to input start position $\boldsymbol{p}_s$ and goal position $\boldsymbol{p}_g$ on G_N. Then, the nearest graph node v_s of $\boldsymbol{p}_s$ and v_g of $\boldsymbol{p}_g$ are automatically determined. After that, a set of DHM's walking paths $V^W = \{V^i\}$ is extracted automatically by applying a depth-first search (DFS) repeatedly to G_N. Each path V^i consists of a set of graph nodes and edges, which are connected from v_s to v_g. If multiple walking paths exist between v_s and v_g, all of them are extracted by DFS. However, in general, extracting a lot of walking path exhaustively using DFS takes a lot of computation time. Therefore, in this study, to extract multiple paths within a practical time as much as possible, the maximum number of the iterations of DFS is specified as 50,000,000 times. After extracting V^W,

one suitable walking path $V^P \in V^W$ is automatically selected from V^W using the equation,

$$P = \arg\min_i(\boldsymbol{c}_i \cdot \boldsymbol{P}_P) \tag{3.1}$$

where $\boldsymbol{P}_P = [\beta_1, \beta_2](\beta_k \in [0,1])$ and $\boldsymbol{c}_i = [d_i,\ b_i]$ represent the user's path preference and path cost vector of each path V^i. Each element β_k specifies the degree of preference between the travel distance and the narrowness of the path. In the vector $\boldsymbol{c}_i$, $d_i \in [0,1]$ and $b_i \in [0,1]$ represent the normalized travel distance along V^i and the normalized narrowness of V^i, respectively. Each path cost vector $\boldsymbol{c}_i$ is automatically estimated from each path V^i. By selecting V^P based on $\boldsymbol{P}_P$, for example, when the user specifies the preference $\boldsymbol{P}_P$ as $\boldsymbol{P}_P = [1,0]$**,** the shortest walking path V^P can be automatically selected from V^W.

However, the selected suitable walking path V^P represents only the pathway connected from v_s to v_g. Therefore, after that, as shown in Figs. 3.6 and 3.7, the walking trajectory of the DHM, i.e., pelvis movements, needs to be generated on V^P in the optimization-based motion planning process described in the following subsection.

3.4.3 Optimization-based motion planning

3.4.3.1 Overview

Once the walking path V^P has been determined, as shown in Fig. 3.9, DHM's walking trajectory $S^O = \langle \boldsymbol{t}_i \rangle$ is generated automatically, where S^O represents a sparsely discretized sequence of the DHM pelvis positions $\boldsymbol{t}_i$ during the walking simulation.

In the proposed algorithm, first, the initial walking trajectory S^I is generated from V^P. Next, path boundary representing the boundary lines of the path V^P is generated. Finally, S^O is generated by applying an optimization algorithm to S^I, in order to make S^I to the human-like walking trajectory, i.e., short and smooth trajectory without any contact with walls. In the optimization algorithm, a weighted sum of an internal energy $E_{in}(\boldsymbol{t}_i)$ and an external energy $E_{ex}(\boldsymbol{t}_i)$ of the trajectory S^O are minimized, where the former energy becomes smaller as S^O becomes shorter and more smooth, and the latter one becomes smaller as the distance between S^O and the nearest walls becomes larger. Details are described in the following subsections.

3.4.3.2 Initial walking trajectory and path boundary generation

First, as shown in Fig. 3.11 (a), an initial walking trajectory $S^I = \langle \boldsymbol{t}_0, \cdots, \boldsymbol{t}_n \rangle$ is automatically generated from V^P. The starting point $\boldsymbol{t}_1$ of S^I and the end point $\boldsymbol{t}_n$ of S^I is calculated as $\boldsymbol{t}_1 = \boldsymbol{t}(v_s) + h_P\boldsymbol{Z}$ and $\boldsymbol{t}_n = \boldsymbol{t}(v_g) + h_P\boldsymbol{Z}$, where h_P and $\boldsymbol{Z} = [0,0,+1]$ represent a vertical

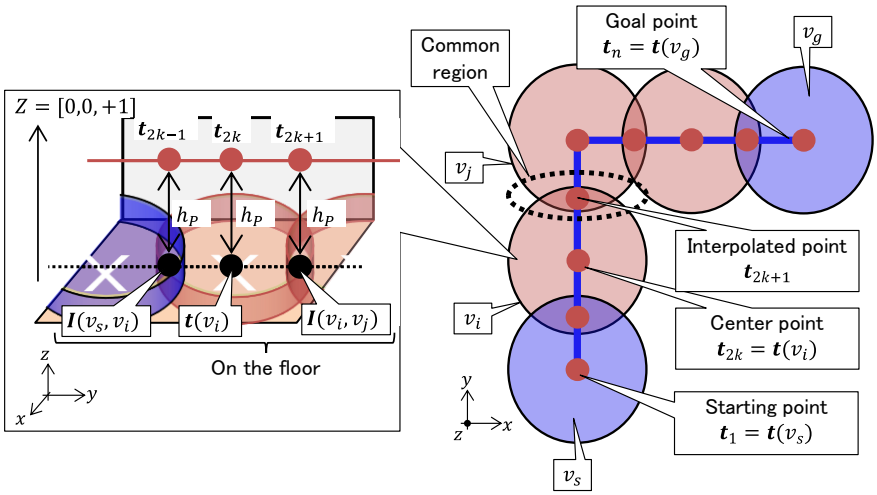

(a) Initial walking trajectory generation

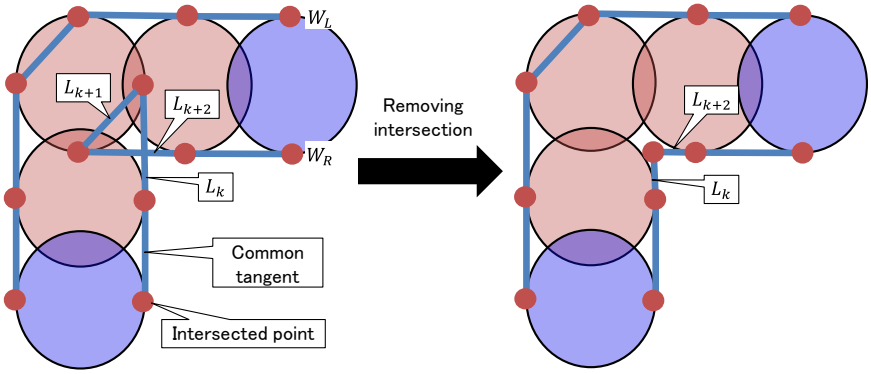

(b) Path boundary generation

Fig. 3.11 Overviews of initial walking trajectory and path boundary generation

distance between the heel and the pelvis of the selected DHM, and a vertical unit vector, respectively. The points between $\boldsymbol{t}_0$ and $\boldsymbol{t}_n$ represent a sequence of the center points $\boldsymbol{t}_{2k} = \boldsymbol{t}(v_i) + h_P\boldsymbol{Z}$ of each node and the interpolated points $\boldsymbol{t}_{2k+1} = \boldsymbol{I}(v_i, v_j) + h_P\boldsymbol{Z}$, where $\boldsymbol{I}(v_i, v_j)$ represent a point located at the centroid of the common region between two adjacent nodes $v_i, v_j \in V^P$.

After that, to optimize the initial trajectory while avoiding contact with the walls, the path boundaries are generated as the imitated walls of the walkway. As shown in Fig. 3.11 (b), the common tangent of two top circles of the adjacent node cylinders is first calculated. Then, the intersected points between the tangent and the circles are extracted. Next, two sets of line segments which respectively connect intersected points on the right or left side are created as right or left path boundaries W_R and W_L. To make a correct boundary, as shown in Figs. 3.11 (b), if a line segment L_k intersects with L_{k+2}, then L_{k+1} is removed. At the same time, the end point of L_k and the starting point of L_{k+2} are changed to its intersected point.

3.4.3.3 Walking trajectory optimization

Finally, the walking trajectory S^O is generated by moving each point $\boldsymbol{t}_i$ of S^I using the iterative calculation of "Snakes" [Kass 88] to minimize the following energy function $E(S)$,

$$E(S) = \sum_{i=1}^{n-1} \{\alpha_{op} E_{in}(\boldsymbol{t}_i) + (1-\alpha_{op}) E_{ex}(\boldsymbol{t}_i)\} \tag{3.2}$$

where $E_{in}(\boldsymbol{t}_i)$ is an internal energy, and $E_{ex}(\boldsymbol{t}_i)$ is an external energy at point $\boldsymbol{t}_i$ on the trajectory and α_{op} is a weight coefficient of two energies. As shown in Fig. 3.12 (a), $E_{in}(\boldsymbol{t}_i)$ increases as the local trajectory length and its approximated curvature around $\boldsymbol{t}_i$ increase, and it is defined by the equation,

$$E_{in}(\boldsymbol{t}_i) = \frac{n}{2\sum_{i=1}^{n} \|\boldsymbol{u}_i\|^2} (\|\boldsymbol{u}_i\|^2 + \beta_{in} \|\boldsymbol{u}_{i+1} - \boldsymbol{u}_i\|^2) \tag{3.3}$$

where $\boldsymbol{u}_i = \boldsymbol{t}_i - \boldsymbol{t}_{i-1}$, and β_{in} is a weight coefficient for the approximated curvature. Conversely, as shown in Fig. 3.12 (b), $E_{ex}(\boldsymbol{t}_i)$ increases as the distance between $\boldsymbol{t}_i$ and the nearest path boundary decreases, and it is defined by the equations,

$$\begin{aligned} &E_{ex}(\boldsymbol{t}_i) = \gamma\, e^{\frac{r_p - d_i}{\beta_{ex1}}} + \beta_{ex2}\, g(r_p - d_i) \\ &\gamma = e^{2r_p - pc_i}, g(x) = \begin{cases} x\ (x > 0) \\ 0\ (otherwise) \end{cases} \end{aligned} \tag{3.4}$$

where d_i is the distance from the nearest wall, pc_i is the path clearance and r_p represents the personal space of the DHM, respectively. In this equation, a part of the social force model in the crowd simulation [Helbing 00] is introduced into the first and second term. The first term of equation (3.4) represents a potential energy due to repulsive force from the path boundary, and the second term does a penalty, which has a non-zero value when the DHM touches the path boundaries. Moreover, as shown in Fig. 3.12 (c), we applied the coefficient $\gamma = e^{2r_p - pc_i}$ to the first term to reduce the potential energy when the DHM passes through the large space. β_{ex1} and β_{ex2} are the weight coefficients.

In this study, as a default setting, the weight coefficients are specified as $\alpha_{op} = 0.5$, $\beta_{in} = 10.0$, $\beta_{ex1} = 50$ and $\beta_{ex2} = 1000$. The weight coefficient α_{op} can be changed by the user in accordance with the walking simulation scenario. The setting strategies of the weight coefficients are described in Appendix B, where the coefficients are found and validated by a comparison of the walking trajectory between the simulation and the measurements from younger participants in an experiment.

As a result of the optimization-based motion planning, the human-like walking trajectory

$S^O = \langle \boldsymbol{t}_0, \cdots, \boldsymbol{t}_n \rangle$ of the DHM connecting from $\boldsymbol{p}_s + h_P \boldsymbol{Z}$ to $\boldsymbol{p}_g + h_P \boldsymbol{Z}$ are obtained.

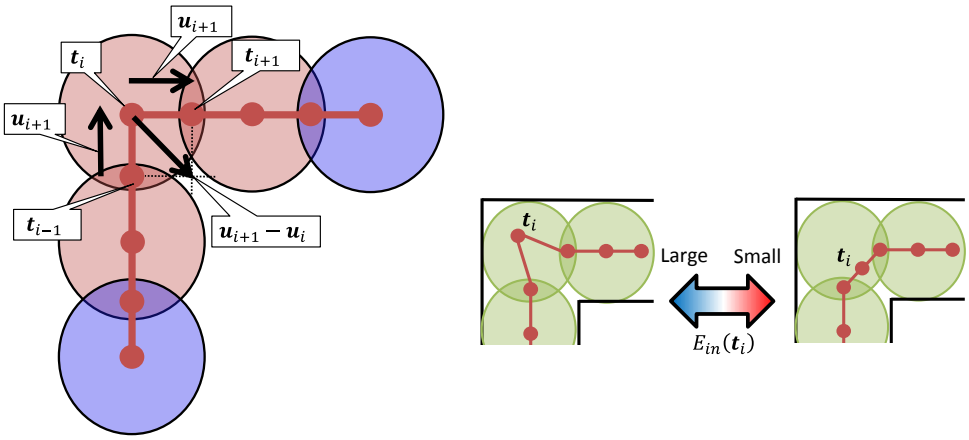

(a) Internal energy $E_{in}(\boldsymbol{t}_i)$

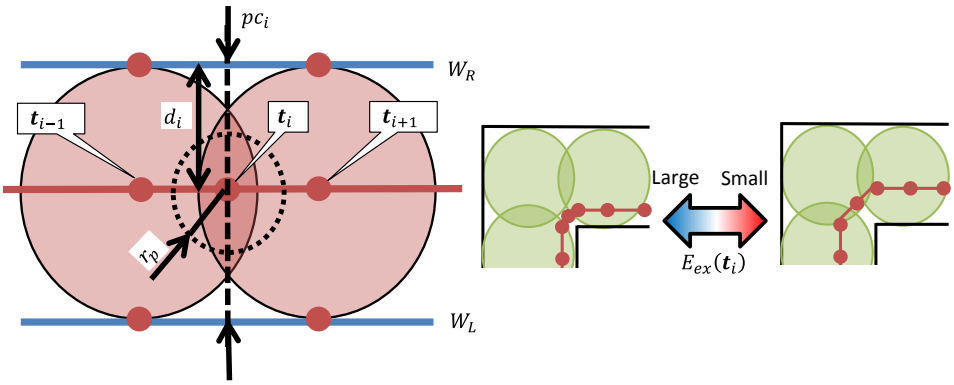

(b) External energy $E_{ex}(\boldsymbol{t}_i)$

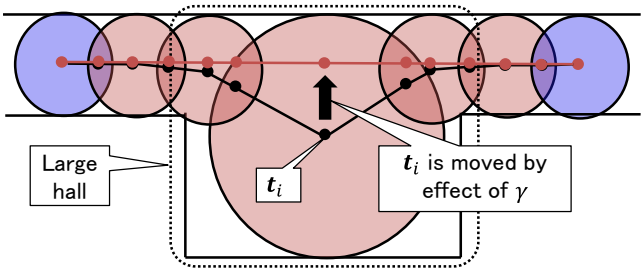

(c) Effect of coefficient γ in $E_{ex}(\boldsymbol{t}_i)$

Fig. 3.12 Internal and external energies

3.4.4 MoCap-based adaptive walking motion generation

3.4.4.1 Overview

After the walking trajectory S^O is determined, as shown in Figs. 3.6 and 3.7, the one-step walking motion of the DHM is generated along the walking trajectory S^O in the MoCap-based adaptive walking motion generation process. The walking motion of the DHM is generated by performing the processes (A23)–(A28) shown in Fig. 3.9.

In the algorithm, first, a next footprint $\boldsymbol{x}_f$ is determined on the walk surface points $W_i \subseteq W_S$ (Fig. 3.9 (A23)). Next, a virtual flat walking motion of the DHM is pre-generated using the single reference MoCap data for flat walking (Fig. 3.9 (A24)). As a result, a pelvis position trajectory $\boldsymbol{f}_P(\phi)$ and an ankle position trajectory of a swing leg (hereafter, called swing ankle position trajectory) $\boldsymbol{f}_A(\phi)$ for one-step virtual flat walking are obtained, where $\phi \in [0,1]$ represents the normalized phase of one-step walking. Then, the trajectories $\boldsymbol{f}_P(\phi)$ and $\boldsymbol{f}_A(\phi)$ are adapted to the actual walking terrains (Fig. 3.9 (A25)). In consequence, the adapted trajectories $\boldsymbol{f}'_P(\phi)$ and $\boldsymbol{f}'_A(\phi)$ are obtained. At the same time, the stance foot angle $\theta_E^{st}(\phi)$ and swing foot angle $\theta_E^{sw}(\phi)$ are interpolated using the "elevation angle" representation of each foot (Fig. 3.9 (A26)). After that, in the case of walking on stairs, a collision-free ankle position trajectory $\boldsymbol{f}''_A(\phi)$, which has no collisions with stair treads, can be further obtained by modifying the adapted ankle trajectory $\boldsymbol{f}'_A(\phi)$ (Fig. 3.9 (A27)). In contrast, in the case of walking on other terrains, $\boldsymbol{f}''_A(\phi)$ is directly copied from $\boldsymbol{f}'_A(\phi)$. Finally, the one-step motion of the DHM is generated based on the adapted pelvis trajectory $\boldsymbol{f}'_P(\phi)$, swing ankle trajectory $\boldsymbol{f}''_A(\phi)$, and interpolated elevation angles $\theta_E^{st}(\phi)$ and $\theta_E^{sw}(\phi)$ by solving IK analytically (Fig.3.9 (A28)). Details are given in the following subsections.

3.4.4.2 Estimating next footprint

As shown in Fig. 3.13, when the DHM passes through a point $\boldsymbol{t}_k$ in the walking trajectory S^O, a next subgoal position $\boldsymbol{x}_t$ is determined as $\boldsymbol{x}_t = \boldsymbol{t}_{k+2}$, which serves as a temporal target position during the walking simulation. The subgoal position $\boldsymbol{x}_t$ is continuously updated as the DHM walks along S^O. Next, as shown in the figure, a next locomotion vector $\boldsymbol{v}$ is determined as $\boldsymbol{v} = (\boldsymbol{x}_t - \boldsymbol{x}_c)/\|\boldsymbol{x}_t - \boldsymbol{x}_c\|$, where $\boldsymbol{x}_c$ is the current pelvis position of the DHM.

Following this, as shown in Fig. 3.14, a next footprint point $\boldsymbol{x}_f$, which represents a heel placement of the swing leg, is determined on the set of walk surface points W_S. The following algorithms are performed to locate $\boldsymbol{x}_f$ on different terrains: stair treads and others such as flat, sloping or bumpy terrain.

As shown in Fig. 3.14 (a), in the case of walking on a flat, sloping or bumpy terrain, a cylindrical search space C_F is generated centered at a point $\boldsymbol{p}_f$ horizontally located ahead of the current heel position $\boldsymbol{x}_{hs}$ by an initial walking stride w_f. w_f is specified as $w_f = w_I$ initially, where w_I is

an original stride length in the reference MoCap data from the gait DB. Note that any user-defined stride length w' that is different from w_I can be specified as w_f in the simulation. If the multiple walk surface points are included in C_F, the walk surface points having the maximum point number $W_i \subseteq W_S$ are extracted from W_S in order to locate the heel of the swing leg on the widest walkable region inside of C_F. Finally, the next footprint point $\boldsymbol{x}_f$ is determined as a centroid of W_i.

On the other hand, as shown in Fig. 3.14 (b), in the case of walking on stairs, the next footprint point $\boldsymbol{x}_f$ is located so that 3/4 of the total foot length L_f is placed on the tread according to an observational result of the literature [Reed 09], where the walking motion of subjects on stairs are experimentally observed and analyzed.

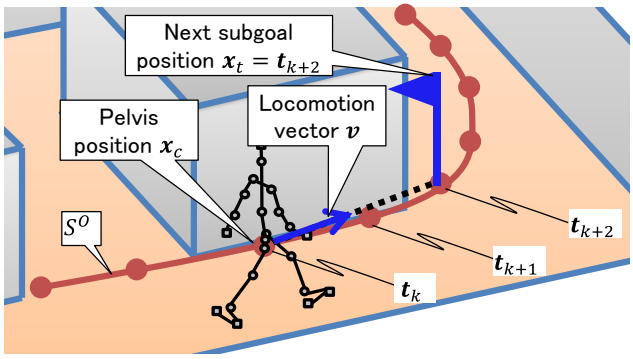

Fig. 3.13 Updating next subgoal position and locomotion vector

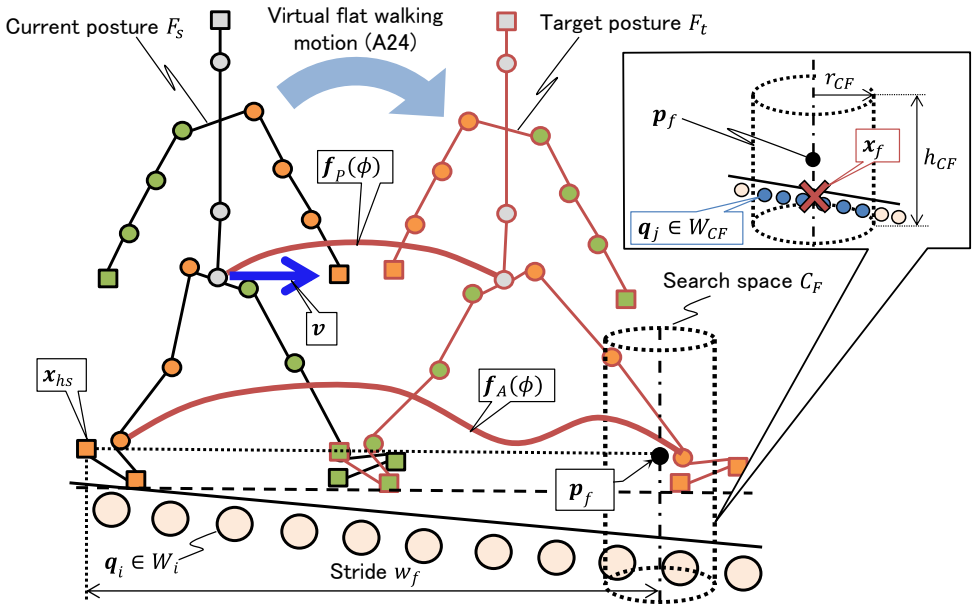

(a) Estimatiing next footprnt on a flat sloping or eneven terrain

Fig. 3.14 Next footprint estimation

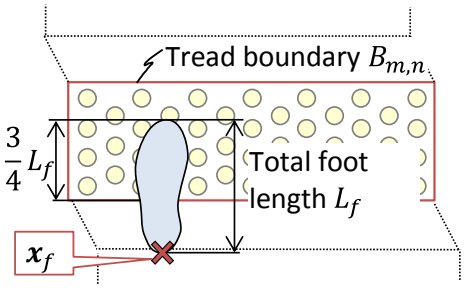

(b) Estimating next footprint on a stair tread

Fig. 3.14 Next footprint estimation (cont.)

3.4.4.3 Pre-generation of virtual flat walking motion

Once the next footprint point $\boldsymbol{x}_f$ is determined, as shown in the part (A24) in Fig. 3.9, an one-step virtual flat walking motion of the DHM with a stride length w, which differs from w_f, is pre-generated based on MoCap data for flat walking. Since $\boldsymbol{x}_f$ was determined by searching for walk surface points in 3.4.4.2, the horizontal distance between $\boldsymbol{x}_f$ and $\boldsymbol{x}_{hs}$ is different from w_f, where $\boldsymbol{x}_{hs}$ is the heel position of the swing leg of the DHM. Therefore, the stride length w is newly determined as $w = dist_H(\boldsymbol{x}_f, \boldsymbol{x}_{hs})$, where $dist_H(\boldsymbol{x}_f, \boldsymbol{x}_{hs})$ is the horizontal distance between $\boldsymbol{x}_f$ and $\boldsymbol{x}_{hs}$.

As shown in Fig. 3.15, the virtual flat walking motion of the DHM is pre-generated by the following processes (A241)–(A243).

(A241) Target posture generation

As shown in Fig.3.16, to achieve the next footprint point $\boldsymbol{x}_f$, target posture F_t of the DHM is generated using cyclic-coordinate-descent inverse kinematics (CCDIK) [Pan 13], which is an iterative inverse kinematics (IK) solver for redundant link-mechanisms. First, a key-frame posture F_I, representing the full-body posture at the initial heel contact frame in the next walking step is obtained from among a set of frames in the reference MoCap data selected from the gait DB. Then, a CCDIK method is applied to the key-frame posture F_I in order to determine the 14 DOF leg posture of the DHM. During the CCDIK, a range of motion (ROM) and symmetric hip joint angles are introduced as the constraints for CCDIK, in order to obtain a plausible target posture F_t.

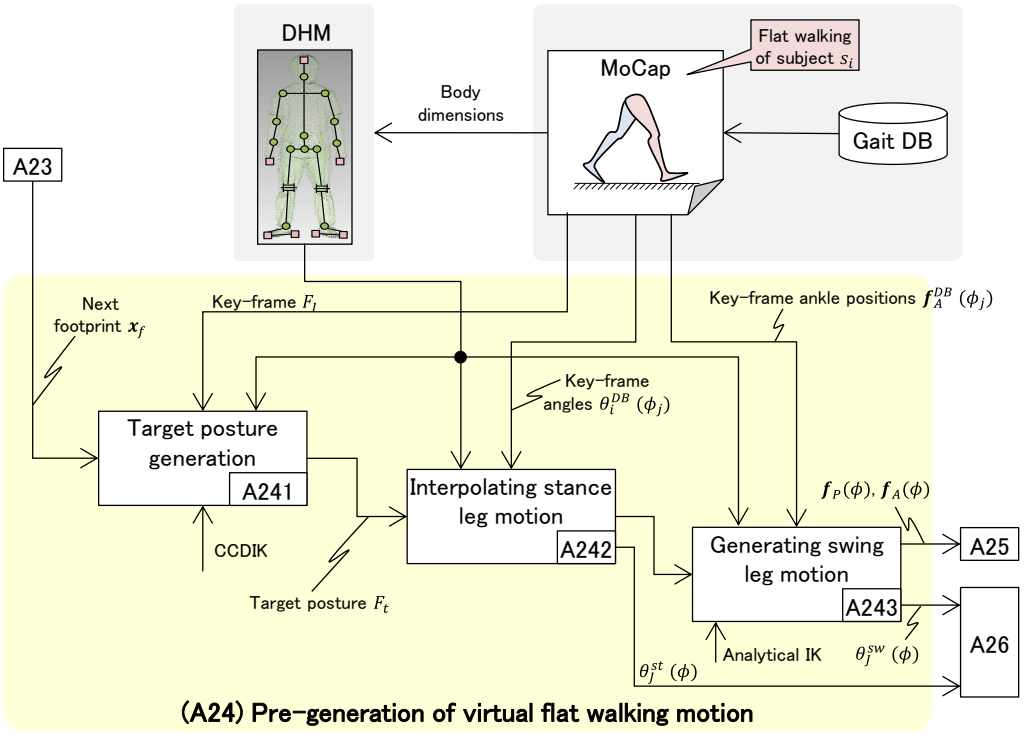

Fig. 3.15 Overview of pre-generation of virtual flat walking motion

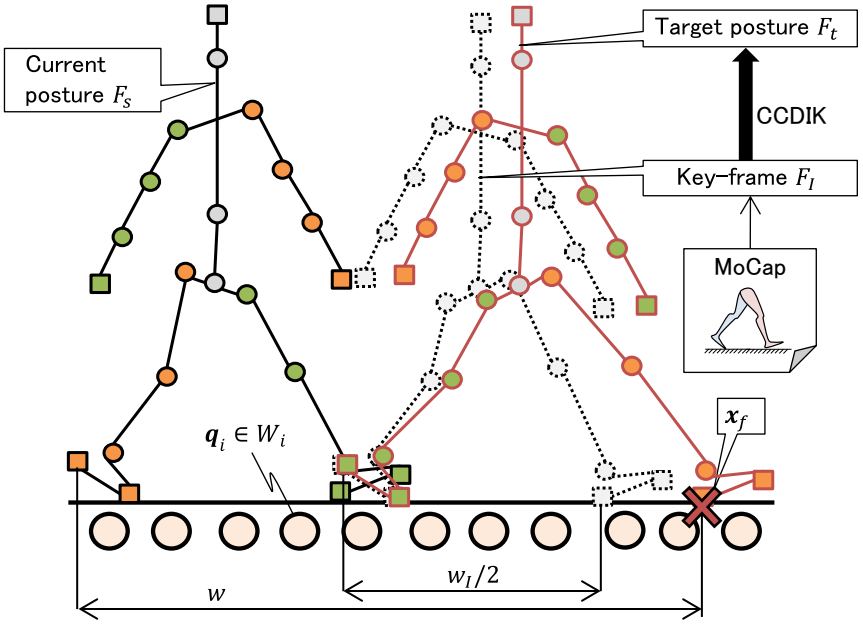

Fig. 3.16 Target posture generation

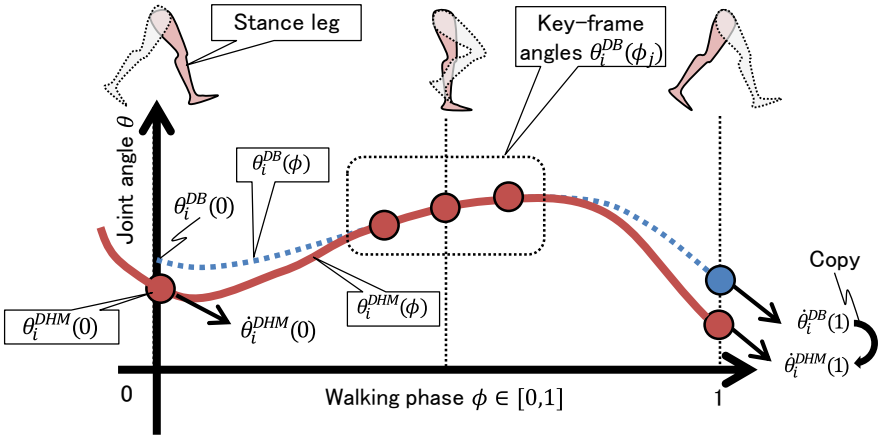

Fig. 3.17 Interpolating stance leg motion

(A242) Interpolating stance leg motion

After the target posture F_t is obtained, the stance leg motion, i.e., joint angles of the stance leg, is interpolated so that the motion finally satisfies F_t at the end of the interpolation. Fig. 3.17 shows the interpolation algorithm. In Fig. 3.17, $\theta_i^{DHM}(\phi)$, $\theta_i^{DB}(\phi)$, $\phi \in [0,1]$ represent the ith joint angle of the DHM's stance leg, the corresponding joint angle obtained from the single reference MoCap data, and the normalized walking phase, respectively

In the interpolation algorithm, first, the specific key-frame angle $\theta_i^{DB}(\phi_j)$ of the ith joint at ϕ_j is loaded from the reference MoCap data. Then, angles $\theta_i^{DB}(\phi_j)$ at $\phi_j \in \{0.4, 0.5, 0.6\}$ are selected as the key-frame angles to be left unchanged, under the assumption that the angles of the stance leg at the middle stance phase changed less against strides. After that, the stance leg angles $\theta_i^{DHM}(\phi)$ are interpolated using a cubic spline curve, so that they coincide with the key-frame angles $\theta_i^{DB}(\phi_j)$ at $\phi_j \in \{0.4, 0.5, 0.6\}$. The angles $\theta_i^{DHM}(0)$ and $\theta_i^{DHM}(1)$ and the angular velocities $\dot{\theta}_i^{DHM}(0)$ and $\dot{\theta}_i^{DHM}(1)$ at the current and target postures F_s and F_t, respectively, are also used as the boundary conditions. The angular velocity $\dot{\theta}_i^{DHM}(0)$ is determined by fitting a cubic polynomial curve locally to the corresponding joint angles of the DHM. Similarly, $\dot{\theta}_i^{DHM}(1)$ is also determined by fitting a cubic polynomial curve locally to the reference MoCap data.

If a turning or steering motion is required on the floor, the internal or external angle of the hip joint of stance leg is increased gradually in each frame during one-step walking until the rotation angle θ^{rot} is reached. θ^{rot} is the angle between the current locomotion vector $\boldsymbol{v}$ and the locomotion vector $\boldsymbol{v}^{pre}$ at the previous one-step walking.

As a result, a set of all joint angles $\theta_j^{st}(\phi) = \{\theta_i^{DHM}(\phi)\}$ of the DHM's stance leg during one-step virtual flat walking are obtained. Following this, by applying $\theta_j^{st}(\phi)$ to each joint of the DHM's stance leg, i.e., solving forward kinematics, the pelvis position trajectory $\boldsymbol{f}_P(\phi) = [x_P(\phi), y_P(\phi), z_P(\phi)]$ of the DHM is then obtained.

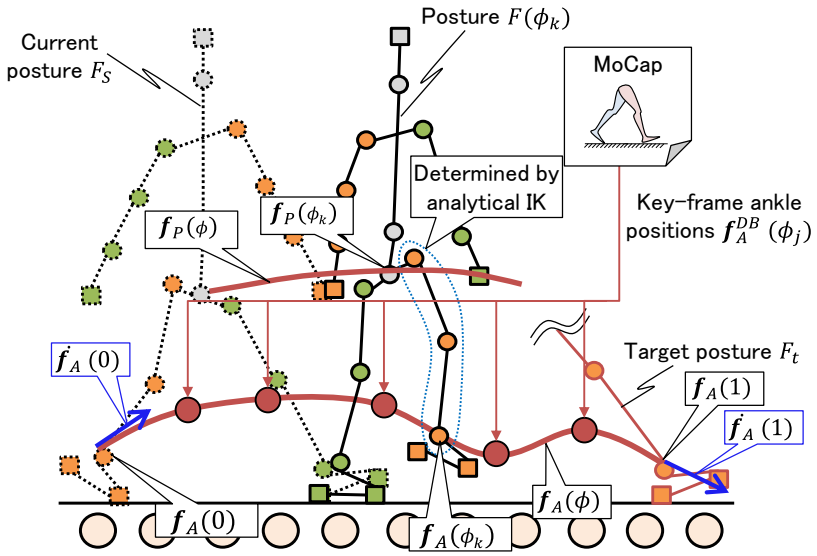

Fig. 3.18 Generating swing leg motion

(A243) Generating swing leg motion

After determining $\theta_j^{st}(\phi)$ and $\boldsymbol{f}_P(\phi)$, as shown in Fig. 3.18, the swing ankle position trajectory $\boldsymbol{f}_A(\phi)$ is interpolated by a cubic spline curve, so that they coincide with the key-frame ankle positions $\boldsymbol{f}_A(\phi_j)$ at $\phi_j \in \{0.2, 0.4, 0.6, 0.8, 0.9\}$. The positions $\boldsymbol{f}_A(0)$ and $\boldsymbol{f}_A(1)$ and the velocities $\dot{\boldsymbol{f}}_A(0)$ and $\dot{\boldsymbol{f}}_A(1)$ at the current and target postures F_s and F_t, respectively, are also used as the boundary conditions. The velocities $\dot{\boldsymbol{f}}_A(0)$ and $\dot{\boldsymbol{f}}_A(1)$ are estimated by fitting a cubic polynomial curve locally to the reference MoCap data, as well as the stance leg interpolation in the previous process (A242).

Finally, all of the joint angles of the swing leg are determined by solving IK analytically so as to achieve the interpolated ankle position trajectory $\boldsymbol{f}_A(\phi)$.

As a result of these processes, the ankle position trajectory $\boldsymbol{f}_A(\phi) = [x_A(\phi), y_A(\phi), z_A(\phi)]$, pelvis position trajectory $\boldsymbol{f}_P(\phi) = [x_P(\phi), y_P(\phi), z_P(\phi)]$, joint angles of stance leg $\theta_j^{st}(\phi)$, and one of swing leg $\theta_j^{sw}(\phi)$ during one-step virtual flat walking of the DHM could be obtained.

3.4.4.4 Adapting joint position trajectories

After the one-step virtual flat walking motion of the DHM is generated, the trajectories $\boldsymbol{f}_P(\phi)$ and $\boldsymbol{f}_A(\phi)$ of the virtual flat walking motion are then adapted to actual walking terrains. Fig. 3.19 shows an overview of the adaptations for $\boldsymbol{f}_A(\phi)$ and $\boldsymbol{f}_P(\phi)$. An adapted pelvis position trajectory $\boldsymbol{f}'_P(\phi) = [x'_P(\phi), y'_P(\phi), z'_P(\phi)]$ and adapted ankle position trajectory $\boldsymbol{f}'_A(\phi) = [x'_A(\phi), y'_A(\phi), z'_A(\phi)]$, which are adapted to the changes in the terrain height h_t per step, are obtained from

$$\begin{cases} x'_P(\phi) = x_P(\phi) \\ y'_P(\phi) = y_P(\phi) \\ z'_P(\phi) = z_P(0) + d_P(\phi'_P) + g_P(\phi'_P) \\ \phi'_P = (y'_P(\phi) - y'_P(0))/(y_P(1) - y_P(0)) \end{cases} \tag{3.5}$$

$$\begin{cases} x'_A(\phi) = x_A(\phi) \\ y'_A(\phi) = y_A(\phi) \\ z'_A(\phi) = z_A(0) + d_A(\phi'_A) + g_A(\phi'_A) \\ \phi'_A = (y'_A(\phi) - y'_A(0))/(y_A(1) - y_A(0)) \end{cases} \tag{3.6}$$

, where

$$\begin{cases} d_P(\phi'_P) = z_P(\phi'_P) - z_P(0) \\ g_P(\phi'_P) = \dfrac{(y_P(1) - y_P(0))}{(y_A(1) - y_A(0))} h_t \phi'_P \end{cases} \tag{3.7}$$

$$\begin{cases} d_A(\phi'_A) = z_A(\phi'_A) - z_A(0) \\ g_A(\phi'_A) = (v_{A1} + v_{A2} - 2h_t)\phi'^{3}_A + (-2v_{A1} - v_{A2} + 3h_t)\phi'^{2}_A + v_{A1}\phi'_A \end{cases} \tag{3.8}$$

In these equations, as shown in Fig.3.19 (b), the adapted pelvis height $z'_P(\phi)$ is determined by increasing or decreasing the original height $z_P(\phi)$ by the linear function $g_P(\phi'_P)$ of equation (3.7) depending on the changes in the terrain height h_t. Conversely, as shown in Fig.3.19 (a), the adapted ankle height $z'_A(\phi)$ is determined by increasing or decreasing the original height $z_A(\phi'_A)$ by the cubic function $g_A(\phi'_A)$ of equation (3.8), while respecting the original ankle positions of the swing leg at the beginning of the swing phase. This was caused by the fact that the swing foot of a real human is rotated about a toe contact position (toe locker) during the phase, as reported in [Perry 10]. In equation (3.8), the cubic function $g_A(\phi'_A)$ is determined so as to satisfy its boundary conditions $g_A(0) = 0$, $g_A(1) = h_t$, $g_A(0) = v_{A1}$, and $g_A(1) = v_{A2}$, where v_{A1} and v_{A2} are specified as $v_{A1} = 0$ and $v_{A2} = h_t$ according to our analysis of the preliminary experiment to measure human walking motion on different walking terrains described in Appendix C.

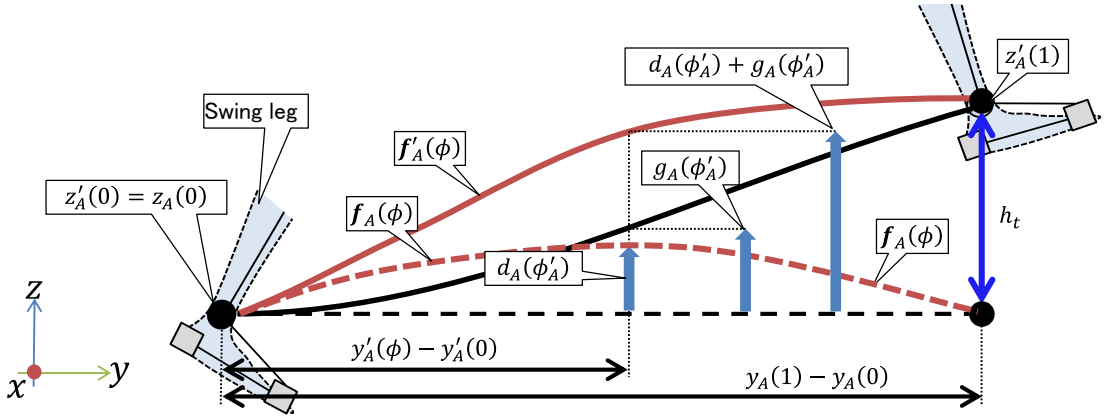

(a) Adapting ankle position trajectory $\boldsymbol{f}_A(\phi)$ to terrain height h_t

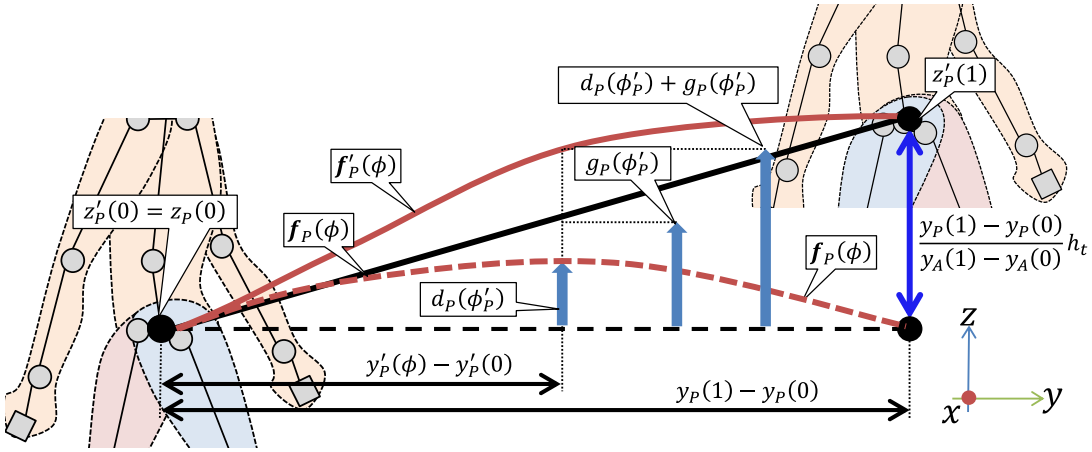

(b) Adapting pelvis position trajectory $\boldsymbol{f}_P(\phi)$ to terrain height h_t

Fig. 3.19 Adapting joint position trajectories

3.4.4.5 Elevation angle interpolation

After the joint angles of stance leg $\theta_J^{st}(\phi)$, and one of swing leg $\theta_J^{sw}(\phi)$ during one-step virtual flat walking are obtained in 3.4.4.3, the stance and swing foot elevation angles $\theta_E^{st}(\phi)$ and $\theta_E^{sw}(\phi)$ are then interpolated to determine the ankle joint angles during one-step walking.

As shown in Fig. 3.20 (a), a foot elevation angle θ_E represents the angle between the sole and the vertical axis, whereas an ankle joint angle θ_J represents the relative angle between the foot and the lower leg. Using the elevation angle representation makes it possible to adapt the foot orientation to the actual walking environment. Details are given below.

As shown in Fig. 3.20 (b), the foot elevation angles $\theta_E^{st}(\phi)$ and $\theta_E^{sw}(\phi)$ are interpolated using

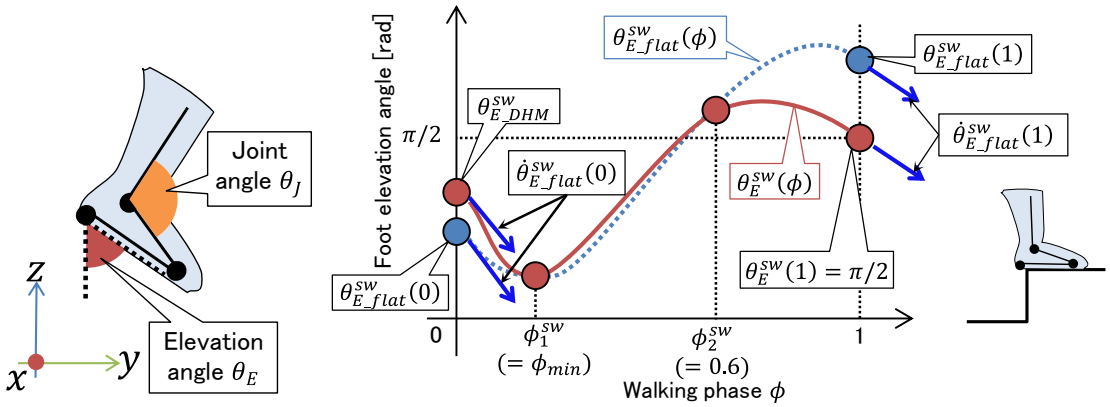

(a) Foot elevation angle (b) Elevation angle interpolation for swing foot on stairs

Fig. 3.20 Elevation angle interpolation

cubic spline curves so as to satisfy $\theta^{st}_E(\phi^{st}_i) = \theta^{st}_{E\_flat}(\phi^{st}_i)$ and $\theta^{sw}_E(\phi^{sw}_j) = \theta^{sw}_{E\_flat}(\phi^{sw}_j)$, where $\theta^{sw}_{E\_flat}(\phi^{st}_i)$ and $\theta^{st}_{E\_flat}(\phi^{sw}_j)$ represent the elevation angles of the pre-generated virtual flat walking at ϕ^{st}_i $(i = 1, 2, 3, 4)$ and ϕ^{sw}_j $(j = 1, 2)$, respectively. $\phi^{sw}_1 = \phi_{min}$ is dynamically determined, whereas ϕ^{sw}_2 is fixed as 0.6. The walking phase ϕ_{min} is determined as the walking phase when $\theta^{sw}_{E\_flat}(\phi)$ takes a minimum value between $\phi = 0.1$ and $\phi = 0.5$. In contrast, ϕ^{st}_i is determined as fixed values $\phi^{st}_i = 0.2 \times i$. The angles $\theta^{sw}_{E\_DHM}$, $\theta^{sw}_{E\_flat}(1)$, $\theta^{st}_{E\_DHM}$, and $\theta^{st}_{E\_flat}(1)$ and the angular velocities $\dot{\theta}^{sw}_{E\_flat}(0)$, $\dot{\theta}^{sw}_{E\_flat}(1)$, $\dot{\theta}^{st}_{E\_flat}(0)$, and $\dot{\theta}^{st}_{E\_flat}(1)$ are also used as the boundary conditions for the swing and stance foot of the DHM, respectively. The angles $\theta^{sw}_{E\_DHM}$ and $\theta^{st}_{E\_DHM}$ are the current elevation angles of the swing and stance foot, respectively. The angular velocities are estimated by fitting a line locally to each of the angles $\theta^{st}_{E\_flat}(\phi)$ and $\theta^{st}_{E\_flat}(\phi)$ between $\phi = 0.9$ and $\phi = 1.0$.

Furthermore, as shown in Fig.3.20 (b), when the DHM walks on stairs, $\theta^{sw}_{E\_flat}(1)$ is updated as $\theta^{sw}_{E\_flat}(1) = \pi/2$, which represents a foot orientation parallel to the horizontal plane, in order to realize the sole-contact on the stair tread.

3.4.4.6 Foot collision avoidance on stairs

As shown in Fig. 3.9, by executing the previous processes (A23)–(A26) with next process (A28), the DHM could walk in flat, sloping, and bumpy terrains. However, if the DHM walks on stairs based only on these processes, collision of the swing foot with a stair nosing may occur, where the nosing represents the edge of a stair tread as shown in Fig. 3.21 (a). Therefore, in order to avoid the foot collision with the stair nosing, after determining the adapted swing ankle trajectory $\boldsymbol{f}'_A(\phi) = [x'_A(\phi), y'_A(\phi), z'_A(\phi)]$ and swing foot elevation angle $\theta^{sw}_E(\phi)$, the swing ankle height $z'_A(\phi)$ of $\boldsymbol{f}'_A(\phi)$ needs to be modified accordingly.

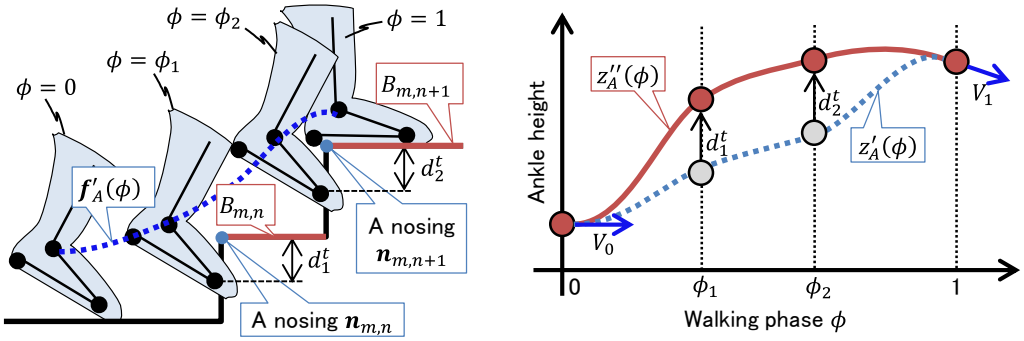

(a) Estimating penetration depths d_1^t and d_2^t (b) Interpolating ankle position trajectory $\boldsymbol{f}''_A(\phi)$

Fig. 3.21 Foot collision avoidance on stairs

As shown in Fig. 3.21 (a), first, the swing foot motion during one-step walking is virtually generated using both $\boldsymbol{f}'_A(\phi)$ and $\theta_E^{sw}(\phi)$ by solving IK analytically. Consequently, the penetration depths d_1^t and d_2^t are obtained along with the walking phases ϕ_1 and ϕ_2, where the toe of the swing foot is located just under the nosing of the stairs at ϕ_1 and ϕ_2. These penetration depths d_1^t and d_2^t are determined as $d_1^t = dist_V(\boldsymbol{p}_t^{sw}(\phi_1), \boldsymbol{n}_{m,n})$ and $d_2^t = dist_V(\boldsymbol{p}_t^{sw}(\phi_2), \boldsymbol{n}_{m,n+1})$, where $\boldsymbol{p}_t^{sw}(\phi)$, $\boldsymbol{n}_{m,n}$, and $dist_V(\boldsymbol{p}_t^{sw}(\phi), \boldsymbol{n}_{m,n})$ are the toe position of the swing foot, a nosing point estimated from the tread boundary $B_{m,n}$ and the vertical distance between $\boldsymbol{p}_t^{sw}(\phi)$ and $\boldsymbol{n}_{m,n}$, respectively. Finally, as shown in Fig. 3.21 (b), the collision-free ankle height $z''_A(\phi)$ is obtained by cubic spline interpolation of $z'_A(\phi)$, such that it satisfies $z''_A(\phi_1) = z'_A(\phi_1) + d_1^t$ and $z''_A(\phi_2) = z'_A(\phi_2) + d_2^t$ at the phases ϕ_1 and ϕ_2, respectively. The ankle positions $z'_A(0)$ and $z'_A(1)$ and velocities V_0 and V_1 are also used as the boundary conditions, where V_0 and V_1 are specified as $V_0 = 0$ and $V_1 = \dot{z'_A}(1)$, respectively. V_0 and V_1 are determined based on our analysis of the preliminary experiment to measure human walking motion on different walking terrains described in Appendix C.

As a result, a collision-free ankle position trajectory $\boldsymbol{f}''_A(\phi) = [x''_A(\phi), y''_A(\phi), z''_A(\phi)]$, which has no collisions of the swing foot with the stair treads, can be obtained.

3.4.4.7 Walking motion generation

Finally, as shown in Fig. 3.9, all of the joint angles of the stance and swing legs are determined using the calculation results of previous processes (A25)–(A27).

As shown in Fig. 3.22, first, the pelvis position of the DHM moves to $\boldsymbol{f}'_P(\phi)$ at the phase ϕ, where $\boldsymbol{f}'_P(\phi)$ was already adapted to the actual walking environment by the process (A25) in 3.4.4.4. The swing and stance foot orientations are determined by applying $\theta_E^{sw}(\phi)$ and $\theta_E^{st}(\phi)$ to each

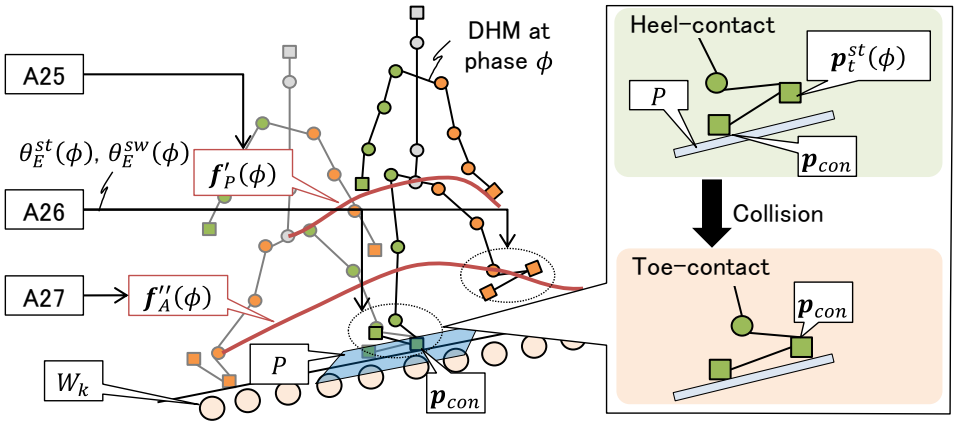

Fig. 3.22 Generating walking motion

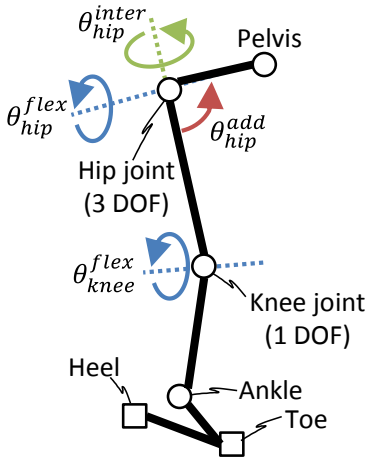

Fig. 3.23 Joint angle definition in this study

foot, which were interpolated by the process (A26) in 3.4.4.5. After that, all the joint angles of the stance leg are determined by solving IK analytically so as to achieve the current contact position $\boldsymbol{p}_c$ between the sole and the walking terrain surface. $\boldsymbol{p}_c$ is initialized as the heel position of the stance leg at the phase $\phi = 0$. Finally, all the joint angles of the swing leg are also determined by solving IK analytically so as to achieve $\boldsymbol{f}''_A(\phi)$. In the case of walking on stairs, $\boldsymbol{f}''_A(\phi)$ has been already adapted to the stairs so as to avoid collision of the swing foot with a stair nosing in the process (A27) in 3.4.4.6. By contrast, in the case of walking in the other terrains, $\boldsymbol{f}''_A(\phi)$ is directly copied from $\boldsymbol{f}'_A(\phi)$ which has been already adapted to an actual walking environment by the process (A25) in 3.4.4.4.

In this process, both leg motions are determined by solving the inverse kinematics analytically. Details of the inverse kinematics calculation are given below.

As shown in Fig. 3.23, given a pelvis point and an ankle point, it is necessary to determine the hip joint angle (3 DOF) and knee joint angle (1 DOF). To estimate all the joint angles, the

internal/external rotation angle of the hip joint θ_{hip}^{inter} is first determined. The internal/external rotation angle of the hip joint obtained from the pre-generated flat walking motion of the DHM is copied to the hip joint of the DHM θ_{hip}^{inter}. In cases where a turning or steering motion is required, the θ_{hip}^{inter} of the stance leg is increased gradually in each frame during one-step walking until the rotation angle θ^{rot} is reached. θ^{rot} is the angle between the current locomotion vector $\boldsymbol{v}$ and the locomotion vector $\boldsymbol{v}^{pre}$ in the previous one-step walking. Finally, the three joint angles, i.e., the flexion/extension rotation angle θ_{hip}^{flex} and adduction/abduction rotation angle θ_{hip}^{add} of the hip joint , and the flexion/extension rotation angle θ_{knee}^{flex} of the knee joint, are determined so as to achieve the given ankle point by simple geometric computation using trigonometric functions.

In addition, as shown in Fig. 3.22, a collision check between the stance toe position $\boldsymbol{p}_t^{st}(\phi)$ and a local walking terrain surface P is performed at every walking step. When a collision occurs, the contact position $\boldsymbol{p}_{con}$ is updated as $\boldsymbol{p}_{con} = \boldsymbol{p}_t^{st}(\phi)$ in order to realize the transition from heel contact to toe contact. The local walking terrain surface P is estimated by applying the least-square method to the walk surface points $W_k \subseteq W_S$ locally.

3.5 Results and validations of autonomous walking simulation

3.5.1 Results of autonomous walking simulation in indoor environments

We validated the effectiveness of the proposed autonomous walking simulation of the DHM in the four types of the as-is environment models, which were generated from the point clouds of one-floor indoor environment, two-story indoor environment, outdoor environment, and urban environment in Chapter 2.

In this section, first, using the as-is environment models of the one-floor and two-story indoor environments, we validated the basic functions of the proposed autonomous walking simulation: (1) preference-based path selection, (2) optimization-based motion planning and MoCap-based adaptive walking motion generation, (3) walking simulation on stairs, (4) walking simulation based on a variety of MoCap data for flat walking, (5) walking simulation with variable walking stride, and (6) Walking simulation in two-story indoor environment. Details are given below.

(1) Preference-based path selection (Fig. 3.24)

Fig. 3.24 shows the results of the preference-based path selection in the as-is environment models of one-floor and two-story as-is environments. In Fig. 3.24, the different path preferences $\boldsymbol{P}_P$ were specified for each environment. In particular, the preference vector $\boldsymbol{P}_P = [0.9,0.0]$ was used in Figs. 3.24 (a) and (c), i.e., putting a priority only on the travel distance along the path, and

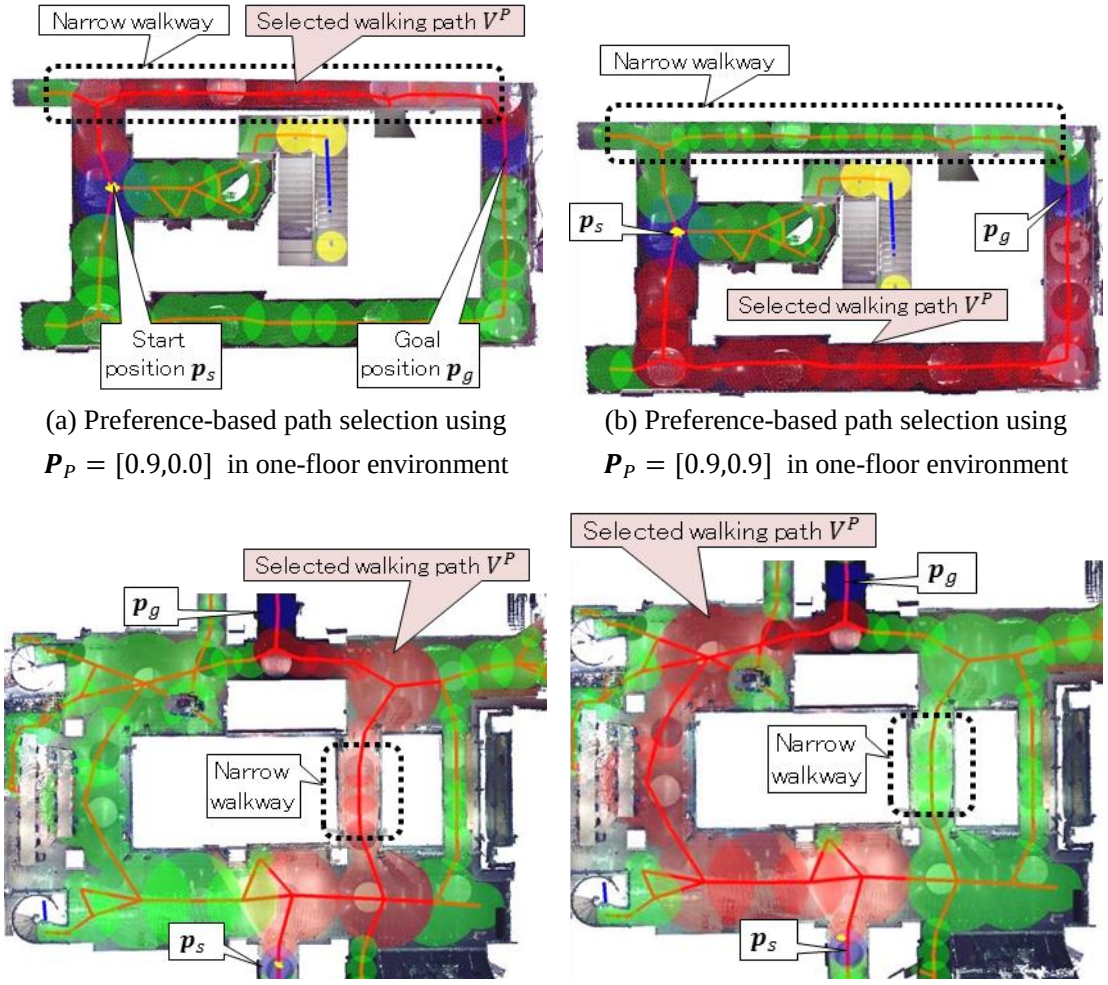

(a) Preference-based path selection using $\boldsymbol{P}_P = [0.9,0.0]$ in one-floor environment

(b) Preference-based path selection using $\boldsymbol{P}_P = [0.9,0.9]$ in one-floor environment

(c) Preference-based path selection using $\boldsymbol{P}_P = [0.9,0.0]$ in two-story environment

(d) Preference-based path selection using $\boldsymbol{P}_P = [0.9,0.9]$ in two-story environment

Fig. 3.24 Results of preference-based path selection

the different one $\boldsymbol{P}_P = [0.9,0.9]$ was used in Figs. 3.24 (a) and (c), i.e., putting a same priority on both travel distance and narrowness of the path. In Fig. 3.24 (a) and (b), a narrow walkway was artificially created by manually removing a part of the point clouds of the one-floor indoor environment.

As shown in Fig. 3.24 (a) and (c), when the user put the preference only on the distance of the path, the shortest walking paths were automatically selected. By contrast, as shown in Fig. 3.24 (b) and (d), when the user increases the preference on the narrowness of the path, the walking paths, which are wider than the selected ones of Fig. 3.24 (a) and (c), were automatically selected.

Therefore, it was confirmed that the walking path of the DHM could be automatically selected in accordance with the user-specified path preference $\boldsymbol{P}_P$.

(2) Optimization-based motion planning and MoCap-based adaptive walking motion generation (Fig. 3.25)

Fig. 3.25 shows the walking simulation results in the 3D as-is environment model of one-floor indoor environment. Figs. 3.25 (a) and (b) show the results of the preference-based path selection, and the optimization-based motion planning, respectively. As shown in Fig. 3.25 (a), the walking path V^P of the DHM from $\boldsymbol{p}_s$ to $\boldsymbol{p}_g$ could be automatically selected. In addition, as shown in Fig. 3.25 (b), the walking trajectory S^O of the DHM could be automatically generated in the selected walking path V^P. Finally, Figs. 3.25 (c) and (d) show the results of autonomous walking simulation of the DHM in corridors. In the figures, the MoCap data of an older subject (female, aged 72) was used in the simulation. As shown in the figure, the DHM was able to walk in corridors autonomously along the walkway including the stairs from the user-specified start position $\boldsymbol{p}_s$ to goal position $\boldsymbol{p}_g$, while generating the articulated walking movements of the DHM.

Therefore, it was confirmed that the proposed walking simulation algorithm enabled the DHM to walk autonomously in the point clouds-based as-is environment models, only by specifying the preference vector $\boldsymbol{P}_P$, start position $\boldsymbol{p}_s$ and goal position $\boldsymbol{p}_g$.

(3) Walking simulation on stairs (Fig. 3.26)

In addition, Fig. 3.26 shows the walking simulation results on stairs included in the one-floor indoor environment. In the figure, right and left toe trajectories are also displayed with tread boundaries of the stairs. As shown in Fig. 3.26, the DHM could autonomously walk even on the stairs, while avoiding the contact of its toe with the nosing of the stairs.

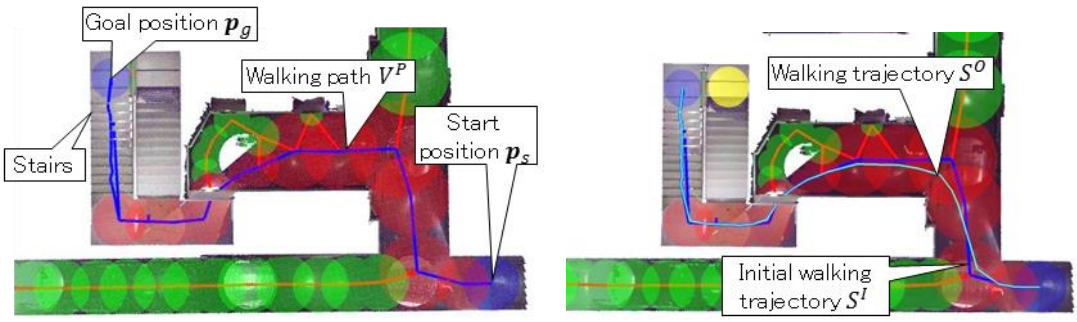

(a) Preference-based path selection ($\boldsymbol{P}_P = [0.9, 0.1]$)

(b) Optimization-based trajectory generation

Fig. 3.25 Autonomous walking simulation in one-floor indoor environment

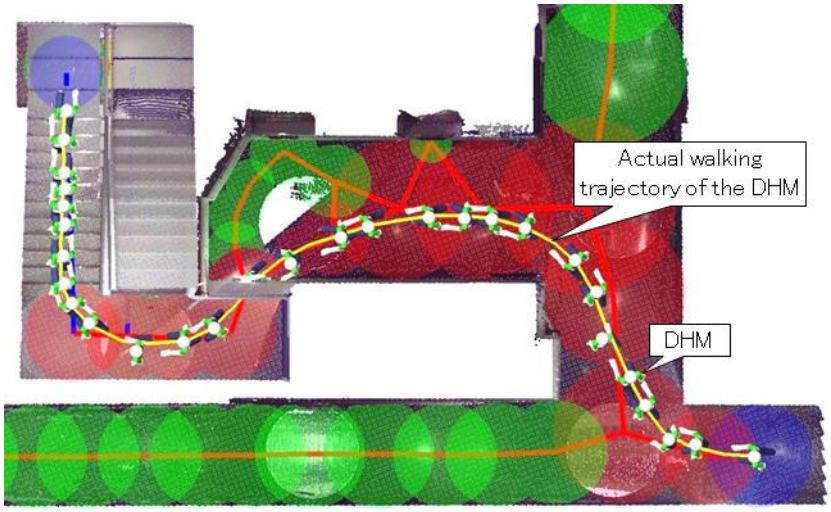

(c) Autonomous walking simulation on corridors and stairs (top view)
(reference subject: female, aged 72)

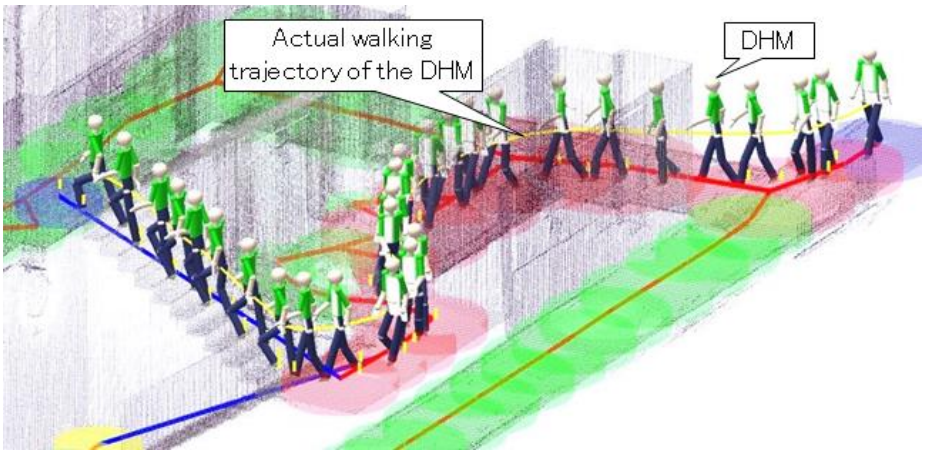

(d) Autonomous walking simulation on corridors and stairs
(reference subject: female, aged 72)

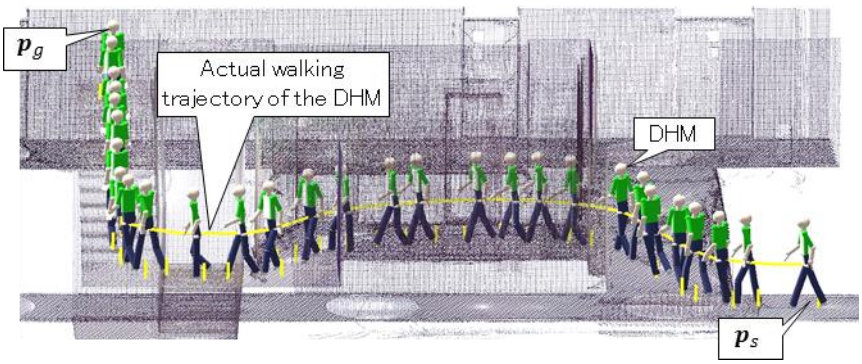

(e) Autonomous walking simulation on corridors and stairs
(without navigation graph rendering)

Fig. 3.25 Autonomous walking simulation in one-floor indoor environment (cont.)

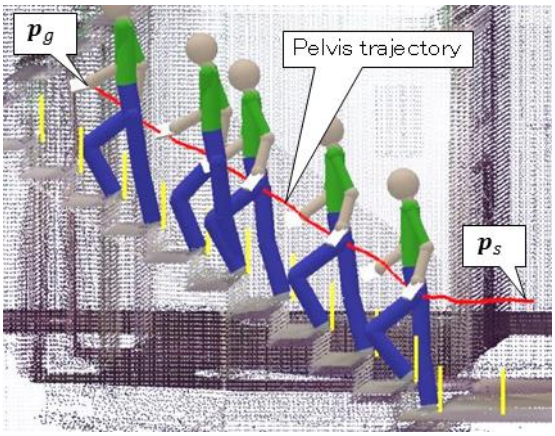

(a) Walking on stairs
(reference subject: female, aged 72)

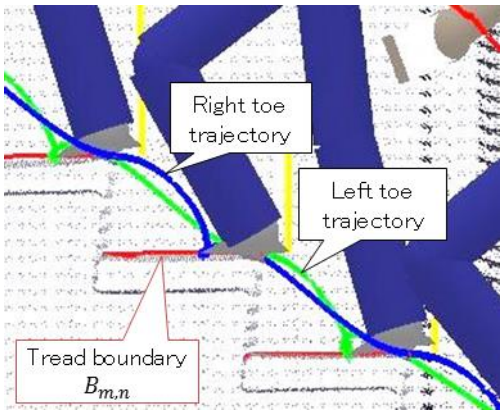

(b) Toe trajectories during walking on stairs

Fig. 3.26 Autonomous walking simulation on stairs

(4) Walking simulation based on a variety of MoCap data for flat walking (Fig. 3.27)

On the other hand, Fig. 3.27 shows the simulated walking motions of the DHM using the different MoCap data: male aged 23, female aged 13, and female aged 72. As shown in Figs. 3.27 (a)–(c), the DHM could generate its walking motion based on the different MoCap data, while plausibly recreating the oscillation of the pelvis (Fig. 3.27 (d)) that has been observed as a feature of human walking [Perry 10] without any direct specification or interpolation of the pelvis movements.

Therefore, it was confirmed that the proposed walking simulation algorithm enabled the DHM to generate its articulated walking movements based on a variety of MoCap data, while respecting human walking features.

(5) Walking simulation with variable walking stride (Fig. 3.28)

Fig. 3.28 shows the simulated walking motions of the DHM when the different walking stride w' was specified. Fig. 3.28 (a) shows the walking motion of the DHM using the original walking stride w_I that was obtained from the MoCap data. By contrast, Figs. 3.28 (b)–(e) show the simulated walking motion of the DHM using the user-specified walking stride w' which is longer or shorter than w_I. As shown in Fig. 3.28, the DHM could generate walking motion with the different user-specified walking stride w_I, while plausibly recreating the oscillation of the pelvis (Fig. 3.27 (d)).

Therefore, it was confirmed that the proposed walking simulation made it possible to generate

human-like walking motion of the DHM with any user-specified walking stride w'.

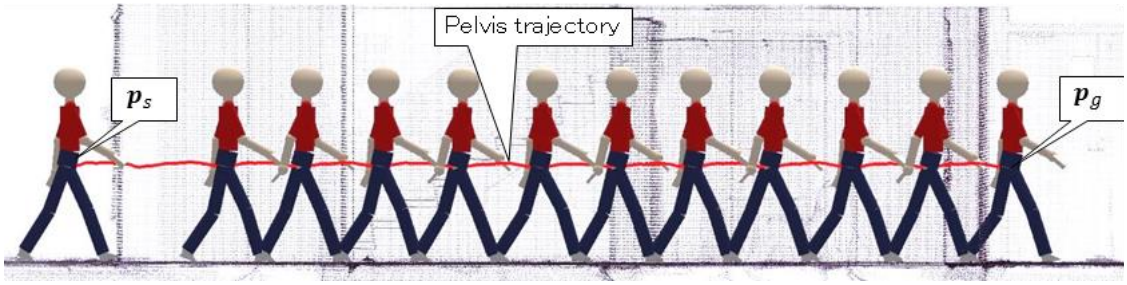

(a) Male aged 23

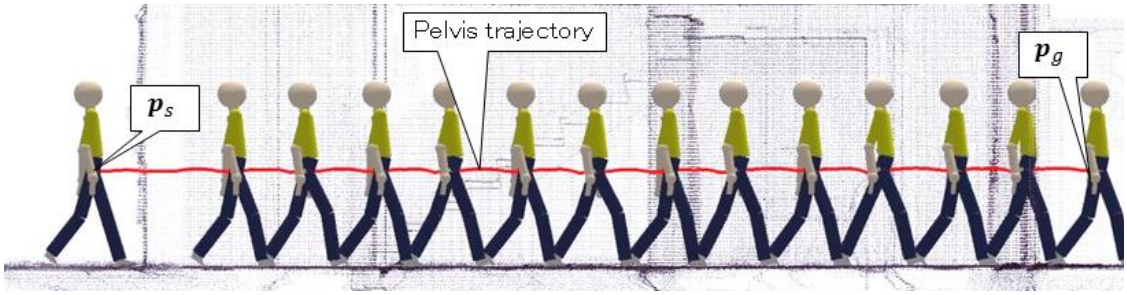

(b) Female aged 13

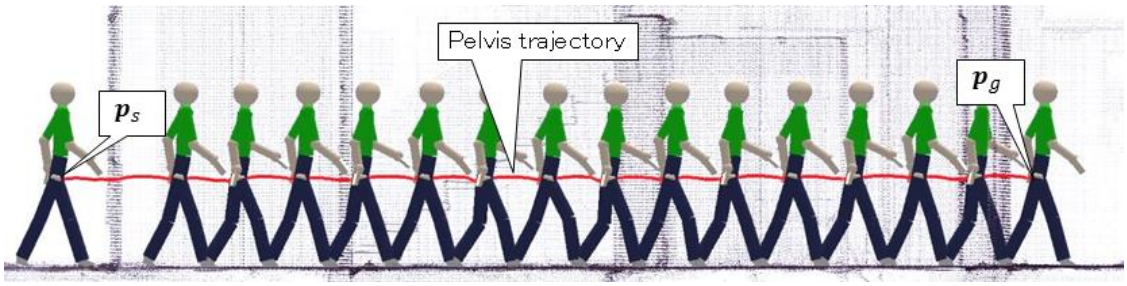

(c) Female aged 72

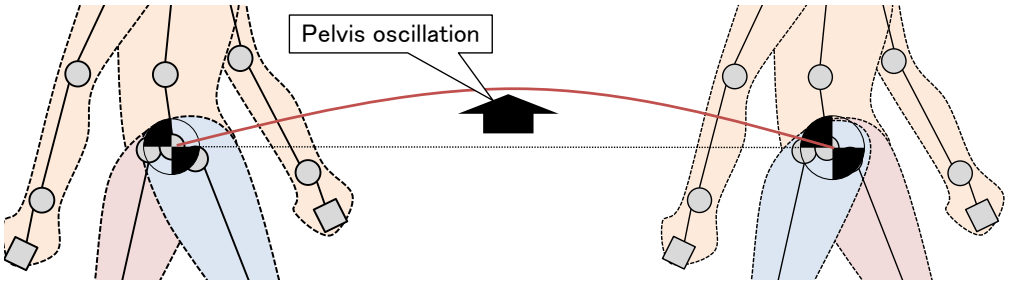

(d) Pelvis oscillation

Fig. 3.27 Comparison of simulated walking motion of DHM using different MoCap data

(a) Female aged 72 with the original stride w_I

(b) Female aged 72 with the specified stride $w' = w_I + 0.3$ m

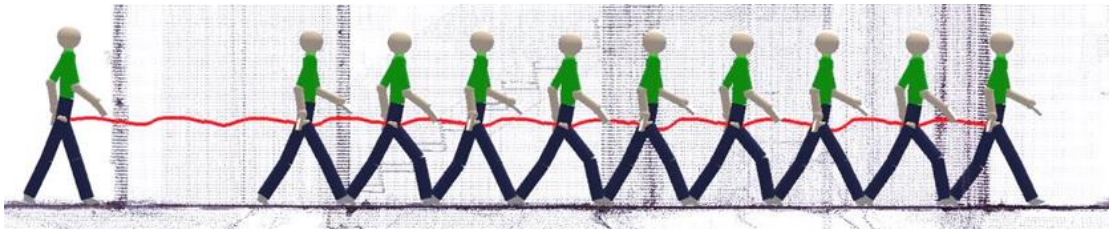

(c) Female aged 72 with the specified stride $w' = w_I + 0.5$ m

(d) Female aged 72 with the specified stride $w' = w_I - 0.2$ m

(e) Female aged 72 with the specified stride $w' = w_I - 0.4$ m

Fig. 3.28 Comparison of simulated walking motion of DHM using different strides
(red lines: pelvis trajectory)

(6) Walking simulation in two-story indoor environment (Fig. 3.29)

Finally, Fig. 3.29 shows the walking simulation results in the two-story indoor environment. In the figure, the start position $\boldsymbol{p}_s$ was specified on the first floor, and the goal position $\boldsymbol{p}_g$ was specified on the second floor. As shown in Figs. 3.28 (a) and (b), the walking path V^P could be successfully selected even if the user specified $\boldsymbol{p}_s$ and $\boldsymbol{p}_g$ on the different floors. In addition, Figs. 3.28 (c)–(f) show the walking simulation results using the selected walking path V^P. As shown in Fig. 3.29, the DHM could autonomously walk from $\boldsymbol{p}_s$ on the first-floor to $\boldsymbol{p}_g$ on the second-floor by autonomously ascending the caracole.

Therefore, it was confirmed that the proposed walking simulation algorithm enabled the DHM to autonomously walk even in the two-story environment through complex stairs such as caracoles.

Considering the autonomous walking simulation results in (1)–(6), i.e., Figs. 3.24–3.29., it was concluded that the proposed autonomous walking simulation algorithm enabled the DHM to walk autonomously in various walking terrains with any user-specified walking stride, while respecting human walking features based on a variety of MoCap data for flat walking. This showed the effectiveness of the basic functions of the proposed autonomous walking simulation.

3.5.2 Results of autonomous walking simulation in outdoor environment

We further validated the effectiveness of the proposed autonomous walking simulation using the as-is environment model of the outdoor environment.

Fig. 3.30 shows the walking simulation results in the as-is environment model of the outdoor environment including 3-deg, 6-deg, and consecutive slopes. As shown in Fig. 3.30 (a) and (b), the DHM could autonomously ascend and descend slopes, without any penetration of the toe of stance leg of the DHM into the slopes. Furthermore, as shown in Figs. 3.30 (c) and (d), it was also confirmed that the DHM could autonomously walk on consecutive slopes, while making its turning motions at the corners.

Therefore, considering the walking simulation results in the indoor and outdoor environments in 3.5.1 and 3.5.2, it was concluded that the DHM could autonomously walk in the as-is environment model regardless of indoor and outdoor environments, while adapting its strides, turning angles, and footprints to the point clouds-based 3D as-is environment models.

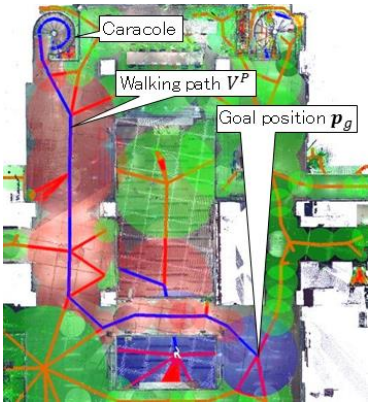

(a) Selected walking path

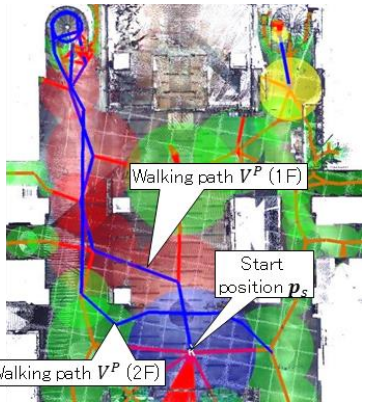

(b) Selected walking path
(point clouds of first floor were not rendered)

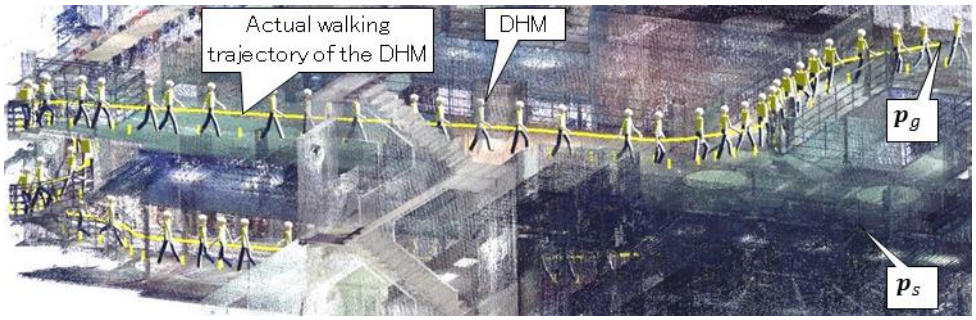

(c) Autonomous walking simulation of DHM (reference subject: female, aged 23)

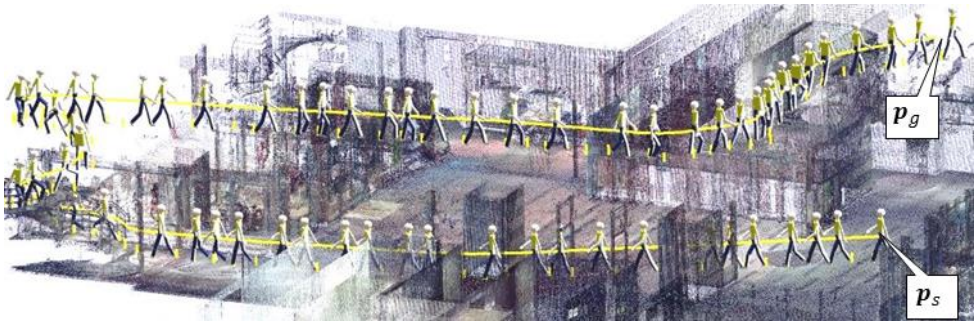

(d) Autonomous walking simulation of DHM (reference subject: female, aged 23)
(point clouds of first floor were not rendered)

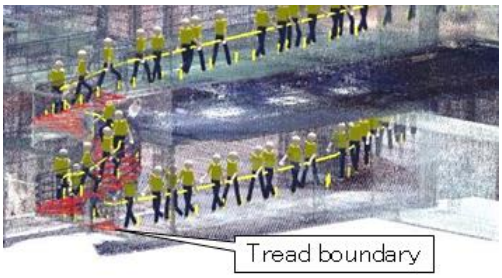

(e) Walking on caracole

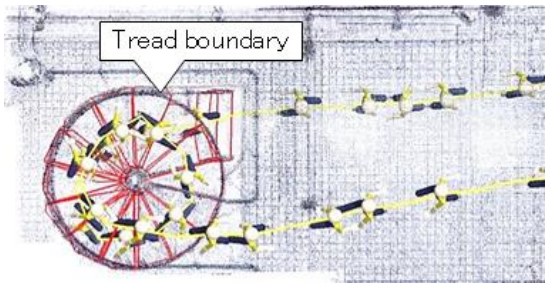

(f) Walking on caracole (top view)

Fig. 3.29 Autonomous walking simulation in two-story indoor environment

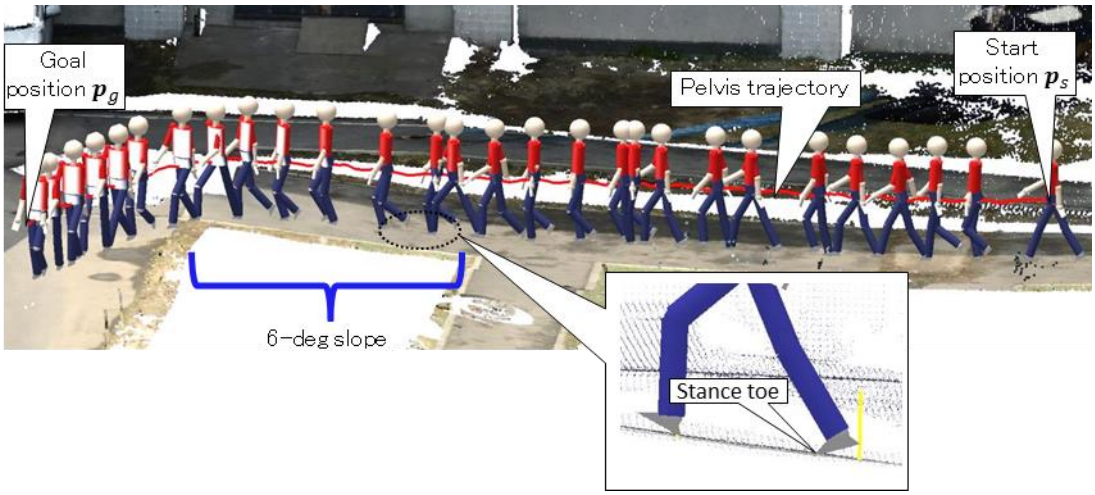

(a) Ascending outdoor slope (6 deg) (reference subject: male, aged 23)

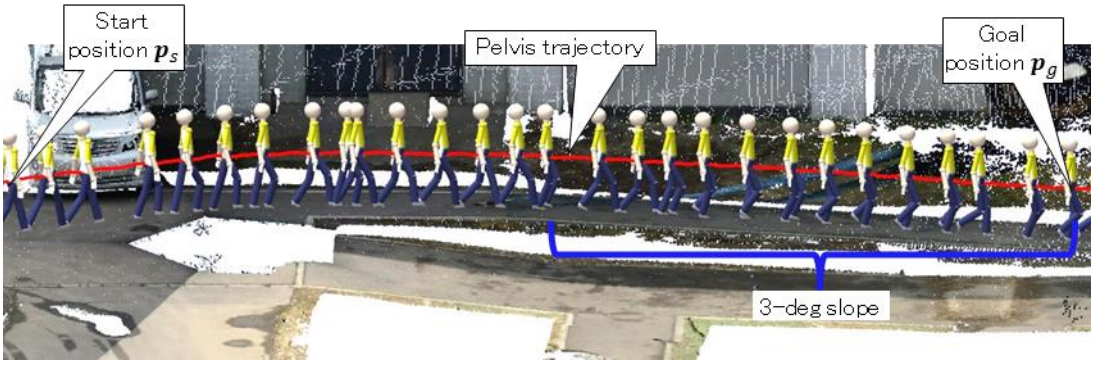

(b) Descending outdoor slope (3 deg) (reference subject: female, aged 13)

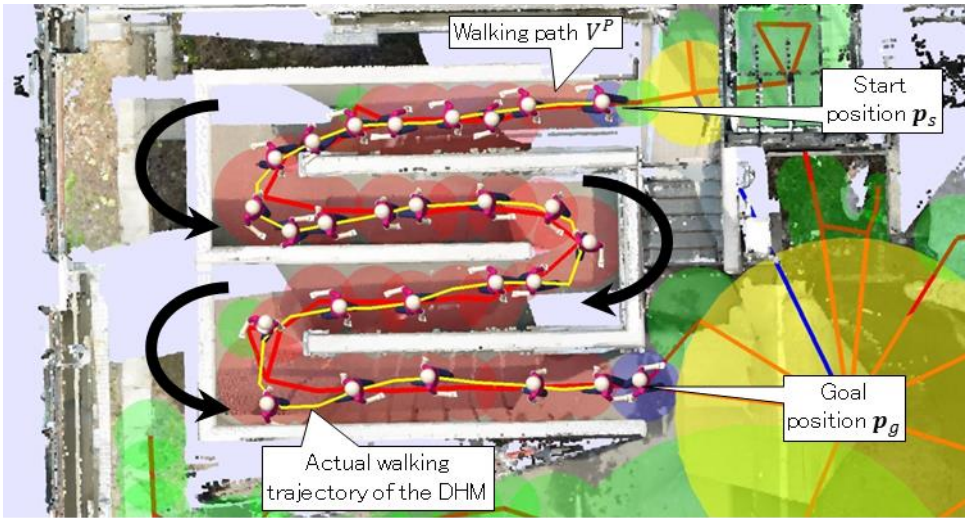

(c) Walking on consecutive slopes (reference subject: male, aged 70)

Fig. 3.30 Autonomous walking simulation in outdoor environment

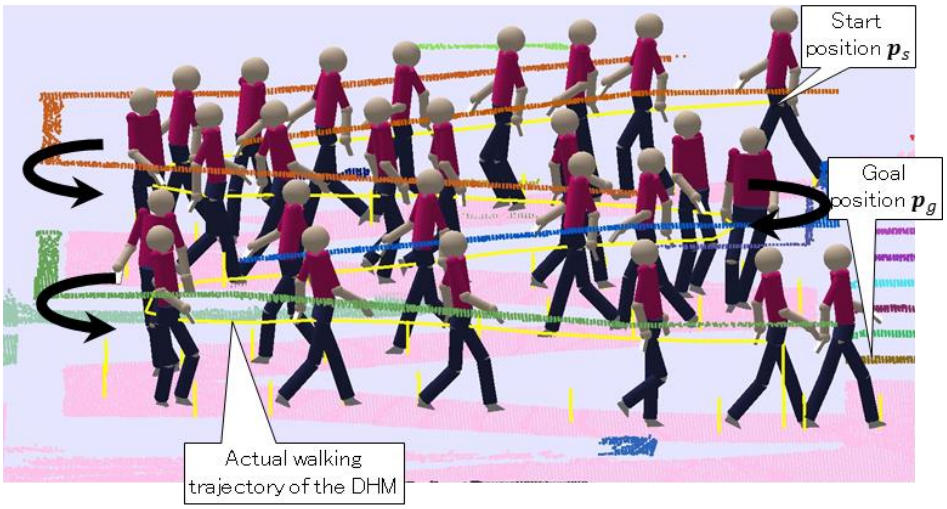

(d) Walking on consecutive slopes (reference subject: male, aged 70)
(rendered with set of walk surface points)

Fig. 3.30 Autonomous walking simulation in outdoor environment (cont.)

3.5.3 Results of autonomous walking simulation in large-scale urban environment

We further validated the proposed autonomous walking simulation in the 3D as-is environment model of the large-scale urban environment.

Fig. 3.31 shows the results of the preference-based walking path selection in the 3D as-is environment model of the urban environment. As shown in Fig. 3.31 (a), the walking path could be automatically selected from the navigation graph G_N. However, as shown in Fig. 3.31 (b), depending on the user-specified start and goal positions $\boldsymbol{p}_s$ and $\boldsymbol{p}_g$, the walking path could not be always selected automatically in large-scale as-is environment model. This was caused by that the DFS algorithm could not find one or multiple walking paths from $\boldsymbol{p}_s$ to $\boldsymbol{p}_g$ within the maximum number of iterations (specified as 50,000,000 times in 3.4.2). Increasing the maximum number of iterations has a potential for finding the one or multiple walking path even from the large-scale as-is environment model. However, in that case, the path selection algorithm could not be performed within a practical time.

Therefore, as one of solutions for this problem, in this study, as shown in Fig. 3.31 (c), in case that the walking path could not be selected automatically, we further specified the one or multiple passing points $\boldsymbol{p}_p$ in addition to $\boldsymbol{p}_s$ and $\boldsymbol{p}_g$. By applying the passing points $\boldsymbol{p}_p$, the path selection algorithm performed to extract the walking path from $\boldsymbol{p}_s$ to $\boldsymbol{p}_g$, while dividing the path selection step into multiple small steps: finding path from $\boldsymbol{p}_s$ to $\boldsymbol{p}_p$, and one from $\boldsymbol{p}_p$ to $\boldsymbol{p}_g$. As shown in Fig. 3.31 (c), it enabled the user to obtain the walking path within a permissible time. For example, in the case of Fig. 3.31 (c), the elapsed time of path selection was 117s.

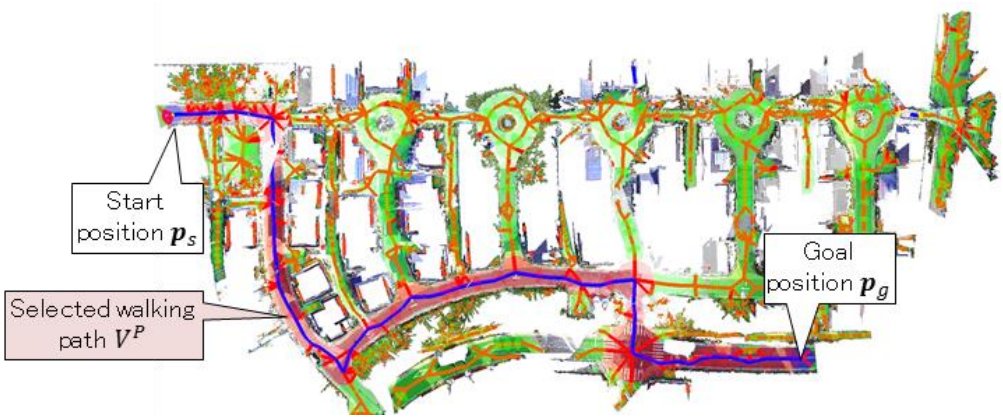

(a) Successful example of preference-based path selection

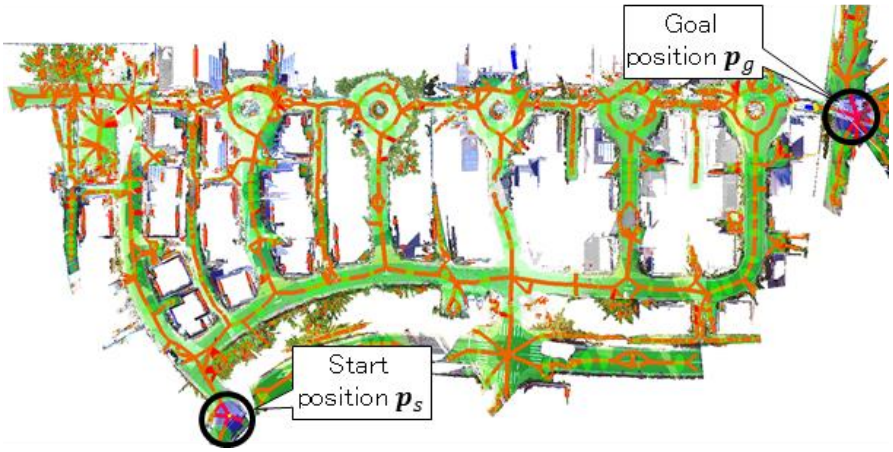

(b) Failed example of preference-based path selection

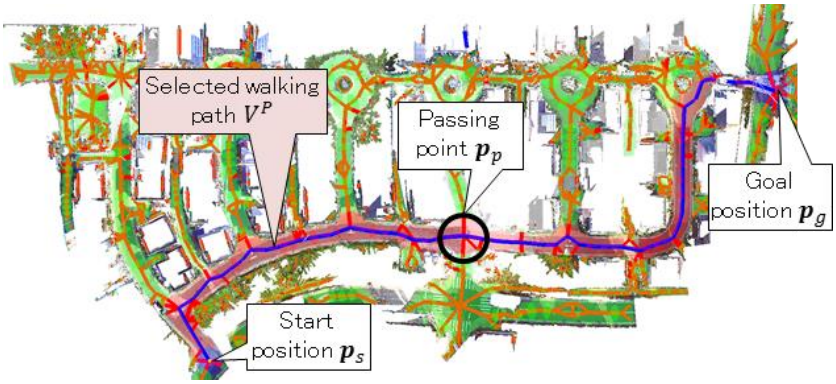

(c) Preference-based path selection with a user-specified passing point p_p

Fig. 3.31 Preference-based path selection in large-scale urban environment

On the other hand, Fig. 3.32 shows the autonomous walking simulation result in the urban environment. As shown in the figure, the DHM could autonomously walk on the pathways even in large-scale urban environment, while turning around the rotary.

In addition, Fig. 3.33 shows the walking simulation results on stairs included in the urban environment. As shown in the figure, it was confirmed that the DHM could autonomously walk in the urban environment though the stairs.

Therefore, considering the walking simulation results in the urban environment, it was concluded that the DHM could autonomously walk even in large-scale urban environment. However, to extract the pathways from an arbitary start and goal positions within a practical time without specifying any passing points, the algorithm of preference-based path selection needs to be improved. This improvement will remain as our future work.

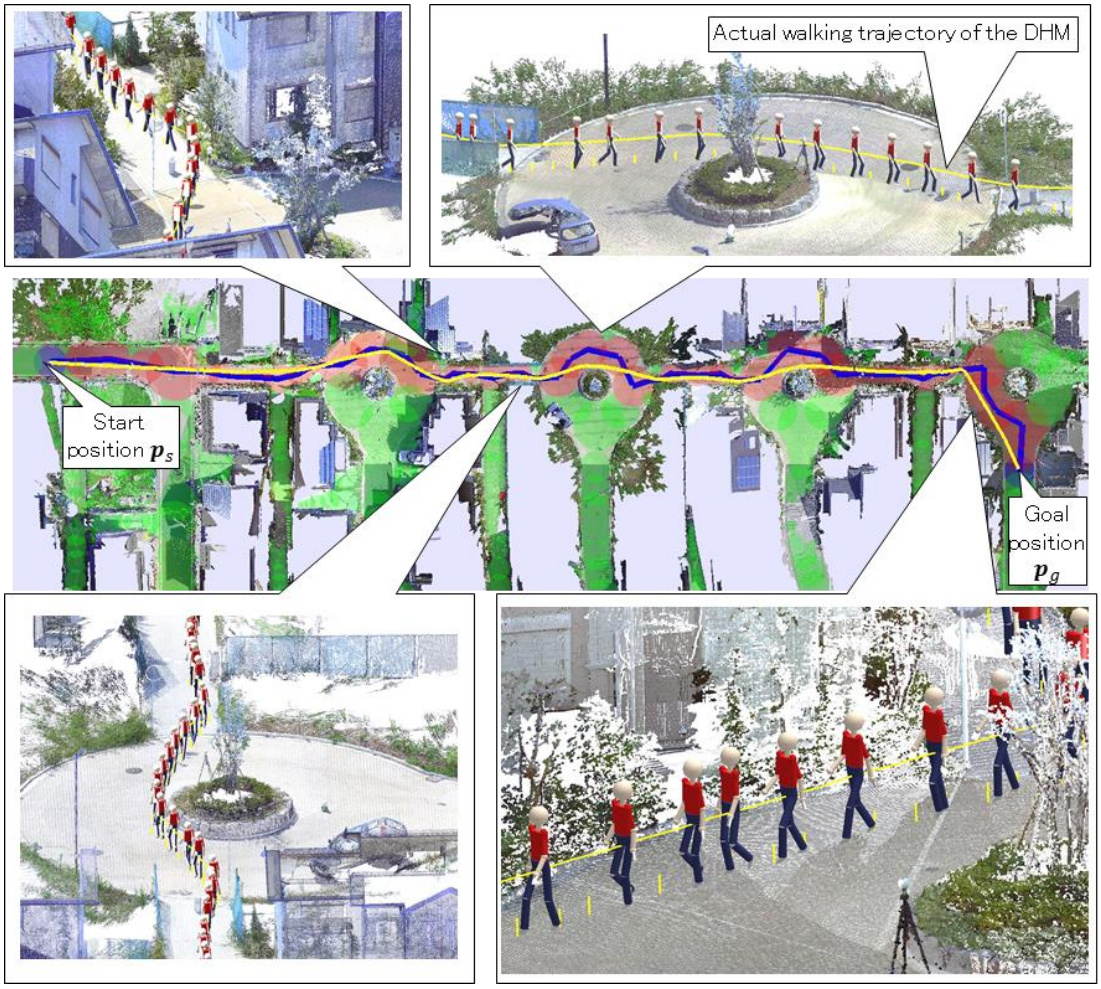

Fig. 3.32 Autonomous walking simulation in urban environment
(reference subject: male, aged 20)

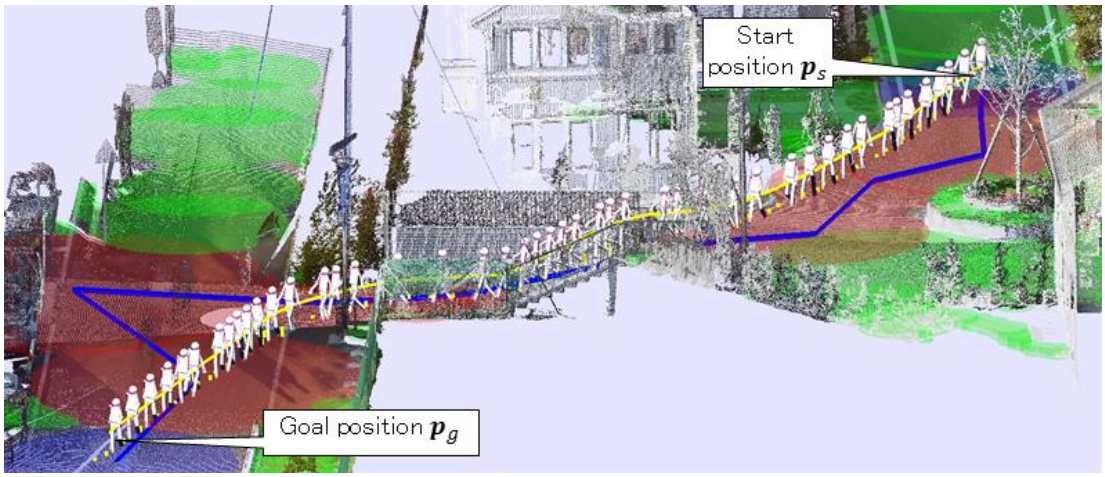

(a) Autonomous walking simulation in urban environment
(reference subject: male, aged 70)

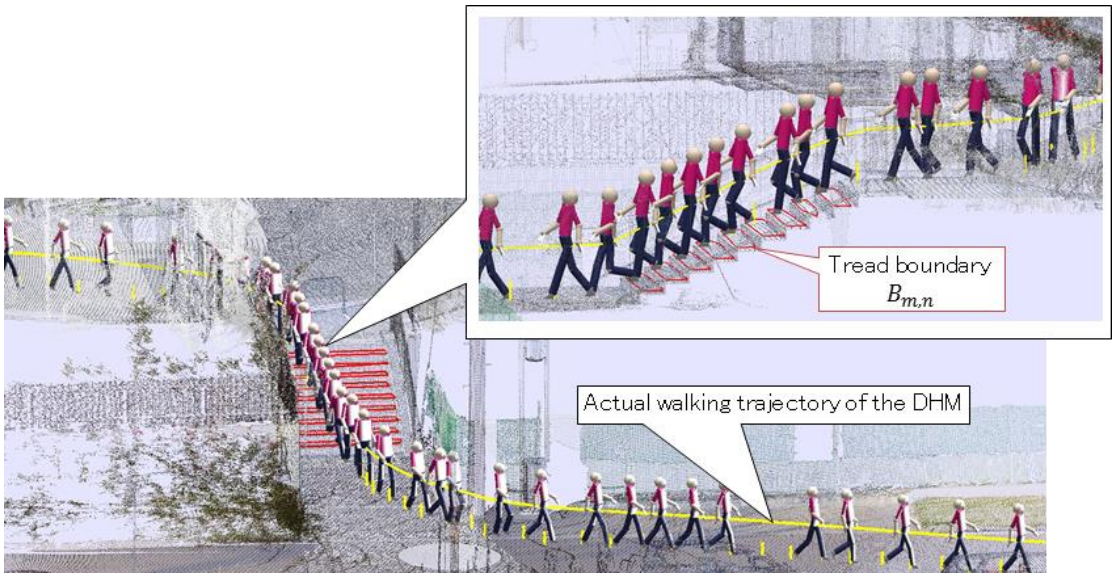

(b) Descending on stairs
(reference subject: male, aged 70)

Fig. 3.33 Autonomous walking simulation in urban environment including stairs

Table 3.2 Elapsed time of autonomous walking simulation
(CPU: Intel Core i7 3.30GHz, RAM: 32GB, GPU: Quadro K4200)

	(a) One-floor indoor environment	(b) Two-story indoor environment	(c) Outdoor environment	(d) Urban environment
# points	7,058,731	346,457,626	41,067,944	617,105,730
# down-sampled point	1,043,386	9,287,847	2,530,737	35,968,315
Preference-based path selection	less than 1 ms	140 ms	less than 1 ms	117 s *with one passing point specification
*Path selection using the Dijkstra method	less than 1 ms	16 ms	less than 1 ms	20 ms
Optimization-based motion planning	less than 1 ms	312 ms	less than 1 ms	560 ms
One-step walking motion generation with 100-frames interpolation	76 ms	94 ms	97 ms	1475 ms

3.5.4 Efficiency and accuracy validations of autonomous walking simulation

3.5.4.1 Efficiency of autonomous walking simulation

The elapsed time of the autonomous walking simulation of the DHM is summarized in Table 3.2. As shown in Table 3.2, the preference-based path selection and of the optimization-based path selection could be performed within a practical time in indoor and outdoor environments. However, as described in 3.5.3, the elapsed time of the preference-based path selection increased to a higher value in the large-scale as-is environment even if one passing point was specified. On the other hand, when the Dijkstra method was used for the shortest path selection, its elapsed time became significantly short time even in the large-scale environment. Therefore, it was confirmed that the preference-based path selection algorithm needed to be improved to extract the walking path within a practical time as well as the Dijkstra method.

On the other hand, the elapsed time for one-step walking motion simulation with 100-frame interpolation, i.e., $\phi \in [0,1]$ increases 0.01 in each frame, in the MoCap-based adaptive walking motion generation was significantly fast both in indoor and outdoor environment. However, the execution speed of the simulation in the large-scale urban environment dropped to a lower value. This was caused by a high-computational load for the point clouds rendering. Therefore, the computational time still needs to be improved for real-time walking simulation of DHM in more large-scale environments.

These improvements will remain as our future work.

3.5.4.2 Validation of joint angles of digital human model by comparison with motion-capture data

In this study, the articulated walking movements of the DHM were validated by a comparison of the joint angles between the DHM and real human on flat and sloping terrains. Fig. 3.34 shows a comparison result of the joint angle of the DHM with those of real human subjects of different ages and genders on flat terrain. MoCap data for flat walking of two younger subjects (male, aged 22, female, aged 13) and for two older subjects (male, aged 73, and female, aged 72) were selected from the gait DB, and used for both simulation and comparison. The motions of the DHM were generated based on the MoCap data for flat walking of these subjects. As shown in Fig. 3.34, it was confirmed that the DHM could generate joint angle patterns similar to those of younger and older subjects. The maximum angle differences between the simulation and the reference MoCap data were approximately 10 and 5 deg in the knee and hip joints, respectively. This showed that the proposed walking simulation algorithm could generate human-like walking motion of older and younger people on flat walking terrain based only on the single reference MoCap data for flat walking.

On the other hand, Fig. 3.35 shows a comparison result of the joint angle of the DHM with those of a real younger subject (male, aged 23) in 6-deg slope. As shown in Fig. 3.35 (a), the motion of the DHM was generated based on the reference MoCap data of the subject for flat walking. We then performed the proposed walking simulation on a 6-deg slope, and obtained the walking motion of the DHM on the slope. Finally, its joint angle patterns of the DHM on the 6-deg slope were compared

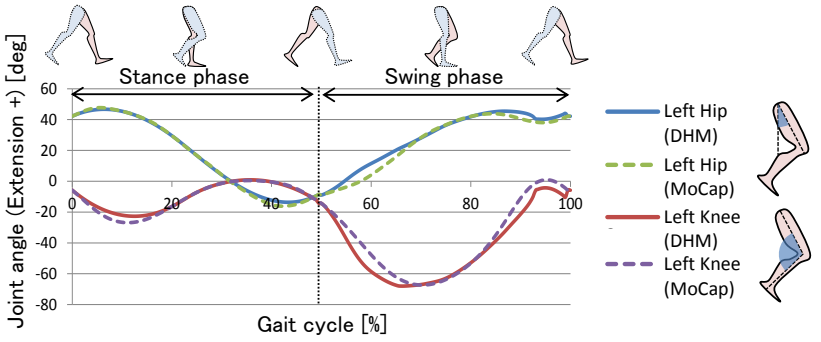

(a) Male, aged 22

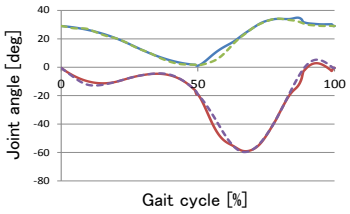

(b) Female, aged 13

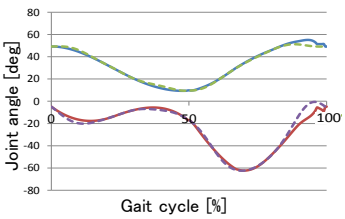

(c) Male, aged 73

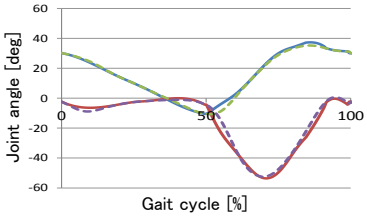

(d) Female, aged 72

Fig. 3.34 Comparisons of joint angles of DHM with those of younger subjects

with MoCap data actually measured from the subject on the 6-deg slope in a walking experiment described in Appendix C.

Fig. 3.35 (b) shows the comparison results in the 6-deg slope. As shown in Fig. 3.35 (b), it was confirmed that the DHM could generate joint angle patterns similar to those of the human subject on the 6-deg slope. The averaged angle differences between the simulation and the MoCap data were approximately 5 and 6 deg in the hip and knee joints, respectively. This showed that the proposed walking simulation algorithm could generate human-like walking motion even in the different environments based only on the single reference MoCap data for flat walking for young subject.

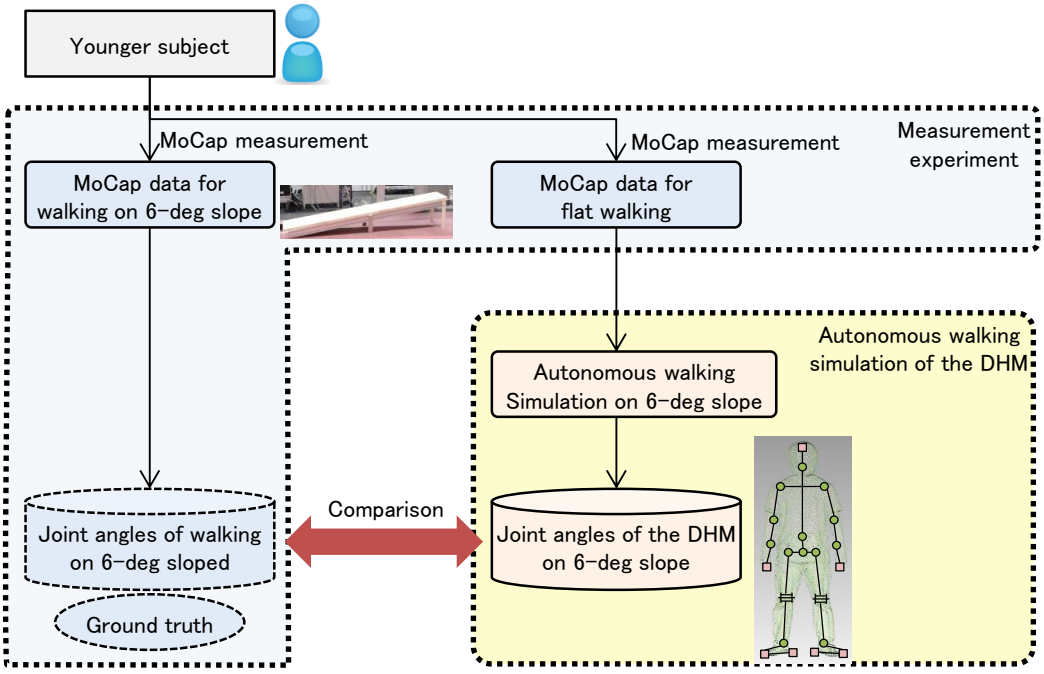

(a) Overview of comparison of joint angles of DHM with real human in 6-deg slope

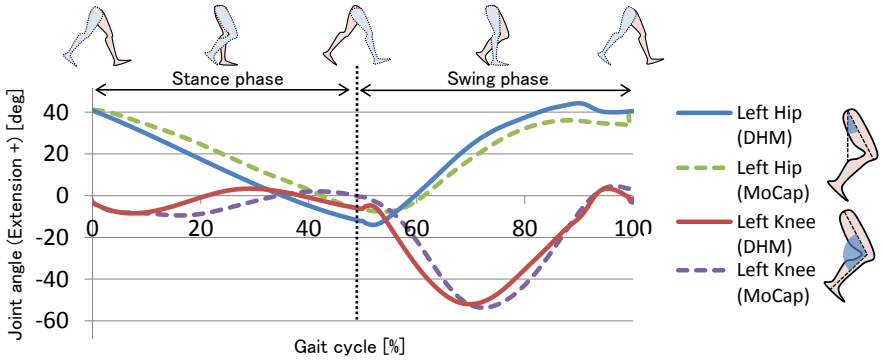

(b) Comparison results of joint angles between DHM and younger subject in 6-deg slope

Fig. 3.35 Comparisons of joint angles of DHM with real human in 6-deg slope

Regrettably, a comparison with an elderly person's gait on non-flat walking terrain could not be performed because MoCap data for an elderly subject acquired in non-flat walking terrain was not available in the gait DB [Kobayashi 13]. It is both practically and ethically difficult to persuade elderly persons to join a prolonged experiment on walking motion in various walking environments such as flat terrain, 3-deg and 6-deg slopes, and stairs. We leave this comparison to future work.

3.5.4.3 Validation of toe position of digital human model by comparison with MoCap data

In this study, the autonomous walking simulation of the DHM was developed for the human-centered accessibility evaluation such as the tripping risk evaluation and ease of wayfinding evaluation. Among them, the tripping evaluation results are greatly affected according to the simulated walking motion of the DHM, since the tripping risk is evaluated based on the toe clearance (TC) of the DHM during the walking simulation. Therefore, we further verified the difference in Minimum Toe Clearance (MTC) between the DHM and the corresponding MoCap data, where MTC represents the minimum vertical distance between the bottom of toe of the swing leg and the walking surface during the swing phase of the gait cycle [Barrett 10].

In the validation, a set of MoCap data for 7 younger subjects S_y ranging in age from 13 to 24 and one for 7 older subjects S_e ranging in age from 69 to 72 were randomly selected from the gait DB. The age and body height of the subjects included in S_y and S_e are shown in Table 3.3. Then, the MTC MTC_{MoCap} of each subject included in S_y or S_e, were obtained from the subject's MoCap data for flat walking. After that, the proposed walking simulation of the DHM was performed on the flat walking terrains using these MoCap data, and MTC of the DHM MTC_{DHM} during one-step walking was recorded. Finally, the differences between the MTC MTC_{DHM} of simulated walking motion of the DHM and the MTC MTC_{MoCap} of the original MoCap data, its averaged value of the absolute difference μ_{MTC}, and its standard deviation σ_{MTC} were validated.

The validation results are summarized in Fig. 3.36 and Table 3.3. As shown in the table and figure, it was confirmed that μ_{MTC} for S_y, and μ_{MTC} for S_e ranged approximately from 5 to 7 mm, respectively. In addition, it was confirmed that the MTC of the DHM MTC_{DHM} tended to slightly larger than that of the subjects MTC_{MoCap}. Furthermore, the maximum difference in MTC ranged approximately from 9 to 10 mm, respectively. Therefore, it was concluded that the proposed walking simulation could be applied to the tripping risk evaluation in Chapter 4 within an accuracy limit of approximately 10 mm in terms of MTC.

Table 3.3 Age and body height of selected subjects, and difference in MTC between simulated walking motion and original MoCap data

	Age	Body height [m]	μ_{TC} [mm]	σ_{TC} [mm]	Maximum difference [mm]
Subjects in S_y	13 – 24	1.55 – 1.76	4.7	2.8	10.3
Subjects in S_e	69 – 72	1.56 – 1.68	6.5	2.7	8.9

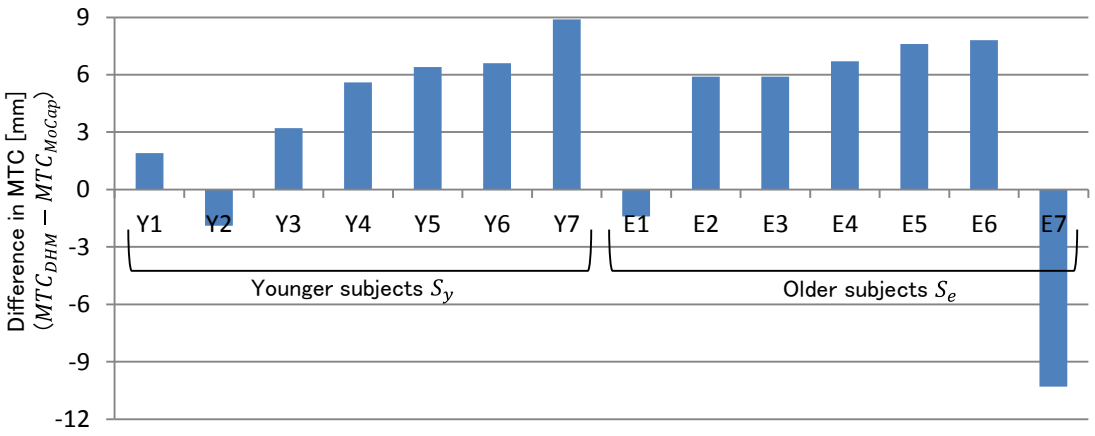

Fig. 3.36 Difference in MTC between simulated walking motion and original MoCap data

3.6 Summary

In this chapter, we developed an algorithm of an autonomous walking simulation of a DHM in the point clouds-based as-is environment models, which can satisfy the three requirements in 3.1, walking autonomoy, gait reproducibility, and environmental flexibility. Our autonomous walking simulation enabled the DHM to generate human-like walking motion in various as-is environments including slopes and stairs, using a single reference MoCap data for flat walking selected from the gait DB [Kobayashi 13].

In addition, the effectiveness of our walking simulation algorithm was validated using the multiple 3D as-is envirnment models generated from the point clouds of two types of indoor environments, outdoor environment, and large-scale urban environment. The results showed the effectiveness of the walking simulation algorithm. In addition, it was confirmed that the DHM could walk autonomously, while adapting its strides, turning angles and footprints to different point clouds-based as-is environment models.

Furthermore, our walking simulation results were valiated by a comparison of the walking motion between the DHM and MoCap data. The differences in joint angles between the DHM and MoCap data for flat walking of two younger and two older subjects were achieved at 10 and 5 deg

at a maximum for the hip and knee joints, respectively. In addition, the differences in joint angles between the DHM and MoCap data for walking on 6-deg slope of younger subject were achieved at 5 and 6 deg for the hip and knee joints, respectively. This showed that the walking simulation algorithm could generate the human-like articulated movements on flat and non-flat walking terrains based only on the single reference MoCap data for flat walking.

In addition, our walking simulation results were further validated by a comparison of MTC between the DHM and MoCap data of 14 subjects including 7 younger and 7 older subjects. As a result, it was confirmed that the maximum differences in MTC for 7 younger and 7 older subjects ranged from 9 to 10 mm, respectively. Therefore, it was concluded that the proposed walking simulation could be applied to the tripping risk evaluation in Chapter 4 within an accuracy limit of approximately 10 mm in terms of MTC.

On the other hand, the elapsed time for one-step walking motion generation was less than one second in indoor and outdoor environments, which is short enough for practical application. However, in the large-scale urban environment, the elapsed times of the one-step walking motion generation and the preference-based path selection increased to higher values. Therefore, to achieve more efficient autonomous walking simulation even in the more large-scale and complex environments, the path selection algorithm and walking motion generation algorithm need to be improved. This works will remain as our future work.

Chapter 4 Tripping Risk Evaluation based on Autonomous Walking Simulation

4.1 Background and requirements

In the last chapter, an algorithm of autonomous walking simulation of a DHM in point clouds-based 3D as-is environment models was proposed and introduced. As discussed in Chapter 1, accessibility must be evaluated from physical and cognitive human aspects. Among the physical behavior, walking is an essential and basic behavior of all people in a given environment. Therefore, in this chapter, as an indispensable accessibility criterion from human physical aspect, we aim to develop an evaluation system of tripping risk during walking.

As reported by WHO [WHO 07], falls injuries are the leading cause of unintentional death in older people. It is concerned that our rapidly aging society will accelerate falls-related healthcare costs [Moller 05], [Stevens 06], since the risk of falls increases with aging [Sattin 92]. The fatal causes of falls in older people are tripping, slipping, unexpected stepping down, and fainting [Smeesters 01]. Among them, tripping during walking is a primary cause of falls in older people as reported by several studies [Blake 88], [Sattin 98], [Overstall 77], [Best 08], [Begg 14]. As an example, Blake et al. [Blake 88] have reported that 53% of falls is caused by tripping. Therefore, as an important and essential accessibility criterion from human physical aspect, tripping risks of the environments must be evaluated to ensure the safety of walking in the environments.

In accordance with the definition in [Nagano 11], tripping can be defined as an event where the lowest part of a shoe or foot makes unanticipated contact with the walking terrain itself or some objects on the terrain with sufficient force to destabilize the pedestrian. On the other hand, the risk factors of tripping-related falls are classified into intrinsic factors such as aging and gait disorders, and into extrinsic factors such as environmental hazards including small barriers and uneven walking terrains [Rubenstein 06], [Catarina 09], [Moreland 03]. In general, falls are caused by one or more risk factors described above, as reported in the literature [Rubenstein 06]. Therefore, to prevent falls in all people in a given environment, both intrinsic and extrinsic factors needs to be removed as much as possible [Todd 04], [Cohen 03].

Currently, several studies have been conducted to prevent falls by removing the intrinsic factors, by improve physical and cognitive health of people [Sherrington 11], [Latham 03], [Gschwind 13]. However, since the primary causes of falls have been reported as the environment-related falls such as tripping on barriers [Zhou 02], finding and removing extrinsic factors is indispensable, as

mentioned in many studies [Moreland 03], [Todd 04], [Cohen 03], [Ståhl 08], [Reis 12], [NICE 13], [Yanagihara 14a], [Yanagihara 14b], [Cumming 99], [Suminski 05].

Currently, the environmental-inspection has been conducted to find and remove the environmental hazards [Yanagihara 14a], [Cumming 99]. The inspection is realized by asking residents living in the local community about their falls history in their neighborhood environments [Yanagihara 14a], or by examining the environments visually [Cumming 99]. However, as reported in the literature [Yanagihara 14a], as shown in Fig. 4.1, the falling places detected by the visual inspection not always correspond to the actual falling place examined by hearing survey. In addition, it was observed that older people tend to stumble at a little uneven pavement that the inspectors do not think dangerous, since the place satisfy the barrier-free guideline [MLIT 13]. Consequently, as mentioned in the literature [Yanagihara 14b], it is difficult to find and remove the environmental hazards exhaustively before the accident happens only by the visual inspection. Therefore, as one of the falls prevention strategies, it is important to develop a more efficient method of finding the environmental hazards exhaustively [Ståhl 08], by taking account of both intrinsic and extrinsic factors for falls.

Therefore, in this chapter, to realize the human-centered accessibility evaluation from human physical aspect, we aim to develop the tripping risk evaluation system based on the interaction between the DHM and the point clouds-based 3D as-is environment model, which can detect the environmental hazards exhaustively by taking account of both intrinsic and extrinsic factors.

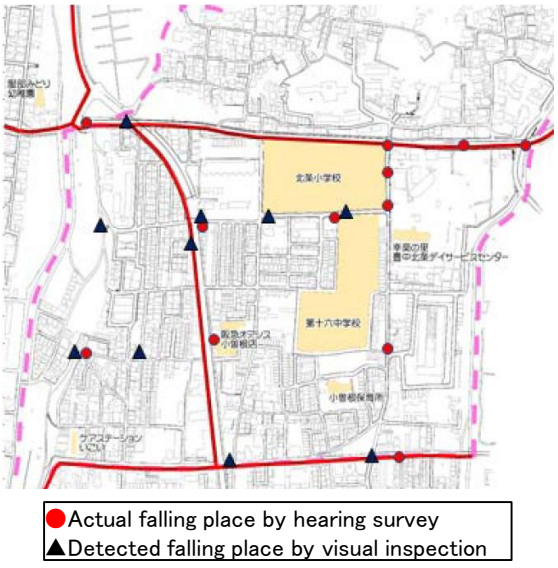

Fig. 4.1 Comparison of falling place between visual inspection and hearing survey [Yanagihara 14a]

4.2 Related work on falls prevention

4.2.1 Strategies for current falls prevention

Currently, many falls prevention studies have been conducted. As reviewed in the literatures [Rubenstein 06], [Catarina 09], [Moreland 03], the risk factors of falls are classified into intrinsic factors and extrinsic factors. Therefore, the falls prevention studies generally aim for identifying and removing the risk factors, and are categorized according to the type of factor as follows.

(a) Removing intrinsic factors by health improvement

Several studies focus on removing or reducing the intrinsic factors by improving physical or cognitive health of people by exercise [Sherrington 11], [Gschwind 13], quadriceps resistance exercise with taking vitamin D [Latham 03]. These falls prevention interventions have proven a positive effect on the intrinsic falls risk factors.

On the other hand, since the primary cause of falls is tripping during walking [Blake 88], [Sattin 98], [Overstall 77], [Begg 14], several studies aim to prevent tripping accidents. As discussed in Barrett et al. [Barret 10], the variability in minimum foot clearance (MFC) or minimum toe clearance (MTC) greatly affects the increase in the tripping risk during walking. MFC or MTC represents the minimum vertical distance between the bottom of foot or toe of the swing leg and the walking surface during the swing phase of the gait cycle, respectively [Barret 10]. As shown in Fig. 4.2, it is observed that the variability of MTC in older people is consistently larger than one in younger people [Nagano 11], [Mills 08], [Barret 10]. In addition, the potential for a tripping-related falls is considered to be greatest at MTC [Barret 10], [Winter 92]. Therefore, several interventions have been proposed to reduce the MTC variability by improving the gait of the users.

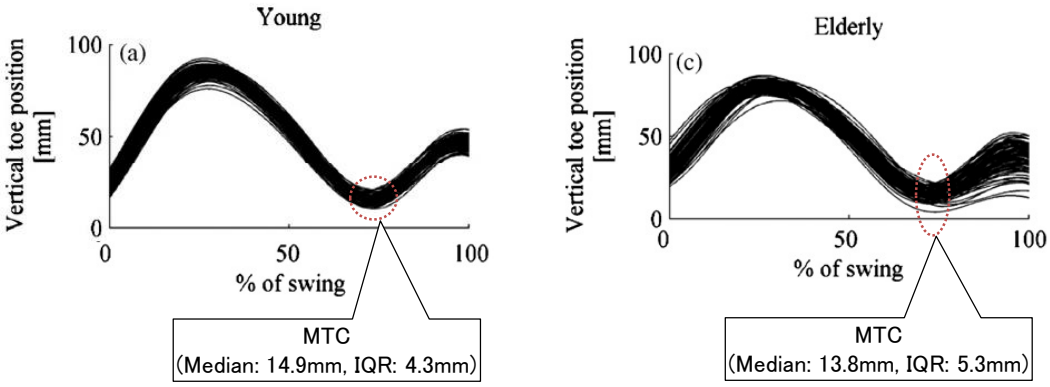

Fig. 4.2 Difference of toe clearance distribution between younger and older people [Mills 08]

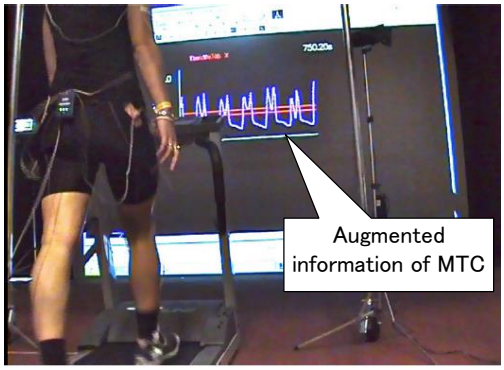

(a) Real-time gait information projection [Begg 14]

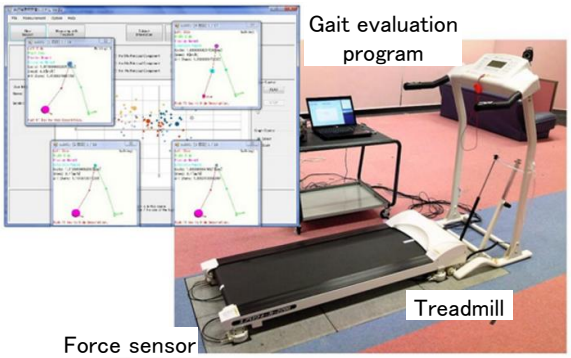

(b) Tripping risk age estimation and feedback [Kobayashi 12], [DHRC]

Fig. 4.3 Reducing MTC variability by improving human gait

As shown in Fig. 4.3 (a), Begg et al. [Begg 14] proposed a tripping prevention system by graphically indicating the augmented information of MTC using a real-time projection of the right foot sagittal trajectory. They found that the visual indication of the information of MTC to a subject was effective in changing foot trajectory control, and could reduce the tripping probability in older people. In addition, as shown in Fig. 4.3 (b), Kobayashi et al. [Kobayashi 12] proposed a system of estimating the "tripping risk age" of subjects based on their MTC distribution. They found that the tripping risk might decrease after the feedback of the tripping risk age.

These studies are effective for removing the intrinsic factors. However, removing the extrinsic factors were not focused in their studies, in spite that the primary causes of falls have been reported as the environment-related falls such as tripping on barriers [Zhou 02].

(b) Removing extrinsic factors by environmental inspections

As mentioned in many studies [Moreland 03], [Todd 04], [Cohen 03], [Ståhl 08], [Reis 12], [NICE 13], [Yanagihara 14a], [Yanagihara 14b], [Cumming 99], [Suminski 05], removing or minimizing extrinsic factors for falls, i.e., the environmental hazards, is indispensable for falls prevention. Currently, environmental-inspection has been conducted by asking residents living in the local community about their falls history in their neighborhood environments [Yanagihara 14a], or by examining the environments visually [Cumming 99], [Yanagihara 14a]. However, as reported in the literature [Yanagihara 14b], older people tend to stumble even at a little uneven pavement that the inspectors did not recognize as dangerous place, in spite that the place satisfies the barrier-free guideline [MLIT 13]. Therefore, it is difficult to detect the environmental hazards exhaustively before the accident happens only by visual inspection [Yanagihara 14b]. As an advanced approach, as shown in Fig. 4.4, Andres et al. [Andres 13] proposed an accessibility evaluation system using mobile laser-scanning technology. In the study, by utilizing recent vehicle mounted mobile

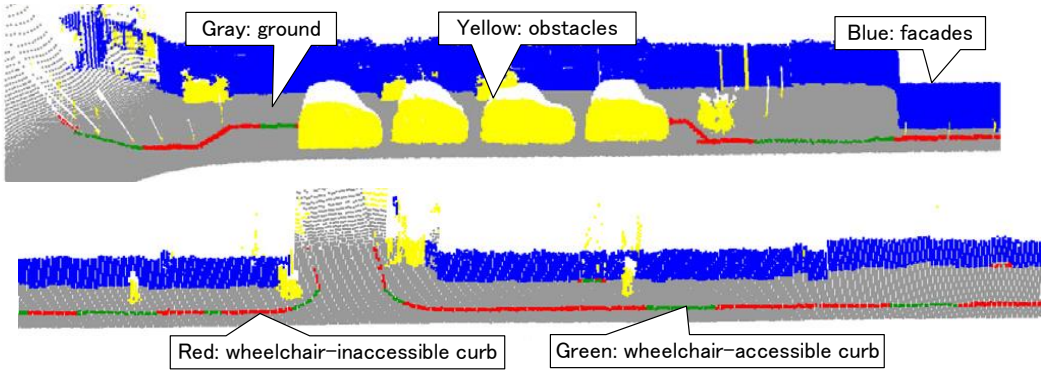

Fig. 4.4 Accessibility diagnosis from mobile laser-scanning data [Andress 13]

laser-scanner, the urban environment can be captured as the accurate and massive 3D point clouds. In addition, the clearance of the walkways and the obstacles on the walkways such as cars and poles are automatically extracted from the point clouds as the criteria of urban accessibility. However, in their algorithm, the tripping-related environmental hazards such as small barriers and uneven terrains were not considered and extracted. Therefore it is impossible to evaluate the accessibility criteria such as tripping risk from the aspect of falls prevention.

(c) Quantifying the tripping risk based on the analysis of human walking motion

Recently, a study has been conducted on quantifying the tripping risk based on the experimental analysis on human walking motion. Best et al. [Best 08] proposed a method of quantifying a probability of tripping (PT) during walking based on the statistical distribution of MTC for a subject. In their method, the statistical distribution of MTC can be estimated from the video data of treadmill walking of 60 minutes. Then, the PT for a barrier having a certain height can be quantified based on the estimated MTC distribution. However, in their study, PT is quantified based only on the MTC distribution, and the entire toe clearance distribution, i.e., the trajectory of the toe during one-step walking, were not considered in the quantification. Therefore, it is basically impossible to consider the footprint factors such as the difference in the foot contact position relative to the barrier in the quantification. Consequently, estimating the PT for various environmental hazards existing in real worlds (e.g., uneven terrain, wavy pavement, small barriers with complex cross-section) is basically impossible in the study. Moreover, the study only focuses on estimating the PT from the walking measurements, and do not focus on how to find the environmental hazards from the large-scale environment.

(d) Removing extrinsic factors based on real-time falls or near-miss falls detection

On the other hand, as shown in Fig. 4.5, recently, the real-time falls or near-miss falls detection systems using wearable sensors have been developed mainly in construction research [Zhou 02],

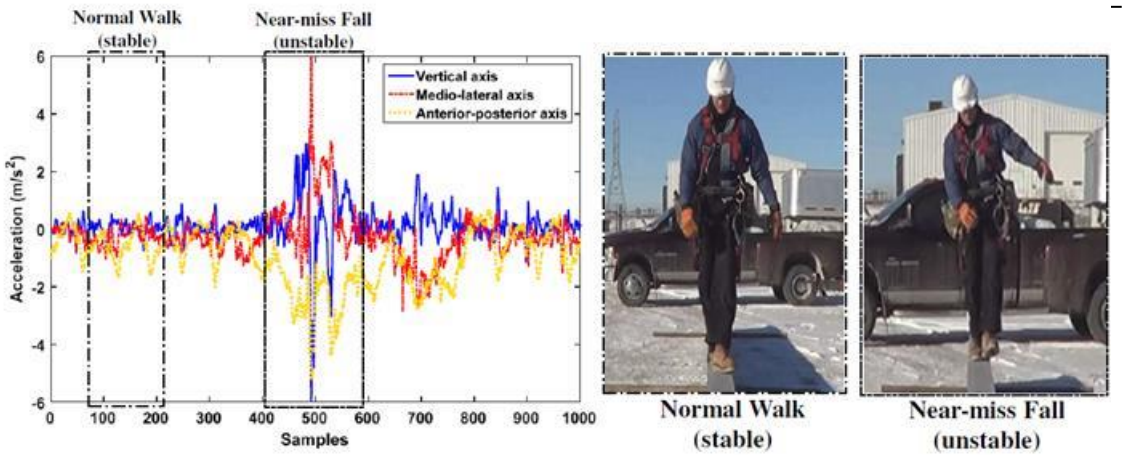

Fig. 4.5 Real-time falls and near-miss falls detection [Yang 16]

[Kangas 11], [Lai 11], [Yang 16], [Dzeng 14]. Kangas [Kangas 11] and Lai et al. [Lai 11] developed a falls detection system based on accelerometers attached on human body. In addition, Yang et al. [Yang 16] and Dzeng et al. [Dzeng 14] developed a detection system of near-miss falls based on wireless inertial measurement units [Yang 16] and smartphone built-in accelerometers [Dzeng 14], respectively. These researches are useful for finding the environmental hazards, especially in construction fields having danger zones, in consideration of both intrinsic and extrinsic factors. However, these systems basically aim for detecting the falls or sign of falls on-the-fly, so they are not effective to find out and remove the environmental hazards before the falls happen. In addition, to exhaustively find the hazards in local community, the long-time data collection with various subjects living in the community is required.

As discussed above, in the current falls prevention studies, it is impossible to find the environmental hazard exhaustively before actual falls happen, in consideration of both intrinsic and extrinsic factors.

4.2.2 Human behavior simulation

In human behavior simulations, studies have been mainly conducted on crowd behavior analysis and emergency evacuation planning [Duives 13], [Kakizaki 14], [Helbing 00], [Tecchia 01]. Different methods exist for simulating the pedestrian movements, such as social forces [Helbing 00] and cellular automata [Tecchia], as reviewed by Duives et al. [Duives 13]. These simulations focus on evaluating the evacuation time, and crowd density, which are important accessibility criteria in emergencies. However, the pedestrian models in these studies are represented as simplified 2D model, so the model cannot reproduce 3-dimentional articulated movements similar to the real human. Thus, the model is insufficient for evaluating the accessibility in daily life situation such as falls or tripping risk. In addition, in these studies, the simulation is only performed in as-planned

environment models with simplified geometry, so the detailed 3D as-is geometry of the environment including small barriers and uneven terrains are ignored in the model. Such over-simplified environment models are insufficient for the tripping risk evaluation.

Recently, Kakizaki et al. [Kakizaki 12] proposed an evacuation-planning simulator that enabled kinematics-based walking simulation in a 3D as-planned environment model. In their study, the pedestrian model can generate an articulated walking movement similar to real human. However, the articulated movements do not change in various groups of people such as the elderly, children, males, and females. In addition, in their study, the simplified 3D as-planned environment model is used in the simulation.

Therefore, it is basically impossible to evaluate the tripping risk based non the current human behavior simulation studies, from the aspect both of pedestrian model and of environment model.

4.2.3 Tripping risk evaluation approach in this study

As discussed in 4.2.1, in the current falls prevention studies, the environmental hazard cannot be found exhaustively before actual falls happen, in consideration of both intrinsic and extrinsic factors. In addition, as discussed in 4.2.2, it is basically impossible to evaluate the tripping risk using current human behavior simulation, from the aspect both of the presentation level of the pedestrian model and of environment model.

Therefore, in this study, in contrast to the previous studies, we aim to newly develop a tripping risk evaluation system, by taking account both of intrinsic and extrinsic factors with the interaction between the environments and human behaviors. To consider the extrinsic factors such as small barriers and uneven terrain, we utilize the point clouds-based as-is environment modeling technology developed in Chapter 2. On the other hand, to consider the intrinsic factors such as the difference in walking motion among individuals, we further utilize the autonomous walking simulation of the DHM developed in Chapter 3. By combining the autonomous walking simulation with the point clouds-based 3D as-is environment models, the tripping risk can be evaluated by taking account both of intrinsic and extrinsic factors with the 3-dimensional interactions between human behaviors and the environment.

4.3 Objective and overview

As discussed in the last section, the objective of this chapter is to develop a tripping risk evaluation system based on the autonomous walking simulation of the DHM in the point clouds-based 3D as-is environment models.

Fig. 4.6 shows an overview of the proposed tripping risk evaluation system. As shown in Fig. 4.6,

in the proposed tripping risk evaluation system, the point clouds-based as-is environment modeling and autonomous walking simulation developed in Chapter 2 and Chapter 3 are partly used.

In the system, first, the 3D as-is environment model including the down-sampled points with normal vectors Q, set of walk surface points $W_S = \{W_i\}$, navigation graph G_N, and tread boundaries $B_{m,n}$ is automatically generated from the laser-scanned point clouds. Then, the tripping-hazard map is automatically generated from W_s by estimating the degree of unevenness on local walking terrains. However, the map only indicates the possible tripping-hazard regions, i.e., the regions on which high possibility of tripping are expected, with the degree of tripping-hazard. Therefore, after that, the user picks up a set of regions of interest A from the map by taking account of the degree of tripping-hazard. Finally, the tripping risk on A is quantitatively evaluated based on our autonomous walking simulation of the DHM combined with Monte Carlo simulation.

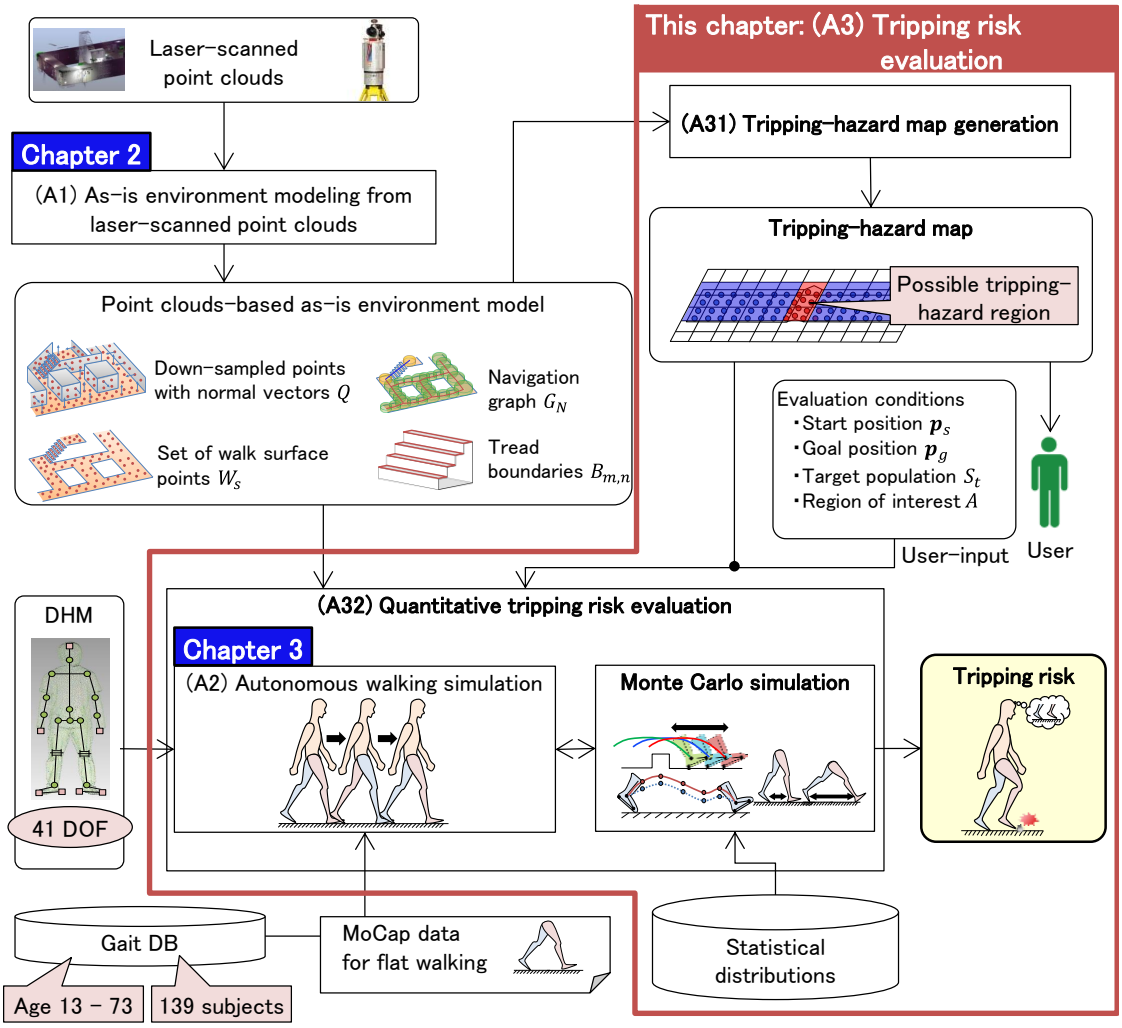

Fig. 4.6 Overview of the tripping risk evaluation

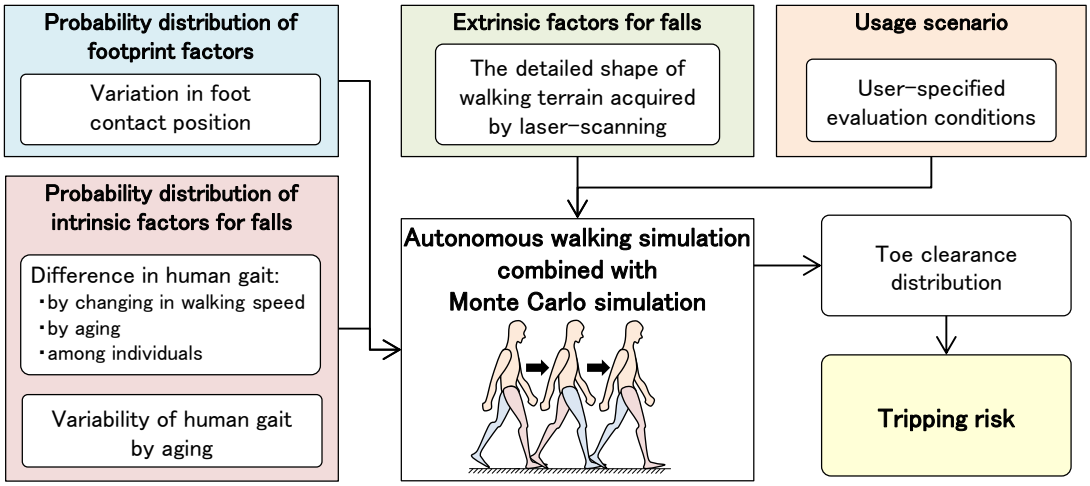

Fig. 4.7 Basic concept of tripping risk evaluation

On the other hand, Fig. 4.7 shows a basic concept of the quantitative tripping risk evaluation based on the simulation. In the evaluation, the tripping risk is evaluated by taking account of the stochastic properties of interactions between human behaviors and hazard regions, such as the probability distribution of intrinsic factors and footprint factor, extrinsic factors, and a usage scenario of the environment. The usage scenario of the environment is represented by the user-specified evaluation conditions, such as a start position $\boldsymbol{p}_s$, goal position $\boldsymbol{p}_g$, target population S_t (younger or older), and the region of interest A. In addition, the difference in human gait, and the variability of human gait by aging is represented as the probability distributions of intrinsic factors, while the detailed shape of walking terrain acquired by laser-scanning of the environment can be considered as extrinsic factors. Moreover, the variation in foot contact position relative to A can be further considered as the footprint factor. Taking all factors into account, the tripping risk is evaluated as a probability of tripping on A based on the toe clearance distribution, when multiple people included in S_t walks from $\boldsymbol{p}_s$ to $\boldsymbol{p}_g$.

As a result, the tripping-related environmental hazards can be detected from the laser-scanned point clouds with the quantitative value of the tripping risk for a given target population S_t such as the elderly. The results contributes to assess the accessibility objectively from the aspect of human physical behavior, and to prioritize the environmental hazards to be removed, for the dominant users in the environment.

In contrast with the studies on current falls prevention, our tripping risk evaluation system can evaluate the tripping risk before actual falls happen, in consideration of both intrinsic and extrinsic factors. The contributions of the proposed system can be summarized as follows:

– The system can find the tripping-related hazards exhaustively from the laser-scanned point clouds of large-scale indoor and outdoor environments, by estimating the unevenness of local terrains.

- The system can quantitatively evaluate the tripping risk based on the 3D realistic human walking simulation combined with the Monte Carlo simulation, which can simulate the stochastic properties of the interaction between human walking behaviors and a hazard.
- As the interaction, the probability distribution of intrinsic factors and footprint factor, extrinsic factors, and usage situation of the environment can be considered.
- As the probability distribution of intrinsic factors, the difference in human gait, and the variability of human gait by aging can be considered.
- As the probability distribution of footprint factor, the variation in foot contact positions relative to the hazard can be considered.
- As extrinsic factors, the detailed shape of walking terrain captured by a laser-scanner can be considered.
- As the usage scenario, the start position $\boldsymbol{p}_s$, goal position $\boldsymbol{p}_g$, target population S_t, and the region of interest A are specified by the user.
- The risk evaluation results were validated by a comparison with the tripping risk measured from the walking experiments and their analysis.

The rest of this chapter is organized as follows. First, the algorithms of the tripping-hazard map generation and of the tripping risk evaluation based on the autonomous walking simulation of the DHM combined with the Monte Carlo simulation are described in Section 4.4. After that, the demonstrations and validation results using the point clouds of virtual indoor and outdoor environments are shown in Section 4.5. Finally, the summary of this chapter is described in Section 4.6.

Note that our evaluation system only focuses on the tripping risk for unseen and unrecognized objects on the floor. Evaluating the risk for seen and recognized objects [Galna 09] will remain as our future work.

4.4 Methods of tripping risk evaluation

4.4.1 Tripping-hazard map generation

Fig. 4.8 shows an overview of the tripping-hazard map generation. As shown in Fig. 4.8 (a), first, the degree of unevenness $DoN(\boldsymbol{q}_i, r_s, r_l)$ around a walk surface point $\boldsymbol{q}_i \in W_i$ ($W_i \subseteq W_S$) is estimated by calculating the difference of normals (DoN) [Ioannou 12], where r_s and r_l represent user-specified small and large radii, respectively. The DoN is a method for estimating the local distribution of the point clouds relative to the surrounding distribution of them, and used for the point clouds segmentation [Ioannou 12]. In this study, the DoN is used to estimate the degree of local

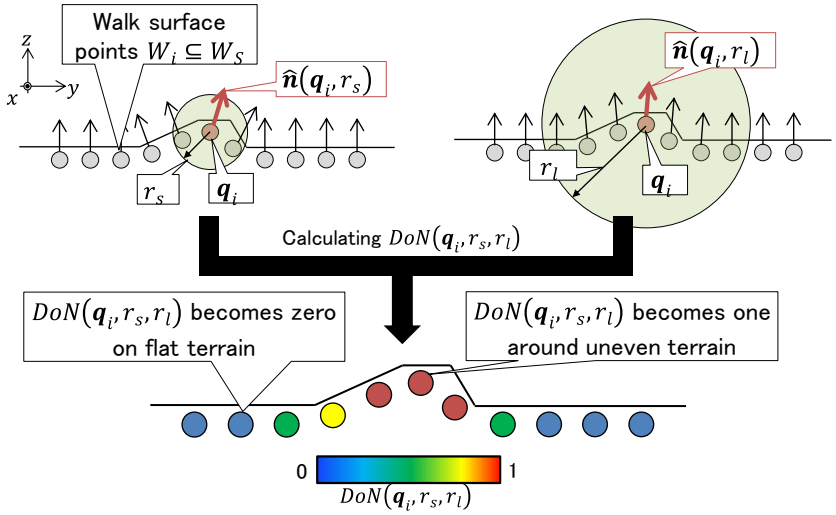

(a) Estimating degree of unevenness $DoN(\boldsymbol{q}_i, r_s, r_l)$ of the terrain

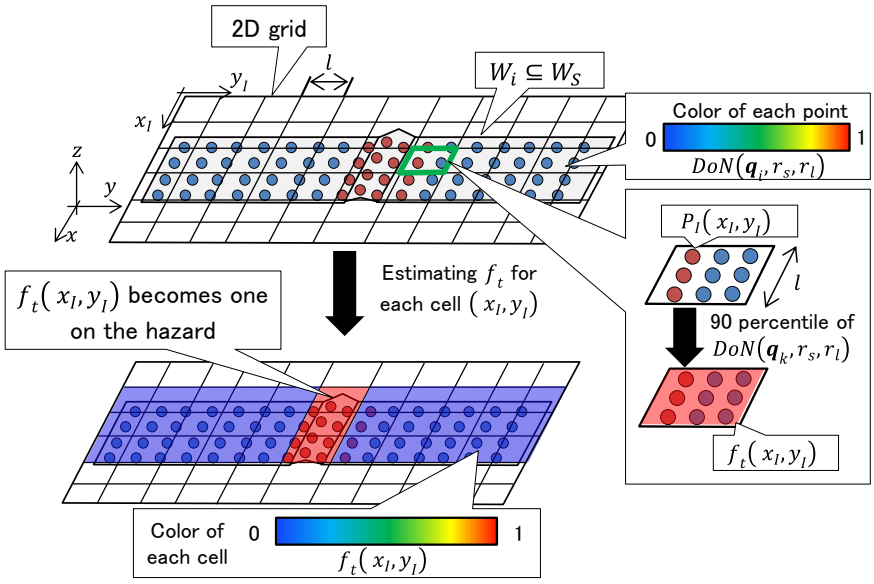

(b) Generating tripping-hazard map based on $DoN(\boldsymbol{q}_i, r_s, r_l)$

Fig. 4.8 Overview of tripping-hazard map generation

unevenness of the point clouds on local terrain.

$DoN(\boldsymbol{q}_i, r_s, r_l)$ is calculated by the equation (4.1),

$$DoN(\boldsymbol{p}_i, r_s, r_l) = \begin{cases} \dfrac{1 - \{\hat{\boldsymbol{n}}(\boldsymbol{p}_i,\, r_s) \cdot \hat{\boldsymbol{n}}(\boldsymbol{p}_i,\, r_l)\}}{2\cos(\theta_{max})} & (\hat{\boldsymbol{n}}(\boldsymbol{q}_i,\, r_s) \cdot \hat{\boldsymbol{n}}(\boldsymbol{q}_i,\, r_l) \geq \cos(\theta_{max})) \\ 1 & (\hat{\boldsymbol{n}}(\boldsymbol{q}_i,\, r_s) \cdot \hat{\boldsymbol{n}}(\boldsymbol{q}_i,\, r_l) < \cos(\theta_{max})) \end{cases} \tag{4.1}$$

where $\hat{\boldsymbol{n}}(\boldsymbol{q},\, r)$ represents a unit normal vector at $\boldsymbol{q}$, which is estimated by principal component analysis (PCA) [Rusu 13] from the neighboring points included in a sphere of radius r centered at $\boldsymbol{q}$, and θ_{max} is a user-specified threshold value for normalization. As shown in Fig. 4.8 (a), the degree

of unevenness $DoN(\boldsymbol{q}_i, r_s, r_l)$ is calculated based on the angle between two normal vectors $\hat{\boldsymbol{n}}(\boldsymbol{q}_i, r_s)$ and $\hat{\boldsymbol{n}}(\boldsymbol{q}_i, r_l)$, which are calculated by PCA with different radii r_s and r_l, respectively. Therefore, in the equation (4.1), if the angle between $\hat{\boldsymbol{n}}(\boldsymbol{q}_i, r_s)$ and $\hat{\boldsymbol{n}}(\boldsymbol{q}_i, r_l)$ becomes greater than θ_{max}, $DoN(\boldsymbol{q}_i, r_s, r_l)$ takes one. As shown in Fig. 4.8 (a), $DoN(\boldsymbol{q}_i, r_s, r_l)$ tends to zero at the point clouds on flat terrains, and to one on the tripping-related environmental hazards such as uneven terrains and small barriers.

After the calculation of $DoN(\boldsymbol{q}_i, r_s, r_l)$ for each point $\boldsymbol{q}_i$, the tripping-hazard map is generated on the walk surface points $W_i \subseteq W_S$. As shown in Fig. 4.8 (b), first, the 2D grid is overlaid onto W_i. Then, the degree of tripping-hazard $f_t(x_I, y_I)$ derived from $DoN(\boldsymbol{q}_i, r_s, r_l)$ is estimated in each cell (x_I, y_I) in the grid using the equation (4.2),

$$\begin{aligned} f_t(x_I, y_I) &= ninth\_decile(S_{x_I, y_I}) \\ S_{x_I, y_I} &= \{DoN(\boldsymbol{q}_k, r_s, r_l) | \boldsymbol{q}_k \in P_I(x_I, y_I)\} \end{aligned} \tag{4.2}$$

where $ninth\_decile(X)$ and $P_I(x_I, y_I)$ represent 90-percentile value of a set X, and a set of points included in a cell (x_I, y_I). In this study, the 90-percentile value of $DoN(\boldsymbol{q}_k, r_s, r_l)$ in $P_I(x_I, y_I)$ are assigned to $f_t(x_I, y_I)$ instead of the mean or median value of that. This makes it possible to detect the possible tripping-hazard regions exhaustively without missed detection, while reducing the effect of noise on laser-scanned point clouds. As shown in Fig. 4.8 (b), $f_t(x_I, y_I)$ also tends to become zero on flat terrain, and become one on the possible tripping-hazard region. Finally, as shown in Fig. 4.8 (b), the tripping-hazard map is completed by assigning the color to each cell (x_I, y_I) in the map in accordance with its $f_t(x_I, y_I)$, to enhance the visibility of the map. Determining the appropriate parameter settings of θ_{max}, r_s, and r_l are described in Section 4.5.

4.4.2 Quantitative evaluation of tripping risk

4.4.2.1 Overview

After the tripping-hazard map generation, the quantitative value of the tripping risk is then evaluated on the user-selected hazardous region (i.e., region of interest A). The evaluation is realized using the autonomous walking simulation of the DHM combined with the Monte Carlo simulation, by taking account of the stochastic properties of the interaction between human walking behaviors and the region.

In this study, the tripping risk $R_t(S_t, A)$ is defined as a probability of tripping, when multiple people included in the target population S_t walk on a region of interest A including the tripping-related hazard. A represents a set of cells (x_I, y_I) on the map, and S_t represents a set of MoCap data for a certain population such as one of older people S_e and of younger people S_y. The user has to select the region A from the possible tripping-hazard regions, where the high degree of

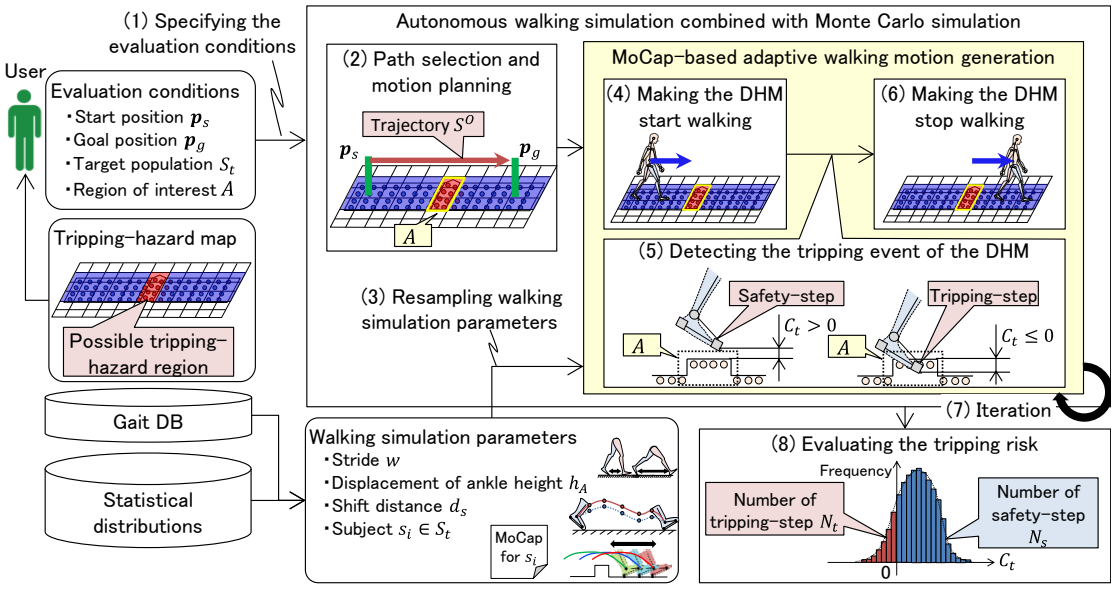

Fig. 4.9 Overview of autonomous walking simulation combined with Monte Carlo simulation

tripping-hazard $f_t(x_I, y_I) \simeq 1$ was estimated on the region. Note that the presence of the tripping is detected based on the toe clearance of the DHM during walking.

Fig. 4.9 shows an overview of the tripping risk evaluation. As shown in the figure, the evaluation can be realized by the following processes, where the MoCap-based adaptive walking motion generation process is repeated, while resampling the walking simulation parameters among their stochastic distribution.

(1) Specifying the evaluation conditions

First of all, as shown in Fig. 4.9, the user specifies the evaluation conditions such as start position $\boldsymbol{p}_s$, goal position $\boldsymbol{p}_g$ of walk, target population S_t, and interested region A. A set of cells with the high degree of tripping-hazard $f_t(x_I, y_I)$ are manually selected as A by the user on the tripping-hazard map. The tripping risk can be evaluated as a probability of tripping on A, when multiple people included in the target population S_t walk from $\boldsymbol{p}_s$ to $\boldsymbol{p}_g$. Changing $\boldsymbol{p}_s$ and $\boldsymbol{p}_g$ enables the user to evaluate the risk in different walking scenario of the environment.

(2) Path selection and motion planning

To make the DHM walk from $\boldsymbol{p}_s$ to $\boldsymbol{p}_g$, the walking path V^P, and the walking trajectory S^O of the DHM are automatically generated using the preference-based path selection and optimization-based motion planning processes introduced in 3.4.2 and 3.4.3, respectively.

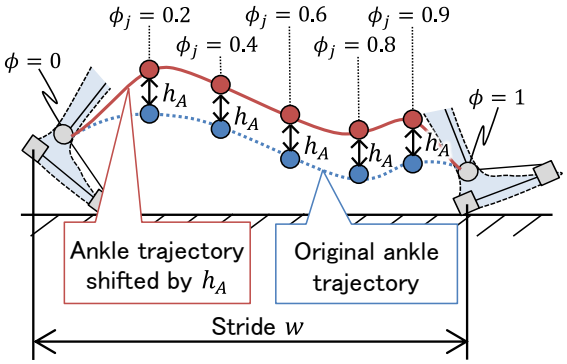

Fig. 4.10 Walking stride and offset value of ankle height

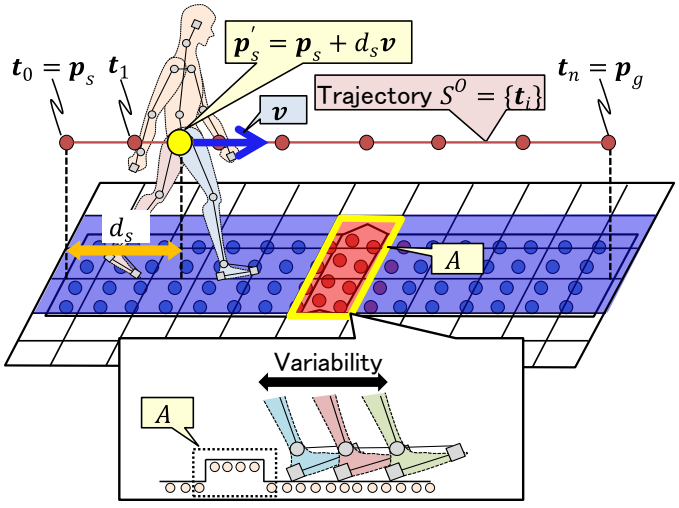

Fig. 4.11 Making the DHM start walking

(3) Resampling the walking simulation parameters

As shown in Fig. 4.9, the walking simulation parameters such as the stride w, displacement of ankle height h_A, shift distance d_s, and subject s_i are resampled to the other values. As shown in Fig. 4.10, the parameter w and h_A represent the walking stride, and an offset value of the ankle height of the swing leg during the walking simulation, respectively. In particular, the heights of ankle trajectory of the DHM at $\phi = \phi_j$ are shifted by h_A, where $\phi \in [0,1]$ represents the normalized phase of one-step walking, and $\phi_j \in \{0.2, 0.4, 0.6, 0.8, 0.9\}$ is an element of set of walking phase. This motion modification is actually done in the process "(A243) Generating swing leg motion" of the autonomous walking simulation introduced in 3.4.4.3. d_s represents an offset value for the start position $\boldsymbol{p}_s$ in the direction of locomotion vector $\boldsymbol{v}$ of the DHM. s_i represents a subject included in S_t, whose MoCap data for flat walking is used in the walking simulation. Details are described in

4.4.2.2.

(4) Making the DHM start walking

As shown Fig. 4.11, the DHM is set to walk from the updated start position $\boldsymbol{p}_s' = \boldsymbol{p}_s + d_s\boldsymbol{v}$, where $\boldsymbol{v} = (\boldsymbol{t}_1 - \boldsymbol{t}_0)/\|\boldsymbol{t}_1 - \boldsymbol{t}_0\|$ represents a unit vector representing the walking direction of the DHM, and $\boldsymbol{t}_0 \in S^O$ and $\boldsymbol{t}_1 \in S^O$ are the first and second discretized pelvis position on the trajectory S^O. By changing the start position of the DHM based on the dynamically resampled shift distance d_s, the foot contact position relative to the region A can be varied in the tripping risk evaluation.

(5) Detecting the tripping event of the DHM

As shown in Fig. 4.9, whether the tripping event of the swing leg of the DHM happens or not is determined based on the toe clearance C_t of the DHM, when the swing foot passes over or under the region A. If the tripping is detected at least once during one-step walking on A, this step is treated as "tripping-step"; otherwise, it is treated as "safety-step". As a result of the Monte Carlo simulation, the number of tripping-steps N_t, and one of safety-steps N_s are obtained. The occurrence of the tripping is detected based on the toe clearance of the DHM during the walking simulation. Details of the tripping detection algorithm are described in 4.2.2.3.

(6) Making the DHM stop walking

When the DHM arrives at $\boldsymbol{p}_g$, one trial of the walking simulation is stopped.

(7) Iteration

Processes (3)–(6) are repeated N times, while resampling the walking simulation parameters in the process (3), where N represents a user-specified maximum number of the iterations.

(8) Evaluating the tripping risk

Based on the results of the iteration, the tripping risk $R_t(S_t, A)$ [%] is finally calculated as a probability of the tripping by the equation (4.3).

$$R_t(S_t, A) = \frac{N_t}{N_s + N_t} \times 100\ [\%] \tag{4.3}$$

where N_t and N_s represent the number of tripping-steps and safety-steps during N times iteration

Table 4.1 Resampling strategy and setting of walking simulation parameters

	Distribution	Purpose	Setting	Reference
Stride w	$G_D(\mu_w, {\sigma_w}^2)$	Gait variation with speed-changing	$\mu_w = w_I$ $\sigma_w = 0.077$ m	[Sekiya 94]
Displacement of ankle height h_A	$G_D(\mu_h, {\sigma_h}^2)$	Gait variability by aging	$\mu_h = 0$ $\sigma_h = 0.003$ m for S_y $\sigma_h = 0.005$ m for S_e	[Mills 08]
Shift distance d_s	$U_D(0, w_I)$	Difference in the foot contact position relative to the hazard		
Subject s_i	Equal proportion	Gait difference among individuals		

of the walking simulation.

As shown in Fig. 4.9, by performing these processes, the quantitative value of the tripping risk can be evaluation by taking account of the stochastic properties of the interaction between human walking behaviors and the hazardous region.

4.4.2.2 Resampling the walking simulation parameters

During the Monte Carlo simulation, the walking simulation parameters of the DHM including the stride w, displacement of ankle height h_A, shift distance d_s, and subject s_i are dynamically resampled according to their own probability distributions. The strategies of the resampling are summarized in Table 4.1.

As shown in Table 4.1, w is resampled according to Gaussian-distribution $G_D(\mu_w, {\sigma_w}^2)$, to represent the difference in human gait by changing in the walking speed. In addition, h_A is resampled according to $G_D(\mu_h, {\sigma_h}^2)$, to represent the variability of human gait by aging. Furthermore, as shown in Fig. 4.11, d_s is resampled according to an uniform-distribution $U_D(0, w_I)$ to represent the difference in the foot contact position relative to A. Finally, single subject s_i is selected from the target population S_t in equal proportion, i.e., the number of times of a subject is resampled is identical to one of others in S_t, to represent the difference in human gait among individuals included in the same age population.

In this study, as shown in Table 4.1, we specified the parameters of $G_D(\mu_w, {\sigma_w}^2)$ as $\mu_w = w_I$, and $\sigma_w = 0.077$ m according to the observations in Sekiya et al. [Sekiya 94], where a correlation between walking speed and stride of 64 Japanese subjects are analyzed experimentally. On the other hand, the mean value μ_h of $G_D(\mu_h, {\sigma_h}^2)$ is specified as $\mu_h = 0$, since h_A represents an offset value for the original height in the MoCap data for s_i. Conversely, the standard deviation σ_h of $G_D(\mu_h, {\sigma_h}^2)$ is specified as $\sigma_h = 0.003$ m or $\sigma_h = 0.005$ m for younger or older people, respectively, according to the observations in Mills et al. [Mills 08], where the variability of MTC is experimentally observed from 10 younger and 9 older subjects.

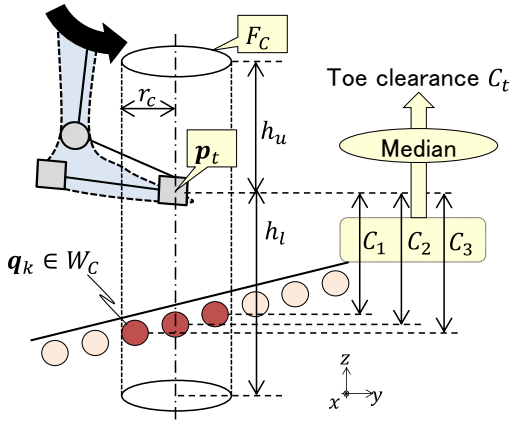

Fig. 4.12 Toe clearance estimation

4.4.2.3 Detecting the tripping event of the DHM during the walking simulation

During the walking simulation, the tripping event of the DHM on the region A is detected based on the toe clearance C_t of the DHM. Fig. 4.12 shows the diagram of the toe clearance estimation.

As shown in Fig. 4.12, first, when the toe of the swing leg of the DHM passes on A, a cylindrical search space F_C with the height $h_u + h_l$ and the radius r_c is created. The cylinder is defined such that the axis of cylinder passes on the toe position $\boldsymbol{p}_t$, and the distance between $\boldsymbol{p}_t$ and the center of top surface of the cylinder is h_u. A set of the walk surface points $W_C = \{\boldsymbol{q}_k \mid \boldsymbol{q}_k \in W_i \wedge \boldsymbol{q}_k$ is included in $F_C\}$ are then extracted. After that, the vertical difference $C_k = (\boldsymbol{p}_t - \boldsymbol{q}_k) \cdot \boldsymbol{Z}$ are calculated for each point $\boldsymbol{q}_k \in W_C$, where $\boldsymbol{Z} = [0,0,+1]$ represents a vertical vector. Finally, the median value of these differences C_k is assigned to the toe clearance C_t of the DHM.

The heights h_u and h_l need to be specified so as to include the walk surface points over or under $\boldsymbol{p}_t$. Therefore, in this study, we specified both h_u and h_l as larger value, $h_u = 0.45$ m and $h_l = 0.75$ m, to ensure that F_C includes a part of the walk surface points W_S, under the assumption that the foot of the DHM do not passes 0.75 m above (0.45 m below) the walking terrains. In addition, the radius r_c needs to be specified as a small value to the maximum possible extent to obtain the nearest walk surface points just under or over $\boldsymbol{p}_t$. In this study, r_c is specified as $r_c = 0.01$ m initially. After that, if $W_C = \emptyset$, then r_c increases 0.01 m until W_C becomes $W_C \neq \emptyset$.

When the toe is contacting or having collision with the walking terrains, the estimated toe clearance C_t becomes $C_t \leq 0$. Therefore, if $C_t \leq 0$ holds at least once during one-step walking on A, this step is treated as “tripping-step”; otherwise it is treated as “safety-step”. Finally, as described in the process (5) and (7) in 4.4.2, the tripping risk is evaluated based on the number of tripping-steps N_t, and one of safety-steps N_s using the equation (3). Note that N_t is incremented twice during one trial of the walking simulation, if both legs of the DHM pass on A with tripping at the different walking steps. Moreover, when the foot of the swing leg grounds on A at the beginning or end of swing phase, this one-step is not treated as “tripping-step”.

4.5 Results and validations of tripping risk evaluation

4.5.1 Overview

In this study, the proposed tripping evaluation system was applied to the point clouds both of a virtual indoor environment, and of a real outdoor environment. Furthermore, the system was validated by comparing the risk from the system with the one from the experiments by younger people's walking.

In the simulation, S_y and S_e were assigned to the target population S_t, where S_y and S_e represent a set of MoCap data for flat walking of 7 younger subjects and 7 older subjects, respectively. S_y and S_e are the same subjects used in 3.5.4.3. As validated in 3.5.4.3, the averaged differences in MTC between the simulated walking motion of the DHM and the MoCap data of the subjects in S_y and S_e were 4.68 mm and 6.51 mm, respectively.

On the other hand, the maximum number of the iterations N of the Monte Carlo simulation was specified as $N = 3{,}500$ such that the walking simulation was repeated 500 times for each subject $s_i \in S_t$. On the other hand, in the tripping-hazard map generation, the small radius r_s for the DoN calculation needed to be specified. In general, using 20 points or more is enough for normal vector estimation. Therefore, in this study, the radius was specified as $r_s = 0.04$ m, since the original laser-scanned point clouds have been spatially down-sampled so that the density of the points corresponded to 10,000 points / m^2 (i.e., the averaged difference between the two adjacent points corresponded to 0.01 m). Moreover, the large radius r_l for the DoN calculation needed to be specified as a value sufficiently larger than r_s, to capture the micro geometry of the walking terrains relative to the surrounding terrains. Therefore, in this study, the radius was specified as $r_l = 0.8$ m to detect the tripping-related hazard exhaustively, while avoiding the large increase in the processing time. The threshold value θ_{max} was specified as 2.5 deg, to highlight the small barriers and small unevenness in the environment.

4.5.2 Results of tripping risk evaluation in virtual indoor environment

4.5.2.1 Point clouds of virtual indoor environment

First, the proposed tripping risk evaluation system was applied to the multiple point clouds of the virtual indoor environments $Q_{VI} = \{Q_{H_b,W_b}\}$, and its result was then verified, where the point clouds Q_{H_b,W_b} include a small barrier with a height of H_b[mm] and a width of W_b[mm]. The point clouds $Q_{0,20}$, $Q_{20,20}$, $Q_{30,20}$, $Q_{40,20}$, and $Q_{50,20}$ were artificially generated by a scan simulation software [BLENSOR]. Fig. 4.13 (a) shows the generated point clouds $Q_{20,20}$. The systematic error and accidental error of the laser-scanner were not considered in the scan simulation, to validate the tripping risk evaluated from the proposed system without any effect of noise in the point clouds.

4.5.2.2 Tripping-hazard map generation results

Fig. 4.13 (b) shows the result of the tripping-hazard map generation using the point clouds $Q_{20,20}$ shown in Fig. 4.13 (a). In Fig. 4.13 (b), the degree of tripping-hazard $f_t(x_I, y_I)$ of each cell (x_I, y_I) is shown with color gradient. As shown in the figure, most of the cells on flat terrains were detected as the safety area, in which $f_t(x_I, y_I)$ corresponded approximately to zero. On the other hand, the cells including the barrier were detected as the possible tripping-hazard region, in which $f_t(x_I, y_I)$ corresponded approximately to one. Therefore, it was confirmed that the tripping-related hazard such as barriers could be successfully detected and visualized on the generated tripping-hazard map.

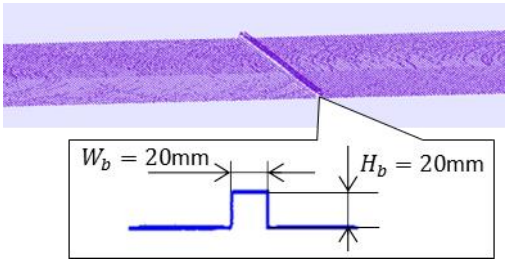

(a) Point clouds of a virtual indoor environment with a barrier ($H_b = 20$ mm, $W_b = 20$ mm)

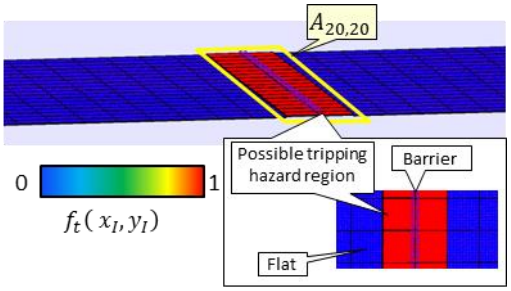

(b) Tripping-hazard map and detected possible tripping-hazard region

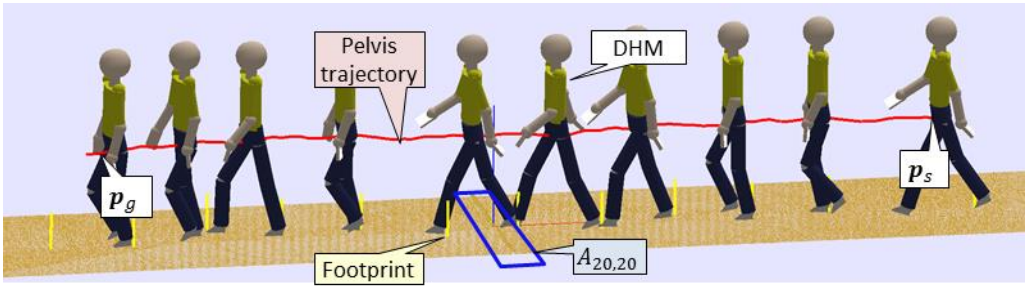

(c) Results of one trial of autonomous walking simulation of DHM

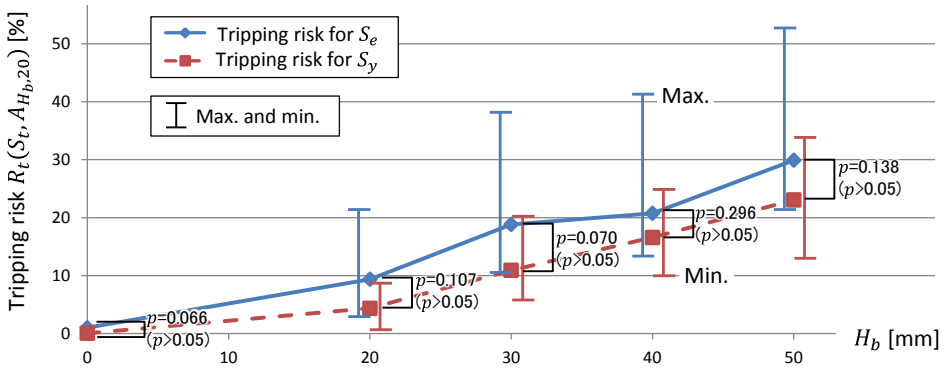

(d) Tripping risk evaluation results in different barrier heights

Fig. 4.13 Tripping risk evaluation results in virtual indoor environment

4.5.2.3 Quantitative tripping risk evaluation results

After the tripping-hazard map generation, the tripping risk $R_t(S_y, A_{H_b,W_b})$ and $R_t(S_e, A_{H_b,W_b})$ for younger and older people were then evaluated by the autonomous walking simulation combined with the Monte Carlo simulation, where A_{H_b,W_b} represents a user-specified region of interest specified on the cells including a barrier with a height of H_b and a width of W_b. In this study, the five regions of interest with different barrier heights $A_{0,0}$, $A_{20,20}$, $A_{30,20}$, $A_{40,20}$, and $A_{50,20}$ were used for the tripping risk evaluation. $A_{0,0}$, $A_{20,20}$, $A_{30,20}$, $A_{40,20}$, and $A_{50,20}$ contained an identical number of cells, since the width W_b was fixed to 20 mm. Note that $A_{0,0}$ means the cells on the flat terrain specified for the comparison purpose, where $f_t(x_I, y_I)$ of all cells in $A_{0,0}$ corresponded to zero. The region of interest $A_{20,20}$ is bounded by yellow rectangle in Fig. 4.13 (b).

Fig. 4.13 (c) shows an example of the autonomous walking simulation of the DHM in the same environment. In addition, Fig. 4.13 (d) shows the results of the tripping risk evaluation. In Fig. 4.13 (d), the risks for S_e and S_y were calculated from 7 subjects included in S_e and S_y, respectively. The error bars in Fig. 4.13 (d) show the maximum and minimum of the tripping risks among the subjects. In addition, p-value in the figure were calculated by the independent two-sided t-test. In this study, a p-value less than 0.05 was considered statistically significant. As shown in the figure, the p-values of the tripping risks in every barrier heights were greater than 0.05, so the significant differences in the tripping risks between S_e and S_y were not observed in this experiment. This was caused by the fact that the number of subjects was not enough for statistical hypothesis testing. However, as shown in the figure, the averaged, minimum, and maximum tripping risks for S_e were consistently larger than those for S_y in every barrier heights clearly. Therefore, the tripping risks for S_e could be considered as consistently larger than those for S_y in every barrier heights. This tendency well corresponds with the general observations that the risk of tripping-related falls for older people is larger than that of younger people [Nagano 11], [Mills 08], [Barret 10].

Furthermore, the tripping risks both for S_e and S_y increased with an increase in the barrier height H_b. In this study, the tripping risk was evaluated without considering the cognitive aspects of humans, and thus the discoverability or saliency of the barrier was ignored. Therefore, monotonously increasing the risk with a rise in H_b could be regarded as a legitimate consequence under the assumption that the DHM was unable to find the barrier.

4.5.3 Results of tripping risk evaluation in real outdoor environment

4.5.3.1 Point clouds of real outdoor environment

The proposed tripping risk evaluation system was further applied to the point clouds of a real outdoor environment. Fig. 4.14 (a) shows the point clouds of the outdoor environment acquired by a terrestrial laser-scanner (RIEGL VZ-1000). As shown in Fig. 4.14 (a), the environment includes

several hazards such as the curbstones, utility holes, and gravel terrains, each of which could cause tripping-related falls. Furthermore, for the autonomous walking simulation of the DHM, the as-is environment model was constructed from the point clouds. The modeling results were shown in 2.5.3.

4.5.3.2 Tripping-hazard map generation results

Fig. 4.14 (b) shows the results of the tripping-hazard map generation using the point clouds shown in Fig. 4.14 (a). As shown in Fig. 4.14 (b), the tripping-related environmental hazards such as curbstones, utility holes, and gravel terrains were exhaustively detected as the possible tripping-hazard regions with the high value of tripping-hazard $f_t(x_I, y_I)$, whereas $f_t(x_I, y_I)$ nearly corresponded to zero on the paved flat terrain. However, the generated tripping-hazard map did not necessarily consider the human behaviors in the environments in real usage scenario. For instance, in the examples on Fig. 4.14, pedestrians normally walked only on the paved flat terrain, and did not walk on the unpaved terrain. Therefore, after the map generation, the tripping risk needs to be evaluated quantitatively under the realistic usage scenario, by taking account of the stochastic properties of the interaction between human walking behaviors and the region.

4.5.3.3 Quantitative tripping risk evaluation results

In this study, the tripping risk on three regions of interest A_1, A_2, and A_3 were evaluated in consideration of the realistic usage scenario in the outdoor environment. A_1, A_2, and A_3 were specified on the tripping-hazards (A1), (A2), and (A3), which are shown in Fig. 4.14 (b), respectively. Fig. 4.15 shows the results of the autonomous walking simulation, where the DHM passed through the regions A_1, A_2, and A_3. In the figures, the quadrilaterals squares with black boundaries represent the user-specified regions of interest, A_1, A_2, and A_3. The white dot-dash-lines represent the approximated sectional shape indicating changes in terrain height. A_1 is a near-flat terrain including very small bumps with a height of 4 mm at a maximum, and has lower value of tripping-hazard $f_t(x_I, y_I) \in [0, 0.25]$. A_2 is a region with barriers ranging from 100 mm to 200 mm of height, and has the high ($f_t(x_I, y_I) \simeq 1$) hazard value. A_3 is a slope region upward from the convex area (utility hole) ranging from 30 mm to 70 mm, and has high ($f_t(x_I, y_I) \simeq 1$) hazard value. In the risk evaluation on A_1, the usage scenario of walking from right to left was assumed. In the evaluation on A_2, the scenario of entering the building from a car was assumed. In the evaluation on A_3, the scenario of traveling between two neighboring buildings was assumed. The evaluation on A_3 was executed under two walking conditions: the walking from the original start position $\boldsymbol{p}_s$ to goal position $\boldsymbol{p}_g$ (namely, the direction $\boldsymbol{v}_3$), and the reverse one from $\boldsymbol{p}_g$ to $\boldsymbol{p}_s$ (namely, the opposite direction $(-\boldsymbol{v}_3)$).

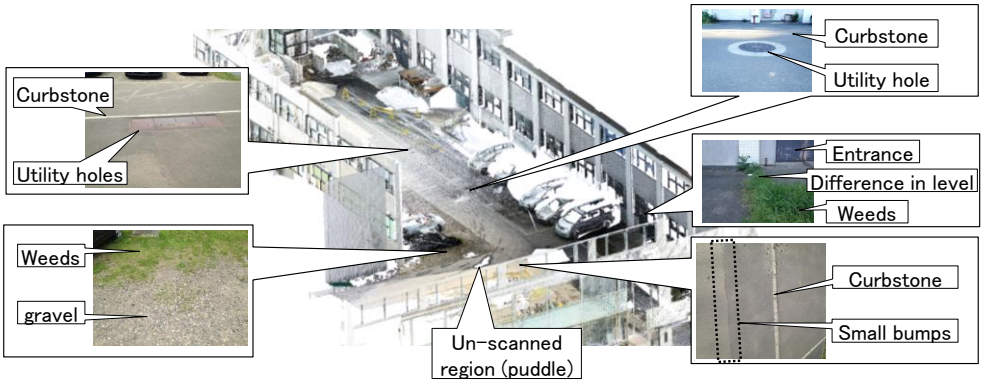

(a) Point clouds of an outdoor environment

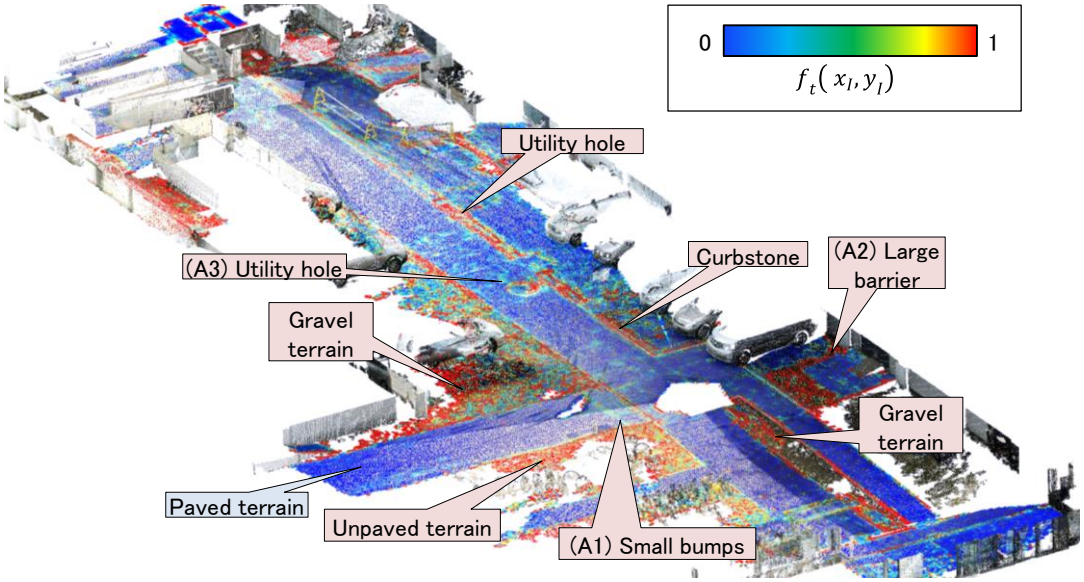

(b) Tripping-hazard map

Fig. 4.14 Tripping-hazard map generation results in outdoor environment

Fig. 4.16 summarizes the results of the tripping risk evaluation for S_e and S_y on these regions. In the figure, p-values were calculated by the independent two-sided t-test. In this study, a p-value less than 0.05 was considered statistically significant. As shown in the figure, the p-values of the tripping risks in every regions were greater than 0.05, so the significant differences in the tripping risks between S_e and S_y were not observed. This was caused by the fact that the number of subjects was not enough for statistical hypothesis testing. However, as shown in the figure, the averaged, minimum, and maximum tripping risks for S_e were consistently larger than those for S_y in every regions clearly, which fit well with the general observations that the risk for older people larger than younger people [Nagano 11], [Mills 08], [Barret 10].

On the other hand, as shown in Fig. 4.16, the evaluated tripping risk on the region A_2 ($R_t(S_e, A_2)$ and $R_t(S_y, A_2)$) were much higher than that on A_1 ($R_t(S_e, A_1)$ and $R_t(S_y, A_1)$). This difference

was caused by the fact that the height of barrier included in A_2 was much larger than the one in A_1. This result shows the same tendency as observed in the experiment using the point clouds of virtual indoor environment described in 4.5.2, and can be regarded as the reasonable one. Therefore, the difference in risk between younger and elderly is not significant in these regions, since these regions do not have any tripping effect only on the older people.

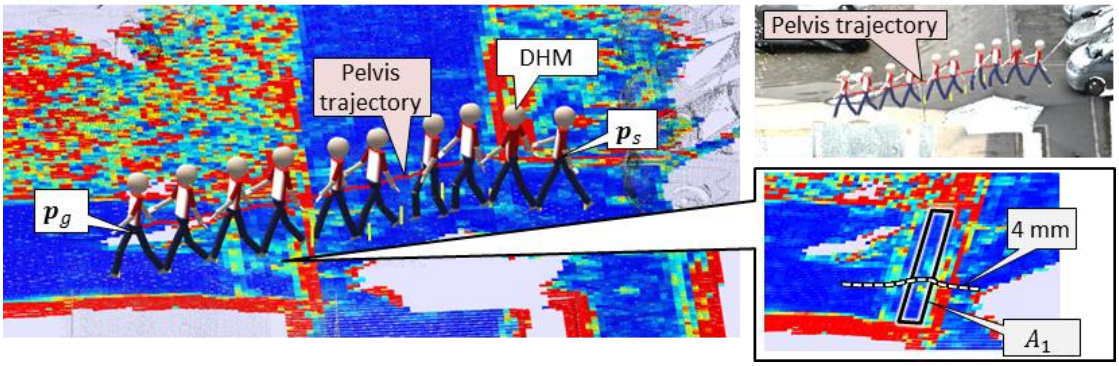

(a) Results of autonomous walking simulation passing on A_1

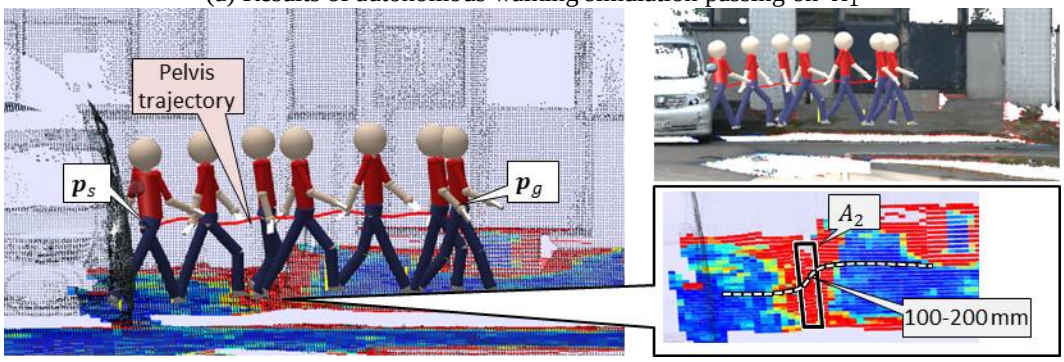

(b) Results of autonomous walking simulation passing on A_2

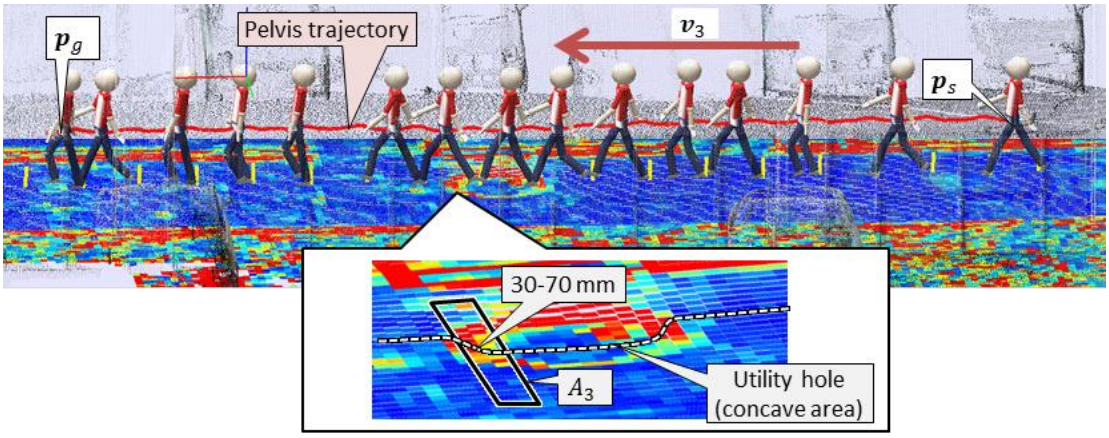

(c) Results of autonomous walking simulation passing on A_3 in direction v_3

Fig. 4.15 Tripping-hazard map generation results in the outdoor environment

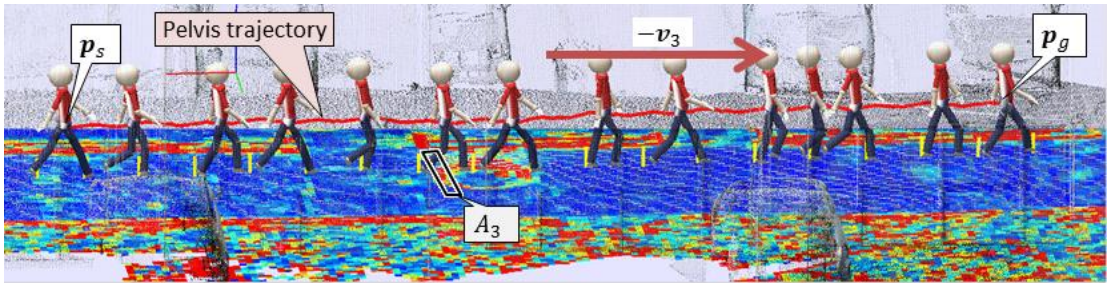

(a) Results of autonomous walking simulation passing on A_1

Fig. 4.15 Tripping-hazard map generation results in the outdoor environment (cont.)

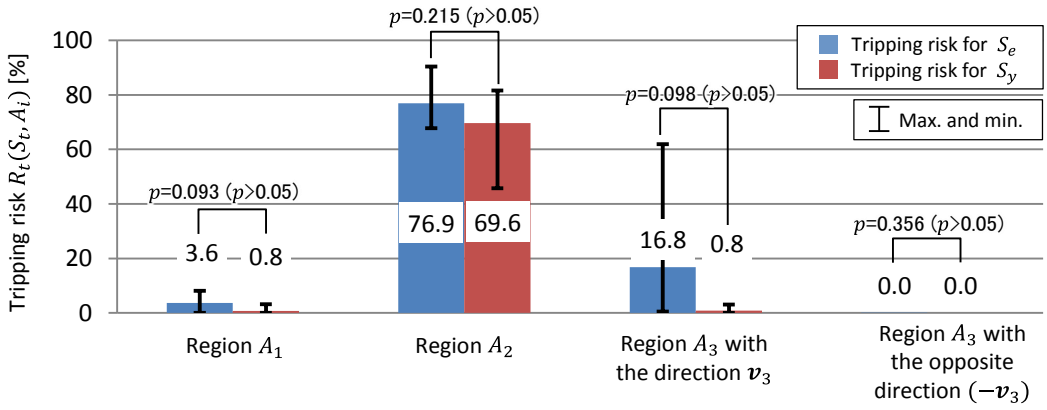

Fig. 4.16 Tripping risk evaluation results in outdoor environment

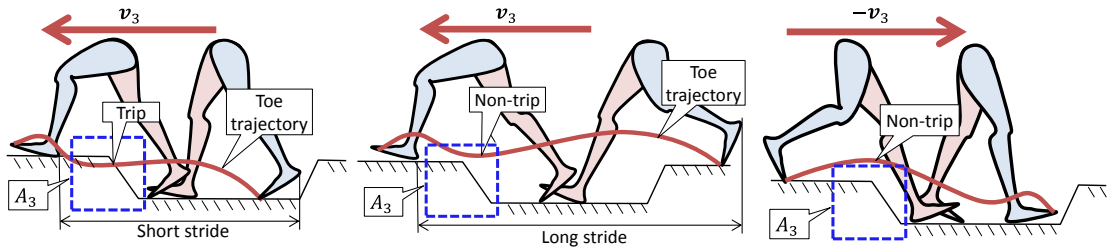

(a) Walking with short stride in older people

(b) Walking with long stride in younger people

(c) Walking in the opposite direction ($-v_3$)

Fig. 4.17 Walking motion of the DHM on interested region A_3

In contrast, as shown in Fig. 4.16, on the region A_3, the tripping risk for older people $R_t(S_e, A_3)$ along with the direction $\boldsymbol{v}_3$ was considerably higher than that for younger $R_t(S_y, A_3)$. With careful attention to the simulation results, as shown in Fig. 4.17 (a), it was observed that the tripping frequently occurred on A_3 in the simulation of S_e, when ascending the foot of the swing leg from the concave area to the upper area. This was caused by the fact that the stride of S_e was 0.2 m shorter than the one of S_y, in average. In the case of generating the motion of older people S_e, the DHM frequently took the double-leg supporting on the concave area. As shown in Fig. 4.17 (a), this double-leg supporting on the area resulted ascending motion of a foot of the swing leg from the area. In contrast, in case of younger people walking motion, as shown in Fig. 4.17 (b), the DHM could frequently walk over the concave area without grounding both legs on the area at the same time.

Therefore, it was confirmed that the proposed risk evaluation system could clarify the differences in the tripping risk among individuals by taking account of the difference in human gait depending on the age and on the detailed shape of the walking terrain.

In addition, the tripping risk $R_t(S_e, A_3)$ of the opposite direction $(-\boldsymbol{v}_3)$ was nearly zero even for the older people. As shown in Fig. 4.17 (c), this was due to the fact that only descending motion occurred on A_3. Since the toe of the DHM always passes over the downslope, the tripping risk $R_t(S_e, A_3)$ and $R_t(S_y, A_3)$ of the opposite direction $(-\boldsymbol{v}_3)$ almost corresponded to zero.

Therefore, it was further confirmed that the proposed risk evaluation system could clarify the difference in the tripping risk among the human behaviors such as the difference in walking directions.

4.5.4 Efficiency of tripping risk evaluation system

In the proposed risk evaluation system, the tripping-hazard map generation required approximately 19 s for the point clouds of the outdoor environment with 2.2 million down-sampled points. In addition, repeating the human behavior simulation 500 times for each subject required approximately 210 s in the outdoor environments. Therefore, the elapsed time of the quantitative tripping risk evaluation for all the subjects in S_y or S_e took approximately 25 min. The map generation time and the tripping risk evaluation time in the proposed system were significantly lower than the time required for actual environmental inspections reported in previous studies [Yanagihara 14a], [Cumming 99].

4.5.5 Experimental validation of tripping risk evaluation results by comparison with tripping risk measured from actual human

4.5.5.1 Overview

The results of the proposed risk evaluation system were demonstrated in 4.5.2 and 4.5.3. However, these simulation results were not experimentally validated. Therefore, in this section, the evaluated tripping risk is further compared with that measured from actual human walking, to validate the simulation results.

In general, measuring the tripping risk from actual human is very challenging, since making the subjects trip on barriers are incredibly dangerous, and prohibited in experiments. Recently, an innovative treadmills, such as the split-belt treadmill [Nakashima 14], the treadmill enabling the subjects to take active walking [von Zitzeeitz 07], and the treadmill having lifting device for falls prevention [Hocoma] have been developed. These treadmills are potentially utilized for measuring the tripping risk from actual human in safety. However, the occurrence of tripping still place stress on the subject's body, even if we take careful note of fall prevention after tripping. These experiments become physically taxing both for younger and older subjects, when the sufficient number of trials by many subjects are needed in the measurement.

Instead, in this study, we propose an alternative experiment-based tripping risk measurement without making the subjects trip. In the experiment, first, we measure the tripping risk of actual human walking using the photoelectric sensor (OMRON E3Z-R81 2M) [OMRON] on flat terrains, and then compare the tripping risk measured in the experiment with the simulated tripping risk obtained from the proposed system. Details are described in the following subsection.

4.5.5.2 On-site measurement of tripping risk of actual human

In this study, the tripping risks were measured from 7 younger participants on a barrier with a height of 20 mm using the photoelectric sensor [OMRON]. Fig. 4.18 shows an overview of the measurement and the system. Before the experiment, as shown in Fig. 4.18, a photoelectric sensor and a camera were attached with a jack placed on the floor. Then, a reflective plate was located on the floor, so as to be faced toward the sensor. The height of the sensor and the plate were adjusted to 20 mm. Therefore, when the swing leg passed below 20 mm, a straight laser beam from the sensor was interrupted. Consequently, the laser beam of the sensor could be considered as a virtual barrier with a height of 20 mm.

As shown in Fig. 4.18, during the experiment, the participants were asked to walk naturally on the floor for approximately 400 times, while keeping both legs located on both sides of the reflective plate. During each walking trial, the photoelectric sensor detected whether the tripping on the virtual barrier takes place or not. When the reflected light was interrupted during one walking trial, this trial

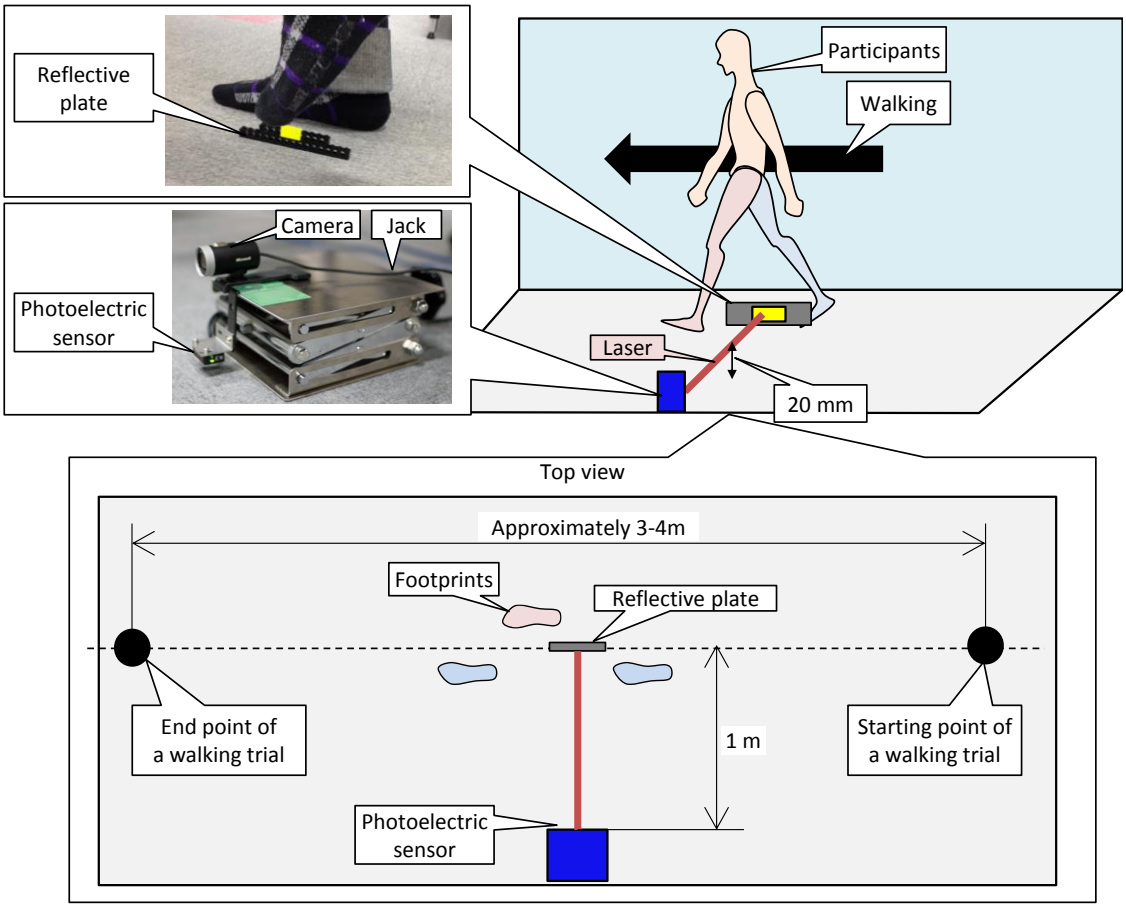

Fig. 4.18 On-site tripping risk measurement

Table 4.2 Age and body height of participants in measurement experiment

Participants	Y1	Y2	Y3	Y4	Y5	Y6	Y7
Age	24	22	22	24	23	25	23
Body height [m]	1.62	1.82	1.63	1.74	1.77	1.76	1.70

was considered as a "tripped" trial. By counting the number of tripped trial N_t' and non-tripped trial N_s' based on the sensor output, the tripping risk for actual human could be estimated using the same equation as (4.3) in 4.4.2.1.

As show in Table 4.2, 7 younger male participants belonging to our laboratory joined the experiment. The participants differed from any subject of MoCap data collection included in younger people dataset S_y. Most of the participants completed the 400 times walking trials within an hour including a short break taken voluntarily. During the experiment, the participants walked with socks. Note that the purpose of the experiment and the overview of the measurement system were not noticed in advance to the participants.

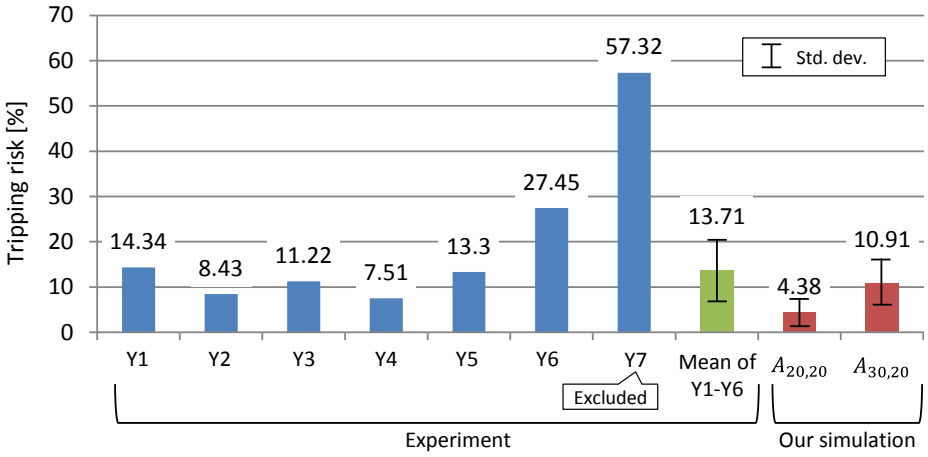

Fig. 4.19 Comparison of tripping risk between simulation and measurements from actual human

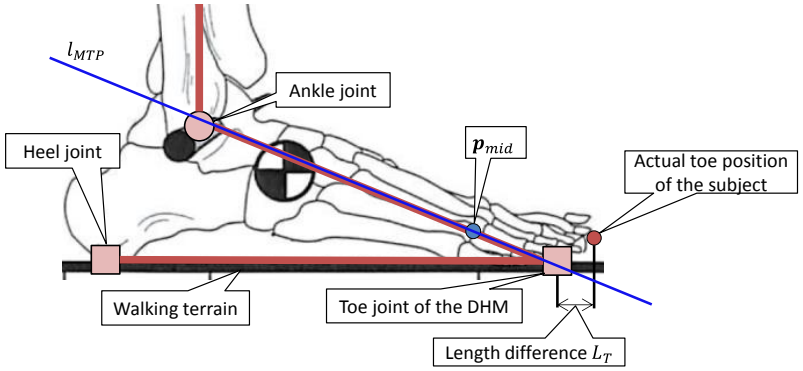

Fig. 4.20 Comparison of toe position between link model of DHM and subjects of MoCap data

4.5.5.3 Validation results of tripping risk evaluation system

Fig. 4.19 shows a comparison of the tripping risk between the simulation and the measurement for 7 younger participants. In Fig. 4.19, each error bar represents the standard deviation. The values of $A_{20,20}$, $A_{30,20}$, and $A_{40,20}$ represent the tripping risks $R_t(S_y, A_{20,20})$, $R_t(S_y, A_{30,20})$, and $R_t(S_y, A_{40,20})$, which were evaluated in 4.5.2. As shown in Fig. 4.19, the measurements of the tripping risk from the participant Y7 were singularly higher than the ones from the other subjects. This was caused by that Y7 had a greater tendency to walk with a shuffle than the others did, i.e., the toe and foot of the swing leg were too closes to the walking terrain during walking. Therefore, in this study, the measurements of Y7 was not used in the validation.

As shown in Fig. 4.19, the difference in the tripping risk between the mean risk and $R_t(S_y, A_{20,20})$ was approximately 9 percentage point, and the mean risk was more close to $R_t(S_y, A_{30,20})$ than $R_t(S_y, A_{20,20})$. Therefore, this difference could be represented as 10 mm, in terms of the height of barrier.

This difference was caused by the differnce in the toe position between the DHM and subject of MoCap data. As shown in Fig. 4.20, in this study, the toe joint of the DHM was estimated at the intersection point between the walking terrain in MoCap measurement experiment and a line l_{MTP} passing through the mid point $\boldsymbol{p}_{mid}$ between the subject's first metatarsophalangeal (MTP) joint in thumb and fifth MTP joint in pinkey, where $\boldsymbol{p}_{mid}$ was preliminarily estimated by the MoCap data analysis software, Visual 3D [C-Motion]. However, as shown in Fig. 4.20, the foot link model of the DHM is expected to have the length difference L_T between the estimated toe joint of the DHM and the actual toe position of the subject. It is not easy to find the appropriate length of L_T, since the MoCap data ser does not contain any measurements related to teh actual toe position of subjects. Therefore, to improve the proposed tripping risk evaluation system, we need to develop an algorithm of estimating the appropriate length of L_T for the subject of MoCap data utilizing both MoCap data and statistical anthropometric databases such as [Kouchi 05]. These improvements will remain as a future work.

In addition, to validate the system in more detail, some measurement experiments need to be conducted, such as measuring the tripping risk from participants with MoCap system, and measuring the tripping risk in daily living environments for a prolonged period with more participants as challenged by Kobayashi et al. [Kobayashi 14]. These experiments will be addressed in future work.

4.5.5.4 Discussions

Considering the results of tripping risk evaluation described in 4.5.2 and 4.5.3, it was confirmed that our tripping risk evaluation system made it possible to

- find the tripping-related environmental hazards exhaustively from as-is environments acquired as the laser-scanned point clouds, as described in 4.5.2.2 and 4.5.3.2,
- evaluate the tripping risk quantitatively in consideration of real usuage scenario in the environments, as described in 4.5.3.3,
- clarify the extent of difference in the tripping risk between younger and older people, as described in 4.5.2.3 and 4.5.3.3,
- clarify the difference in the tripping risk when changing usuage scenario of the environment, such as the difference in human walking routes, as described in 4.5.3.3.

Moreover, considering the simulation results in 4.5.2, and the validation results described in 4.5.5,

we obtained the following observations:

- The tripping risk evaluated by the simulation well corresponded with the general observations that the risk of tripping-related falls for older people is larger than that of younger people [Nagano 11], [Mills 08], [Barret 10], as shown in 4.5.2.3 and 4.5.3.3.
- The difference in the tripping risk between the simulation and the measurements from younger participants was corresponded approximately to 9 percentage point, as validated in 4.5.5.3.
- This difference could be represented as 10 mm in terms of the barrier height, as described in 4.5.5.3.

4.6 Summary

In this chapter, for the human-centered accessibility evaluation from human physical aspect, we developed a tripping risk evaluation system based on the autonomous walking simulation of the DHM in the point clouds-based 3D as-is environment models. Our system consists of the tripping hazard map generration, and the quantitative tripping risk evaluation. The tripping hazard map generation made it possble to find the tripping-related environmental hazards exhaustively from the laser-scanned point clouds. Furthermore, the quantitative tripping risk evaluation made it possible to clarify the difference in the tripping risk on the detected hazard by taking account of the stochastic properties of interactions between human behaviors and regions.

In addition, our tripping risk evaluation system was demonstrated in the point clouds of a virtual indoor environment, and of a real outdoor environment. As a result, the follwoing conclusions were obtained:

- The system could find the possible tripping-hazard regions exhaustively.
- The system could evaluate the tripping risk quantitatively, by taking account of the stochastic properties of interactions between human behaviors and hazard regions, such as the probability distribution of intrinsic factors and footprint factor, extrinsic factors, and a usage scenario of the environment.
- The system could clarify the difference in the tripping risk between younger and older people.
- The system could clarify the difference in the tripping risk when changing usuage scenario of the environment, such as the difference in human walking route.
- The map generation time and the tripping risk evaluation time in the system was significantly lower than the time required for actual environmental inspections.

Furthermore, by comparing the tripping risk between the simulation and the measurements of younger participants, it was confirmed that the difference between the risks was approximately 9

percentage point, which corresponded to approximately 10 mm difference in terms of the barrier height. This showed that the proposed system had a possibility of evaluating the tripping risk of the environment within the limit of accuracy of 10 mm in terms of barrier height.

To improve our system, as described in 4.5.5.3, an algorithm of estimating actual toe position of the subjects of MoCap data needs to be developed. In addition, to validate the system in more detail, some tripping risk measurement experiments need to be conducted, such as measuring the risk from the participants with MoCap system, and measuring the risk in daily living environments for a prolonged period with more participants. These improvements and validations will remain as future works.

Furthermore, our tripping risk evaluation system is potentially utilized for evaluating the tripping risk in a more specific environment, such as rehabilitation facilities and construction site. To realize the evaluation in the rehabilitation facilities, the tripping risk needs to be evaluated for people with gait deficit, by generating the walking motion of the DHM based on the MoCap data for flat walking with gait deficit. On the other hand, to realize the evaluation in the construction site, the tripping risk needs to be evaluated by making the DHM mimic the working behavior of construction worker. Validation of such scalability of the proposed system will remain as a future work.

Chapter 5 Ease of Wayfinding Evaluation based on Vision-based Wayfinding Simulation

5.1 Background and requirements

In the last chapter, for the human-centered accessibility evaluation from physical aspect, a tripping risk evaluation system was proposed and introduced. As discussed in Chapter 1, accessibility must be assessed not only from physical aspect, but also from cognitive aspect. In addition, wayfinding is an essential and basic cognitive behavior of all people in a given unfamiliar environment. Therefore, in this chapter, as an indispensable accessibility criterion from human cognitive aspect, we aim to develop an evaluation system of ease of wayfinding.

Wayfinding is an behavior that people try to find their way to their destinations in unfamiliar environments [Hunt 99]. Since wayfinding is an essential and basic cognitive behavior, the ease of wayfinding must be ensured for various people of different ages, genders, body dimensions, and visual capabilities, in indoor and outdoor environments. Table 5.1 and Fig. 5.1 show the information used for wayfinding [Hiiro 93]. As shown in Table 5.1, the wayfinding behavior can be affected not only by the memory information such as background knowledge of people, but also by the environmental information such as visual information including signage and landmarks.

On the other hand, according to ISO 21542 [ISO 21542, 11], visual, audible and tactile information should be provided at every key decision point such as a fork, in indoor and outdoor environments in order to assist people in wayfinding. Audible and tactile information such as voice-guided navigation and braille brock have an important role in visual impaired people including blind, while the visual information such as signage and landmarks assists healthy or mild impaired vision people in wayfinding.

As reported by Hiiro et al. [Hiiro 93], different visual information is used for wayfinding in the indoor and outdoor environments. Among them, the presence of landmarks greatly contributes to the wayfinding in familiar and unfamiliar outdoor environments. This was due to the fact that the known landmarks such as large building and towers are identifiable environmental-markers associated with specific locations [Hajibabai 07], and can be seen from anywhere in the outdoor environments. However, when the landmarks are not available in the outdoor environments, visual signage has an important role for the wayfinding. On the other hand, visual signage (e.g., directions and maps) greatly contributes to wayfinding in the unfamiliar indoor environments, since the people tend to lose their orientation when the landmarks are not available [Hölscher 07], [Hiiro 93].

Table 5.1 Information used for wayfinding [Hiiro 93]

Information	Explanation
Environmental information	Information given by environments
Memory information	Information given by human memory (e.g., background knowledges, visiting histories)
Physical information	Information for limiting movable region (e.g., walls and floors)
Symbol information	Information given by symbols in environments
Visual information	Information perceived by visual perception (e.g., landmarks and buildings)
Signage information	Information given by perceived signage (e.g., visual signage, maps)
Guide information	Information given by other people (e.g., verbal navigation)

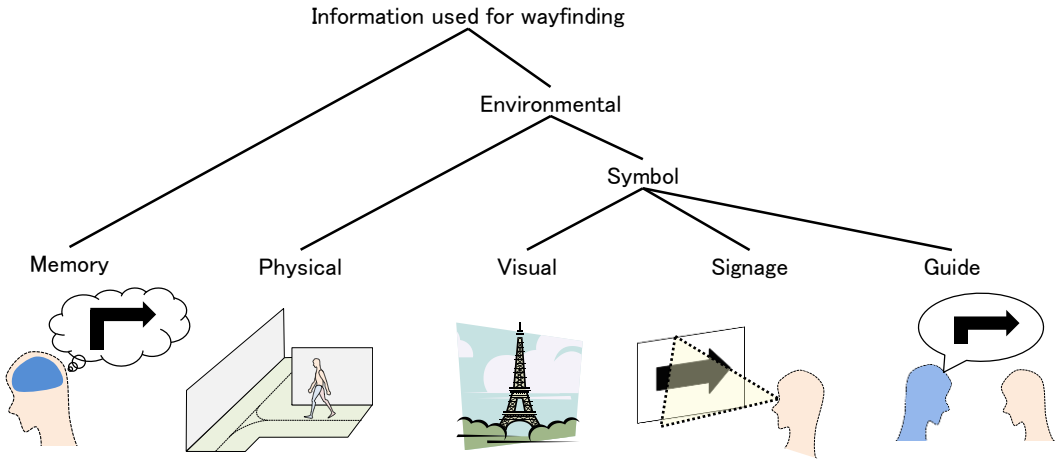

Fig. 5.1 Relation among information used for wayfinding [Hiiro 93]

Therefore, visual signage must be arranged, to ensure the ease of wayfinding in both indoor and outdoor environments. If any of the location, visibility, legibility, and continuity of the signage is inadequate at a certain place in the environments, there is a high probability that people lose their way at the place, so called “disorientation place”. Therefore, such disorientation place must be detected by taking account of the location, visibility, legibility, and continuity of the signage into the ease of wayfinding evaluation.

On the other hand, Table 5.2 shows a classification of visual signage. As shown in Table 5.2, the visual signage in indoor and outdoor environments are classified into the identification sign, directional sign, orientation sign, explanation sign, and regulation sign. Among them, the identification sign, direction sign, and orientation sign contribute to the wayfinding in unfamiliar environments, and need to be sufficiently arranged in the environments for ensuring the ease of wayfinding.

Table 5.2 Classification of visual signage

Types of signage	Drawing	Purposes
Identification sign	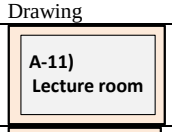	Making people identify the current place
Direction sign	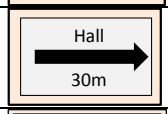	Making people recognize the direction and/or distance to their destination
Orientation sign	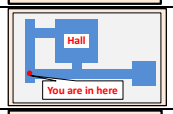	Making people recognize the current position in the environments
Explanation sign		Providing people with the additional information around the signage
Regulation sign		Alerting the regulations to people around the signage

On the other hand, as discussed in Chapter 1, the presence of extra objects, and the textures on walls and signage, has an effect on signage visibility, and legibility. In addition, Brunnhuber et al. [Brunnhuber 12] mentioned that the ease of wayfinding should be evaluated in consideration of visual appearance of the environments, i.e., realistic textures and detailed shapes, for helping the user to easily understand the evaluation results. Therefore, the ease of wayfinding must be evaluated for the 3D as-is environment model including the visual appearance information such as textures on walls and signage.

In addition, when the disorientation place is found by the evaluation, a facility manager needs to propose the plans of rearranged signage around the place for enhancing the ease of wayfinding. Therefore, the ease of wayfinding method needs to be designed to make it possible to evaluate the rearranged signage immediately, without prolonged wayfinding experiment.

Based on the above discussions, the requirements for the ease of wayfinding evaluation can be summarized as follows:

(a) The ease of wayfinding must be evaluated under assumption that the user is unfamiliar to the environments.

(b) The ease of wayfinding must be evaluated for various people of different ages, genders, body dimensions, and visual capabilities.

(c) The ease of wayfinding must be evaluated by taking account of the interaction between human wayfinding behaviors and the signage location, visibility, legibility, and continuity.

(d) The disorientation place needs to be detected by the evaluation.

(e) The ease of wayfinding must be evaluated in the 3D as-is environment model including the obstacles and realistic textures on walls and signage.

(f) The evaluation method needs to be designed to make it possible to evaluate the effect of rearranged signage immediately, without prolonged wayfinding experiments.

Therefore, in this chapter, for the human-centered accessibility evaluation from human cognitive aspect, we aim to develop the ease of wayfinding evaluation system satisfying these requirements, by utilizing the point clouds-based as-is environment modeling system in Chapter 2 and autonomous walking simulation of a DHM in Chapter 3.

5.2 Related work on ease of wayfinding evaluation studies

5.2.1 Ease of wayfinding evaluation based on field tests

Currently, the ease of wayfinding has been evaluated based on real field tests, and virtual field tests.

The real field tests such as [Thora 11], [Akagi 10] have been conducted to evaluate the ease of wayfinding, and to reveal the human characteristics related to the wayfinding behavior. In the real field tests, various human subjects are asked to perform a variety of experimental wayfinding tasks in a real environment, and the ease of wayfinding is evaluated based on their wayfinding behavior. In particular, Thora et al. [Thora 11] analyzed the walking route during the wayfinding in an indoor environment, and revealed a diversity of wayfinding behaviors. In addition, Akagi et al. [Akagi 10] analyzed the difference in the wayfinding behavior between younger and older people in motorway rest areas. In their study, to reveal visual search characteristics of older people, the gaze duration and gaze direction are further analyzed with their walking routes.

On the other hand, as well as the real field tests, virtual field tests have been actively conducted. In contrast to the real field tests, virtual field tests are conducted in the virtual environments represented as the textured 3D models, or a set of photographs imitating human eyesight in the environments. In particular, as shown in Fig. 5.2 (a), Vilar et al. [Vilar 14] proposed a virtual filed test for evaluating the effect of vertical signage (i.e., signage on walls) and horizontal signage (i.e., navigation lines on floors) on wayfinding in a textured 3D as-planned environment model. In their study, various subjects need to perform a variety of experimental wayfinding tasks in the textured 3D mesh model utilizing a Virtual Reality (VR) system. On the other hand, as shown in Fig. 5.2 (b), Buechner et al. [Buechner 12] proposed a virtual field test, which can evaluate the effect of the additional signage on wayfinding based on the gaze behavior of the subjects. In their study, a set of photographs of the airport was introduced into a VR system, and used as the imitated human eyesight during the test.

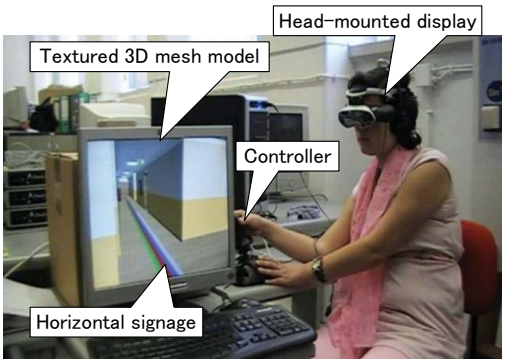

(a) Signage evaluation using VR system [Vilar 14]

(b) Eye tracking-based signage evaluation using photographs of the airport [Buechner 12]

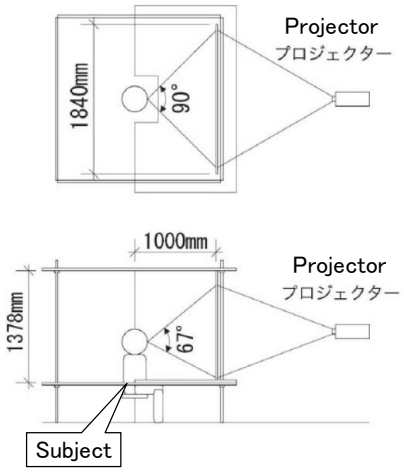

(c) WASS [Mori 11]

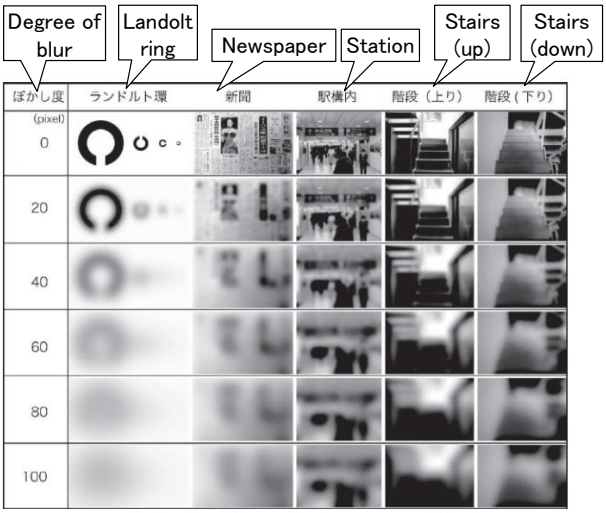

(d) Imitated eyesight of low-vision [Mori 11]

Fig. 5.2 Virtual field tests

These real or virtual field tests can evaluate the ease of wayfinding experimentally, and reveal the human characteristics related to the wayfinding behavior. However, these tests require various human subjects of different ages, genders, body dimensions, and visual capabilities, to evaluate the ease of wayfinding for various people. In addition, these tests require a prolonged wayfinding experiments with various subjects, and analyzing the test results is very time-consuming work. Therefore, it is difficult to propose rearranged signage plans and evaluate the plans immediately.

On the other hand, as shown in Figs. 5.2 (c) and (d), several virtual filed tests have been recently proposed to evaluate the ease of wayfinding, while simulating the eyesight of visual impaired people. Imamura et al. [Imamura 07] proposed a wayfinding active simulation system (WASS) to evaluate the ease of wayfinding in nursing home. In the WASS, a sequence of photographs is provided to the subject depending on the route choice by the subject. In their study, the provided

photographs were edited to imitate the blurred vision and misty vision. Therefore, the difference in the wayfinding characteristics between the blurred vision and the misty vision is revealed based on the analysis of the test results. Similarly, as shown in Figs. 5.2 (c) and (d), Mori et al. [Mori 11] also proposed the WASS based on the photographs representing the imitated eyesight of low-visions.

Therefore, these virtual field tests with imitated vision are potentially utilized for evaluating the ease of wayfinding with a few subjects, while simulating the eyesight of different visual capabilities. However, as one insoluble problem of these real or virtual field tests, a variety of wayfinding tasks needs to be performed by each subject, since the ease of wayfinding needs to be evaluated in consideration of various wayfinding scenarios. However, the ease of wayfinding must be evaluated for people who are "unfamiliar" to the environment. Therefore, making a subject perform several wayfinding tasks in a given environment is unsuitable approach for the ease of wayfinding evaluation.

As discussed above, these virtual or real field tests can satisfy the requirements (a)–(d) in the last section. However, satisfying the requirement (f) is basically feasible in these field tests. In addition, even if imitating the different visual capabilities in the recent virtual field tests [Mori 11], [Imamura 07], they require various human subjects to perform a variety of experimental wayfinding tasks under assumption that the subjects is unfamiliar to the environment. From these reasons, the current real or virtual field tests are insufficient for the ease of wayfinding evaluation.

5.2.2 Ease of wayfinding evaluation based on current human behavior simulation

On the other hand, several studies have been proposed to evaluate the ease of wayfinding based on the simulated wayfinding behaviors of the pedestrian models.

Hajibabai et al. [Hajibabai 07] proposed a signage-based wayfinding simulation in an as-planned 2D indoor environment model in the situation of fire emergency evacuation. In their study, each agent model made a decision depending on the signage information and fire propagation around the agent in the 2D as-planned environment model. However, in their study, signage visibility and legibility were evaluated by oversimplified human visual perception. In addition, a precise 3D wayfinding simulation using the 3D as-is environment models was basically impossible. Therefore, in this study [Hajibabai 07], satisfying the requirements (b), (c), and (e) in Section 5.1 is infeasible.

On the other hand, Chen et al. [Chen 11] proposed a wayfinding simulation algorithm based on architectural information such as egress width, height, contrast intensity, and room illumination in a 3D as-planned environment model. However, their work only focused on modeling human egress choice based on architectural information, without incorporating any signage information. Consequently, this study cannot satisfy the requirements (c) and (e) in Section 5.1.

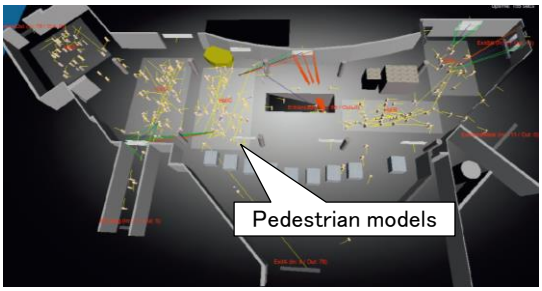

(a) Evaluation of the success rate of the navigation [Becker-Asano 14]

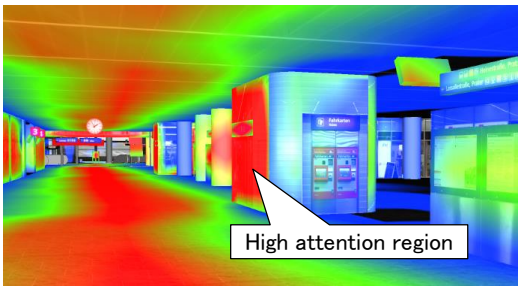

(b) Evaluation of the pedestrian's attention regions [Brunnhuber 12]

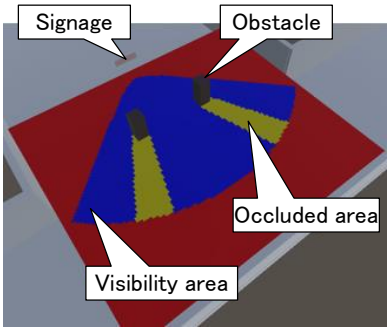

(c) Evaluation of the visibility area of the signage [Motamedi 16]

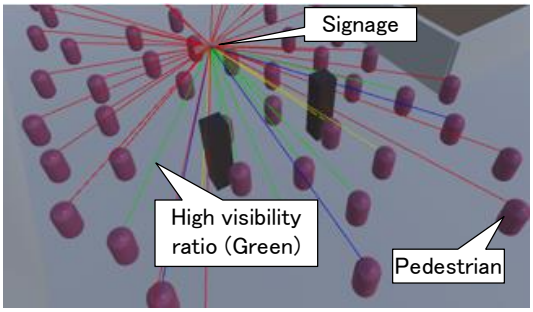

(d) Evaluation of the visibility ratio [Motamedi 16]

Fig. 5.3 Ease of wayfinding evaluation based on wayfinding simulation in 3D as-planned indoor environment

Recently, as shown in Fig. 5.3, several signage-based wayfinding simulation algorithms in the 3D environment models have been proposed [Brunnhuber 12], [Becker-Asano 14], [Motamedi 16]. In these studies, signage visibility and legibility were evaluated based on the imitated visual perception of the pedestrian model. In these studies, signage legibility was estimated based on Visibility Catchment Area (VCA) method, which is originally proposed by Fillipidis et al. [Fillipidis 06], and extended by Xie et al. [Xie 07]. VCA represents a 2D region, where the people can recognize the signage information written in the signage. In these studies, by changing the parameters of VCA, the signage legibility was evaluated by taking account of the different visual capabilities. In addition, in the simulations [Brunnhuber 12], [Becker-Asano 14], the walking path of the pedestrian model was dynamically generated depending on the perceived signage information, so the ease of wayfinding was evaluated in consideration of signage continuity. Therefore, these studies could satisfy the requirement (c) in Section 5.1. In contrast, in the simulation of Motamedi et al. [Motamedi 16], only the signage visibility and legibility for the pedestrian model were evaluated, and the walking path of the pedestrian model was not dynamically generated depending on the perceived signage information. Therefore, in their simulation, the ease of wayfinding was not evaluated from the aspect of the continuity of the signage system, so it cannot satisfy the

requirement (c) in Section 5.1.

On the other hand, from the aspect of the requirement (d) in Section 5.1, these studies evaluated the ease of wayfinding by the different approaches. As shown in Fig. 5.3 (a), in the simulation of Becker-Asano et al. [Becker-Asano 14], the ease of wayfinding was evaluated as the success rate of the agent's wayfinding task depending on the arranged signage in a 3D as-planned environment model. On the other hand, as shown in Fig. 5.3 (b), in the simulation of Brunnhuber et al. [Brunnhuber 12], the success rate of the wayfinding task, and the pedestrian's attention regions during the wayfinding simulation can be further evaluated as the criteria of the ease of wayfinding. On the other hand, as shown in Fig. 5.3 (c) and (d), in the simulation of Motamedi et al. [Motamedi 16], signage visibility ratio for the pedestrian models and visibility area of the signage were evaluated as the criteria of the ease of wayfinding.

However, in these simulations, when the pedestrian model cannot find any signage, the pedestrian model walks in the randomly determined direction, and tries to continue its wayfinding behavior. However, in the ease of wayfinding evaluation, the disorientation place must be detected as the criteria of ease of wayfinding, since the environment should provide information at every key decision point as recommended by the ISO guideline [ISO 21542, 11]. Therefore, making the pedestrian model walk randomly can be considered as an unsuitable approach from the aspect of ensuring the ease of wayfinding. Therefore, these studies [Brunnhuber 12], [Becker-Asano 14], [Motamedi 16] cannot satisfy the requirement (d) in Section 5.1.

On the other hand, from the aspect of the requirement (e) in Section 5.1, in these simulations [Brunnhuber 12], [Becker-Asano 14], the 3D as-planned environment model was used in the simulation. However, manually creating such 3D environment models for the simulation was still time-consuming, labor-intensive and costly work. On the other hand, in the simulation of Motamedi et al. [Motamedi 16], building information model (BIM) of the environment is used for the wayfinding simulation, which includes the updated geometries of all existing elements including signage. Therefore, 3D BIM-based environment model can be considered as an as-is environment model in terms of ease of wayfinding evaluation, even it does not contain small barriers and uneven walking terrains. Therefore, the simulation studies [Brunnhuber 12], [Becker-Asano 14] cannot satisfy the requirement (e) in Section 5.1, but the study [Motamedi 16] can be considered as satisfying the requirement (e).

As discussed above, these simulation studies are potentially utilized for the ease of wayfinding evaluation, but some requirements in Section 5.1 are not satisfied in each study.

5.2.3 Summary of issues of current ease of wayfinding evaluation studies and approach in this study

Table 5.3 shows a summary of issues of current ease of wayfinding evaluation studies. As shown

in Table 5.3, the current ease of wayfinding evaluation studies cannot satisfy all of the requirements in Section 5.1.

In contrast to these studies, in this chapter, for the human-centered accessibility evaluation from human cognitive aspect, we aim to develop the ease of wayfinding evaluation system, which can detect the disorientation place in the 3D as-is environments by taking account of the interaction between human wayfinding behaviors and signage location, visibility, legibility, and continuity. As shown in Table 5.3, to achieve the efficient ease of wayfinding, evaluating the ease of wayfinding based on the wayfinding simulation is essential. In addition, in the current wayfinding simulation studies, the difference visual capabilities were considered by utilizing the VCA for signage legibility estimation. Therefore, we aim to realize the ease of wayfinding evaluation system by utilizing the current wayfinding simulation such as [Brunnhuber 12], [Becker-Asano 14], [Motamedi 16], while improving their method to detect the disorientation place in the 3D as-is environment models.

5.3 Objective and overview

As discussed in the last section, the objective of this chapter is to develop the ease of wayfinding evaluation system, which can detect the disorientation place in the 3D as-is environment model by simulating the interaction between human wayfinding behaviors and signage location, visibility, legibility, and continuity.

Fig. 5.4 shows an overview of the proposed ease of wayfinding evaluation system. As shown in Fig. 5.4, to achieve the goal of this chapter, i.e., ease of wayfinding evaluation, an algorithm of as-is environment modeling based on SfM, and an algorithm of vision-based wayfinding simulation are further developed in this chapter.

In the proposed system, first, the point clouds-based 3D as-is environment model is automatically generated from the laser-scanned point clouds of the environments. As discussed in Section 5.1, for the ease of wayfinding evaluation, visual appearance such as textures on signage and walls must be reproduced as a part of the 3D as-is environment models. Therefore, after that, the textured 3D as-is environment models are semi-automatically constructed based on SfM using a set of photographs of the environments in addition to the point clouds-based as-is environment model. The textured 3D as-is environment model consists of the interior geometry G^I, and signage $M_i^S \in M$, where M_i^S includes the signage geometry G_i^S, and set of signage information I^i. These geometries G^I and G_i^S can be constructed through SfM, but the automatic estimation of I^i including geometric, navigation, and legibility attributes is generally difficult. Therefore, in this study, I^i is assigned by the simulation user. Details of these textured as-is environment modeling are described in Section 5.4.

Table 5.3 Summary of issues in previous ease of wayfinding evaluation studies

	(a) Unfamiliar environments	(b) Considering various people	(c) Evaluating signage location, visibility, legibility, and continuity	(d) Detecting disorientation place	(e) Evaluation based on 3D as-is environments	(f) Efficiency of evaluation
Real field test [Thora 11] etc.	✔ — Available	✔ — Available	✔ — Available	✔ — Available	✔ — Available	× — Prolonged experiments are required — Analyzing the test results is very time-consuming
Virtual field test [Vilar 14] etc.	✔ — Available	✔ — Available	✔ — Available	✔ — Available	× — Using as-planned environment model or photographs	× — Prolonged experiments are required — Analyzing the test results is very time-consuming
Virtual field test with imitated vision [Imamura 07], [Mori 11]	✔ — Available	✔ — Available	✔ — Available	✔ — Available	× — Using set of photographs	× — Prolonged experiments are required
Wayfinding simulation in 2D as-planned environment model [Hajibabai 07]	✔ — Available	× — Using oversimplified visual perception	× — Cannot evaluate signage visibility and legibility	× — Random walking	× — Using 2D as-planned environment model	✔ — Only by performing the simulation
Wayfinding simulation with egress choice model [Chen 11]	✔ — Available	× — N/A	× — N/A	× — N/A	× — Using 3D as-planned environment model	✔ — Only by performing the simulation
Wayfinding simulation in 3D as-planned environment model [Brunnhuber 12], [Becker-Asano 14]	✔ — Available	✔ — Using 3D VCA	✔ — Available	× — Random walking	× — Using 3D as-planned environment model	✔ — Only by performing the simulation
Wayfinding simulation in 3D BIM-based environment model [Motamedi 16]	✔ — Available	✔ — Using 3D VCA	× — Cannot evaluate signage continuity	× — Random walking	✔ — Using 3D BIM-based environment model	✔ — Only by performing the simulation

Meaning of the mark: ✔: Sufficient, ×: Insufficient

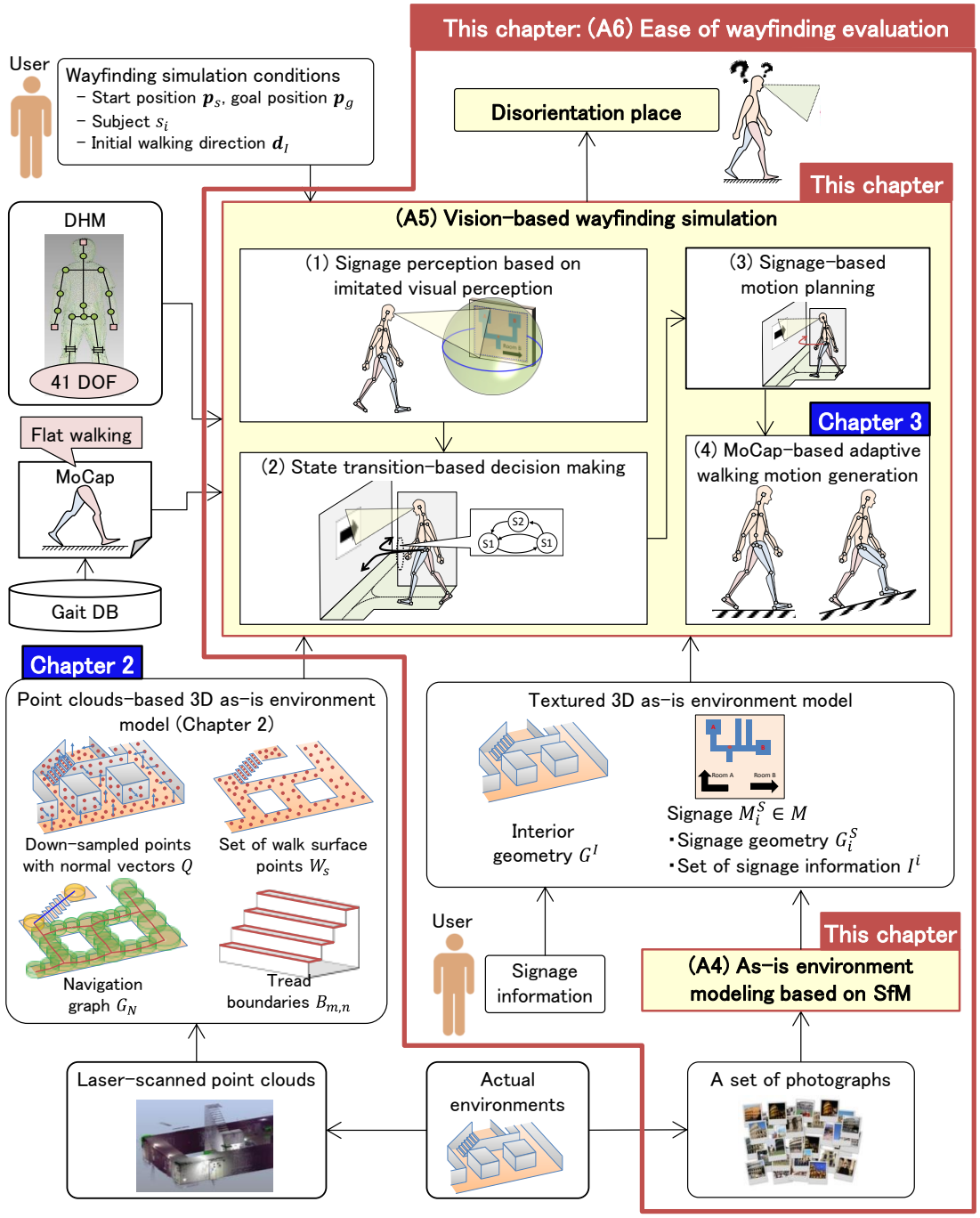

Fig. 5.4 Overview of the wayfinding simulation

After that, as shown in Fig. 5.4, the vision-based wayfinding simulation of the DHM is performed in the 3D as-is environment models, under the user-specified wayfinding simulation conditions such as the start position $\boldsymbol{p}_s$, goal position $\boldsymbol{p}_g$, subject s_i, and initial walking direction $\boldsymbol{d}_I$. When the simulation is performed, the DHM is set to walk in $\boldsymbol{d}_I$ from $\boldsymbol{p}_s$. Then, the following processes

are performed to arrive at $\boldsymbol{p}_g$ based only on the arranged signage.

(1) Signage perception based on imitated visual perception

First, the visibility and legibility of each signage are automatically evaluated based both on the imitated visual perception of the DHM, and on the 3D VCA of the signage, respectively. By evaluating the signage legibility based on 3D VCA, which is modeled based on an actual legibility measurement experiment, the different visual capabilities can be treated in the simulation. Details are described in 5.5.1.

(2) State transition-based decision making

Then, the state of the DHM in wayfinding is dynamically updated depending on the state transition model. For example, when the signage is perceived by the DHM in the previous process, the subgoal position of the DHM is updated depending on the navigation information of the signage.

(3) Signage-based motion planning

Depending on the state of the DHM in wayfinding, the walking trajectory of the DHM is dynamically determined. For example, when a subgoal position of the DHM is updated based on the perceived signage, a walking trajectory $S^O = \{\boldsymbol{t}_i\}$ from the current position to the subgoal position is automatically generated.

(4) MoCap-based adaptive walking motion generation

Finally, walking motion of the DHM is generated along the trajectory S^O. The MoCap-based adaptive walking motion generation developed in Section 3.4 is for this wayfinding simulation.

As shown in Fig. 5.4, as the result of the ease of wayfinding simulation, the proposed vision-based wayfinding simulation automatically detects a disorientation place if existed, where the DHM cannot find any signage indicating a destination expected by the DHM. Among several types of signage shown in Table 5.2, as the first stage of the ease of wayfinding evaluation, the proposed system only treats the direction signage in this study.

In contrast to the conventional systems for the ease of wayfinding evaluation, our system has the following characteristics:

- The system can evaluate the ease of wayfinding only by performing the wayfinding simulation, without prolonged real or virtual field tests.
- The system can evaluate the ease of wayfinding in the 3D as-is environment model including its visual appearance such as textures on walls and signage.
- The system can detect the disorientation place based on the interaction result between the simulated wayfinding behaviors of the DHM and the signage location, continuity, visibility and legibility.
- The system can evaluate the signage legibility using the 3D VCA which has been modeled based on an actual legibility measurement experiment in consideration of different visual capabilities.

The rest of this chapter is organized as follows. First, a method of textured 3D as-is environment modeling based on SfM is introduced in Section 5.4. Then, an algorithm of vison-based wayfinding simulation is described in Section 5.5. After that, the simulation and validation results in the two types of indoor environments are shown in Section 5.6. Finally, the summary of this chapter is described in Section 5.7.

5.4 Textured 3D as-is environment modeling based on structure-from-motion

5.4.1 Overview

For the ease of wayfinding simulation, first, the textured 3D as-is environment model is semi-automatically constructed through SfM. Fig. 5.5 shows an overview of the textured 3D as-is environment modeling. As shown in Fig. 5.5, the model consists of the interior geometry G^I and a set of signage $M = \{M_i^S\}$ In addition, each signage M_i^S has the corresponding signage geometry G_i^S and the set of signage information $I^i = \{\boldsymbol{I}_k^i\}$.

As shown in Fig. 5.5, the proposed construction method is premised on having the laser-scanned point clouds of the environment to be modeled. As shown in the part (A41) in Fig. 5.5, in the proposed algorithm, first, the interior geometry G^I is generated from a set of photographs of the environment using SfM software. At the same time, in the case of using the existing signage, the signage geometry G_i^S is also constructed by SfM. In other cases such as the newly designed signage, as shown in the part (A42) in Fig. 5.5, G_i^S must be created with 3D CAD software. After that, the set of signage information I^i is manually assigned to each signage geometry G_i^S. Finally, the combination of G_i^S and I^i is treated as one signage instance M_i^S, and M_i^S then inserted into the set of signage M.

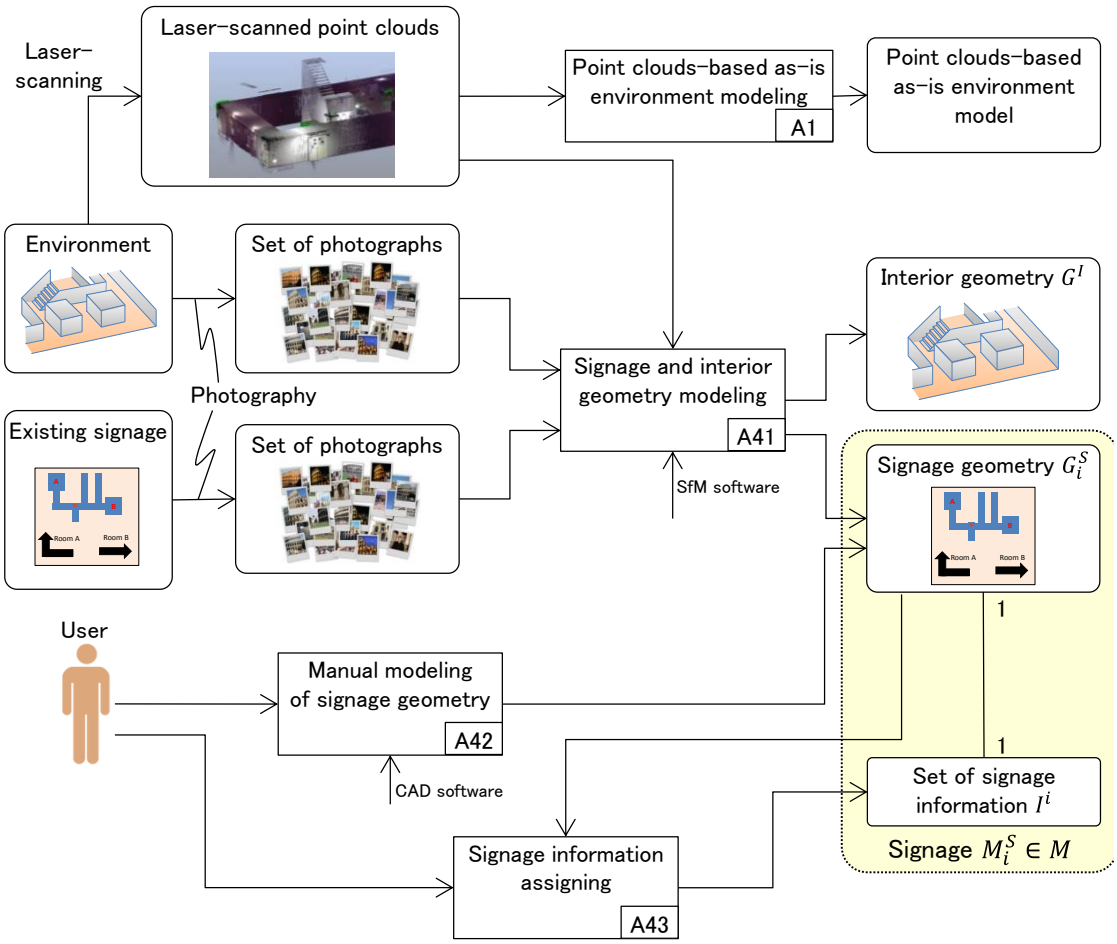

Fig. 5.5 Overview of textured as-is environment modeling

Details are described in the following subsections.

5.4.2 Signage and interior geometry modeling

Fig. 5.6 shows an overview of the interior geometry modeling utilizing SfM. As shown in the part (A411) in Fig. 5.6, first, the interior geometry G^I including a floor, walls, and ceiling is first constructed by SfM using a set of photographs of the environment. In general, the scale of the environment cannot be reproduced in SfM, and the coordinate system of G^I is different from that of laser-scanned point clouds. Therefore, in the process (A411), multiple 2D characteristic points such as corner of column are picked from the photographs used in the SfM. Then, its 3D coordinates with respect to the coordinate system of laser-scanned point clouds are assigned to the corresponding characteristic point, where the 3D coordinates can be obtained from the laser-scanned point clouds in the process (A412). As a result, the interior geometry G^I having the same scale and coordinate system as those of laser-scanned point clouds is obtained.

However, in general, texture-poor planar surfaces such as white walls cannot be well reconstructed

by SfM. Therefore, as shown in the part (A413) in Fig. 5.6, the model is then manually retouched using 3D CAD software (e.g., filling holes and editing mesh boundaries). Unfortunately, these retouched regions lose the suitable texture in the process. Therefore, as shown in the part (A414) in Fig. 5.6, by re-projecting the original photographs on the retouched 3D model again, the completely textured interior geometry G^I is finally constructed.

In addition, the geometry of each signage G_i^S is constructed using SfM or 3D CAD software. In the case of using the existing signage, the signage geometry G_i^S is constructed by SfM as well as the interior geometry G^I. In other cases, G_i^S must be created with 3D CAD software.

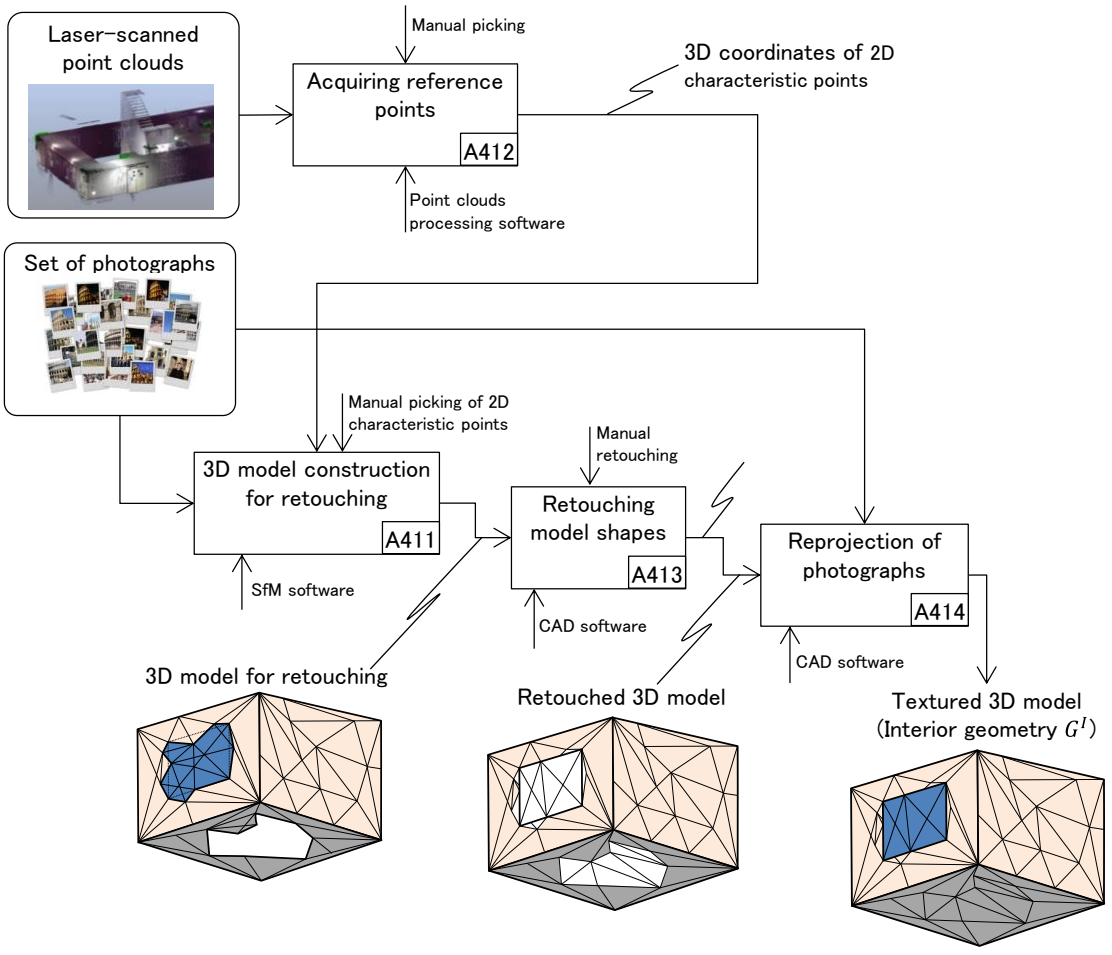

Fig. 5.6 Overview of interior geometry construction utilizing SfM

Table 5.4 Attributes of signage information

Property	Attribute	Description	Assigning method
Geometric property	Description region R_d	Description region of the information written in the signage	Assigned by user
	Center position $\boldsymbol{p}_{center}$	Center position of R_d	Estimated from R_d
	Width CX	Width of R_d	Estimated from R_d
Navigation property	Subgoal position $\boldsymbol{p}_{sub}$	Next goal position indicated by the signage	Assigned by user
	Destination position $\boldsymbol{p}_{des}$	Final destination position indicated by the signage	Assigned by user
Legibility property	Apparent angular separation φ	Angular separation at the perceptible place	Assigned by user
	Center point of 3D VCA $\boldsymbol{p}_{VCA}$	Center of the sphere representing 3D VCA	Estimated from CX, $\boldsymbol{p}_c$, and φ
	Radius of 3D VCA r_{VCA}	Radius of the above sphere	Estimated from CX and φ

5.4.3 Signage information assigning

In the last process, the geometry of each signage G_i^S was created by SfM. However, it does not contain the sematic information such as navigation information indicated by the signage. In general, it is difficult to automatically recognize the information from the textures of signage. Therefore, in this study, a signage information $\boldsymbol{I}_k^i$ ($k \in [1, N_i]$) are assigned by the user to each signage M_i^S, where N_i represents the number of signage information assigned to M_i^S.

As shown in Table 5.4, the attributes of k th signage information $\boldsymbol{I}_k^i = [R_d, \boldsymbol{p}_{center}, CX, \boldsymbol{p}_{sub}, \boldsymbol{p}_{des}, \varphi, \boldsymbol{p}_{VCA}, r_{VCA}]$ is classified into three types: (a) geometric property including the description region R_d, center position $\boldsymbol{p}_{center}$, and width CX, (b) navigation property including the subgoal position $\boldsymbol{p}_{sub}$ and the destination position $\boldsymbol{p}_{des}$, (c) legibility property including the apparent angular separation φ, the center point $\boldsymbol{p}_{VCA}$ of 3D VCA, and the radius r_{VCA} of 3D VCA. Details of each property and its assigning method are given below.

(a) Geometric property ($R_d, \boldsymbol{p}_{center}, CX$)

As shown in Table 5.4, the geometric property includes the description region R_d, center position $\boldsymbol{p}_c$, and width CX. As shown in Fig. 5.7, $R_d = \{\boldsymbol{p}_{top}, \boldsymbol{p}_{bottom}\}$ represents a set of two diagonal points $\boldsymbol{p}_{top}$ and $\boldsymbol{p}_{bottom}$ of the rectangular description region written in the signage. $\boldsymbol{p}_{center}$ represents the center points of R_d, and CX represents the horizontal distance between $\boldsymbol{p}_{top}$ and $\boldsymbol{p}_{bottom}$ of R_d. Among these attributes, the user has to specify $\boldsymbol{p}_{top}$ and $\boldsymbol{p}_{bottom}$ of R_d by picking a two diagonal points on the front surface of G_i^S. The others, $\boldsymbol{p}_{center}$ and CX, are automatically estimated from R_d.

(b) Navigation property ($\boldsymbol{p}_{sub}, \boldsymbol{p}_{des}$)

As shown in Table 5.4, the navigation property includes the subgoal position $\boldsymbol{p}_{sub}$ and the

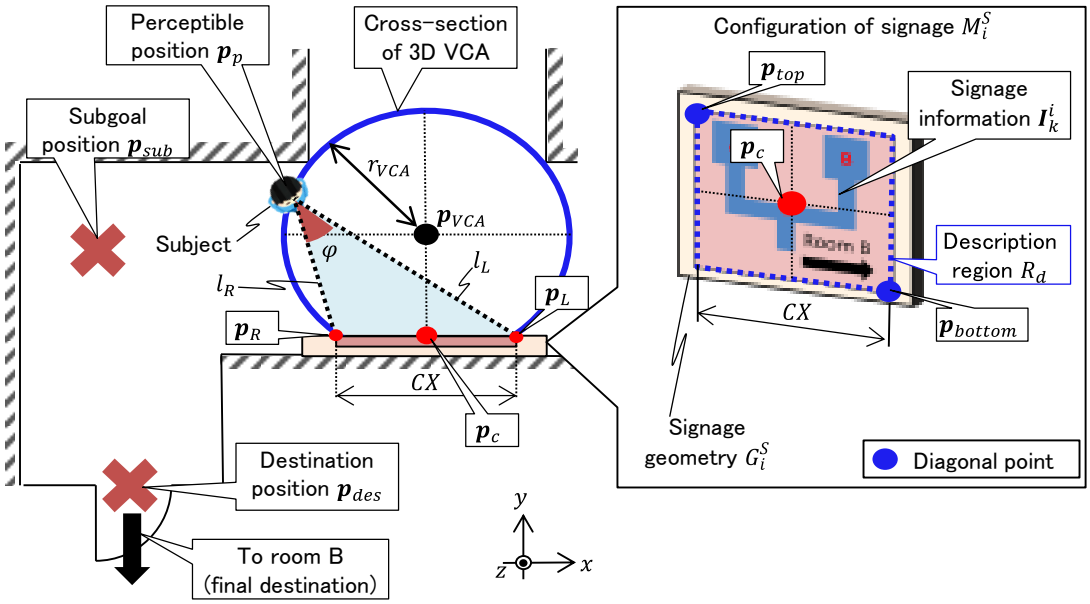

Fig. 5.7 Overview of signage information assigning

destination position $\boldsymbol{p}_{des}$ in the as-is environment model. As shown in Fig. 5.7, $\boldsymbol{p}_{sub}$ represents the next goal position on the floor indicated by the signage, and $\boldsymbol{p}_{des}$ represents the position of the final destination when the DHM walks in accordance with the signage. When the DHM perceived $\boldsymbol{I}_k^i$, the DHM is set to walk toward $\boldsymbol{p}_{sub}$ in case that the user-specified goal position $\boldsymbol{p}_g$ of the DHM, i.e., the destination of the DHM, corresponds to the destination of $\boldsymbol{I}_k^i$, i.e., $\boldsymbol{p}_g = \boldsymbol{p}_{des}$. Both $\boldsymbol{p}_{sub}$ and $\boldsymbol{p}_{des}$ can be specified by picking points on the navigation graph G_N.

(c) Legibility property $(\varphi, \boldsymbol{p}_{VCA}, r_{VCA})$

As shown in Table 5.4, the legibility property includes the apparent angular separation φ, the center point $\boldsymbol{p}_{VCA}$ of 3D VCA, and the radius r_{VCA} of 3D VCA representing a spherical space where a certain subject can recognize and interpret the information written in the signage. To specify the attributes, the user has to measure φ for a certain subject in the real world in an actual legibility measurement experiment, and then has to input φ into $\boldsymbol{I}_k^i$.

As shown in Fig. 5.7, in the legibility measurement experiment, first, a subject having a certain visual capability is asked to stand on the perceptible place $\boldsymbol{p}_p$, where the subject can recognize and interpret the information written in the signage at $\boldsymbol{p}_p$. After that, φ can be obtained by measuring the angle between two line segments l_R and l_L, where the start points of l_R and l_L correspond to the perceptible place $\boldsymbol{p}_p$, and the end points of l_R and l_L correspond to the projected corner points $\boldsymbol{p}_R$ and $\boldsymbol{p}_L$ shown in Fig. 5.7. In this study, we measured φ using a laser distance meter [Leica] with triangulation method. In the case of evaluating the ease of wayfinding for people having

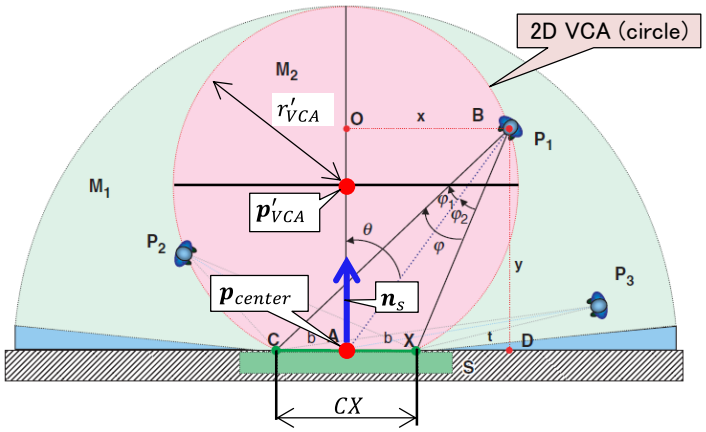

(a) Original 2D VCA represented as a 2D circle [Xie 07]

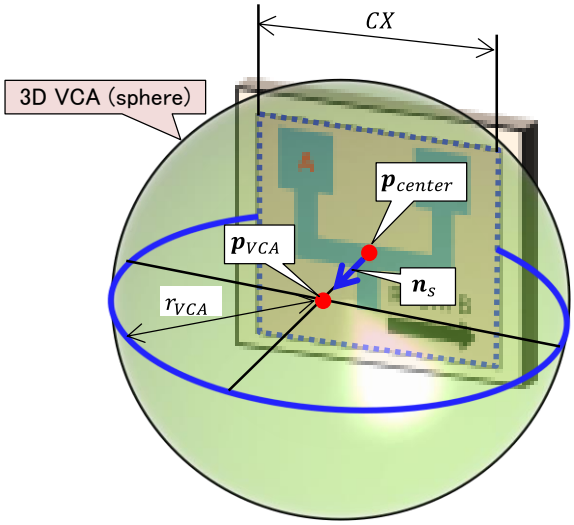

(b) Proposed 3D VCA represented as a 3D sphere

Fig. 5.8 Comparison of 2D VCA with proposed 3D VCA

different visual capabilities, φ must be measured with a subject having different visual capabilities.

After obtaining φ for a certain visual capability, the center point $\boldsymbol{p}_{VCA}$ of 3D VCA, and the radius r_{VCA} of 3D VCA are automatically estimated. As shown in Fig. 5.8 (a), in the original 2D VCA proposed by Xie et al. [Xie 07], its center point $\boldsymbol{p}'_{VCA} = [x'_{VCA}, y'_{VCA}]$ and radius r'_{VCA} was estimated by the following equation (5.1), where the VCA represented as a 2D circle.

$$\begin{aligned} r'_{VCA} &= b/\sin\varphi \\ x'_{VCA} &= x_c + n_x(b/\tan\varphi) \\ y'_{VCA} &= y_c + n_y(b/\tan\varphi) \end{aligned} \tag{5.1}$$

where $b = CX/2$, and $\boldsymbol{n}_s = [n_x, n_y, n_z]$ represents an unit normal vector of the front surface of the signage geometry G_i^S, and $\boldsymbol{p}_{center} = [x_c, y_c, z_c]$. In this study, the proposed wayfinding simulation is performed in the 3D as-is environment, so the VCA needs to be extended to 3D space.

Therefore, in this study, as shown in Fig. 5.8 (b), we extend the VCA as 3D sphere of radius r_{VCA} and center position $\boldsymbol{p}_{VCA}$ which are calculated by the following equation (5.2).

$$\begin{aligned} r_{VCA} &= b/\sin\varphi \\ \boldsymbol{p}_{VCA} &= \boldsymbol{p}_{center} + \boldsymbol{n}_s(b/\tan\varphi) \end{aligned} \tag{5.2}$$

This extension was realized by approximating the characteristics of human eyes in horizontal direction to those in vertical direction. Relevance and issue of this extension are summarized in Appendix D.

Finally, the completed signage information $\boldsymbol{I}_k^i = \{R_d, \boldsymbol{p}_{center}, CX, \boldsymbol{p}_{sub}, \boldsymbol{p}_{des}, \varphi, \boldsymbol{p}_{VCA}, r_{VCA}\}$ and the signage geometry G_i^S are aggregated as one signage M_i^S, and M_i^S is inserted into the set of signage M. Note that the user can specify multiple signage information $\boldsymbol{I}_k^i$ for one signage M_i^S. For example, in Fig. 5.7, the user can specify $\boldsymbol{I}_k^i$ for the information "To room B", and $\boldsymbol{I}_{k+1}^i$ for the information "To room A".

5.5 Methods of vision-based wayfinding simulation

5.5.1 Overview

After the textured 3D as-is environment modeling, the vision-based wayfinding simulation of the DHM is executed. Fig. 5.9 shows an overview of the vision-based wayfinding simulation. As shown in Fig. 5.9, as the simulation conditions, the user has to specify the start position $\boldsymbol{p}_s$, goal position $\boldsymbol{p}_g$, subject s_i, and initial walking direction $\boldsymbol{d}_I$. According to the user-specified simulation conditions, the DHM is set to walk in the direction of $\boldsymbol{d}_I$ from $\boldsymbol{p}_s$. At the same time, the vision-based wayfinding simulation is continuously performed by repeating the following processes until the DHM arrives at $\boldsymbol{p}_g$.

(1) Signage perception based on imitated visual perception

First, as shown in Figs. 5.9 and 5.10 (a), the signage visibility and legibility are estimated based on the imitated visual perception of the DHM, and the 3D VCA of the signage, respectively. As a result, a binary vector $\boldsymbol{s}_{vl}$ representing the current state of the signage visibility and legibility is obtained. Details are described in 5.5.2.

(2) State transition-based decision making

As shown in Figs. 5.9 and 5.10 (b), the state of the DHM in wayfinding is changed depending on $\boldsymbol{s}_{vl}$. After that, the subgoal position $\boldsymbol{p}_{sub}^{DHM}$ representing the temporal destination of the DHM is

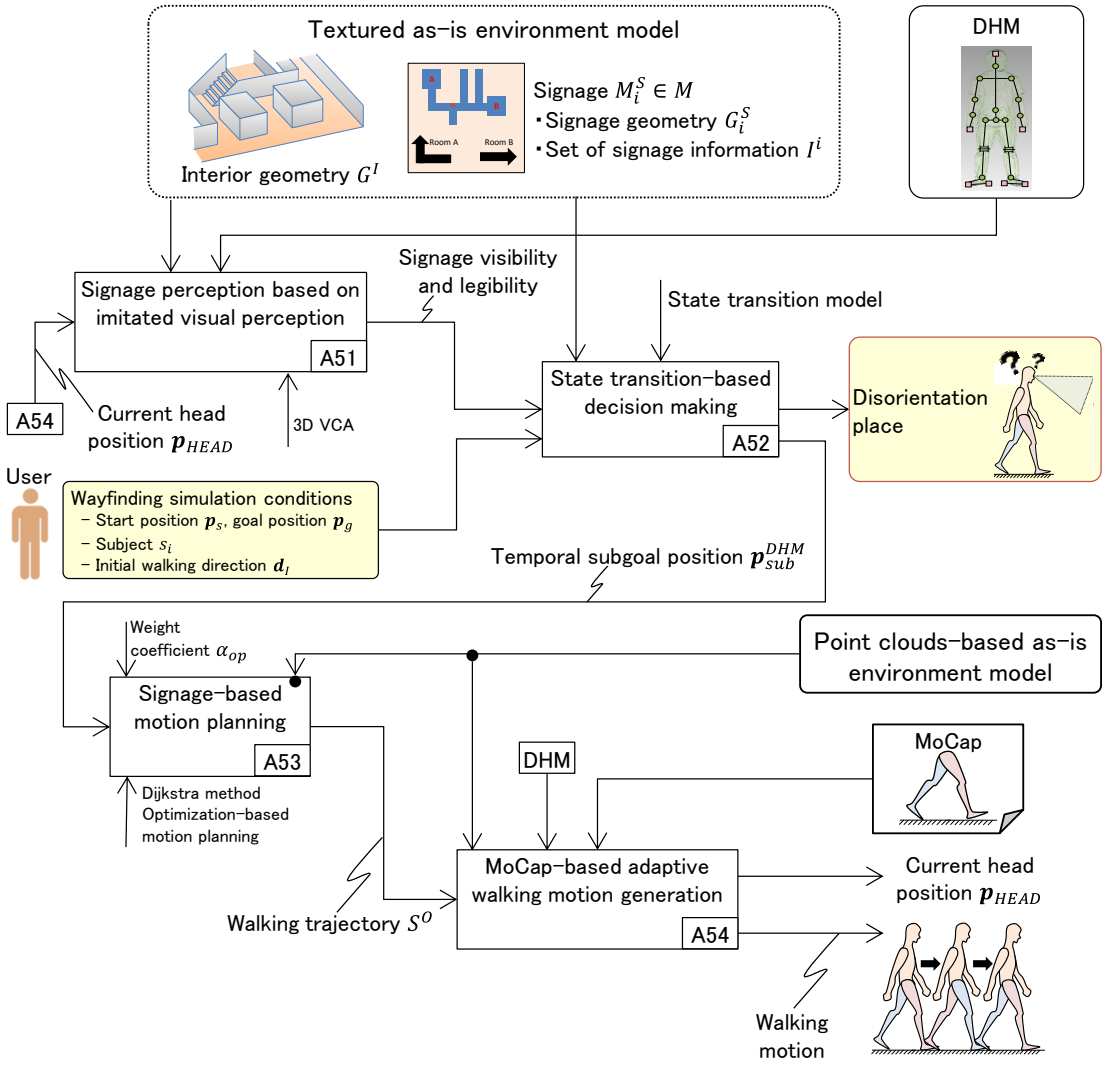

Fig. 5.9 Overview of vision-based wayfinding simulation

dynamically changed depending on the perceived signage information $\boldsymbol{I}_k^i$. Details are described in 5.5.3.

(3) Signage-based motion planning

As shown in Figs. 5.9 and 5.10 (c), the walking path V^P of the DHM from the current position $\boldsymbol{p}_c$ to $\boldsymbol{p}_{sub}^{DHM}$ is automatically selected on the navigation graph G_N using the Dijkstra method. In addition, the walking trajectory S^O of the DHM is then generated using the optimization-based motion planning process developed in 3.4.3. Details are described in 5.5.4.

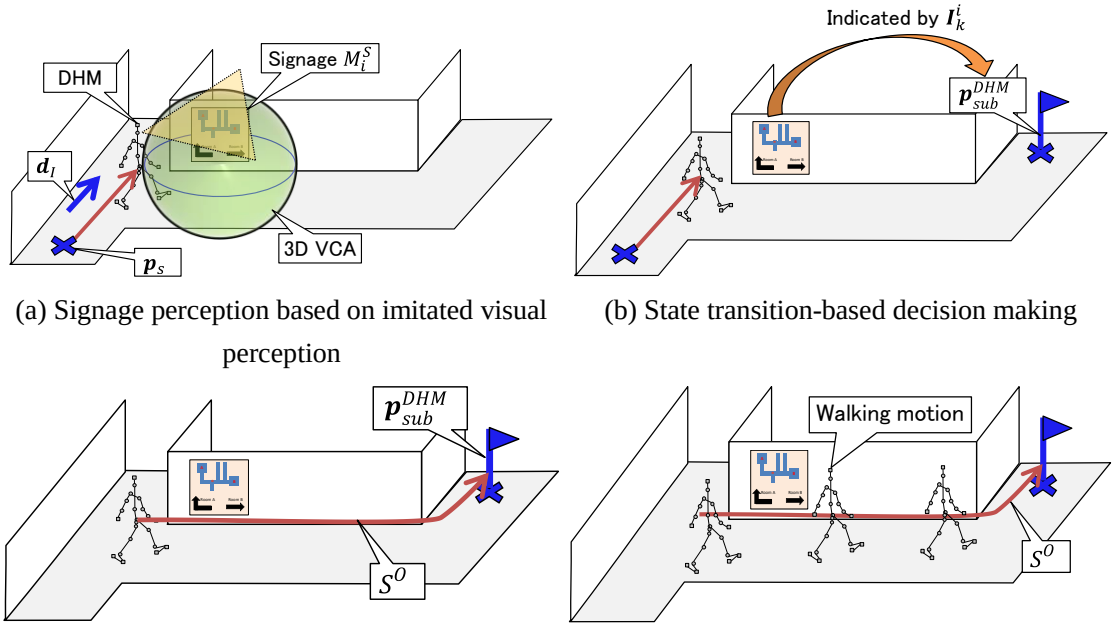

(a) Signage perception based on imitated visual perception

(b) State transition-based decision making

(c) Signage-based motion planning

(d) MoCap-based adaptive walking motion generation

Fig. 5.10 Overview of each process of vision-based wayfinding simulation

(4) MoCap-based adaptive walking motion generation

Finally, as shown in Figs. 5.9 and 5.10 (d), the walking motion of the DHM along S^O is generated. This process is realized by the same process developed in 3.4.3. In this process, the MoCap data for flat walking of the subject s_i is referred to reproduce the human-like walking motion of the DHM.

Finally, if the DHM can arrive at the goal position $\boldsymbol{p}_g$, the wayfinding simulation finishes successfully. By contrast, if the DHM cannot find any walking path to arrive at $\boldsymbol{p}_g$ around a certain place, this place is determined as a disorientation place. In such case, to improve the ease of wayfinding, the signage location, visibility, legibility need to be rearranged around the disorientation place. In the following subsections, details of these processes (1)–(4) are described.

5.5.2 Signage perception based on imitated visual perception

As shown in Fig. 5.11, the visibility of signage M_i^S is estimated based on the eyesight of the DHM. In order to speed up the test of the visibility estimation, a rendering-based visibility estimation using graphics hardware is developed.

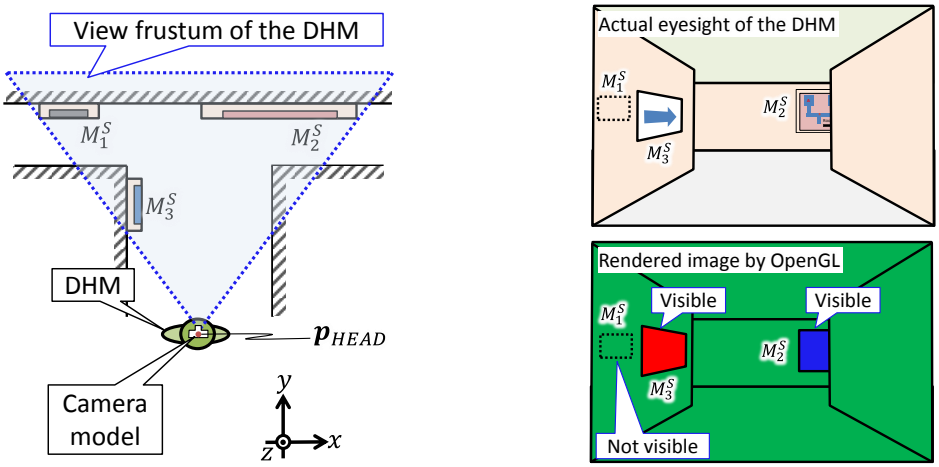

(a) Overhead view (b) Eyesight of DHM

Fig. 5.11 Visibility estimation of signage

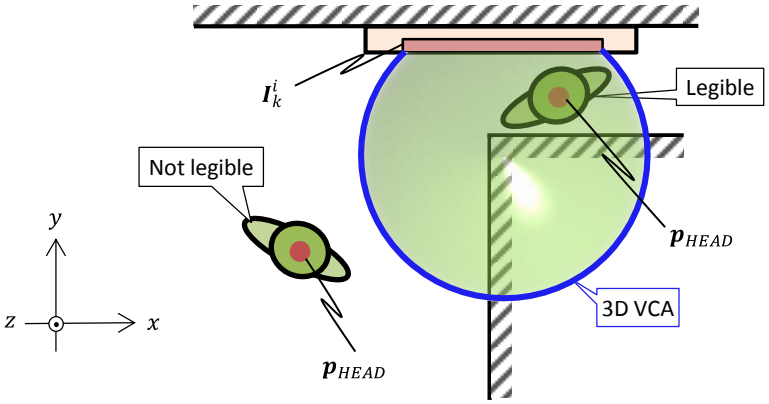

Fig. 5.12 Legibility estimation of signage information

First, as shown in Fig. 5.11 (a), the camera model for the rendering is arranged on the DHM head position $\boldsymbol{p}_{HEAD}$, and the rendered image from the camera model is then obtained by glReadPixels function implemented in OpenGL, where $\boldsymbol{p}_{HEAD}$ is the midpoint between the top of the head and the neck. In this rendering, as shown in Fig. 5.11 (b), the interior geometry G^I and each signage geometry G_i^S of M_i^S are rendered with a single color instead of their original texture. Finally, if the color of M_i^S appears in the rendered image, M_i^S is considered as "visible".

After that, as shown in Fig. 5.12, the legibility of the signage information $\boldsymbol{I}_k^i$ is estimated based on its 3D VCA. If $\boldsymbol{p}_{HEAD}$ is included in the sphere representing the 3D VCA of $\boldsymbol{I}_k^i$, $\boldsymbol{I}_k^i$ is considered as "legible".

Note that the DHM can recognize and interpret $\boldsymbol{I}_k^i$, only when M_i^S is visible and $\boldsymbol{I}_k^i$ is legible.

5.5.3 State transition-based decision making

Fig. 5.13 shows the relationship between the wayfinding state transition and the signage visibility and legibility state for the DHM. The state of the signage visibility and legibility is represented as a binary vector $\boldsymbol{s}_{vl} = (b_1, b_2)$, where b_1 and b_2 represent the binary variables of the signage visibility and legibility, respectively. Initially, b_1 and b_2 are set to zero as a state that any signage is not visible and legible for the DHM. When a signage becomes visible, b_1 becomes one. When its signage information becomes legible, b_2 becomes one. In the figure, $b_i = *$ represents an arbitrary state (i.e., $b_i = 0$ or $b_i = 1$).

Fig. 5.13 (b) shows an example of the wayfinding behavior of a DHM based on the wayfinding state transition appearing in Fig. 5.13 (a). First, when the simulation is performed, the DHM is set to start walking in the direction of the user-specified initial walking direction $\boldsymbol{d}_I$ (state S_w1 in Fig. 5.13 (a)). Then, when the signage M_i^S becomes visible (i.e., $\boldsymbol{s}_{vl} = (1,0)$), the DHM is set to walk toward

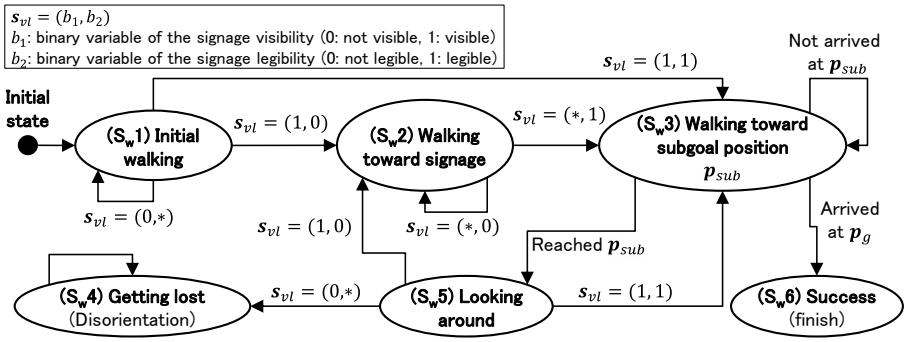

(a) Wayfinding state transition of DHM

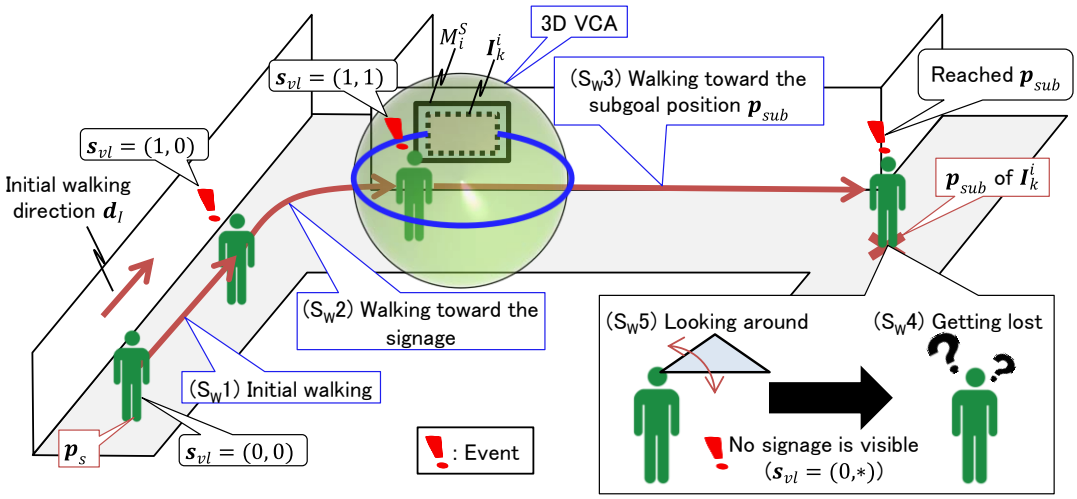

(b) An example of wayfinding behavior based on the state transition

Fig. 5.13 State transition-based decision making

M_i^S (state S_w2). After that, when the signage information $\boldsymbol{I}_k^i$ becomes legible (i.e., $\boldsymbol{s}_{vl} = (1,1)$), the DHM is set to walk toward the subgoal position $\boldsymbol{p}_{sub}$ indicated by $\boldsymbol{I}_k^i$ (state S_w3). Then, when the DHM reaches $\boldsymbol{p}_{sub}$, it is asked to observe the surrounding environment (i.e., look-around) by rotating the neck joint horizontally within its range of motion (state S_w5). If the DHM cannot find a new visible signage M_u^S, the state of the DHM is changed to "Getting lost" (state S_w4), and the current position of the DHM is treated as "a disorientation place". On the other hand, if the DHM finds a new visible signage M_u^S, the state returns to the state S_w2. Finally, when the DHM arrives at the user-specified goal position $\boldsymbol{p}_g$, the simulation is stopped (state S_w6). The state S_w6 is considered as the success state, when the wayfinding finishes successfully, whereas the state S_w4 is considered as a failure state.

When the state moves to the state S_w2 or S_w3, a new DHM walking trajectory S^O is generated on-the-fly in the signage-based motion planning process. Details are described in the following subsection.

5.5.4 Signage-based motion planning

According to the wayfinding state of the DHM, the walking path V^P of the DHM, and the trajectory S^O is automatically determined. When the state moves to the state S_w2, i.e., walking toward the signage, the temporal subgoal position of the DHM $\boldsymbol{p}_{sub}^{DHM}$ is set to $\boldsymbol{p}_{sub}^{DHM} = \boldsymbol{p}_{center}$, where $\boldsymbol{p}_{center}$ is the center position of the description region R_d of the signage information $\boldsymbol{I}_k^i$. On the other hand, when the state moves to the state S_w3, i.e., walking toward the subgoal position $\boldsymbol{p}_{sub}$, $\boldsymbol{p}_{sub}^{DHM}$ is set to $\boldsymbol{p}_{sub}^{DHM} = \boldsymbol{p}_{sub}$, where $\boldsymbol{p}_{sub}$ is a subgoal position indicated by $\boldsymbol{I}_k^i$. Note that both $\boldsymbol{p}_{center}$ and $\boldsymbol{p}_{sub}$ were assigned by the user in 5.4.3.

When the state moves to the state S_w2 or S_w3, the following processes are performed to generate a new walking path V^P and walking trajectory S^O from the current position $\boldsymbol{p}_c$ to $\boldsymbol{p}_{sub}^{DHM}$.

(1) Walking path selection

First, as shown in Fig. 5.14 (a), the graph node $v_c \in V$ and $v_{sub} \in V$ are automatically extracted from the navigation graph G_N, where v_c and v_{sub} have the position vectors $\boldsymbol{t}(v_c)$ and $\boldsymbol{t}(v_{sub})$ nearest to $\boldsymbol{p}_c$ and $\boldsymbol{p}_{sub}^{DHM}$, respectively. After that, as shown in the figure, a shortest walking path V^P from v_c to v_{sub} is automatically selected from G_N using the Dijkstra method.

(2) Motion planning

After the walking path V^P is determined, as shown in Fig. 5.14 (b), the walking trajectory S^O of the DHM is automatically generated using the optimization-based motion planning developed in

3.4.3. In the process in 3.4.3, given a start position $\boldsymbol{p}_1$, goal position $\boldsymbol{p}_2$ and walking path V^P, the trajectory S^O is automatically generated by the optimization algorithm, which minimize the weighted sum of internal and external energies of the trajectory as described in 3.4.3.3. Now, we define the above function as

$$S^O = \mathrm{Traj}(\boldsymbol{p}_1, \boldsymbol{p}_2, V^P) = \langle \boldsymbol{t}_1, \cdots, \boldsymbol{t}_i^p, \ldots, \boldsymbol{t}_2 \rangle \tag{5.3}$$

where $\mathrm{Traj}(\boldsymbol{p}_1, \boldsymbol{p}_2, V^P)$ is a function to generate the walking trajectory S^O from a position $\boldsymbol{p}_1$ to $\boldsymbol{p}_2$ within the boundary lines of V^P. $\boldsymbol{t}_1$ and $\boldsymbol{t}_2$ represent pelvic positions, when the DHM stands on the floor surface just under $\boldsymbol{p}_1$ and $\boldsymbol{p}_2$, respectively.

In the wayfinding simulation, S^O is generated by the function Traj() as:

$$S^O = \mathrm{Traj}(\boldsymbol{p}_c, \boldsymbol{p}_{sub}^{DHM}, V^P). \tag{5.4}$$

By using the above function, the walking trajectory S^O from $\boldsymbol{p}_c$ to $\boldsymbol{p}_{sub}^{DHM}$ is obtained.

Finally, the walking motion of the DHM along S^O is generated by the MoCap-based adaptive walking motion process developed in 3.4.4.

By performing the processes in 5.5.2–5.5.4, the ease of wayfinding can be evaluated based on the vision-based wayfinding simulation of the DHM.

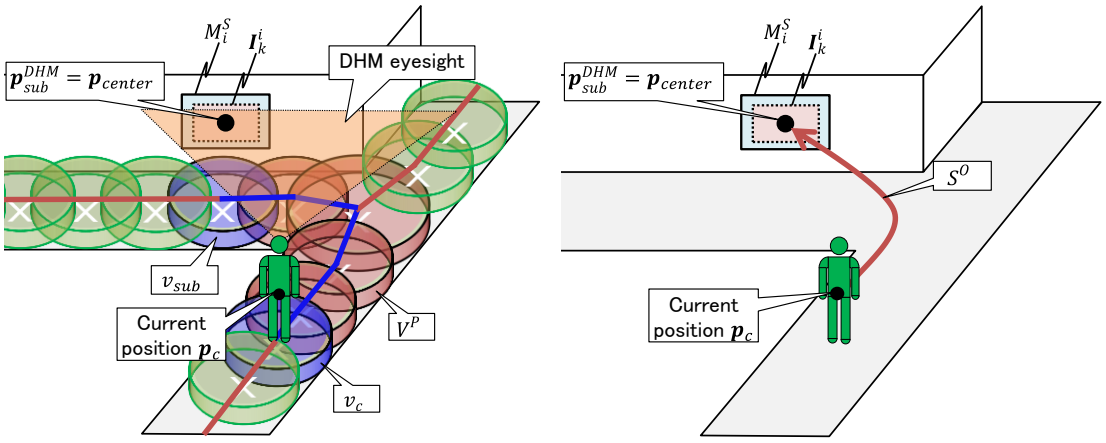

(a) Walking path selection (b) Motion planning

Fig. 5.14 Signage-based motion planning

5.6 Results and validations of ease of wayfinding evaluation

5.6.1 Results of textured 3D as-is environment modeling

In this study, the proposed ease of wayfinding evaluation system is applied to the two types of indoor environments: one-floor and two-story indoor environments. For both environments, the point clouds-based as-is environment models were automatically generated from the laser-scanned point clouds of the environments in Chapter 2.

The textured as-is environment modeling results of one-floor and two-story indoor environments using the SfM are shown in Figs. 5.15 and 5.16, respectively. These textured as-is environment models were constructed using commercial SfM software [Bentley] from the photographs taken in the area shown in Figs. 5.15 (b) and 5.16 (d) and (e). The modeling information such as the number of photographs used in the SfM is summarized in Table 5.5. Note that three parts of the one-floor indoor environment model were constructed separately from three sets of photographs, and then combined into a single model representing the one-floor indoor environment.

As shown in Figs. 5.15 and 5.16, some part of the textured as-is environment model contains distorted regions caused by the performance limitation of the SfM software. However, most part of the model could be successfully generated with high-quality textures. The produced model is used as an interior geometry G^I for the wayfinding simulation and ease of wayfinding evaluation.

Table 5.5 Summary of textured as-is environment modeling

(CPU: XeonE5-2630 v3 2.40GHz, RAM: 32GB, GPU: GeForce GTX 980)

	(a) One-floor indoor environment	(b) Two-story indoor environment
Used camera	Digital single-lens reflex camera (Nikon D3300)	
Photo taking approach	Taking pictures with roller tripod	Extracting pictures from videos taken with roller tripod
Number of photographs	2,000	21,143 (1F: 12,654 2F:8,489)
Resolution of photograph [pix]	3000 × 2000	1920 × 1080
Elapsed time for bundle adjustment (Automatic processing)	Approximately a half day	Approximately two days
Elapsed time for dense matching (Automatic processing)	Approximately a day and a half	Approximately six days
Number of vertices	235,247	625,484 (1F: 319,157 2F:306,327)
Number of faces	451,272	1,241,049 (1F: 633,447 2F:607,602)

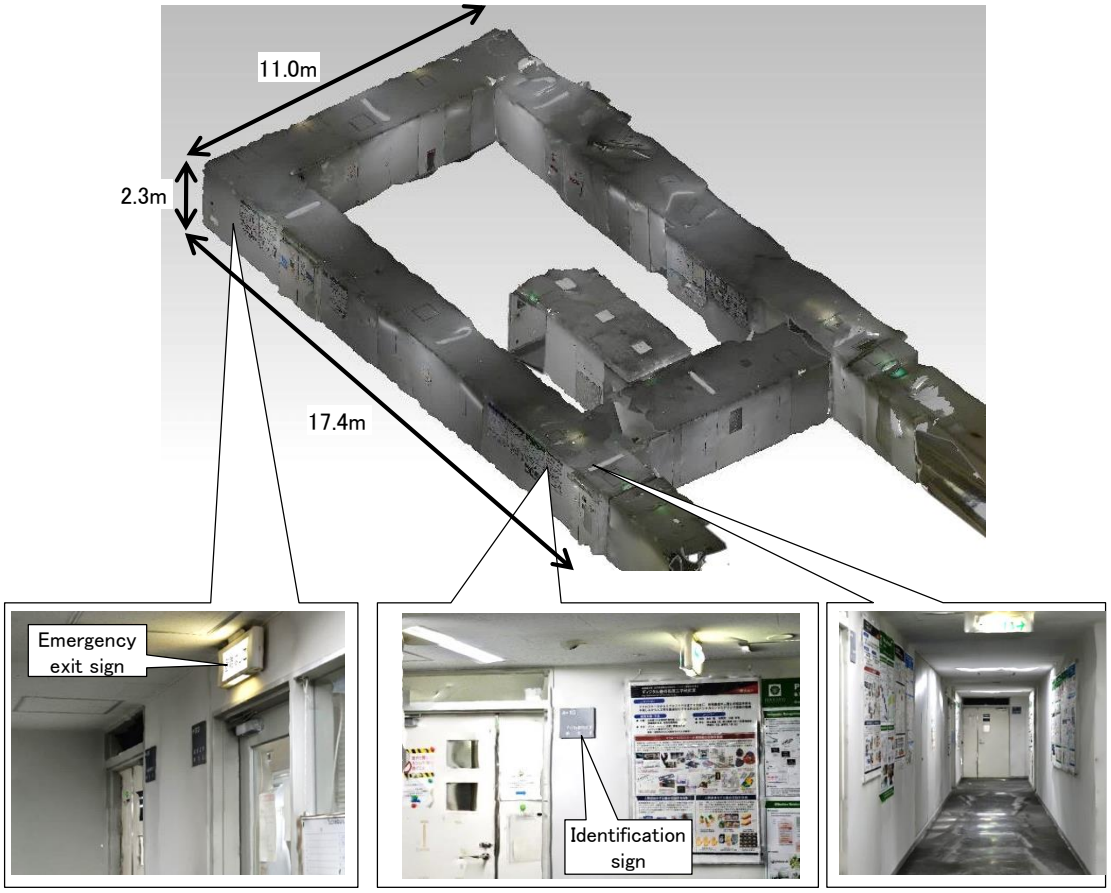

(a) Textured 3D as-is environment model

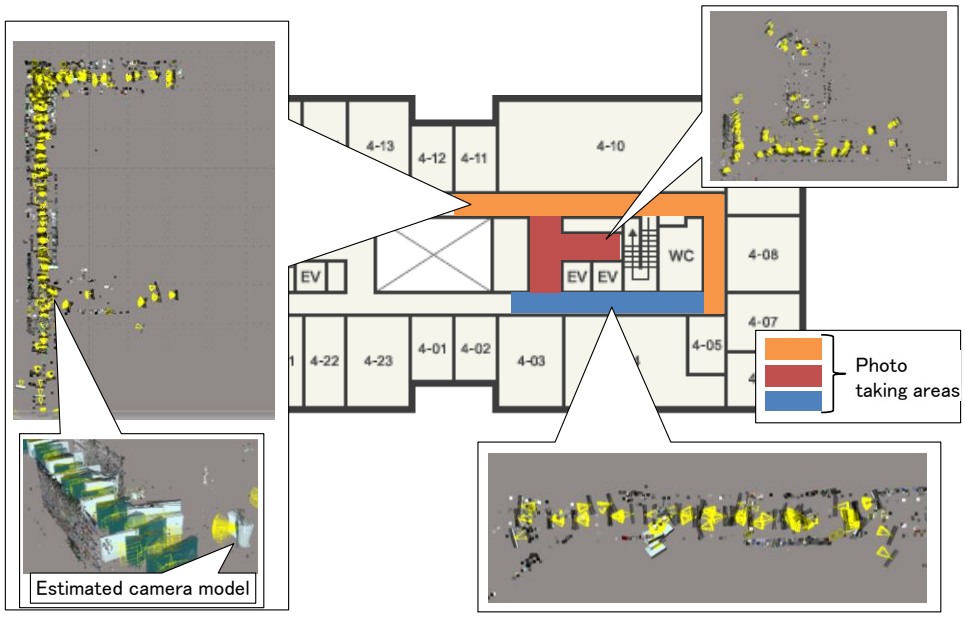

(b) Photo taking area and estimated photo positions and orientations

Fig. 5.15 Textured as-is environment model of one-floor indoor environment

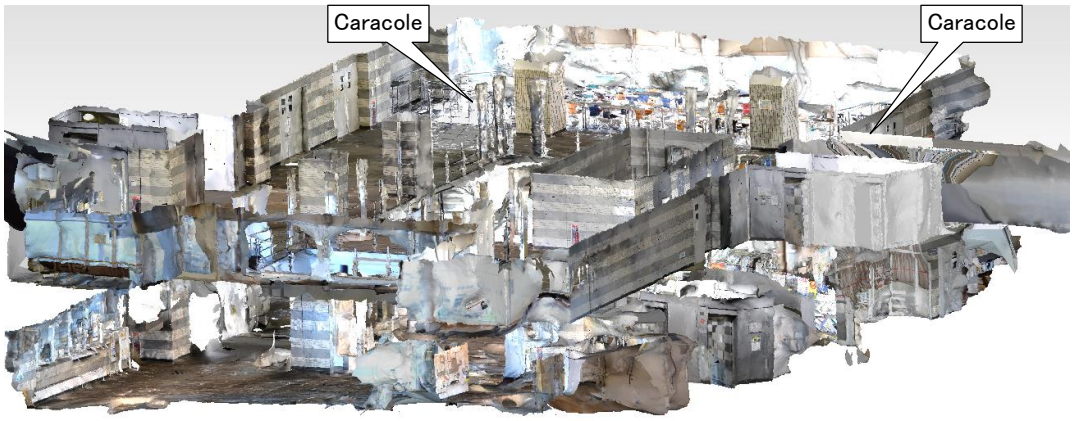

(a) Entire model

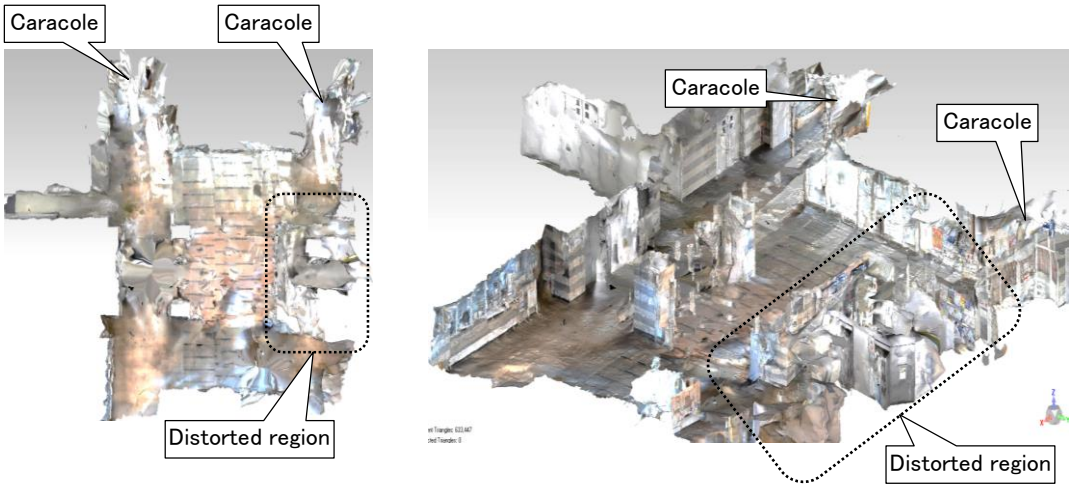

(b) Model of first-floor

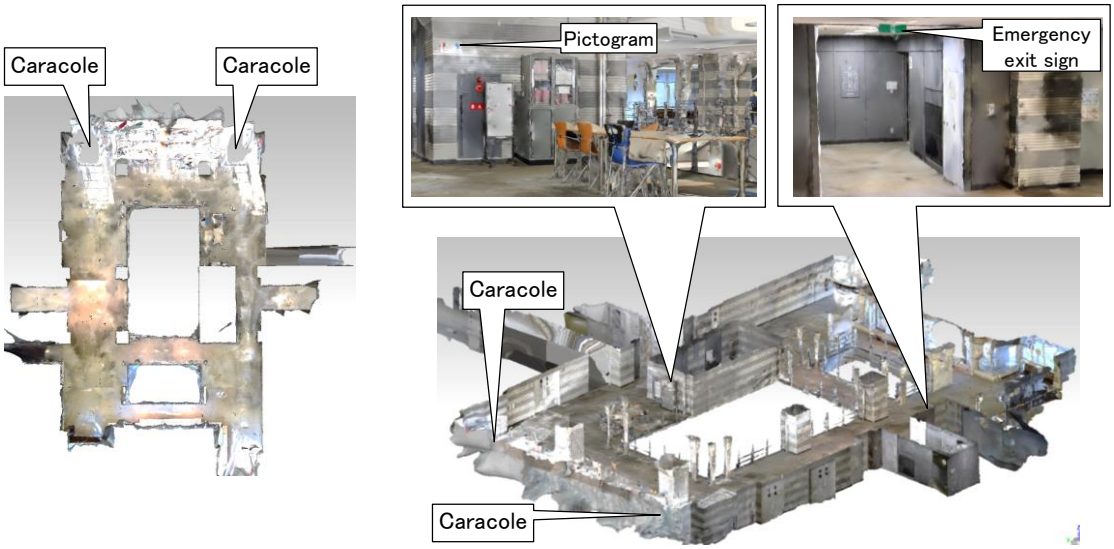

(c) Model of second-floor

Fig. 5.16 Textured as-is environment model of two-story indoor environment by SfM

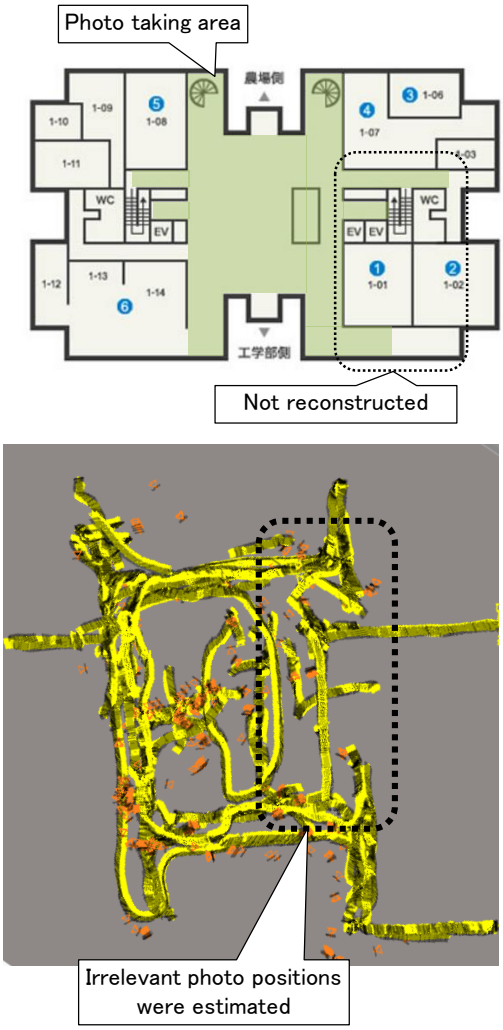

(d) Photo taking area and estimated photo positions and orientations in first-floor

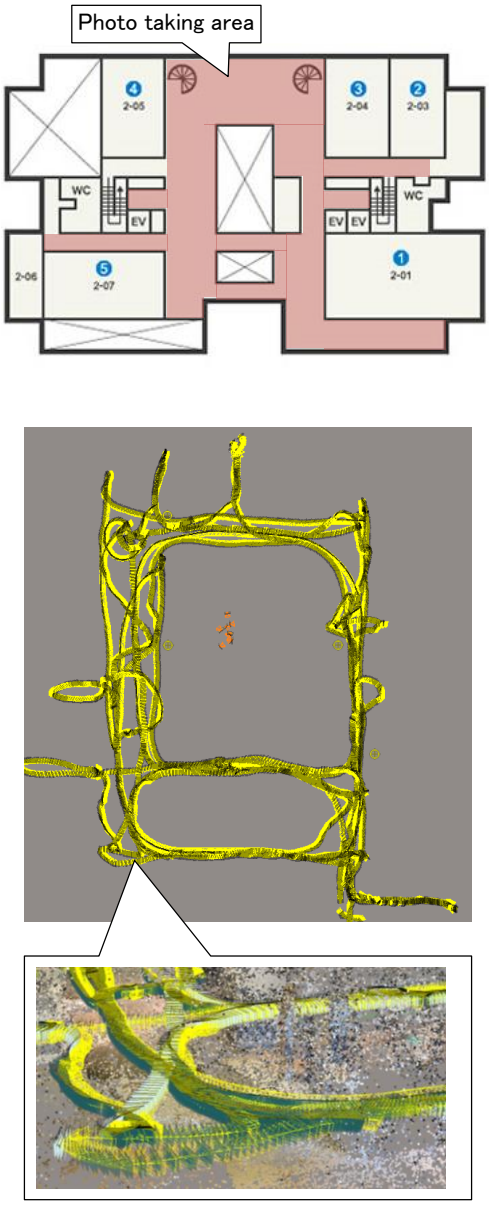

(e) Photo taking area and estimated photo positions and orientations in second-floor

Fig. 5.16 Textured as-is environment model of two-story indoor environment (Cont.)

5.6.2 Results of ease of wayfinding evaluation using vision-based wayfinding simulation

5.6.2.1 Results of ease of wayfinding evaluation in one-floor indoor environment

We performed the vision-based wayfinding simulation with a simple wayfinding task to evaluate its effectiveness. Fig. 5.17 shows top views of the simulation results of the DHM in the as-is environment model of the one-floor indoor environment.

As shown in Figs. 5.17 (a) and (b), one signage M_1^S consisting of its geometry G_1^S and a single signage information $\boldsymbol{I}_1^1$ was added into the environment model. In this simulation, G_1^S was created by 3D CAD software. The apparent angular separation φ of $\boldsymbol{I}_1^1$ was set at 15 deg.

As shown in Figs. 5.17 (c) and (d), when M_1^S becomes visible, the DHM is set to walk to the center position $\boldsymbol{p}_{center}$ of $\boldsymbol{I}_1^1$. After that, as shown in Figs. 5.17 (e) and (f), when $\boldsymbol{I}_1^1$ becomes legible, the DHM is set to walk to the subgoal position $\boldsymbol{p}_{sub}$ of $\boldsymbol{I}_1^1$ indicated by M_1^S. However, as shown in Figs. 5.17 (g) and (h), when the DHM reached $\boldsymbol{p}_{sub}$, the state of the DHM was changed to "(Sw4) Getting lost", since the DHM could not find any new visible signage to arrive at $\boldsymbol{p}_g$, in the state "(Sw5) Looking around". Finally, this place was detected as a disorientation place, so the user has to propose rearranged signage plans around the place.

In the proposed system, the user could check these simulation results using the head-mounted displays. Details are shown in Appendix E.

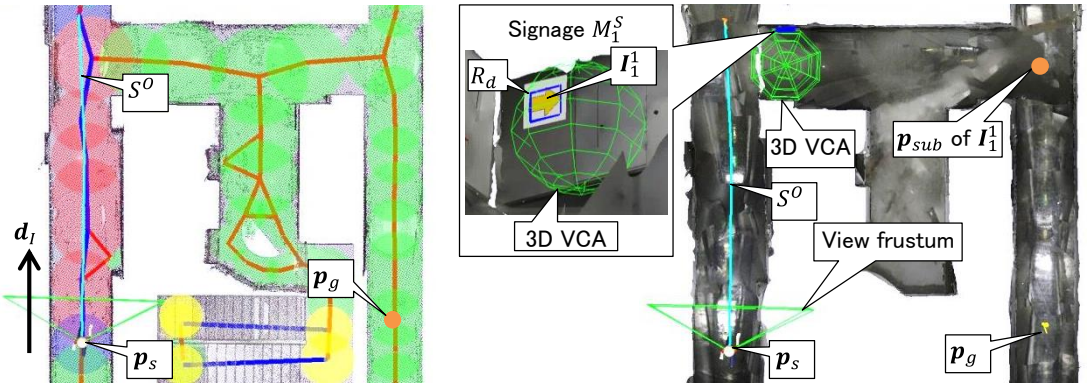

(a) Simulation setting (rendered with point clouds-based as-is environment model)

(b) Simulation setting (rendered with textured as-is environment model)

Fig. 5.17 Ease of wayfinding evaluation in one-floor indoor environment with one signage

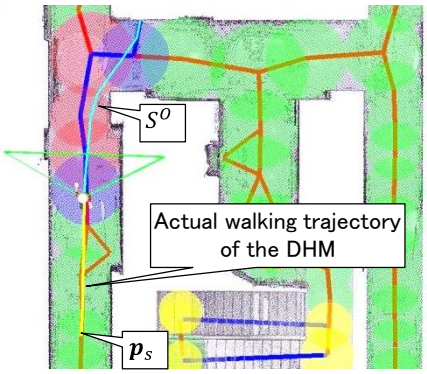

(c) Walking toward signage M_1^S (Wayfinding state Sw2)

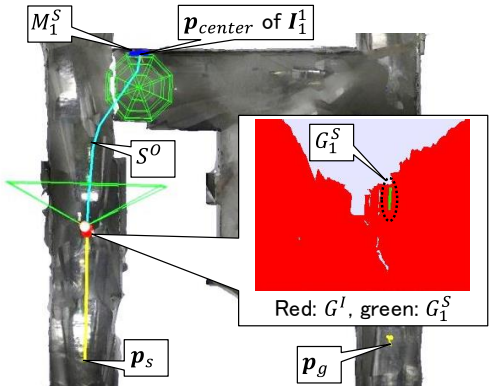

(d) Walking toward signage M_1^S (Wayfinding state Sw2)

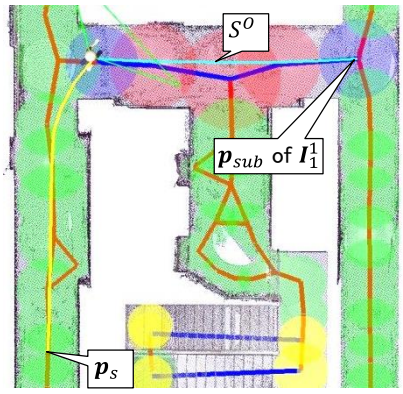

(e) Walking toward subgoal position p_{sub} of I_1^1 (Wayfinding state Sw3)

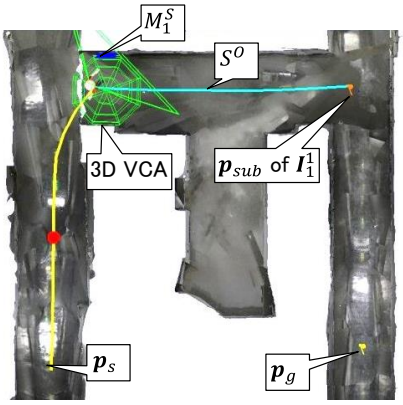

(f) Walking toward subgoal position p_{sub} of I_1^1 (Wayfinding state Sw3)

(g) Getting lost (Wayfinding state Sw4)

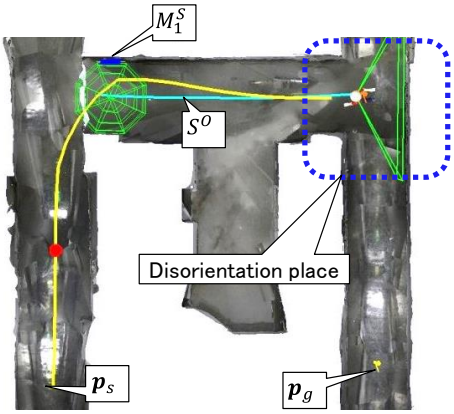

(h) Getting lost (Wayfinding state Sw4)

Fig. 5.17 Ease of wayfinding evaluation in one-floor indoor environment with one signage (cont.)

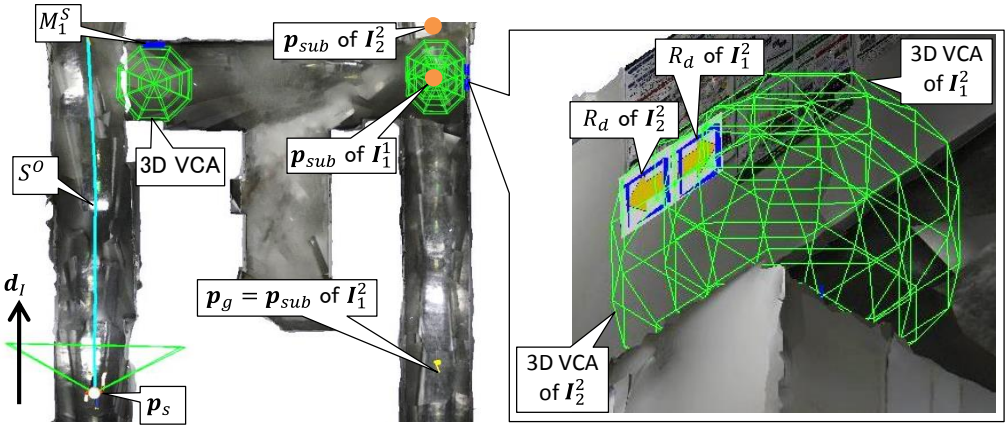

(a) Simulation setting

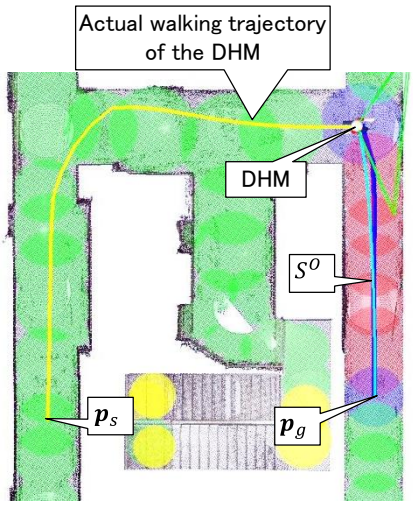

(b) Walking toward subgoal position $\boldsymbol{p}_{sub}$ of $\boldsymbol{I}_1^2$ (Wayfinding state S_w3)

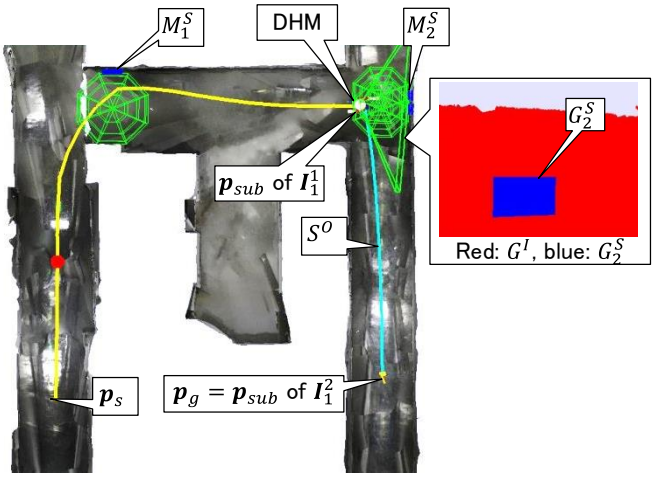

(c) Walking toward subgoal position $\boldsymbol{p}_{sub}$ of $\boldsymbol{I}_1^2$ (Wayfinding state S_w3)

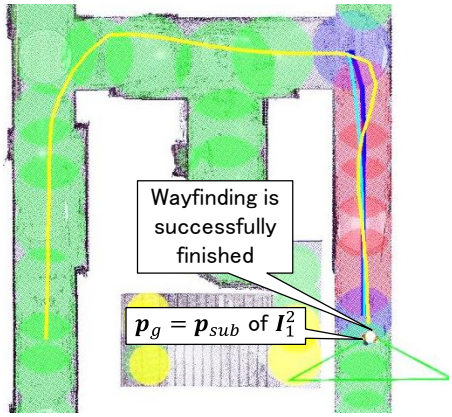

(d) Success (Wayfinding state S_w6)

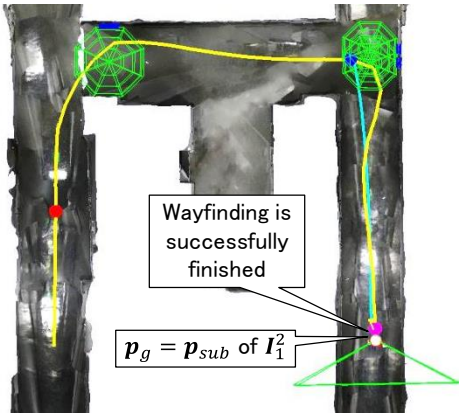

(e) Success (Wayfinding state S_w6)

Fig. 5.18 Ease of wayfinding evaluation in one-floor indoor environment with new signage

In contrast, in Fig. 5.18, one signage M_2^S consisting of two signage information $\boldsymbol{I}_1^2$ and $\boldsymbol{I}_2^2$ and its geometry G_1^S was further added to the environment model. The angular separation φ of $\boldsymbol{I}_1^2$ and $\boldsymbol{I}_2^2$ were set at 10 deg, and $\boldsymbol{I}_1^2$ indicates the goal position $\boldsymbol{p}_g$ as its subgoal position $\boldsymbol{p}_{sub}$. As shown in Fig. 5.18 (a), the start position $\boldsymbol{p}_s$, goal position $\boldsymbol{p}_g$, and initial walking direction $\boldsymbol{d}_I$ were specified as same as those in Fig. 5.17.

As shown in Figs. 5.18 (b) and (c), the DHM took the same wayfinding behavior as the simulation shown in Fig. 5.17 until arriving at the subgoal position $\boldsymbol{p}_{sub}$ of $\boldsymbol{I}_1^1$. However, after that, in contrast to the simulation results in Fig. 5.17, the DHM found a new visible signage M_2^S, and recognized both $\boldsymbol{I}_1^2$ and $\boldsymbol{I}_2^2$. After that, the DHM automatically selected the signage information $\boldsymbol{I}_1^2$ whose $\boldsymbol{p}_{des}$ corresponds to the DHM's goal position $\boldsymbol{p}_g$, i.e., $\boldsymbol{p}_g = \boldsymbol{p}_{des}$. Consequently, the DHM set to walk to $\boldsymbol{p}_{sub}$ of $\boldsymbol{I}_1^2$, and the DHM could finally arrive at the given goal position $\boldsymbol{p}_g$. Therefore, as shown in Fig. 5.18, the ease of wayfinding could be improved by adding a new signage M_2^S around the detected disorientation place in Fig. 5.17.

Considering the wayfinding simulation results in Figs. 5.17 and 5.18, it was confirmed that the disorientation place could be detected by the proposed system, which takes account of the signage location, visibility, legibility, and continuity. In addition, it was further confirmed that the effect of a rearranged signage could be immediately evaluated in a simple indoor environment in the case of a simple wayfinding task by the proposed simulation.

5.6.2.2 Results of ease of wayfinding evaluation in two-story indoor environment

We performed the vision-based wayfinding simulation with a realistic wayfinding task in the as-is environment model of the two-story indoor environment, which was more complex than the environment in 5.6.2.1. Fig. 5.19 shows the signage location and user-specified wayfinding evaluation conditions in the two-story as-is environment model.

As shown in Fig. 5.19, three signage $M_1^S = \{\boldsymbol{I}_1^1, G_1^S\}$, $M_2^S = \{\boldsymbol{I}_1^2, G_2^S\}$, and $M_3^S = \{\boldsymbol{I}_1^3, G_3^S\}$ were added into G^I, which are different from the signage used in 5.6.2.1. The signage geometries G_1^S, G_2^S, and G_3^S were created by 3D CAD software. The apparent angular separations φ of $\boldsymbol{I}_1^1$, $\boldsymbol{I}_1^2$, and $\boldsymbol{I}_1^3$ are set at 2.70 deg based on an actual signage legibility measurement experiment.

Fig. 5.20 shows the wayfinding simulation results in the two-story as-is environment model. In the figure, yellow, cyan, blue, and red lines represent the actual walking trajectory of the DHM, walking trajectory S^O generated in motion planning process, graph edges of selected walking path V^P, and graph edges of the navigation graph G_N, respectively. In addition, frustum rendered by green lines and green cylinders represent a view frustum of the DHM, and graph nodes of G_N, respectively.

As shown in Figs. 5.20 (a) and (b), when the simulation is performed, the DHM set to walking in the user-specified initial walking direction $\boldsymbol{d}_I$ from $\boldsymbol{p}_s$. Then, as shown in Figs. 5.20 (c) and (d), when M_1^S became visible, the DHM was set to walk to the center position $\boldsymbol{p}_{center}$ of $\boldsymbol{I}_1^1$. After that, as shown in Figs. 5.20 (e) and (f), when $\boldsymbol{I}_1^1$ became legible, the DHM was set to walk to the subgoal position $\boldsymbol{p}_{sub}$ of $\boldsymbol{I}_1^1$. Consequently, as shown in Figs. 5.20 (g) and (h), the DHM arrived at $\boldsymbol{p}_{sub}$ of $\boldsymbol{I}_1^1$ on the second-floor by ascending the caracole. Then, as shown in Figs. 5.20 (i) and (j), the DHM was set to walk to $\boldsymbol{p}_{center}$ of $\boldsymbol{I}_1^2$, since M_2^S becomes visible. As shown in Figs. 5.20 (k) and (l), after $\boldsymbol{I}_1^2$ becomes legible, the DHM was set to walk to $\boldsymbol{p}_{sub}$ of $\boldsymbol{I}_1^2$. However, as shown in Figs. 5.20 (m) and (n), when the DHM reached $\boldsymbol{p}_{sub}$ of $\boldsymbol{I}_1^2$, the state of the DHM was changed to "(Sw4) Getting lost", since the DHM could not find new visible signage to arrive at $\boldsymbol{p}_g$, during the state "(Sw5) Looking around". As a result, this place was detected as a disorientation place, so the user has to propose rearranged signage plans around the place.

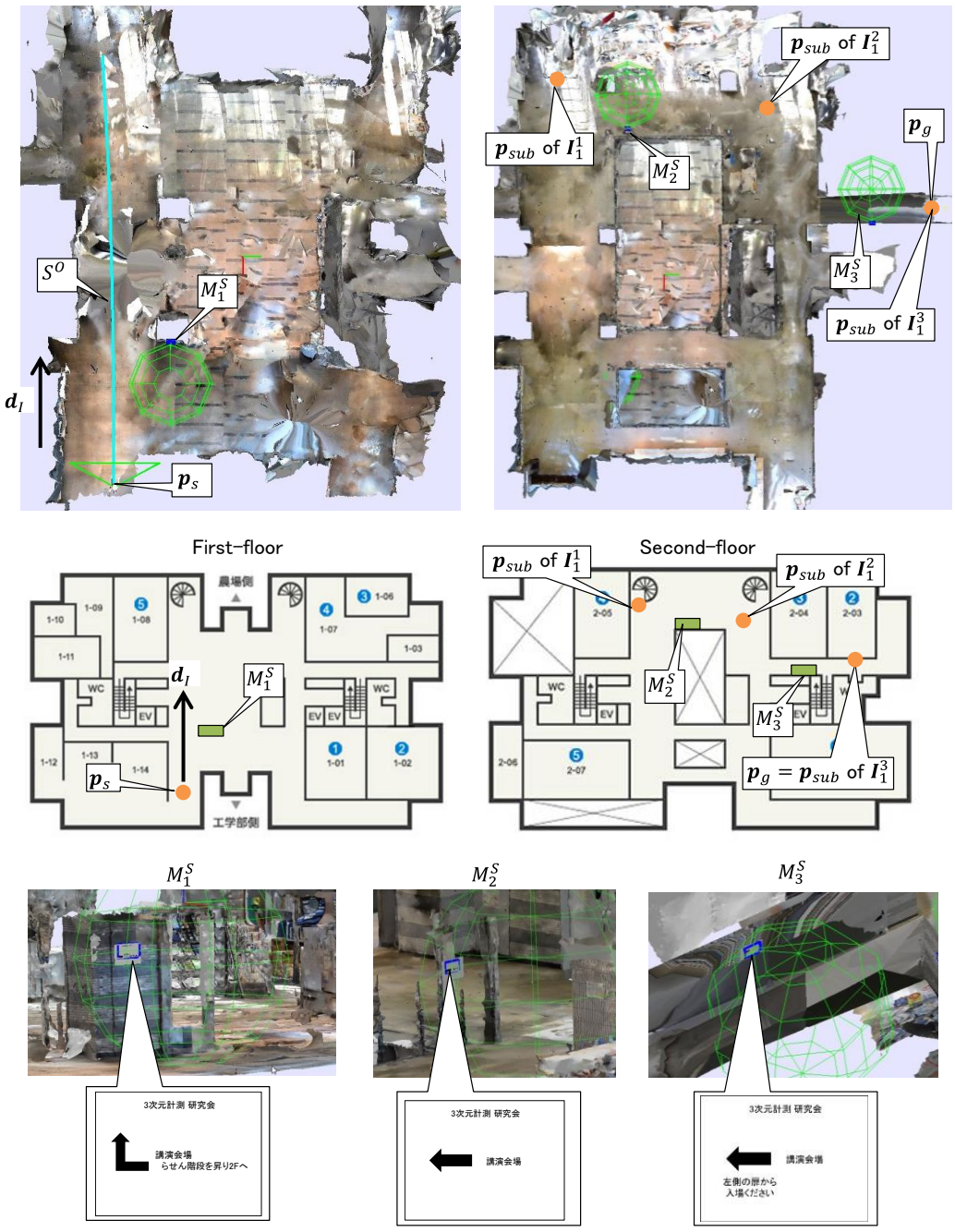

Fig. 5.19 Signage locations and wayfinding evaluation conditions in two-story as-is environment model

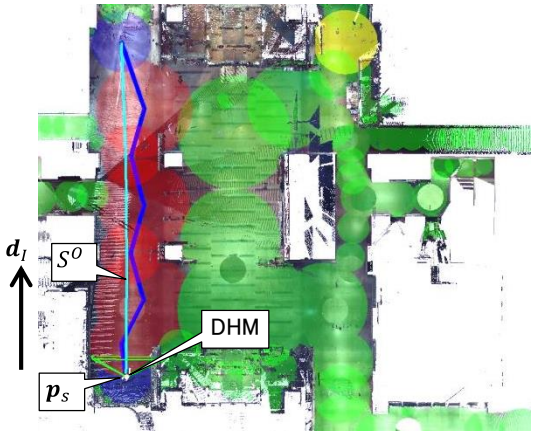

(a) Initial walking (wayfinding state Sw1) (rendered with point clouds-based as-is environment model)

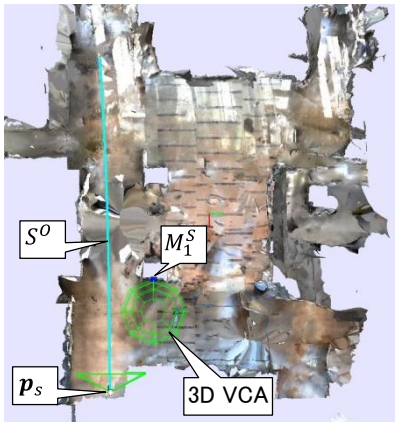

(b) Initial walking (wayfinding state Sw1) (rendered with textured as-is environment model)

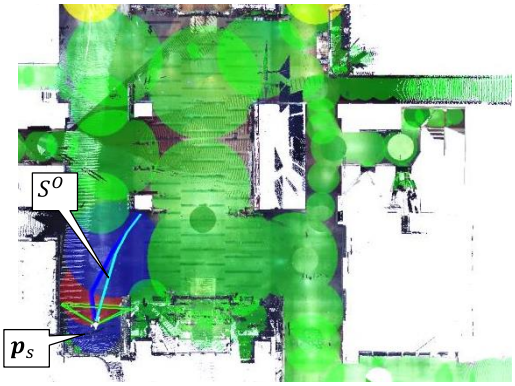

(c) Walking toward signage M_1^S (wayfinding state Sw2)

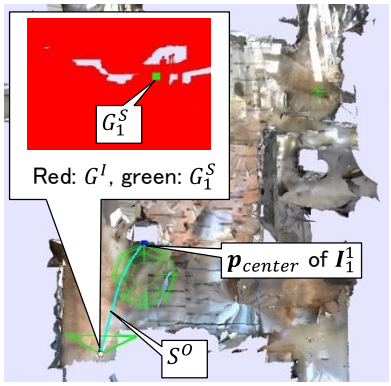

(d) Walking toward signage M_1^S (wayfinding state Sw2)

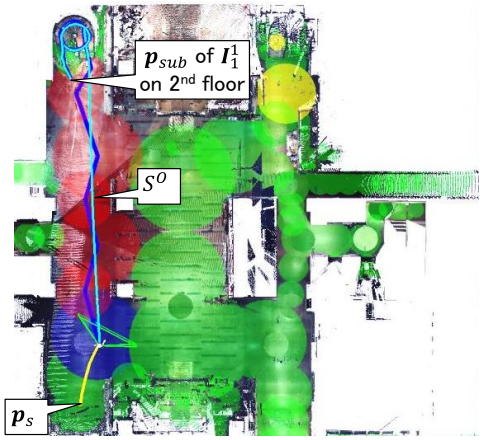

(e) Walking toward subgoal position $p_{sub}$of I_1^1 (Wayfinding state Sw3)

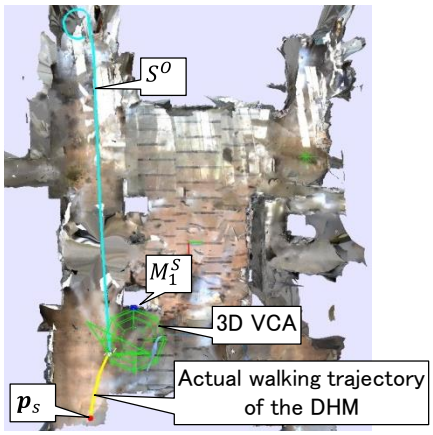

(f) Walking toward subgoal position p_{sub} of I_1^1 (Wayfinding state Sw3)

Fig. 5.20 Ease of wayfinding evaluation in two-story indoor environment with three signage

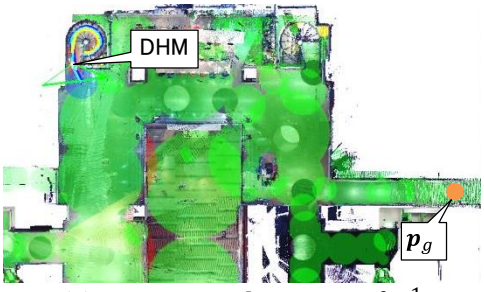

(g) DHM arrived at p_{sub} of I_1^1

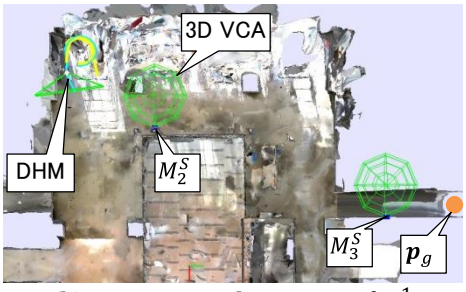

(h) DHM arrived at p_{sub} of I_1^1

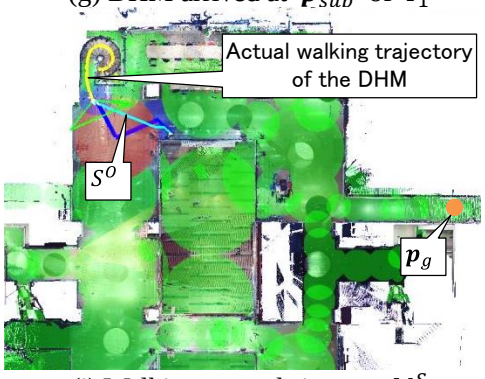

(i) Walking toward signage M_2^S (wayfinding state Sw2)

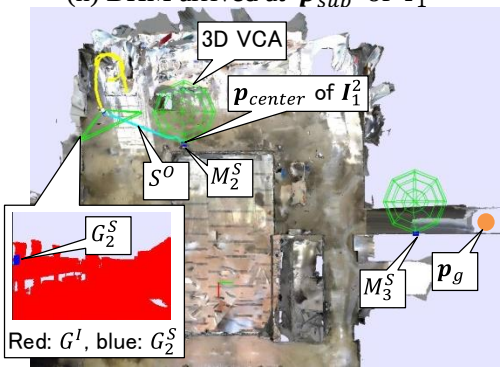

(j) Walking toward signage M_2^S (wayfinding state Sw2)

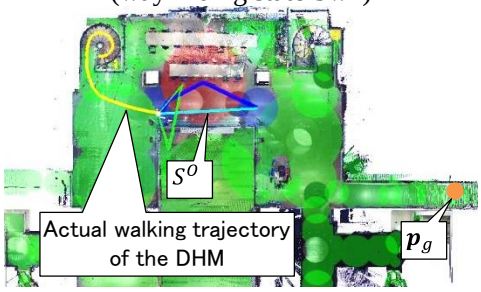

(k) Walking toward subgoal position p_{sub} of I_1^2 (Wayfinding state Sw3)

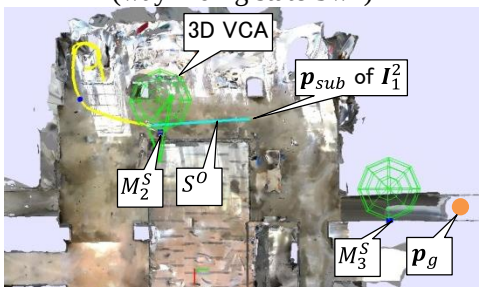

(l) Walking toward subgoal position p_{sub} of I_1^2 (Wayfinding state Sw3)

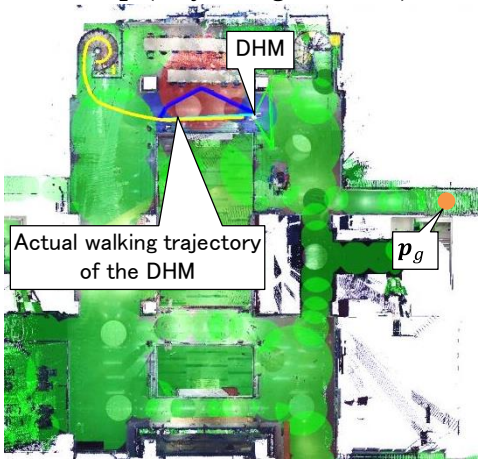

(m) Getting lost (Wayfinding state Sw4)

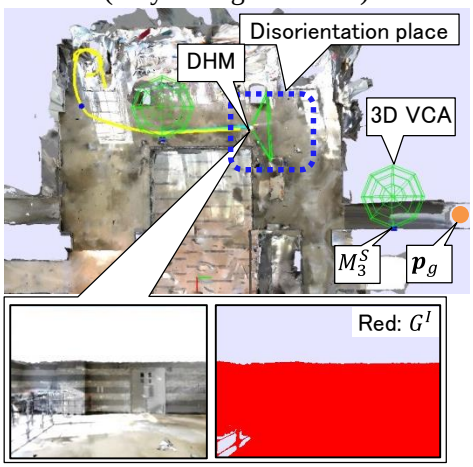

(n) Getting lost (Wayfinding state Sw4)

Fig. 5.20 Ease of wayfinding evaluation in two-story indoor environment with three signage (cont.)

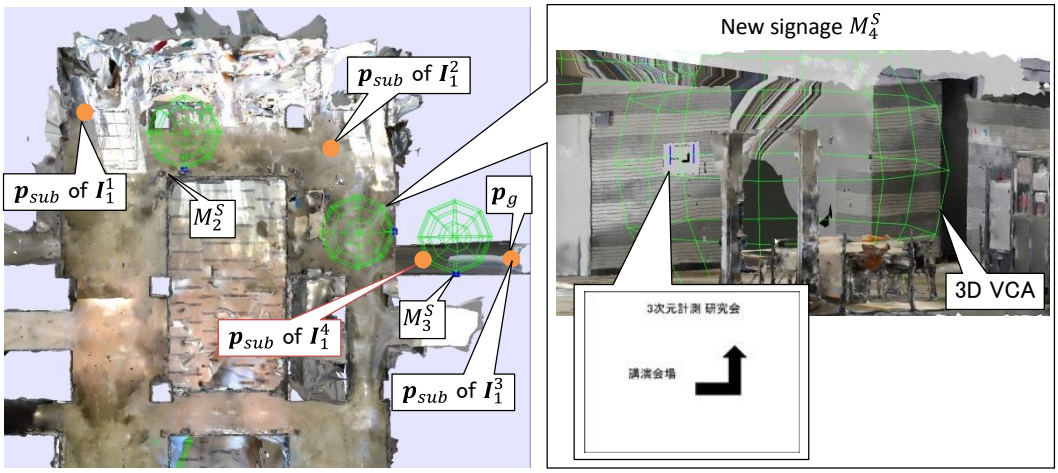

Fig. 5.21 Adding a new signage into two-story as-is environment model

In contrast, in Fig. 5.21, one signage M_4^S is further added around the detected disorientation place. The φ of I_1^4 was set at 2.70 deg. Fig. 5.22 shows the wayfinding simulation results in two-story as-is environment models with new signage M_4^S, where the start position p_s, goal position p_g, and initial walking direction d_I are specified as same as those in Fig. 5.20.

As shown in Figs. 5.22 (a) and (b), the DHM took the same wayfinding behavior as the simulation shown in Fig. 5.20 until arriving at the subgoal position p_{sub} of I_1^2. However, after that, in contrast to the simulation results in Fig. 5.20, the DHM found new visible signage M_4^S, and was set to walk to p_{center} of I_1^4. Then, as shown in Figs. 5.22 (c) and (d), when I_1^4 became legible, the DHM was set to walk to p_{sub} of I_1^4. After that, when the DHM arrived at p_{sub} of I_1^4, M_3^S and I_1^3 become visible and legible at the same time, respectively. In consequence, as shown in Figs. 5.22 (e) and (f), the DHM was set to walk to p_{sub} of I_1^3, and the DHM could arrive at the goal position p_g finally. As shown in Fig. 5.22, the ease of wayfinding could be improved by adding a new signage M_4^S around the detected disorientation place.

Considering the wayfinding simulation results in Figs. 5.20 and 5.22, it was further confirmed that the disorientation place could be detected. In addition, it was further confirmed that the effect of the rearranged signage could be immediately evaluated by the proposed wayfinding simulation even in the complex two-story indoor environment with realistic wayfinding task.

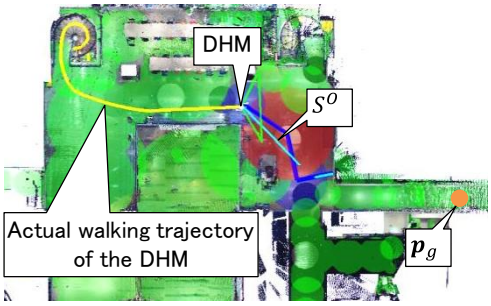

(a) Walking toward signage M_4^S (wayfinding state S_w2)

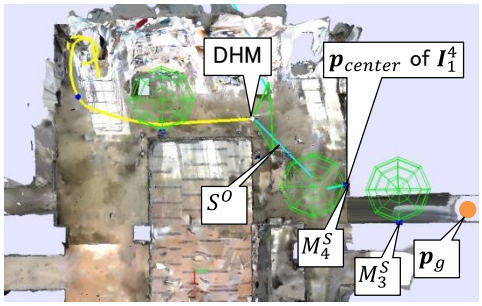

(b) Walking toward signage M_4^S (wayfinding state S_w2)

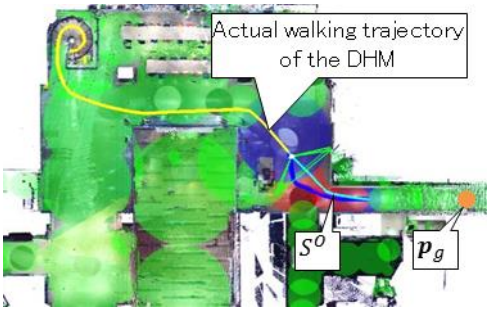

(c) Walking toward subgoal position p_{sub} of I_1^4 (Wayfinding state S_w3)

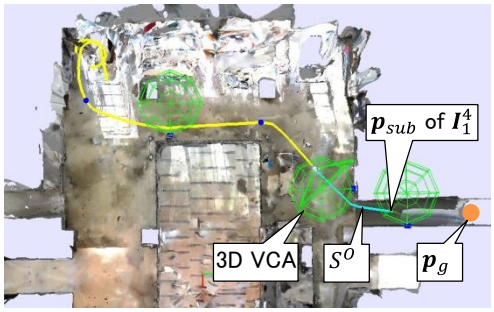

(d) Walking toward subgoal position p_{sub} of I_1^4 (Wayfinding state S_w3)

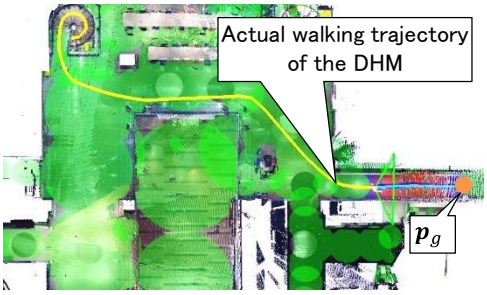

(e) Walking toward subgoal position p_{sub} of I_1^3 (Wayfinding state S_w3)

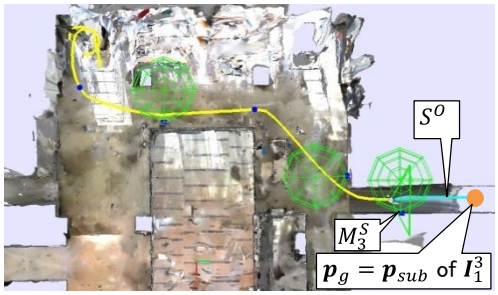

(f) Walking toward subgoal position p_{sub} of I_1^3 (Wayfinding state S_w3)

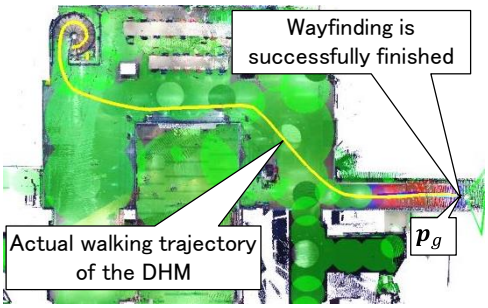

(g) Success (Wayfinding state S_w6)

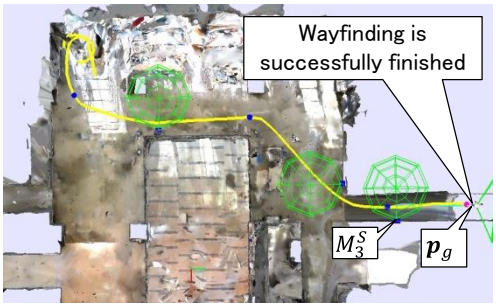

(h) Success (Wayfinding state S_w6)

Fig. 5.22 Ease of wayfinding evaluation in two-story indoor environment with new signage

On the other hand, Fig. 5.23 shows the difference in wayfinding behavior between the eye heights of the DHM. In Fig. 5.23, the signage M_1^S in Fig. 5.19 was used for the simulation. Fig. 5.23 (a) shows the wayfinding simulation results using the DHM sitting on an imitated wheelchair, whose eye height is approximately 1.16 m from the floor. Moreover, Fig. 5.23 (b) shows the simulation results using the different DHM, whose eye height is approximately 1.79 m, i.e., tall DHM.

As shown in Fig. 5.23, both DHM could find M_1^S at the beginning of the wayfinding simulation, and then set to walk to M_1^S. However, as shown in Fig. 5.23 (a), after that, the DHM sitting on the imitated wheelchair could not recognize the signage information $\boldsymbol{I}_1^1$, since its eyes could not reach the inside of 3D VCA of $\boldsymbol{I}_1^1$. Conversely, the tall DHM could recognize the signage information $\boldsymbol{I}_1^1$ by achieving the inside of 3D VCA of $\boldsymbol{I}_1^1$, and continued its wayfinding behavior. This was caused by the fact that the inside of the 3D VCA could not be reached by the DHM sitting on the imitated wheelchair whose eye height is lower than the bottom of the 3D VCA. This showed the effectiveness of the 3D VCA in the wayfinding simulation. Therefore, it was confirmed that the proposed wayfinding simulation using the 3D VCA could clarify the difference in wayfinding behaviors between the different eye heights such as between tall adults and small children or people in wheelchair.

Note that the DHM sitting on the imitated wheelchair was used only for validating the effectiveness of the 3D VCA in Fig. 5.23. The sitting posture of the DHM in wheelchair, i.e., joint angles of the DHM, was manually specified. During the simulation, the wheelchair was set to move along the trajectory S^O, while contacting its wheels on the walk surface points. Note that the detailed wheelchair's movements were not simulated.

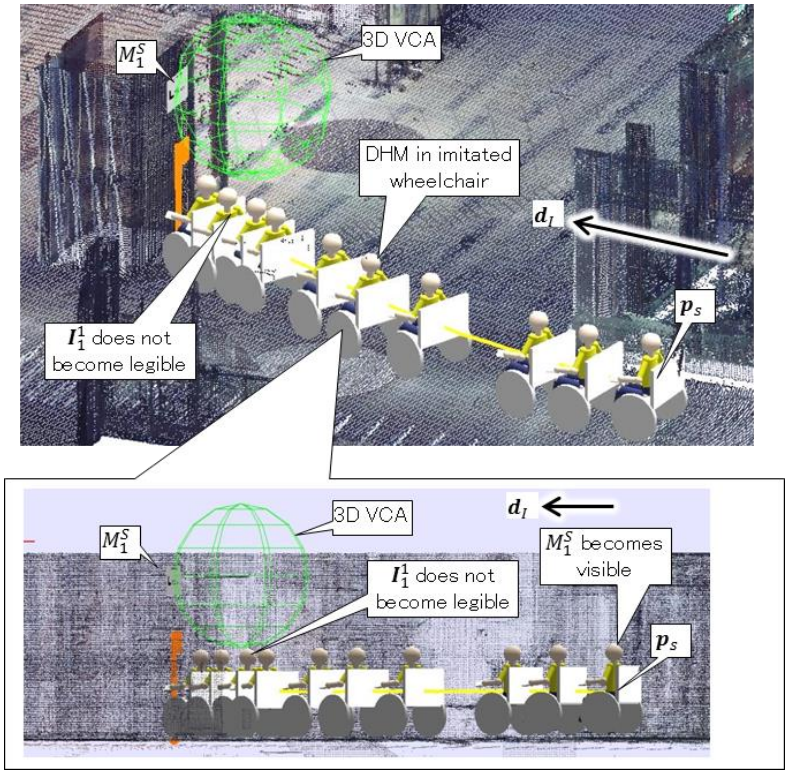

(a) Wayfinding simulation results using DHM in wheelchair

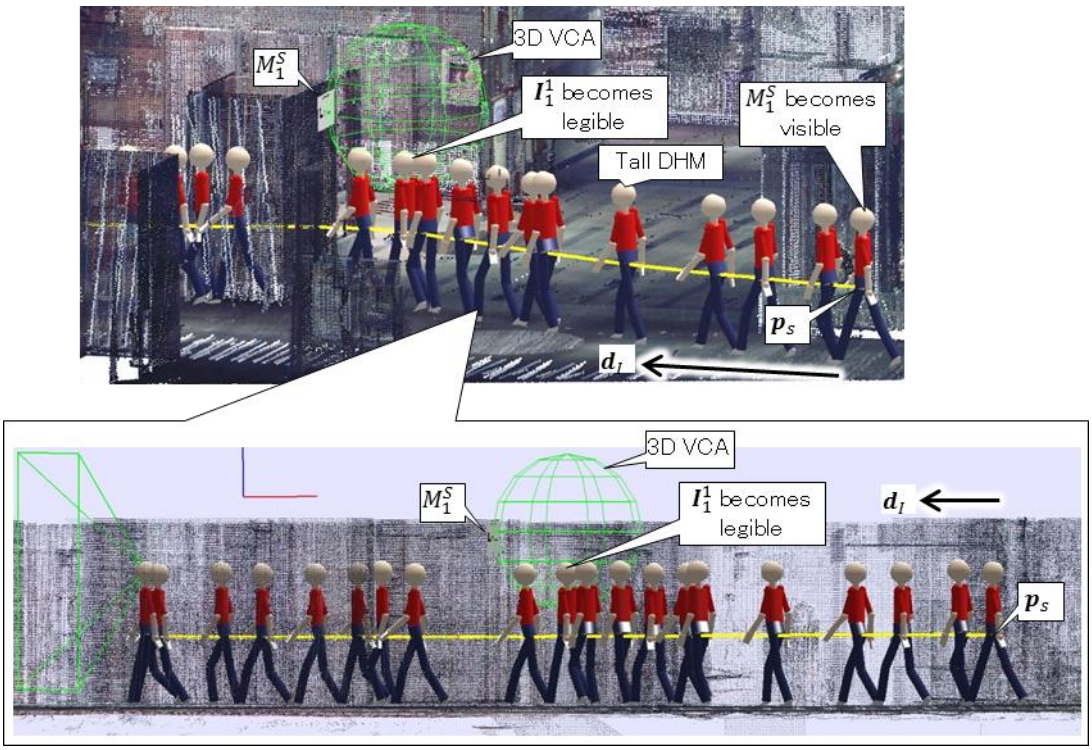

(b) Wayfinding simulation results using tall DHM

Fig. 5.23 Difference in wayfinding simulation results between eye heights

Table 5.6 Elapsed time of vision-based wayfinding simulation

(CPU: Intel Core i7 3.30GHz, RAM: 32GB, GPU: Quadro K4200)

	(a) One-floor indoor environment	(b) Two-story indoor environment
# laser-scanned points	7,058,731	346,457,626
# down-sampled point	1,043,386	9,287,847
# vertices	235,247	625,484
# faces	451,272	1,241,049
Signage perception based on imitated visual perception	15 ms	15 ms
Signage-based motion planning	less than 1 ms	16 ms
One-step walking motion generation with 100-frames interpolation	1731 ms	2975 ms

5.6.2.3 Efficiency of vision-based wayfinding simulation

Table 5.6 shows the elapsed time of vision-based wayfinding simulation of the DHM. As shown in Table 5.6, the signage perception and motion planning processes only took 31 ms at a maximum, and could be performed within a practical time. However, the execution speed of the one-step walking motion generation dropped to a lower value, especially in the two-story indoor environment. This was caused by a high-computational load for rendering the textured 3D as-is environment model using OpenGL. Therefore, the rendering method needs to be improved for real-time wayfinding simulation of the DHM in more large-scale environment.

5.6.3 Experimental validation of simulated wayfinding behavior by comparison with wayfinding behavior of real human

5.6.3.1 Overview

Finally, the ease of wayfinding simulation results were validated by a comparison of the wayfinding behavior between the DHM and real human.

In the validation, first, the wayfinding simulation of the DHM was performed in the two-story as-is environment model with two signage systems, a set of signage $M_A = \{M_1^S, M_2^S, M_3^S\}$ shown in Fig. 5.19, and a set of signage $M_B = \{M_1^S, M_2^S, M_3^S, M_4^S\}$ shown in Fig. 5.21. Then, the actual wayfinding behaviors of 3 younger participants were measured in the same environment with a signage system imitating M_A. Furthermore, the wayfinding behaviors of different 3 younger participants were measured in the same environment with a signage system imitating M_B. Finally, the wayfinding simulation results of the DHM using M_A and M_B shown in Fig. 5.20 and Fig. 5.22 were compared with the measurements from the participants with M_A and M_B, respectively. Note that the same wayfinding simulation conditions, $\boldsymbol{p}_s$, $\boldsymbol{p}_g$, and $\boldsymbol{d}_I$ were used in both simulation and the experiments.

5.6.3.2 Measurement of wayfinding behavior of younger participants

The wayfinding experiment was conducted in the following steps.

(1) Signage system imitating $M_A = \{M_1^S, M_2^S, M_3^S\}$ is manually arranged in the environment.

(2) A participant is asked to stand on $\boldsymbol{p}_s$.

(3) Name of goal position, i.e. room name, was shown to the participant.

(4) The participant is asked to start the wayfinding task.

(5) When the participant arrives at the goal position $\boldsymbol{p}_g$, the experiment finishes.

(6) Steps (1)–(5) are repeated for 3 younger participants.

(7) Steps (1)–(6) are repeated with the different 3 younger participants using the signage system imitating $M_B = \{M_1^S, M_2^S, M_3^S, M_4^S\}$.

As shown in Fig. 5.24, during the step (4), the wayfinding behavior of the participant was recorded by thinking-aloud method, e.g., [O'Neill 91], where the participant was asked to walk while continuously thinking out loud. The verbal information from the participants was recorded by the handheld voice recorder. In addition, as shown in the figure, the participant's walking trajectory was also recorded as video behind the participant by the observer. Finally, the contents of the wayfinding events, such as finding a signage, were extracted from the recorded verbal information. At the same time, the locations of the wayfinding events and the walking trajectory of the participant were estimated from the video, and were mapped onto the as-is environment model. Note that the video recording and voice recording started at the same time, so both data were synchronized with same time axis. In addition, in order to inform the participants to arrive at the goal position $\boldsymbol{p}_g$, an identification signage M_5^S were placed around the goal position in the experiment. Note that the all participants are regularly using the environment, but any information about the signage location and goal position was not given to the participants before the experiment.

5.6.3.3 Comparison of wayfinding behavior between simulation and real human

Fig. 5.25 summarized the wayfinding simulation results of the DHM shown in Fig. 5.20 and Fig. 5.22. Again, the signage locations are shown in Fig. 5.25 (a). Fig. 5.25 (b) shows the wayfinding simulation results in the first-floor of the two-story as-is environment model using the signage system M_A or M_B. Note that the simulation result in the first-floor using M_A is completely same with that using M_B, since the arranged signage system, i.e., M_1^S, is identical in the first-floor in

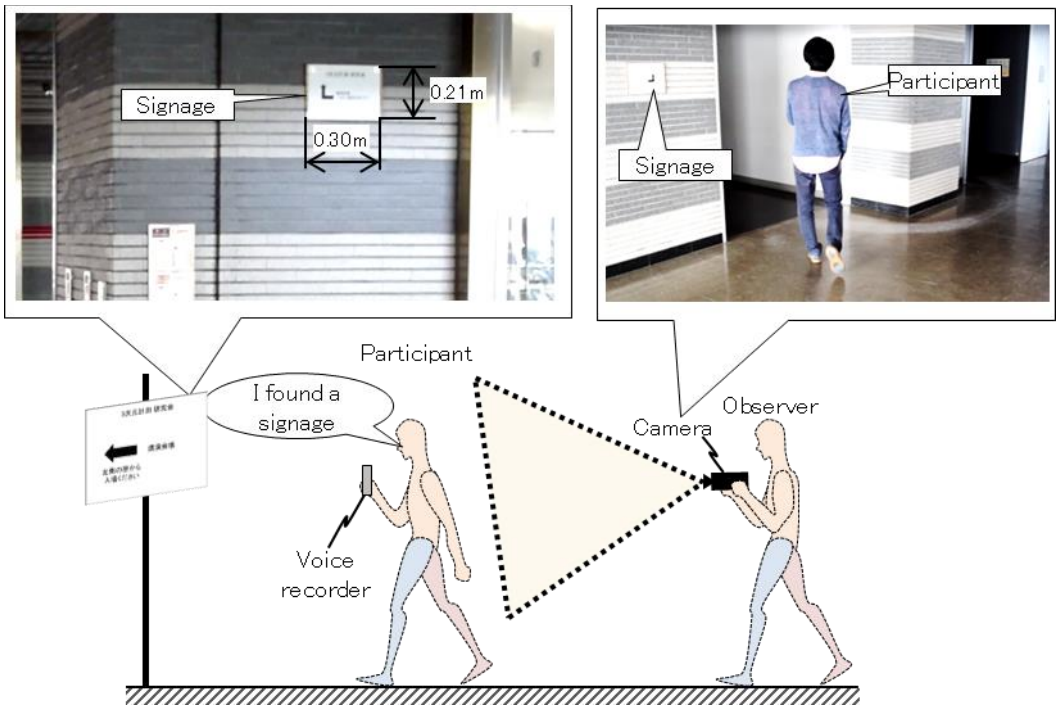

Fig. 5.24 Measurement of wayfinding behavior of younger participant

both cases. Figs. 5.25 (c) and (d) show the wayfinding simulation results in the second-floor using M_A and M_B, respectively. As shown in Figs. 5.25 (b) and (c), in the case of using M_A, the wayfinding simulation of the DHM failed on the disorientation place. In contrast, as shown in Figs. 5.25 (b) and (d), in the case of using M_B, the wayfinding simulation of the DHM successfully finished.

On the other hand, Fig. 5.26 shows the measurements of wayfinding behaviors of 3 younger participants Y1-Y3, when the signage system imitating M_A was arranged in the real environment. In the figure, each small marker indicates a point on the actual walking trajectory estimated from the recorded video data, and each trajectory was interpolated so as to pass these markers. In addition, the wayfinding event Eij was recorded at the red maker, where i and j represent the index of the ith subject and jth recorded event, respectively. Details of the wayfinding events in Fig. 5.26 are summarized in Table 5.7. In the table, "sign k" represents an signage imitating M_k^S arranged in the real environments, and "sign 5" represents the identification sign arranged around the goal position $\boldsymbol{p}_g$.

As shown in Fig. 5.26 and Table 5.7, participants Y1-Y3 could not find any new signage on a certain place, i.e., disorientation place, where the wayfinding events $E15$, $E25$, and $E35$ were recorded. At the place, the all participants lost their way due to the lack of signage. By comparing the simulation results shown in Figs. 5.25 (b) and (c) with the measurements shown in Fig. 5.26, it was observed that the disorientation place found by the experiment approximately identical to the

disorientation place detected by the simulation. Therefore, it was confirmed that the proposed ease of wayfinding evaluation system could detect the disorientation place where people actually lost their way due to the lack of signage.

On the other hand, Fig. 5.27 and Table 5.8 show the measurements of wayfinding behaviors of different 3 younger participants Y4-Y6, when the signage system imitating M_B was arranged in the real environment. As shown in Fig. 5.27, the participants Y4 and Y5 successfully finished the wayfinding task as well as the simulation results shown in Figs. 5.25 (b) and (d). In contrast, the participant Y6 could not find new signage M_2^S after arriving on the second-floor, i.e., disorientation place, where the wayfinding events $E63$ was observed. This was caused by the fact that the participant Y6 overlooked M_2^S at this disorientation place. However, as shown in Figs. 5.25 (b) and (d), this disorientation place could not be detected by the simulation. Therefore, it was confirmed that the proposed simulation could not detect the disorientation place caused by the overlooking signage. This was because the discoverability of the signage was not implemented in the signage perception algorithm in the imitated visual perception of the DHM. Fig. 5.28 shows the eyesight of the DHM around the disorientation place of Y6. As shown in the figure, the signage geometry G_2^S of M_2^S was located on the peripheral field of view and near the boundary of eyesight of the DHM. Therefore, there is a possibility that some people do not notice this signage M_2^S at the place.

On the contrary, as described in 5.5.2, in our signage visibility estimation algorithm, if any part of the signage geometry appears in the eyesight of the DHM, it is always considered as a visible signage. Therefore, in order to more accurately detect the disorientation place caused by overlooking signage, we need to improve the visibility estimation algorithm by taking account of the discoverability of the signage with the peripheral field of view. This improvement will remain as our future work.

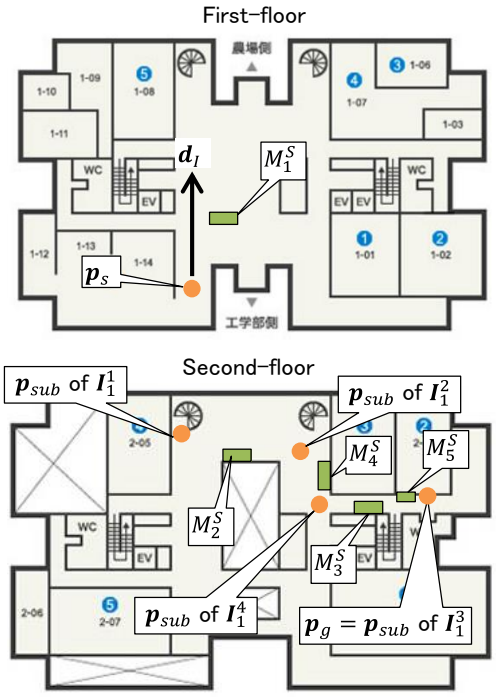

(a) Signage locations

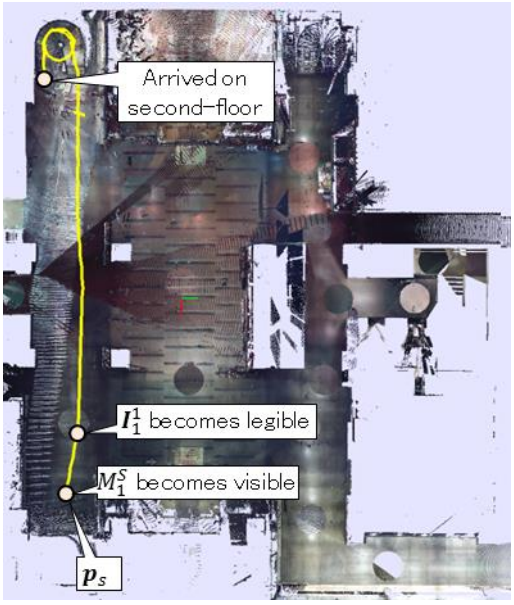

(b) Wayfinding simulation results in first-floor using M_A or M_B (trajectories on second-floor are manually erased)

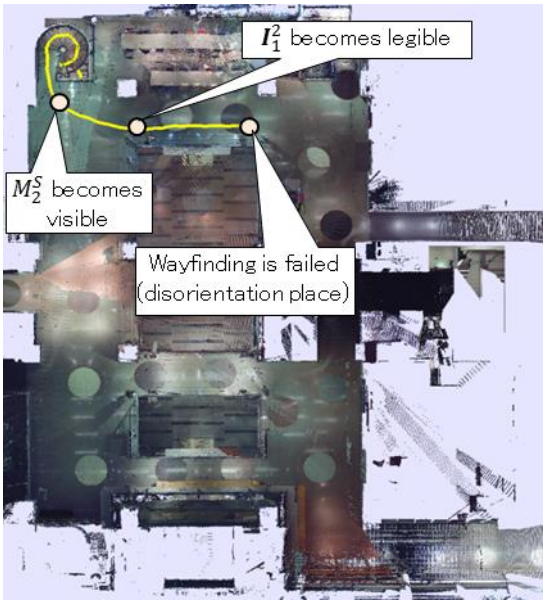

(c) Wayfinding simulation results in second-floor using M_A

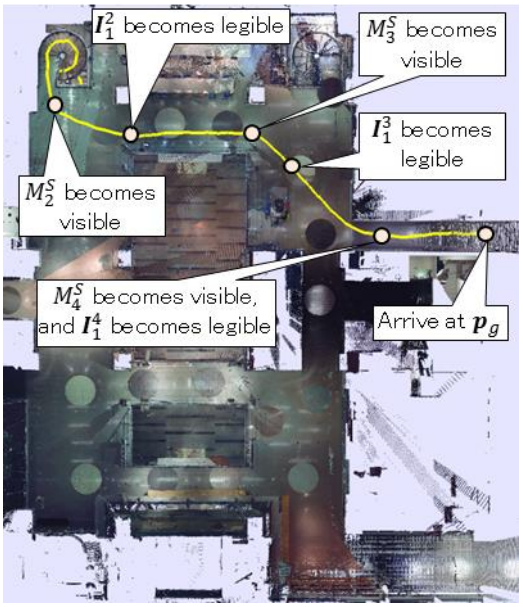

(d) Wayfinding simulation results in second-floor using M_B

Fig. 5.25 Wayfinding behavior of DHM in two-story indoor environment

(a) Behavior of participant Y1 in first-floor

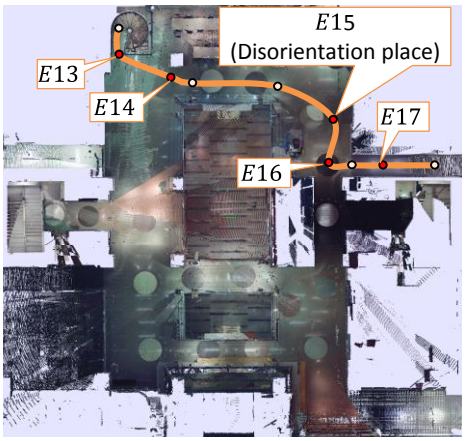

(b) Behavior of participant Y1 in second-floor

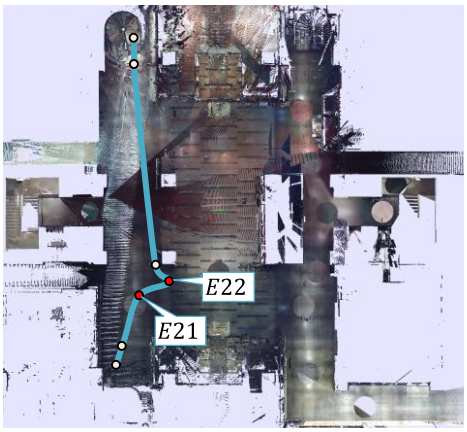

(c) Behavior of participant Y2 in first-floor

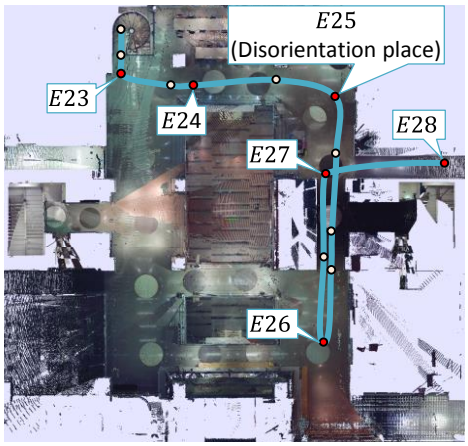

(d) Behavior of participant Y2 in second-floor

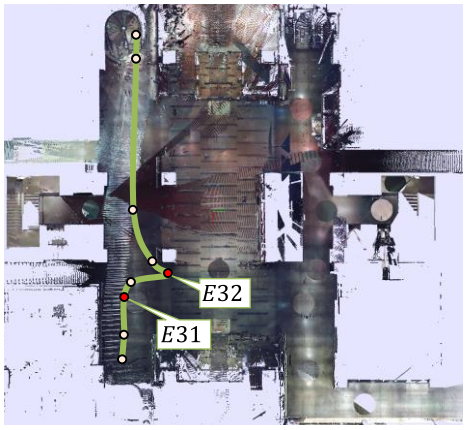

(e) Behavior of participant Y3 in first-floor

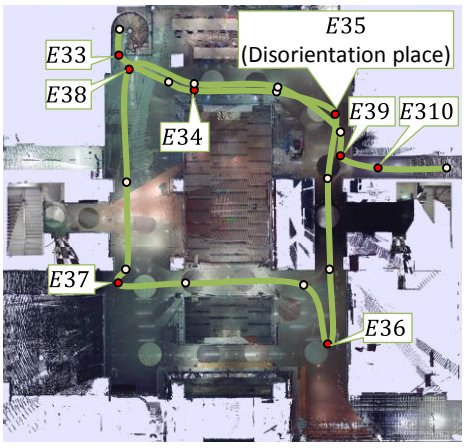

(f) Behavior of participant Y3 in second-floor

Fig. 5.26 Wayfinding behavior of participants Y1-Y3 in two-story indoor environment

(a) Behavior of participant Y4 in first-floor

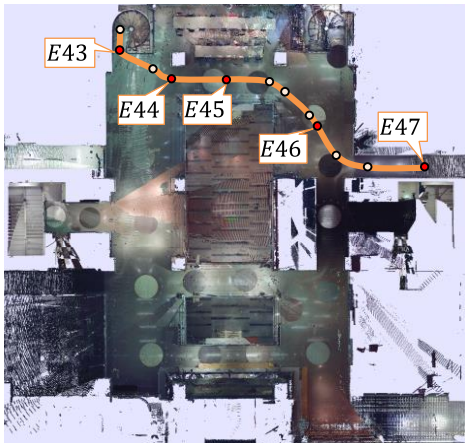

(b) Behavior of participant Y4 in second-floor

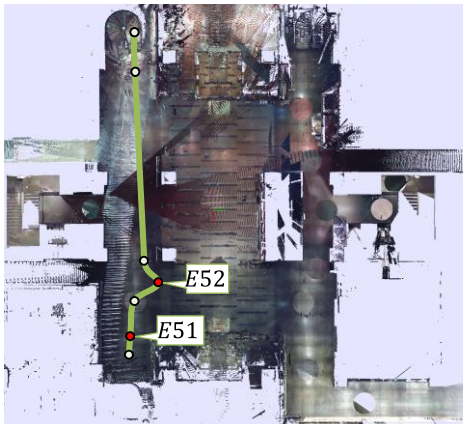

(c) Behavior of participant Y5 in first-floor

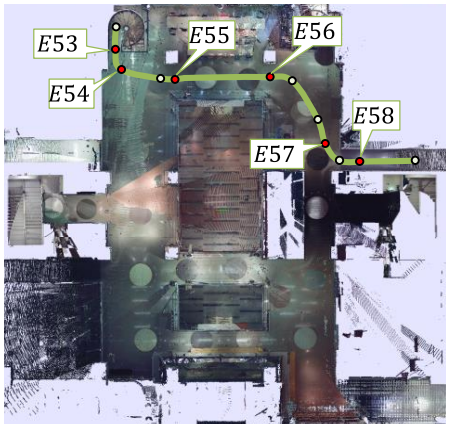

(d) Behavior of participant Y5 in second-floor

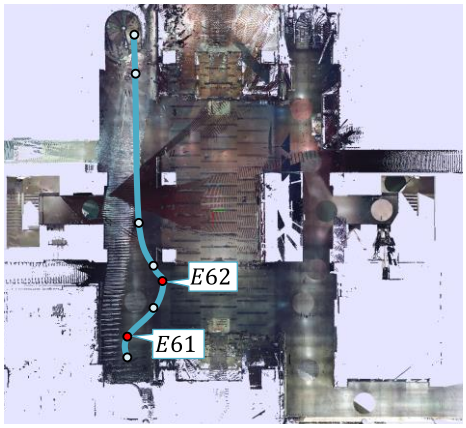

(e) Behavior of participant Y6 in first-floor

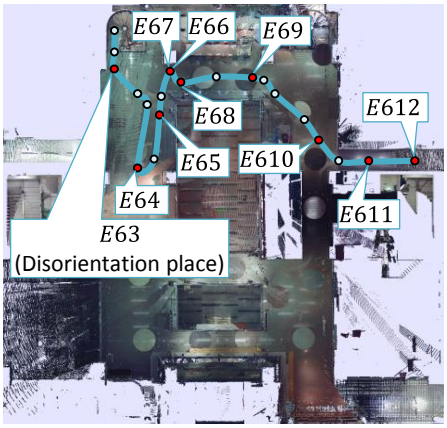

(f) Behavior of participant Y6 in second-floor

Fig. 5.27 Wayfinding behavior of participants Y4-Y6 in two-story indoor environment

Table 5.7 Wayfinding events of participants Y1-Y3

Participants	Events	Details
Y1	$E11$	Sign 1 becomes visible
	$E12$	Sign 1 becomes legible
	$E13$	Sign 2 becomes visible
	$E14$	Sign 2 becomes legible
	E15	Cannot find new signage, and tentatively walk to right **(Disorientation)**
	$E16$	Sign 3 becomes visible
	$E17$	Sign 3 becomes legible, and arrive at the goal position
Y2	$E21$	Sign 1 becomes visible
	$E22$	Sign 1 becomes legible
	$E23$	Sign 2 becomes visible
	$E24$	Sign 2 becomes legible
	E25	Cannot find new signage, and tentatively walk to right **(Disorientation)**
	$E26$	Going back to the disorientation place
	$E27$	Finding the route in the right side, and walking in the route tentatively
	$E28$	Sign 5 becomes legible, and arrive at the goal position
Y3	$E31$	Sign 1 becomes visible
	$E32$	Sign 1 becomes legible
	$E33$	Sign 2 becomes visible
	$E34$	Sign 2 becomes legible
	E35	Cannot find new signage, and tentatively walk to right **(Disorientation)**
	$E36$	Cannot find new signage, and continue to walk tentatively
	$E37$	Cannot find new signage, and tentatively walk to right
	$E38$	Starting the wayfinding again from sign 2
	$E39$	Cannot find new signage again, and finding the route in the right side, and walking in the route tentatively
	$E310$	Sign 3 becomes legible, and arrive at the goal position

Table 5.8 Wayfinding events of participants Y4-Y6

Participants	Events	Details
Y4	$E41$	Sign 1 becomes visible
	$E42$	Sign 1 becomes legible
	$E43$	Sign 2 becomes visible
	$E44$	Sign 2 becomes legible
	$E45$	Sign 4 becomes visible
	$E46$	Sign 4 becomes legible
	$E47$	Sign 3 becomes legible, and arrive at the goal position
Y5	$E51$	Sign 1 becomes visible
	$E52$	Sign 1 becomes legible
	$E53$	Keeping on walking
	$E54$	Sign 2 becomes visible
	$E55$	Sign 2 becomes legible
	$E56$	Sign 4 becomes visible
	$E57$	Sign 4 becomes legible
	$E58$	Sign 3 becomes legible, and arrive at the goal position
Y6	$E61$	Sign 1 becomes visible
	$E62$	Sign 1 becomes legible
	E63	Cannot find new signage, and keeping on walking **(Disorientation)**
	$E64$	Cannot find new signage, and going back to the caracole
	$E65$	Finding a signage
	$E66$	Recognizing that the found signage is not related to the goal position
	$E67$	Sign 2 becomes visible
	$E68$	Sign 2 becomes legible
	$E69$	Sign 4 becomes visible
	$E610$	Sign 4 becomes legible
	$E611$	Sign 3 becomes legible
	$E612$	Sign 5 becomes legible, and arrive at the goal position

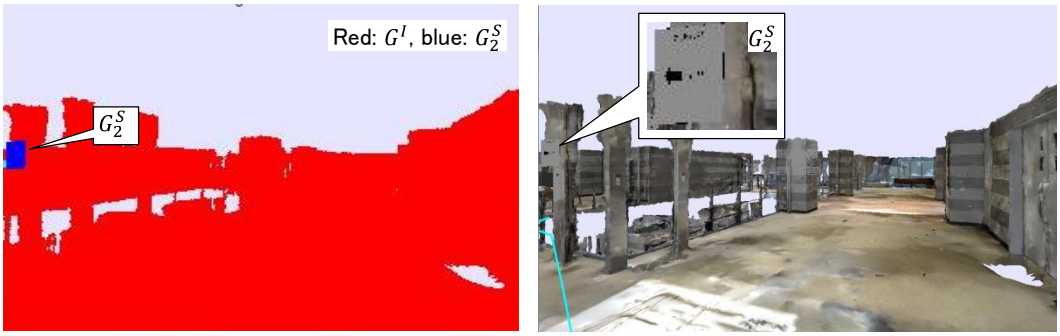

Fig. 5.28 Eyesight of the DHM at a disorientation place

5.7 Summary

In this chapter, we developed a ease of wayfinding evaluation system, which could detect the disorientation place in the 3D as-is environment models by taking account of the interaction between the wayfinding behaviors of the DHM and signage location, visibility, legibility, and continuity. The ease of wayfinding evaluation system was realized by the vision-based wayfinding simulation of the DHM in the 3D as-is environment models including both textured 3D environment models and point clouds-based 3D as-is environment models. The system made it possible to estimate the disorientation places, only by performing the wayfinding simulation in the 3D as-is environment models in consideration of signage location, visibility, legibility, and continuity.

The effectiveness of our ease of wayfinding evaluation system was tested using the 3D as-is environment models of one-floor and two-story indoor environments. The results showed that the system could detect the disorientation place in the complex indoor environment with realistic wayfinding tasks. In addition, it was confirmed that the system could immediately re-evaluate the plans of rearranged signage, only by performing the simulation again. Moreover, it was also confirmed that the proposed 3D VCA enabled the simulation to clarify the difference in wayfinding behavior between the DHMs having different eye heights.

Furthermore, our ease of wayfinding evaluation system was validated by a comparison of the wayfinding behaviors between the DHM and real human. As a result, it was confirmed that the system could detect the expected disorientation place, where the participants actually lost their way due to the lack of signage. However, it was also found that the system must be improved to consider the signage discoverability, for detecting the disorientation place caused by overlooking a signage. This improvement will remains as our future work.

Chapter 6 Conclusions and future works

The objective of this thesis is to develop a novel virtual accessibility evaluation system based on human behavior simulation, which is more accurate and reliable than previous ones, by combining a DHM with as-is environment models. For this objective, an algorithm of as-is environment modeling from laser-scanned point clouds or utilizing SfM, of autonomous walking simulation of a DHM, of tripping risk evaluation based on the autonomous walking simulation, and of ease of wayfinding evaluation based on vision-based wayfinding simulation were proposed and developed. The conclusions of this thesis were summarized as follows:

(1) An algorithm of as-is environment modeling from laser-scanned point clouds was proposed and developed. Our modeling algorithm made it possible to construct the 3D as-is environment models automatically, which are suitable for human behavior simulation aiming to the human-centered accessibility evaluation. The effectiveness, efficiency, and accuracy of the modeling algorithm were validated with the multiple point clouds of indoor, outdoor, and urban environments. As a result, it was confirmed that the modeling algorithm could efficiently construct the accurate 3D as-is environment models in fully automatic way, regardless of indoor, outdoor, and large-scale urban environments.

(2) An algorithm of autonomous walking simulation of a DHM was proposed and developed. Our walking simulation enables the DHM to autonomously walk in various as-is environments including slopes and stairs, by generating the articulated walking movements only using single reference MoCap data. The effectiveness and efficiency of the walking simulation were validated in the different point clouds-based 3D as-is environment models. As a result, it was confirmed that the DHM could walk autonomously, while adapting its strides, turning angles and footprints to different point clouds-based as-is environment models. Furthermore, the walking simulation results were valiated by a comparison of the walking motion between DHM and MoCap data of real human. As a result, it was confirmed that the proposed walking simulation algorithm could generate human-like articulated movements on flat and non-flat walking terrains based only on single reference MoCap data for flat walking.

(3) An algorithm of the tripping risk evaluation based on the autonomous walking simulation was proposed and developed. Our system could find the tripping-related environmental hazards exhaustively from the laser-scanned point clouds. In addition, the system could

evaluate the tripping risk quantitatively, by taking account of the stochastic properties of interactions between human behaviors and hazard regions. The effectiveness and efficiency of the tripping risk evaluation system was validated with the point clouds of virtual indoor and real outdoor environments. As a result, it was confirmed that the system could detect the possible tipping hazard regions from the laser-scanned point clouds, and could clarify the difference in the tripping risk among individuals. In addition, by comparing the tripping risk between the simulation and the measurements of younger participants, it was confirmed that the difference in the tripping risk between them was approximately 9 percentage point, which corresponded to approximately 10 mm difference in terms of the barrier height. This showed that the tripping risk evaluation system had a possibility of evaluating the tripping risk within the limit of accuracy of 10 mm in terms of barrier height.

(4) An algorithm of the ease of wayfinding evaluation based on vision-based wayfinding simulation was proposed and developed. Our system made it possible to detect the disorientation place, only by performing the wayfinding simulation in the 3D as-is environment models in consideration of signage location, visibility, legibility, and continuity. The effectiveness and efficiency of the ease of wayfinding evaluation system was validated using the two types of 3D as-is indoor environment models. As a result, it was confirmed that the system could detect the disorientation place in complex indoor environment with realistic wayfinding tasks. In addition, it was further confirmed that the system could immediately re-evaluate the plans of rearranged signage, only by performing the simulation again. Furthermore, the system was validated by a comparison of the wayfinding behaviors between the DHM and real human. As a result, it was confirmed that the system could detect the disorientation place, where people actually lost their way due to the lack of signage.

From these conclusions, it was concluded that the proposed virtual accessibility evaluation system could evaluate the human-centered accessibility criteria such as tripping risk and ease of wayfinding in an integrative framework, from the aspects both of physical and cognitive behaviors of various people of different ages, genders, and body dimensions, only by utilizing these simulations.

In order to enhance or enrich the current studies, the following improvements are going to be carried out:

(1) To realize the efficient autonomous walking simulation even in more large-scale as-is environment models, the algorithm of preference-based path selection needs to be improved.

(2) To validate the walking simulation in more detail, the simulated articulated movements of the DHM needs to be compared with MoCap data of various subjects including the elderly on various walking terrains.

(3) To improve the accuracy of the tripping risk evaluation system, an algorithm of estimating actual toe position of the subjects of MoCap data needs to be developed.

(4) To validate the tripping risk evaluation system in more detail, some tripping risk measurement experiments need to be conducted, such as measuring the risk from the participants with MoCap system, and measuring the risk in daily living environments for a prolonged period with more participants.

(5) To detect the disorientation place caused by overlooking signage, the vision-based wayfinding simulation algorithm needs to be improved to consider the signage discoverability.

By applying the above improvements to the proposed accessibility evaluation system, more efficient, accurate and reliable accessibility evaluation system could be realized.

Appendix

Appendix A: Estimation of rise and tread width from tread boundaries

In 2.5.5.2, for the verification of the accuracy of the as-is environment model generated from the laser-scanned point clouds, we evaluated the dimensional accuracy of the tread boundaries $B_{m,n}$. In the verification, first, the rise and tread width were estimated from the tread boundaries $B_{m,n}$ of mth stairs. Then, the actual dimensions of the rise and tread width were measured from the corresponding stairs. Finally, the estimated rise and tread width were compared with those of measurements. In this appendix, we explain an algorithm of estimating the rise and tread width from $B_{m,n}$.

(1) Estimation of tread width d_m of mth stairs

As shown in Fig. A1, the tread width $d_{m,n}$ of nth tread of mth stairs is estimated by the following equation (A.1).

$$d_{m,n} = \min_i(\max_k \hat{d}_{i,k}) \tag{A.1}$$

where $\hat{d}_{i,k}$ represents the distance between the line segment $l_{i,i+1}$ connecting the two adjacent vertices $\boldsymbol{p}_i \in B_{m,n}$ and $\boldsymbol{p}_{i+1} \in B_{m,n}$, and the other vertex $\boldsymbol{p}_k \in B_{m,n}$ $(k \neq i, k \neq i+1)$. After that, under the general assumption that each tread included in the stairs has the same dimensions, the tread width d_m of mth stairs are estimated as the median value of $d_{m,n}$ of all treads included in mth stairs.

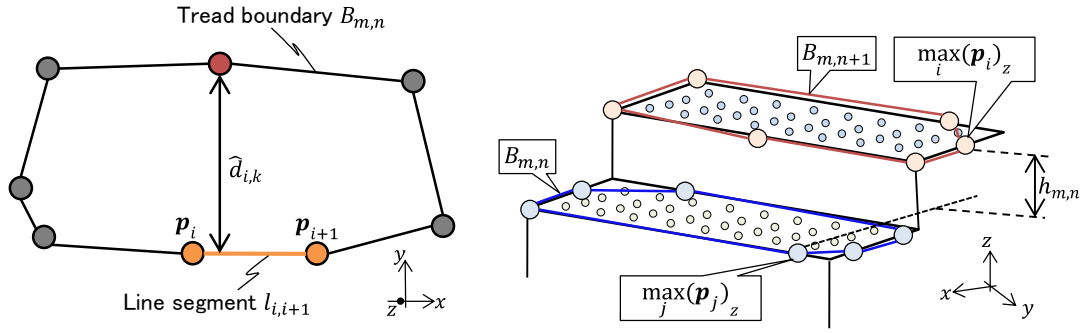

(a) Tread width estimation for a tread (b) Rise estimation for a tread

Fig. A.1 Estimation of stairs dimensions from tread boundaries

(2) Estimation of rise h_m of mth stairs

On the other hand, the rise $h_{m,n}$ between the nth tread and $(n+1)$th tread is estimated by the following equation (A.2).

$$h_{m,n} = \max_i(\boldsymbol{p}_i)_z - \max_j(\boldsymbol{p}_j)_z \qquad (\boldsymbol{p}_i \in B_{m,n+1} \text{ and } \boldsymbol{p}_j \in B_{m,n}) \qquad \text{(A.2)}$$

where $(\boldsymbol{x})_z$ represents the Z-component of the vector $\boldsymbol{x}$. After that, under the same assumption as the tread width estimation, the rise h_m of mth stairs are estimated as the median value of $h_{m,n}$ of all treads included in mth stairs.

By applying the above estimation algorithm to all stairs, we could obtain the dimensions of stairs such as the rise and tread width.

Appendix B: Approach for finding suitable weight coefficients in optimization-based motion planning

In 3.4.3, the algorithm of the optimization-based motion planning are described, where the walking trajectory of the DHM are generated on any selected walking path V^P. In the algorithm, to generate human-like walking trajectory, the weight coefficient α_{op} needs to be specified by the user. As a suitable setting, α_{op} is specified as $\alpha_{op} = 0.5$, to mimic the general human walking trajectory. This value is found by a walking experiment. In this appendix, we show an overview of this experiment, and a comparison results of the walking trajectories of the DHM with those of real human.

First, Fig. B.1 shows a comparison result of the walking trajectories of the DHM with those of 3 younger participants around corners in the one-floor indoor environment. The trajectories of the DHM is generated using the different weight coefficients, $\alpha_{op} = 0.5$, $\alpha_{op} = 0.1$, and $\alpha_{op} = 0.9$. On the other hand, the trajectories of 3 younger participants around the corner are measured by the vision-based localization system using ARToolkit [ARToolkit]. In particular, as shown in Fig. B.2, before the measurement experiment, multiple markers are attached on the walls. Then, a camera is attached on the front side of the waist of the participant. Finally, the walking trajectory of the participant is estimated based on the estimated position and orientation of each marker captured by the camera. Note that the position and orientation of each marker with respect to the world coordinate system, i.e., the coordinate system of the laser-scanned point clouds, were estimated before the experiment.

As shown in Fig. B1, when α_{op} is specified as $\alpha_{op} = 0.5$, we could obtain the walking trajectory of the DHM similar to those of the participants. Therefore, in the propose system, we use $\alpha_{op} = 0.5$ as a default setting of the weight coefficients. On the other hand, when α_{op} is specified as $\alpha_{op} = 0.9$, i.e., the contribution of the internal energy is significantly larger than the one of external energy, we could obtain the more smooth and shorter walking trajectory of the DHM. Conversely, when α_{op} is specified as $\alpha_{op} = 0.1$, i.e., the contribution of the external energy is significantly larger than the one of internal energy, we could obtain the walking trajectory of the DHM which passes on the middle of the walkway.

Therefore, it was confirmed that the walking trajectory of the DHM could be controlled by the user-specified weight coefficient α_{op} in the optimization-based motion planning. In addition, in the above experiment, $\alpha_{op} = 0.5$ is suitable setting to generate the human-like walking trajectory.

In addition to the above comparison, we further compared the walking trajectories of the DHM with the trajectory measured from 1 younger participants in different environments, two-story indoor environment. In the measurement experiment, the participant's walking trajectory was measured based on the site of the sand on the floor, which was dropped just under the participant from equipment attached on the participant's waist. As shown in Fig. B.3, the walking trajectory of the DHM generated using the coefficient $\alpha_{op} = 0.5$ was closer to the trajectory of the participant,

than those of using $\alpha_{op} = 0.1$ and $\alpha_{op} = 0.9$.

Therefore, we concluded that the $\alpha_{op} = 0.5$ was suitable default setting to generate the human-like walking trajectory.

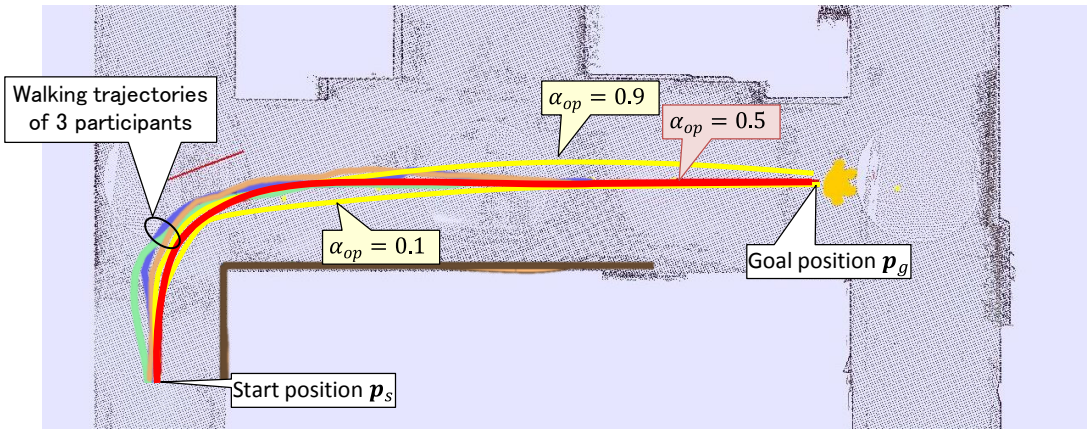

Fig. B.1 Comparison of walking trajectory between DHM and younger participants around corner

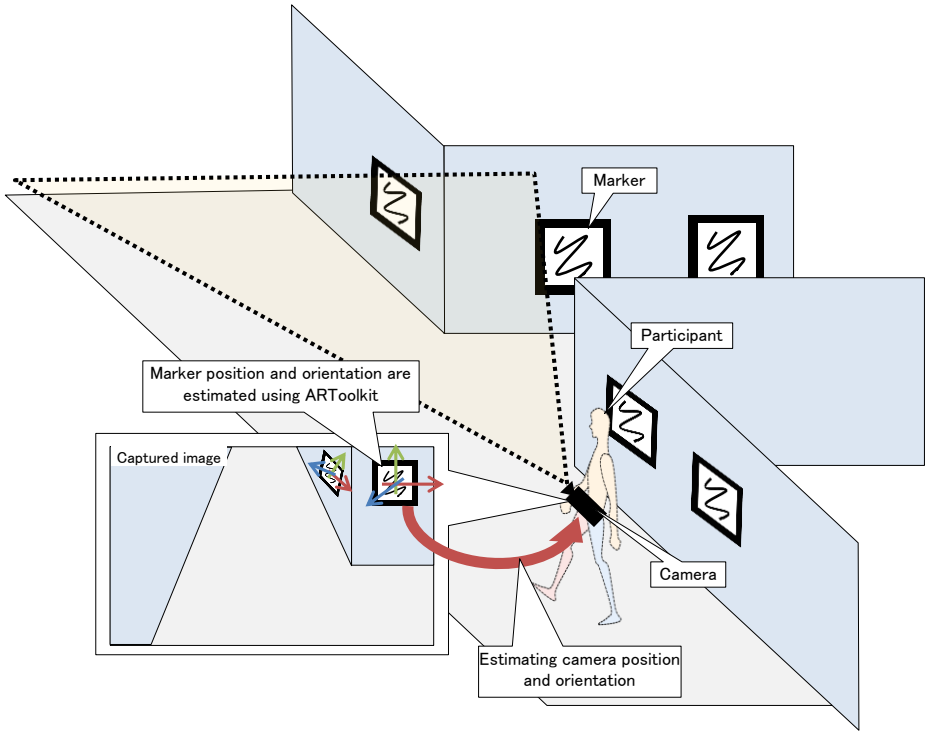

Fig. B.2 Overview of vision-based localization system

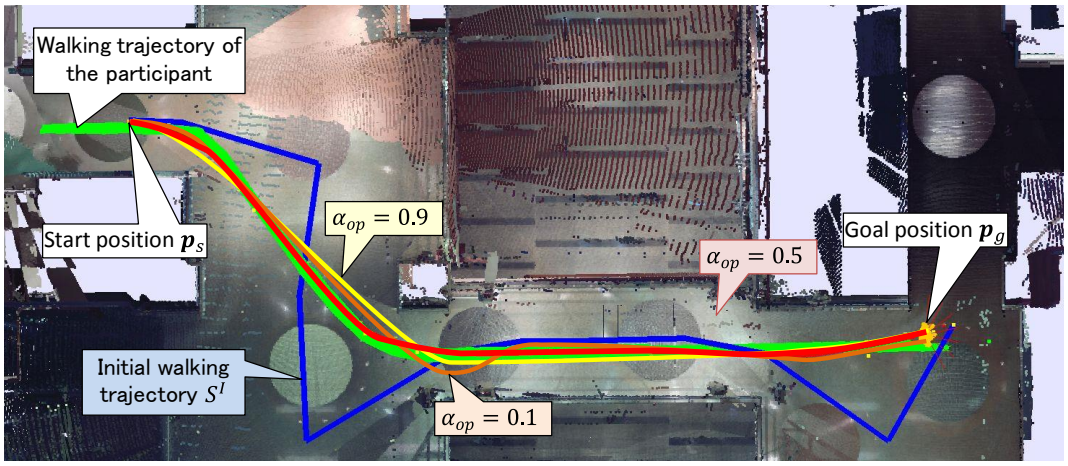

Fig. B.3 Comparison of walking trajectory between DHM and younger participant in corridors

Appendix C: Preliminary experiment for measuring human motion on various walking terrains

We conducted a preliminary experiment to discover the differences in real human walking motion between various walking terrains in cooperation with the Digital Human Research Center (DHRC) of the National Institute of Advanced Industrial Science and Technology (AIST). As shown in Fig. C.1, we acquired MoCap data of human walking motion on a flat terrain, 3-deg slope, 6-deg slope, and stairs using a MoCap system (Vicon MX system and Vicon Nexus [VICON]) for three male subjects (All subjects are 23 years old). These MoCap data were analyzed using commercial software (Visual 3D [C-MOTION]) to obtain the joint angles of the subject during walking.

After the experiment, first, we analyzed the difference in the pelvis position and ankle position of the swing leg between the one-step walking motion on flat terrains and 6-deg slope, since the motion differences between the flat walking and walking on 3-deg slope were too small. The analysis results were used for the MoCap-based adaptive walking motion generation of the DHM. In particular, these were used in the method of adapting pelvis and ankle joint positions during walking on flat terrain to those of during walking on different terrains such as slopes described in 3.4.4.4. Therefore, the purpose of the analysis is to find out the suitable function $g_P(\phi)$ and $g_A(\phi)$, which changes the pelvis and ankle positions according to the changes in the terrain height h_t per step.

Fig. C.2 shows the difference in pelvis height $p_{dk}(\phi)$ and ankle height $a_{dk}(\phi)$ for each subject k. In the figure, joint velocities $\dot{p_{dk}}(0)$ and $\dot{a_{dk}}(0)$ were estimated by applying least-squared line fitting to the corresponding data between $\phi = 0$ and $\phi = 0.1$. $\dot{p_{dk}}(1)$ and $\dot{a_{dk}}(1)$ were estimated by the same method using the corresponding data between $\phi = 0.9$ and $\phi = 1$. The estimated velocities are shown in Table C.1.

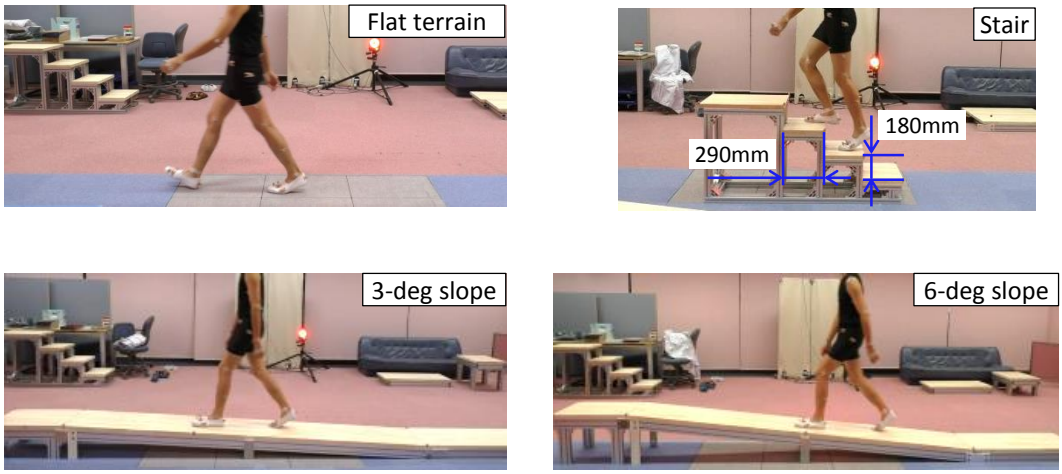

Fig. C.1 Overview of walking measurement experiment

As shown in Figs. C.2 (a), (c) and (e), the shape of curve representing $p_{dk}(\phi)$ is significantly different among the subjects. Therefore, in this study, as shown in 3.4.4.4, to reduce the difference between the DHM and various subjects, we simply assigned a liner function to $g_P(\phi)$.

On the other hand, as shown in Figs. C.2 (b), (d) and (f), the shape of curve representing $a_{dk}(\phi)$ is also different among the subjects. However, as shown in Table C.1, it was observed that $\dot{a_{dk}}(0)$ is nearby zero for all subjects. In addition, as shown in Table C.1, it was further observed that $\dot{a_{dk}}(1)$ can be approximated $a_{dk}(1)$, since $\dot{a_{dk}}(1)$ is sufficiently close to $a_{dk}(1)$. Therefore, in this study, as shown in 3.4.4.4, we assigned a cubic function to $g_A(\phi)$, with the boundary conditions $g_A(0) = 0$, $g_A(1) = h_t$, $g_A(0) = v_{A1}$, and $g_A(1) = v_{A2}$, where v_{A1} and v_{A2} are specified as $v_{A1} = 0$ and $v_{A2} = h_t$.

After that, we further analyzed the difference in the ankle position between the one-step walking motion on flat terrains and those on the stairs. The analysis results were used for the MoCap-based adaptive walking motion generation of the DHM. In particular, these were used in the method of generating ankle position trajectory in the process of foot collision avoidance on stairs in 3.4.4.6. Therefore, the purpose of the analysis is to find out the ankle height trajectory $z_A''(\phi)$ on the stairs.

Fig. C.3 shows the ankle heights during one-step walking of a subject $a_F(\phi)$ and $a_S(\phi)$ on flat terrains and the stairs, respectively. As shown in Fig. C.3, $\dot{a_S}(1)$ is sufficiently close to $\dot{a_F}(1)$. In addition, it was observed that $\dot{a_S}(0)$ is nearby zero. Therefore, in this study, as shown in 3.4.4.7, we make $z_A''(\phi)$ using the cubic spline interpolation with the boundary conditions $z_A'(0)$ and $z_A'(1)$ and velocities V_0 and V_1, where $z_A'(0)$ and $z_A'(1)$ represent the ankle heights after the adaptation, which were obtained in 3.4.4.5, and V_0 and V_1 are specified as $V_0 = 0$ and $V_1 = \dot{z_A'}(1)$ according to this analysis result.

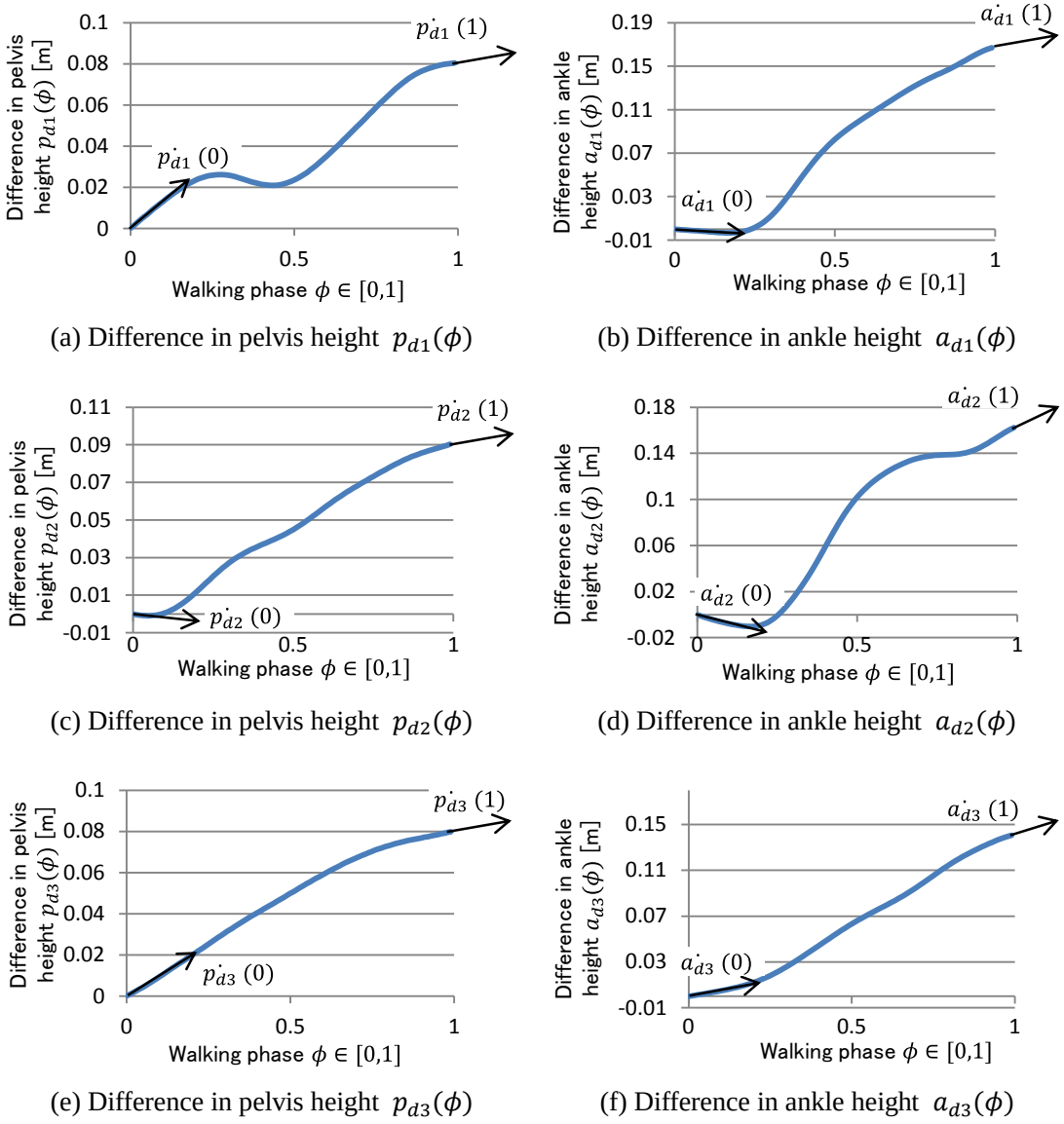

(a) Difference in pelvis height $p_{d1}(\phi)$ (b) Difference in ankle height $a_{d1}(\phi)$

(c) Difference in pelvis height $p_{d2}(\phi)$ (d) Difference in ankle height $a_{d2}(\phi)$

(e) Difference in pelvis height $p_{d3}(\phi)$ (f) Difference in ankle height $a_{d3}(\phi)$

Fig. C.2 Difference in pelvis and ankle height between walking motion on flat terrain and 6-deg slope

Table C.1 Estimated joint velocities and ankle height

	$\dot{p_{dk}}(0)$	$\dot{p_{dk}}(1)$	$\dot{a_{dk}}(0)$	$\dot{a_{dk}}(1)$	$a_{dk}(1)$
Subject 1	0.133	0.036	-0.021	0.145	0.167
Subject 2	-0.000	0.052	-0.081	0.168	0.162
Subject 3	0.091	0.033	0.048	0.112	0.141

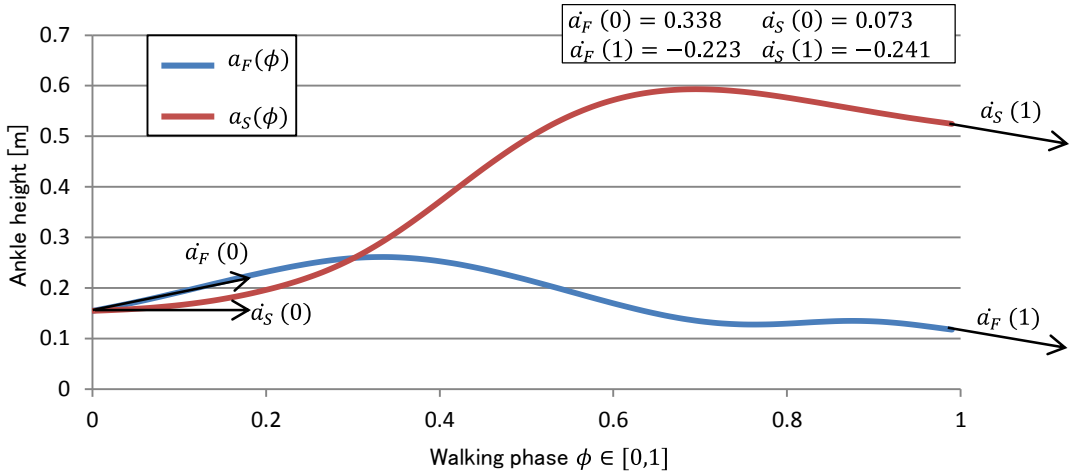

Fig. C.3 Comparison of ankle heights between walking on flat terrains and walking on stairs

Appendix D: Method of extending 2D VCA to 3D VCA

In the proposed vision-based wayfinding simulation of the DHM described in Chapter 5, the visibility catchment area (VCA) which is defined as 2D circle [Xie 07] shown in Fig. D.1 (a) is extended to 3D VCA representing 3D sphere shown in Fig. D.1 (b). This extension is realized by approximating the characteristics of human eyes in horizontal direction to those in vertical direction. In this appendix, we describe the details of this extension.

As shown in Fig. D.2 (a) and (b), when the signage is located at the same height as the eyes of the subject, the subject can recognize the signage at the point $\boldsymbol{p}_p$, where $\boldsymbol{p}_p$ is located at the intersection point of the circumference of the 2D VCA with a line l_{VCA}. As shown in Fig. D.2 (b), this means that the subject can recognized the signage in spite that the signage length CY and the apparent angular separation φ_V in the vertical direction differ from CX and φ_H in the horizontal direction, respectively. Therefore, if we assume that the characteristics of human eyes in horizontal direction as those in vertical direction, 2D VCA in the vertical plane can be defined as shown in Fig. D. 2 (c), whose radius r_{VCA} and center position $\boldsymbol{p}_{VCA}$ are the same as those in horizontal place shown in Fig. D.2 (a). Finally, we can define the 3D VCA as a sphere having these 2D VCA as its great circles.

On the other hand, Fig. D.3 shows the modulation transfer function (MTF) of human eyes in different luminance for visual stimulations of different angles. The measurements of contrast sensitivity of human eyes for visual stimulations of different spatial frequencies are shown in the MTF. As shown Fig. D.3, the MTF of human eyes has the singular dependency, in other words, the characteristics of human eyes are actually different between horizontal and vertical direction. In this study, we defined the 3D VCA by approximating the MTF for vertical visual stimulation to the horizontal one. The making actual 3D VCA reproducing the human eyes characteristics completely is addressed in our future work.

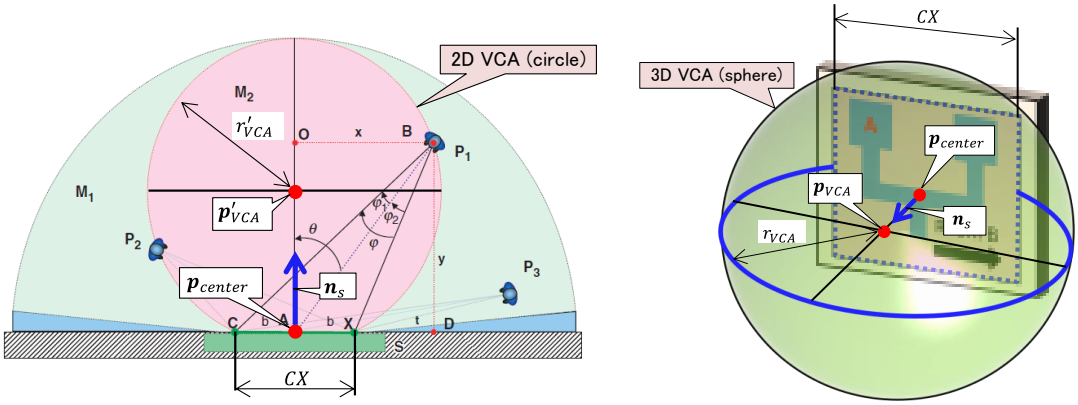

(a) Original 2D VCA [Xie 07] (b) Proposed 3D VCA

Fig. D.1 Comparison of 2D VCA with proposed 3D VCA

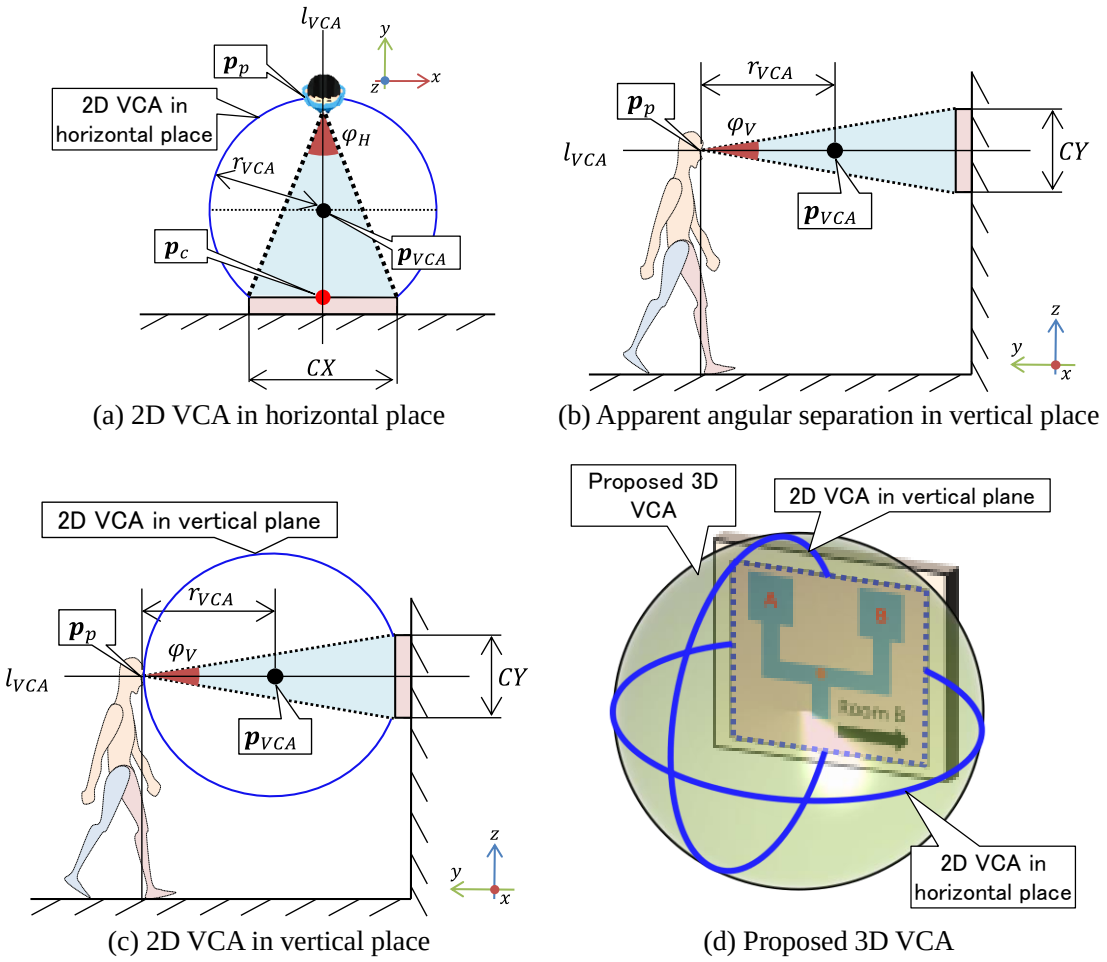

(a) 2D VCA in horizontal place

(b) Apparent angular separation in vertical place

(c) 2D VCA in vertical place

(d) Proposed 3D VCA

Fig. D.2 Extension of 2D VCA to 3D VCA

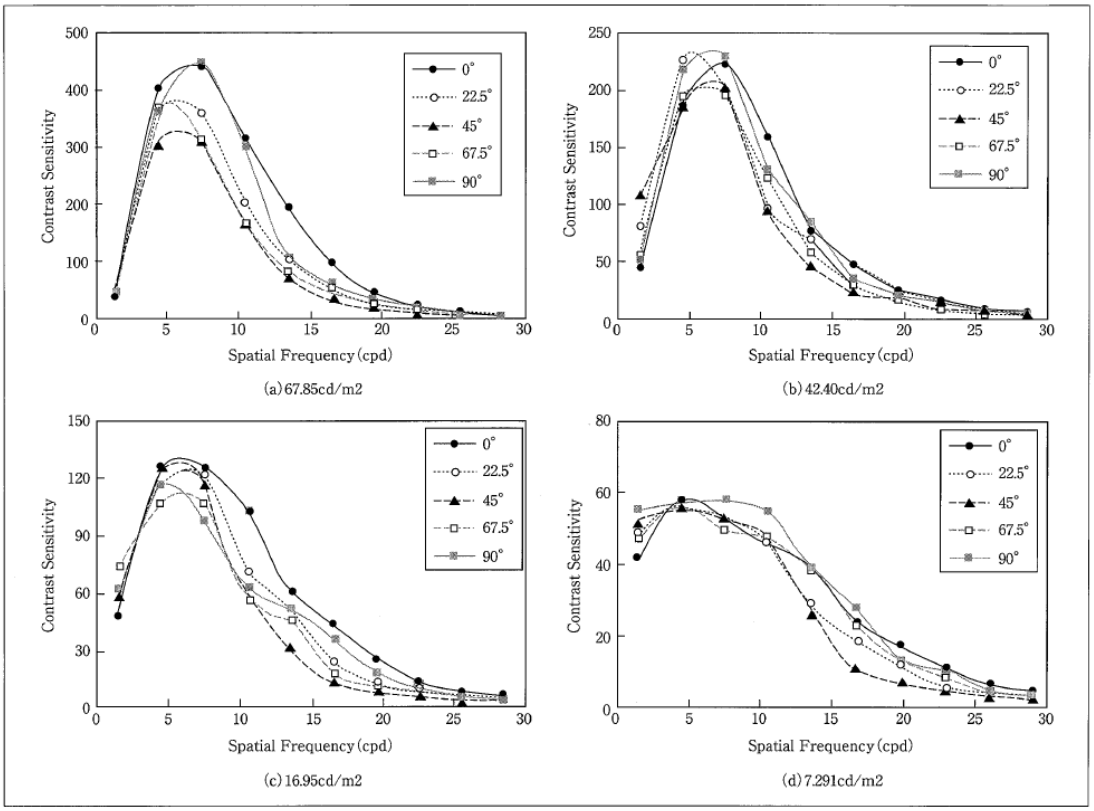

Fig. D.3 MTF of human eyes [Hirai 08]

Appendix E: Virtual eyesight simulator

In the proposed ease of wayfinding simulation of the DHM, when the disorientation place was detected by the vision-based wayfinding simulation, the new signage needs to be arranged around the detected disorientation place. Therefore, in this study, we developed a virtual eyesight simulation (VES), which enables the user to check the eyesight of the DHM virtually, during the vision-based wayfinding simulation through a head-mounted display (HMD). Visual impairment filters mimicking blurred vision and color blindness (protanopia and deuteranopia) are further applied to the HMD image. This enables the user to consider visual impairments such as aged eyes and color blindness during the rearranged signage planning.

Fig. E.1 shows an overview of the VES. As shown in Fig. E.1, the head trajectory $H^{DHM} = \{\langle \boldsymbol{p}_{head}(t)\rangle, \langle \boldsymbol{q}_{head}(t)\rangle\}$ are obtained through the wayfinding simulation of the DHM, where $\boldsymbol{p}_{head}(t)$ represents a 3D position vector representing the head position of the DHM at the discretized simulation time $t \in T$, and $\boldsymbol{q}_{head}(t)$ corresponds to a quaternion representing the orientation of the DHM head at t. T represents a set of the discretized simulation time $T = \{\Delta ti\}(i \in [0, N_F])$, where Δt and N_F represent a time interval between simulation frames, and the total number of frames in the simulation, respectively.

Then, as shown in Fig. E.1, in the VES, first, a camera model position $\boldsymbol{p}_{camera}(t')$ and its orientation $\boldsymbol{q}_{camera}(t')$ at any time $t' \in \mathbb{R}$ are interpolated by the following formulations (E.1) – (E.3).

$$\boldsymbol{p}_{camera}(t') = Lerp(\boldsymbol{p}_{head}(\Delta tk), \boldsymbol{p}_{head}(\Delta tk + \Delta t), t') \quad \text{(E.1)}$$

$$\boldsymbol{q}_{camera}(t') = Slerp(\boldsymbol{q}_{head}(\Delta tk), \boldsymbol{q}_{head}(\Delta tk + \Delta t), t') \quad \text{(E.2)}$$

$$k = \lfloor t'/\Delta t \rfloor \ (k \in \mathbb{N}) \quad \text{(E.3)}$$

where $Lerp(\boldsymbol{p}_1(t_1), \boldsymbol{p}_2(t_2), t)$ represents a linear interpolation between the 3D vectors $\boldsymbol{p}_1(t_1)$ and $\boldsymbol{p}_2(t_2)$ at t, and $Slerp(\boldsymbol{q}_1(t_1), \boldsymbol{q}_2(t_2), t)$ represents a spherical linear interpolation between the quaternions $\boldsymbol{q}_1(t_1)$ and $\boldsymbol{q}_2(t_2)$ at t. By specifying $\boldsymbol{p}_{camera}(t')$ and $\boldsymbol{q}_{camera}(t')$ using (E.1) and (E.2), the continuously rendered image along with H^{DHM} can be obtained from the discretized head trajectory H^{DHM}. Then, as shown in Fig. E.1 (A62), a visual impairment filter is applied to the rendered image of the camera model.

Finally, the user can check the eyesight of the DHM virtually during the wayfinding simulation through head-mounted display, while considering visual impairments.

In this study, we implemented the VES on the Unity game engine using Oculus Rift DK2 [Oculus] as head-mounted display. The user could view stereoscopic vision through Oculus Rift DK2. In addition, we used the visual impairment filters mimicking blurred vision and color blindness such as protanopia and deuteranopia, which are downloaded from the Unity Asset Store [Abanarua], [Gulti]. The degrees of blurred vision $D_b \in [0,1]$, protanopia $D_p \in [0,1]$, and deuteranopia $D_d \in [0,1]$ can

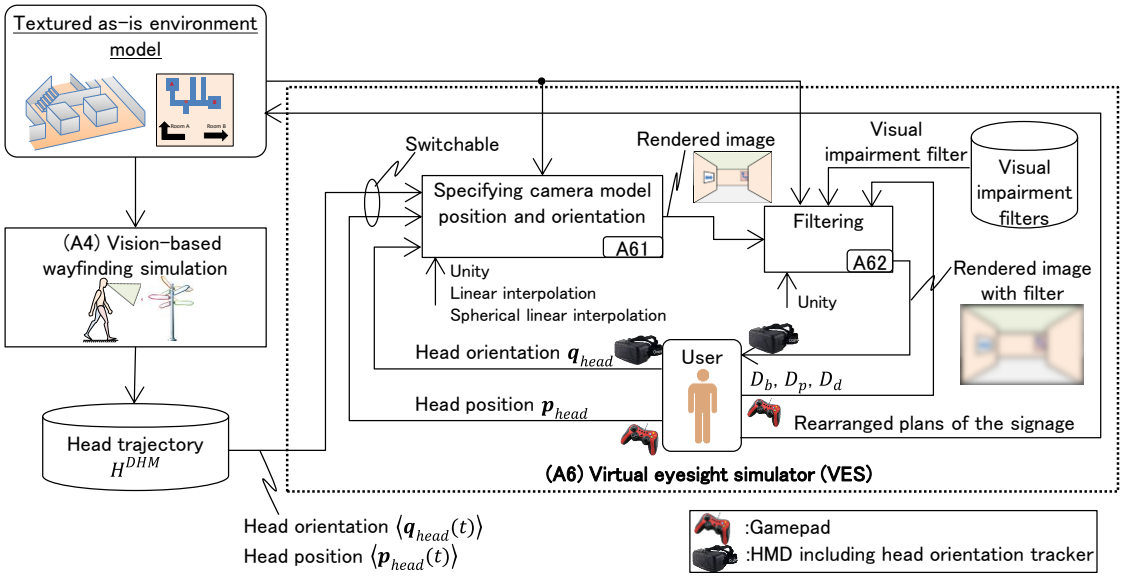

Fig. E.1 Overview of virtual eyesight simulator

be adjusted using the gamepad controller. Note that if the user wants to walk through the environment freely, the user can control the camera model by using a gamepad controller and a head orientation tracker included in Oculus Rift DK2. Using two axis of one joystick of the gamepad controller, the camera model is moved on a horizontal plane at head height of the DHM.

Fig. E.2 shows the results of the VES using visual impairment filters. Fig. E.2 (a) shows the DHM eyesight during the wayfinding simulation at the simulation time t_A in one-floor indoor environment. The user can check the rendered image of Fig. E.2 virtually through HMD. In addition, Figs. E.2 (c) and (d) show the DHM eyesight with visual impairment filters such as a blurred vision filter and a protanopia vision filter, respectively. In addition, as shown in Fig. E.2 (b), the color chart and the landolt ring chart are added into the environment model to confirm the effect of the visual impairment filters. As shown in Fig. E.2 (c), the user can check the eyesight of the DHM, while considering the elderly's vision using the blurred vision filter. In addition, as shown in Fig. E.2 (d), the user can check the protanopia vision using the protanopia vision filter. Therefore, it was confirmed that the VES enabled the user to check the eyesight of the DHM virtually, during the wayfinding simulation, while considering the visual impairments.

The execution speed of the VES was 75.0 fps, which is also enough for a real-time application.

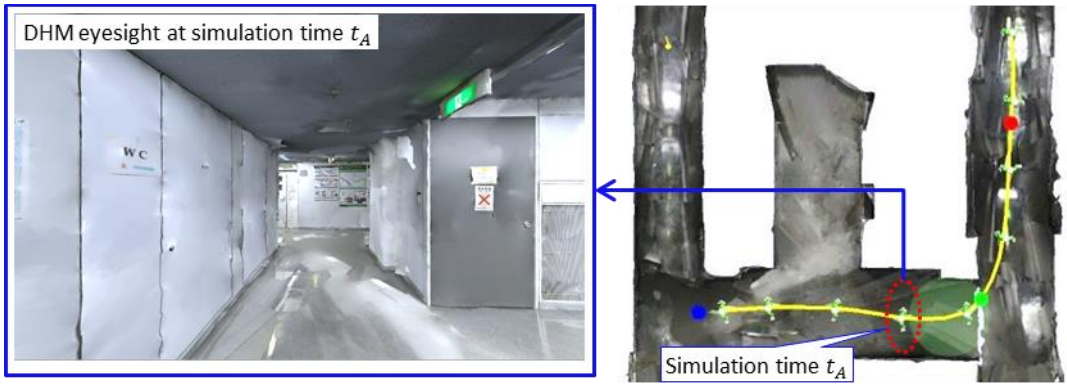

(a) Checking eyesight of the DHM during the wayfinding simulation

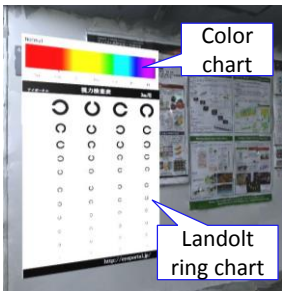

(b) Rendered image without visual impairment filters

(c) Rendered image with blurred vision filter ($D_b = 1$)

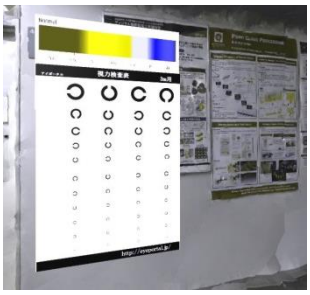

(d) Rendered image with protanope vision filter ($D_p = 1$)

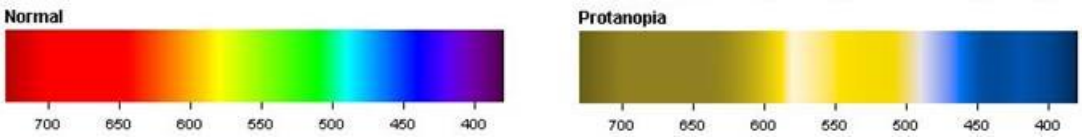

(e) Color difference between normal vision and protanopia vision [Colorblinder]

Fig. E.2 Results of virtual eyesight simulator

References

[Abanarua] Abanarua Todor, Blur shader, [cited 2016 Dec.1]. Available from: https://www.assetstore.unity3d.com/jp/#!/content/6296

[Agarwal 11] Agarwal S., Furukawa Y., Snavely N., Simon I., Curless B., Seitz M. S., and Szeliski R., Bulding Rome in a day, Journal of Communications of the ACM, 54 (10), pp.105-112, (2011).

[Agisoft] Agisoft PhotoScan, [cited 2016 Dec. 1]. Available from: http://www.agisoft.com/

[Akagi 10] Akagi T., Agisaka S., The improving motorway rest area based on visual search of elderly persons, Japanese Journal of Architecture and Planning (Transactions of AIJ), 75 (650), pp.813-820, (2010). (In Japanese)

[Andres 13] Andres S., Beatriz M., Urban accessibility diagnosis from mobile laser scanning data, ISPRS Journal of Photogrammetry and Remote Sensing, 84, pp.23-32, (2013). (DOI: 10.1016/j.isprsjprs.2013.07.001)

[ARToolkit] ARToolkit, [cited 2016 Dec.1]. Available from: https://artoolkit.org/

[Barrett 10] Barrett R. S., Mills P. M., and Begg R. K., A systematic review of the effect of ageing and falls history on minimum foot clearance characteristics during level walking, Journal of Gait & Posture, 32 (4), pp.429-435, (2010). (DOI: 10.1016/j.gaitpost.2010.07.010)

[Becker-Asano 14] Becker-Asano C., Ruzzoli F., Hölscher C., and Nebel B., A multi-agent system based on unity 4 for virtual perception and wayfinding, Transportation Research Procedia, 2, pp.452-455, (2014). (DOI: 10.1016/j.trpro.2014.09.059)

[Begg 14] Begg R. K., Tirosh O., Said C. M., Sparrow W. A., Steinberg N., Levinger P., and Galea M. P., Gait training with real-time augmented toe-ground clearance information decreases tripping risk in older adults and a person with chronic stroke, Frontiers in Human Neuroscience, 8, Article 243, (2014). (DOI: 10.3389/fnhum.2014.00243)

[Bentley] Bentley - Reality Modeling Software, [cited 2016 Dec. 1]. Available from: https://www.bentley.com/en/products/brands/contextcapture

[Best 08] Best R., and Begg R., A method for calculating the probability of tripping while walking, Journal of Biomechanics, 41 (5), pp.1147-1151, (2008). (DOI: 10.1016/j.jbiomech.2007.11.023)

[Blake 88] Blake A. J., Morgan K., Bendall M. J., Dallosso H., Ebarahim S. B., Arie T. H., Fentem P. H., and Bassey E. J., Falls by elderly people at home: prevalence and associated factors, Journal of Age and Aging, 17 (6), pp.365-372, (1988) (DOI: 10.1093/ageing/17.6.365)

[Blensor] Blensor, [cited 2016 Dec. 1]. Available from: http://www.blensor.org/

[Brunnhuber 12] Brunnhuber M., Schrom-Feiertag H., Luksch C., Matyus T., and Hesina G., Bridging the gaps between visual exploration and agent-based pedestrian simulation in a virtual environment, Proceedings of the 18th ACM Symposium on Virtual Reality Software and Technology, pp. 9-16, (2012). (DOI:10.1145/2407336.2407339)

[Buechner 12] Buechner S. J., Wiener J., and Hölscher S., Methodological triangulation to assess sign placement, Proceedings of the Symposium on Eye Tracking Research and Applications, pp.185-188, (2012).

[Catarina 09] Catarina Lino Neto Pereira, Risk of falls, fear of falling, and loss of autonomy on old women: impact of physical activity and fitness in the performance of activities of daily living, Technical University of Lisbon, Ph.D. thesis, (2009).

[Chang 07] Chang S. W., and Wang M. J., Digital human modeling and workplace evaluation: using an automobile assembly task as an example, Human Factors and Ergonomics in Manufacturing, 17 (5), pp.445-455, (2007). (DOI: 10.1002/hfm.20085)

[Chen 11] Chen Q., de Vries B., and Nivf M. K., A wayfinding simulation based on architectural features in the virtual built environment, Proceedings of the 2011 Summer Computer Simulation Conference, pp. 22-29, (2011).

[C-Motion] C-Motion, Visual 3D, [cited 2016 October 20]. Available from: http://www2.c-motion.com/products/visual3d

[Cohen 03] Cohen L., Miller T., Sheppard M. A., Gordon E., Gantz T., and Atnafou R., Bridging the gap: Bringing together intentional and unintentional injury prevention efforts to improve health and well being, Journal of Safety Research, 34 (5), pp.473-483, (2003). (DOI: 10.1016/j.jsr.2003.03.005)

[Colblinder] Colblindor, [cited 2016 Dec.1]. Available from: http://www.color-blindness.com/

[Coros 10] Coros S., Beaudoin P., Panne M., Generalized biped walking control, ACM Transaction on Graphics, 29(4), Article #130, (2010). (DOI: 10.1145/1778765.1781156)

[Cumming 99] Cumming R. G., Thomas M., Szonyi G., Salkeld G., O'Neill E., Westbury C., Frampton G., Home visits by an occupational therapist for assessment and modification of environmental hazards: a randomized trial of falls prevention, Journal of the American Geriatrics Society, 47 (12), pp.1397-1402, (1999). (DOI: 10.1111/j.1532-5415.1999.tb01556.x)

[DHRC] Digital Human Research Center, [cited 2016 Dec. 1]. Available from: http://www.dh.aist.go.jp/jp/research/health/gait_evaluation_system/

[Duives 13] Duives C. D., Daamen W., and Hoogendoorn S. P., State-of-the-art crowd motion simulation models, Journal of Transportation Research Part C: Emerging Technologies, 37, pp.193-209, (2013). (DOI: 10.1016/j.trc.2013.02.005)

[Dzeng 14] Dzeng R. J., Fang Y.C., and Chen I. C., A feasibility study of using smartphone built-in accelerometers to detect fall portents, Journal of Automation in Construction, 38, pp.74-86, (2014). (DOI: 10.1016/j.autcon.2013.11.004)

[FARO] FARO, [cited 2016 Dec. 1]. Available from: http://www.faro.com/en-us/home

[Fillipidis 06] Filippidis L., Galea E. R., Gwynne S., and Lawrence P. J., Representing the influence of signage on evacuation behavior within an evacuation model, Journal of Fire Protection Engineering, 16 (1), pp.37–73, (2006). (DOI: 10.1177/1042391506054298)

[Furukawa 09] Furukawa Y., Curless B., Seitz M. Steven, and Szeliski R., Reconstructing building interiors from images, Proceedings of IEEE 12th ICCV 2009, (2009).

[Galna 09] Galna B., Peters A., Murphy A. T., and Morris M. E., Obstacle crossing deficits in older adults: A systematic review, Journal of Gait & Posture, 30 (3), pp.270-275, (2009). (DOI: 10.1016/j.gaitpost.2009.05.022)

[Grochow 004] Grochow K., Martin L. S. , Hertzmann A., and Popovic Z., Style-based Inverse Kinematics, ACM Transaction on Graphics, 23 (23), pp.522-531, (2004). (DOI: 10.1145/1186562.1015755)

[Gschwind 13] Gschwind Y. J., Kressig R. W., Lacroix A., Muehlbauer T., Pfenninger B., and Granacher U., A best practice fall prevention exercise program to improve balance, strength / power, and psychosocial health in older adults: study protocol for a randomized controlled trial, Journal of BMC Geriatrics, 13 (1), pp.1-13, (2013). (DOI: 10.1186/1471-2318-13-105)

[Gulti] Gulti Co. Ltd., Color Blindness Simulator for Unity, [cited 2016 Dec.1]. Available from: https://www.assetstore.unity3d.com/jp/#!/content/19039

[Hajibabai 07] Hajibabai L., Delavar M. R., Malek M. R., and Frank A. U., Agent-based simulation of spatial cognition and wayfinding in building fire emergency evacuation, Lecture Note in Geoinformation and Cartography, pp.255-270, (2007). (DOI: 10.1007/978-3-540-72108-6_17)

[Hareesh 10] Hareesh P. V., Kimura T., Sawada K., and Thalmann D., Aging algorithm for anthropometric digital humans: quantitative estimation for ergonomic applications, Proceedings of International Multi Conference of Engineers and Computer Scientists 2010, pp. 1917-1921, (2010).

[Helbing 00] Helbing D., Farkas I., and Vicsek T., Simulating dynamical features of escape panic, Nature, 407, pp. 487-490, (2000). (DOI: 10.1038/35035023)

[Hiiro 93] Hiiro M., A Study on the wayfinding behavior in urban space, Department of Architecture Graduate School of Engineering the University of Tokyo, Ph.D. thesis, (1993). (In Japanese)

[Hiiro 94] Hiiro M., Hara K., Monnai T., Wayfinding in urban space as problem slobing concering lostness and finding, Japanese Journal of Architecture and Planning (Transactions of AIJ), 466, pp.65-74, (1994). (In Japanese)

[Hirai 08] Hirai K., and Miyake Y, Image quality evaluation of flat panel display based on spatio-temporal characteristics of human visual system, Japanese Journal of the Institute of Image Information and Television Enginners, 62 (3), pp.322-328, (2008). (In Japanese)

[Hocoma] Hocoma Lokomat, [cited 2016 Dec. 1]. Available from: https://www.hocoma.com/usa/us/products/lokomat/

[Hölscher 07] Hölscher C., Büchner S. J., Brosamle M., Meilinger T., and Strube G., Signs and maps: cognitive economy in the use of external aids for indoor navigation, Proceedings of the 29th Annual Conference of the Cognitive Science Society, pp.377-382, (2007).

[HUMAN SOLUTIONS ASSYST AVM] HUMAN SOLUTIONS ASSYST AVM, [cited 2016 Dec. 1]. Available from: http://www.human-solutions.com/mobility/front_content.php?changelang=8&lang=8

[Hunt 99] Hunt E., and Waller D., Orientation and wayfinding: a review, Technical report, University of Washington, (1999).

[Imamura 07] Imamura S., Mori K., and Shibata R., The Study on the evaluation of spatial legibility and the reprocuction of elderly low vision: Considereration of anchorpoint seen from the eyefixation behavior at the nursing home No. 2, Japanese Journal of Architecture and Planning (Transactions of AIJ), 72 (612), pp.49-56, (2007). (In Japanese)

[Ioannou 12] Ioannou Y., Taati B., Harrap R., Difference of Normals as a multi-scale operator in unorganized point clouds, Proceedings of 2012 Second International Conference on 3D Imaging, Modeling, Processing, Visualization & Transmission (3DIMPVT), pp.501-508, (2012). (DOI: 10.1109/3DIMPVT.2012.12)

[ISO 21542, 11] International Organization for Standardization, ISO21542: Building construction -Accessibility and usability of the built environment, (2011).

[ISO/IEC, 14] International Organization for Standardization / International Electrotechnical Commission, ISO/IEC Guide 71 Second edition: Guide for addressing accessibility in standards, (2014).

[Kakizaki 12] Kakizaki T., Urii J., and Endo M., A three-dimensional evacuation simulation using digital human models with precise kinematic joints, Journal of computing and information science in engineering, 12 (3), “031001-1”-“021010-9”, (2012). (DOI: 10.1115/1.4006737)

[Kakizaki 14] Kakizaki T., Urii J., and Endo M., Post-Tsunami evacuation simulation using 3D kinematic digital human models and experimental verification, Journal of computing and information science in engineering, 14 (2), “021010-1”-“021010-9”, (2014). (DOI: 10.1115/1.4026896)

[Kakizaki 16] Kakizaki T., Urii J., and Endo M., Application of digital human models to physiotherapy training, Proceedings of the ASME 2016 International Design Engineering Technical Conferences and Computers and Information in Engineering Conference (IDETC/CIE) 2016, "DETC2016-59455", (2016).

[Kangas 11] Kangas M., Development of accelerometry-based fall detection, The Acta Universitatis Ouluensis series, D II 40, (2011).

[Kass 88] Kass M., Witkin A., and Terzopoulos D., Snakes: active contour models, International Journal of Computer Vision, 1 (4), pp.321-331, (1988).

[Kobayashi 12] Kobayashi Y., Aoki K., Shibusawa E., and Mochimaru M., The system to evaluate the risk of falling during walking 3 - Short term feedback effect of the "Tripping Risk Age" on the MTCs, Japanese Proceedings of LIFE2012, OS2-5-3, (2012). (In Japanese)

[Kobayashi 13] Kobayashi Y., and Mochimaru M., AIST Gait Database 2013, [cited 2016 Dec. 1]. Available from: https://www.dh.aist.go.jp/database/gait2013/

[Kobayashi 14] Kobayashi Y., Yanagisawa T., Sakanashi H., Nosato H., Takahashi E., and Mochimaru M., Assessment of abnormal detection technology aimed for the clarification of the causes of falls in public area, Japanese Journal of Fall Prevention(JJFP), 1 (1), pp.55-63, (2014). (DOI: 10.11335/tentouyobou.1.1_55)

[Kouchi 05] Kouchi M. and Mochimaru M., AIST Anthropometric Database, National Institute of Advanced Industrial Science and Technology, H16PRO 287, (2005).

[Lai 11] Lai C. F. Chang S. Y., Chao H. C., and Huang Y. M., Detection of cognitive injured body region using multiple triaxial accelerometers for elderly falling, IEEE Sensors Journal, 11 (3), pp.763-770 (2011). (DOI: 10.1109/JSEN.2010.2062501)

[Latham 03] Latham N. K., Anderson C. S., Lee A., Bennett D. A., Moseley A., Cameron I. D., Fitness Collaborative Group, A randomized, controlled trial of quadriceps resistance exercise and vitamin D in frail older people the Frailty Interventions Trial in Elderly Subjects (FITNESS), Journal of the American Geriatrics Society, 51 (3), pp.291-299, (2003). (DOI: 10.1046/j.1532-5415.2003.51101.x)

[Leica] Leica DISTO D3a, [cited 2016 Dec.1]. Available from: http://www.laser-measure.co.uk/leica-disto/leica-disto-d3a.html

[Micheletti 15] Micheletti N., Chandler H. J., and Lane N. S., Structure from Motion (SfM) Photogrammetry, British Society for Geomorphology, Geomorphological Techniques, Chap. 2, Sec. 2.2, pp.1-12, (2015).

[Mills 08] Mills P. M., Barrett R. S., and Morrison S., Toe clearance variability during walking in young and elderly men, Journal of Gait & Posture, 28 (1), pp.101-107, (2008). (DOI: 10.1016/j.gaitpost.2007.10.006)

[Min 10] Min J., Liu H., and Chai J., Synthesis and editing of personalized stylistic human motion, Proceedings of the 2010 ACM SIGGRAPH symposium on Interactive 3D Graphics and Games, pp.39-46, (2010).

[MLIT13] Ministry of Land, Infrastructure, Transport and Tourrism, [cited 2016 Dec. 1]. Available from: http://www.mlit.go.jp/sogoseisaku/barrierfree/sosei_barrierfree_mn_000001.html

[Mochimaru 10] Mochimaru M., digital human gijutsu no saishindoko to kensetsukikai heno tekiyo kanosei, Japanese Journal of kensetu no sekou kikaku, 719, pp.29-33, (2010).

[Moller 05] Moller J., Current costing models: are they suitable for allocating health resources? The example of fall injury prevention in Australia, Journal of Accident Analysis & Prevention, 37 (1), pp.25-33, (2005). (DOI: 10.1016/j.aap.2004.06.001)

[Mordatch 10] Mordatch I., de Lasa M., and Hertzmann A., Robust physics-based locomotion using low-dimentional planning, ACM Transaction on Graphics, 29 (4), Article #71, (2010). (DOI: 10.1145/1778765.1778808)

[Moreland 03] Moreland J., Richardson J., Chan D., O'Neill J., Bellissimo A., Grum R., and Shanks L., Evidence-based guidelines for the secondary prevention of falls in older adults, Journal of Gerontology, 49 (2), pp.93-116, (2003). (DOI: 10.1159/000067948)

[Mori 11] Mori K., Sakai H., and Kaida M., A study on low-vision environment with visual level by computer simulated picture, Japanese Journal of Architecture and Planning (Transactions of AIJ), 76 (665), pp.1213-1221, (2011). (In Japanese)

[Motamedi 16] Motamedi A., Yabuki N., Wang Z., Fukuda T., and Michikawa T., Automatic signage visibility checking system using BIM-enabled VR environments, Proceedings of the 16th International Conference on Computing in Civil and Building Engineering, pp.1601-1608, (2016).

[Mukai 11] Mukai T., Motion rings for interactive gait synthesis, Proceedings of ACM Symposium on Interactive 3D Graphics and Games, pp.125-132, (2011). (DOI: 10.1145/1944745.1944767)

[Nagano 11] Nagano H., Begg R. K., Sparrow W. A., and Taylor S., Ageing and limb dominance effects on foot-ground clearance during treadmill and over ground, Clinical Biomechanics, 26 (9), pp.962-968, (2011). (DOI: 10.1016/j.clinbiomech.2011.05.013)

[Nakashima 14] Nakashima Y., Ando T., Kobayashi Y., Fujie M. G., Evaluation of treadmill velocity control based on user's intention of acceleration or deceleration, Proceedings of World Automation Congress (WAC) 2014, 14th International Symposium on Robotics and Applications (ISORA 2014), pp.555-560, (2014). (DOI: 10.1109/WAC.2014.6936042)

[NICE 13] National Institute for Health and Care Excellence, Falls: assessment and prevention of falls in older people, NICE clinical Guideline 161 (guidance.nice.org.uk/cg161), (2013).

[NILIM] National Institute for Land and Infrastructure Management, [cited 2016 Dec. 1]. Available from: http://www.nilim.go.jp/lab/bcg/siryou/tnn/tnn0667pdf/ks066707.pdf (In Japanese)

[Nüchter 08] Nüchter A., Hertzberg J., Towards semantic maps for mobile robots, Journal of Robotics and Autonomous Systems, 56(11), pp.915-926, (2008). (DOI: 10.1016/j.robot.2008.08.001)

[Oculus] Oculus, Oculus Rift DK2, [cited 2016 Dec.1]. Available from: https://www.oculus.com/en-us/dk2/

[Oesau 14] Oesau S., Lafarge F., Alliez P., Indoor scene reconstruction using feature sensitive primitive extraction, ISPRS Journal of Photogrammetry and Remote Sensing, 90, pp.68-82, (2014). (DOI: 10.1016/j.isprsjprs.2014.02.004)

[OMRON] OMRON photoelectric sensor E3Z-R81 2M, [cited 2016 October 20]. Available from: http://www.fa.omron.co.jp/product/item/721/en/

[O'Neill 91] O'Neill M. J., Evaluation of a conceptual model of architectural legibility, Journal of Environment and Behavior, 23 (3), pp. 259-284, (1991). (DOI: 10.1177/0013916591233001)

[OpenGL] OpenGL, [cited 2016 Dec. 1], Available from: https://www.opengl.org/

[Overstall 77] Overstall P. W., Exton-Smith A. N., Imms F. J., and Johnson A. L., Falls in the elderly related to postural imbalance, The British Medical Journal, 1 (6056), pp.261-264, (1977).

[Pan 13] Pan H., Hou X., Gao C., and Lei Y., A method of real-time human motion retargeting for 3D terrain adaptation, Proc. of 13th IEEE JICSIT, pp.1-5, (2013). (DOI: 10.1109/ANTHOLOGY.2013.6784879)

[PCL] Point Cloud Library, [cited 2016 Dec. 1]. Available from: http://pointclouds.org/

[Perry 10] Perry J., Burnfield M. J., GAIT ANALYSIS Normal and Pathological Function Second Edition, SLACK Inc. New Jersey, 551p., (2010).

[Pettre 05] Pettre J., Laumond J.-P., Thalmann D., A navigation graph for real-time crowd animation on multi-layered and uneven terrain, Proceedings of 1st International Workshop on Crowd Simulation (V-CROWDS'05), pp.81-90, (2005).

[Ramer 72] Ramer U., An iterative procedure for the polygonal approximation of plane curves, Journal of Computer Graphics and Image Processing, 1 (3), pp.244-256, (1972). (DOI: 10.1016/S0146-664X(72)80017-0)

[Rami 13] Rami A. A.-A., Komura T., and Choi M. G.. Relationship descriptors for interactive motion adaptation, Proceedings of the 12th ACM SIGGRAPH/Eurographics Symposium on Computer Animation (SCA '13), pp.45-53, (2013). (DOI: 10.1145/2485895.2485905)

[Reed 09] Reed M. P., Modeling ascending and descending stairs using the Human Motion Simulation Framework, Proceedings of SAE Digital Human Modeling for Design and Engineering Conference, "2009-01-2282",

(2009). (DOI: 10.4271/2009-01-2282)

[Reis 12] Reis P., Moro A., Bins E. V., Fernandes C., Vilagra J., Peres L., Fogaça J. O., Merino E., Universal design and accessibility an approach of the influence of muscle strength loss in the risk of falls in the elderly, Journal of Work, 41 (S1), pp.374-379, (2012). (DOI: 10.3233/WOR-2012-0185-374)

[Rubenstein 06] Rubenstein L. Z., Falls in older people: epidemiology, risk factors and strategies for prevention, Journal of Age and Aging, 35 (S2), ii37-41, (2006). (DOI: 10.1093/ageing/afl084)

[Rusu 08] Rusu R. B., Marton Z. C., Blodow N., Dolha M., Beetz M., Towards 3D point cloud based object maps for household environments, Journal of Robotics and Autonomous Systems, 56 (11), pp.927-941, (2008). (DOI: 10.1016/j.robot.2008.08.005)

[Rusu 13] Rusu R. B, Semantic 3D object maps for everyday robot manipulation, Springer Berlin Heidelberg, Berlin, (2013).

[Saito 10] Saito A. Kimura T., and Hareesh P. V., Physical load prediction method based on digital human simulation, Panasonic Electric Works technical report, 59 (2), pp.19-24, (2010). (In Japanese)

[Sattin 92] Sattin R. W., Falls among older persons: a public health perspective, Annual Review of Public Health, 13, pp.489-508, (1992). (DOI: 10.1146/annurev.pu.13.050192.002421)

[Sattin 98] Sattin R. W., Rodriguez J. G., DeVito C. A., and Wingo P. A., Home environmental hazards and the risk of fall injury events among community-dwelling older persons, Journal of the American Geriatrics Society, 46 (6), pp.669-676, (1998). (DOI: 10.1111/j.1532-5415.1998.tb03799.x)

[Sattin 98] Sattin R. W., Rodriguez J. G., DeVito C. A., and Wingo P. A., Home environmental hazards and the risk of fall injury events among community-dwelling older persons, Journal of the American Geriatrics Society, 46 (6), pp.669-676, (1998). (DOI: 10.1111/j.1532-5415.1998.tb03799.x)

[Sekiya 94] Sekiya N., Nagasaki H., Itou H., and Fruna T., Seijyou hokou ni okeru hokou sokudo, hokou ritsu, hohaba no sougo kankei, Japanese Journal of Physical Therapy Association, 21 (S2), p.416, (1994). (In Japanese)

[Sherrington 11] Sherrington C., Tiedemann A., Fairhall N., Close J. C. T., and Lord S. R., Exercise to prevent falls in older adults: an updated meta-analysis and best practice recommendations, NSW Public Health Bulletin, 22 (4), pp.78-83, (2011). (DOI: 10.1071/NB10056)

[SIEMENS] SIEMENS - Jack and Process Simulate Human, [cited 2016 Dec. 1]. Available from: http://www.plm.automation.siemens.com/en_us/products/tecnomatix/manufacturing-simulation/human-ergonomics/jack.shtml

[Smeesters 01] Smeesters C., Hayes W. C., and McMahon T. A., Disturbance type and gait speed affect fall direction and impact location, Journal of Biomechanics, 34 (3), pp.309-317, (2001).

[Ståhl 08] Ståhl A., Carlsson G., Hovbrandt P., and Iwarsson S., "Let's go for a walk!": identification and prioritization of accessibility and safety measures involving elderly people in a residential area, European Journal of Ageing, 5 (3), pp.265-273, (2008). (DOI: 10.1007/s10433-008-0091-7)

[Stevens 06] Stevens J. A., Corosm P. S., Finkelstein E. A., and Muller T. R., The costs of fatal and non-fatal falls among older adults, Journal of the International Society for Child and Adolescent Injury Prevention, 12 (5), pp.290-295, (2006). (DOI: 10.1136/ip.2005.011015)

[Suminski 05] Suminski R. R., Poston W. S., Petosa R. L., Stevens E., Katzenmoyer L. M., Features of the neighborhood environment and walking by U.S. adults, American Journal of Preventive Medicine, 28 (2), pp.149-155, (2005). (DOI: 10.1016/j.amepre.2004.09.009)

[Tang 10] Tang P., Huber D., Akinci B., Lipman R., and Lytle A., Automatic reconstruction of as-is building information models from laser-scanned point clouds: a review of related techniques, Journal of Automation in Construction, 19 (7), pp.829-843, (2010). (DOI: 10.1016/j.autcon.2010.06.007)

[Tecchia 01] Tecchia F., Loscos C., Conroy R., Chrysanthou Y., Agent behavior simulator (ABS): a platform for urban behavior development, Proceedings of the ACM Games Technology Conference, pp.17–21, (2001).

[Thora 11] Thora T., Bergmann E., and Konieczny L., Wayfinding and description strategies in an unfamiliar complex building, Proceedings of 33rd Annual Conference of the Cognitive Science Society, pp.1262-1297, (2011).

[Todd 04] Todd C., Skelton D., What are the main risk factors for falls among older people and what are the most effective interventions to prevent these falls? Copenhagen, WHO Regional Office for Europe (Health Evidence Network report, Available from: http://www.euro.who.int/document/E82552.pdf), (2004).

[Troje 02] Troje N. F., Decomposing biological motion: a framework for analysis and synthesis of human gait patterns, Journal of Vision, 2 (5), pp.371-387, (2002). (DOI: 10.1167/2.5.2)

[Ueno 07] Ueno M., Kobayashi I., Yamamoto K., and Takeshita S., Constructed the road network for the shelter simulation using Laser Measurement Data, Japanese Journal of Applied Computing in Civil Engineering,

16, pp.192-202, (2007). (In Japanese)

[van den Berg 08] van den Berg J., Lin M. , Manocha D., Reciprocal Velocity Obstacles for real-time multi-agent navigation, Proceedings of the IEEE International Conference on Robotics and Automation (ICRA), pp.1928-1935, (2008).

[VICON] VICON, [cited 2016 Dec. 1]. Available from http://www.irc-web.co.jp/vicon_web/

[Vilar 14] Vilar E., Rebelo F., and Noriega P., Indoor human wayfinding performance using vertical and horizontal signage in virtual reality, Human Factors and Ergonomics in Manufacturing & Service Industries, 24 (6), pp.601-615, (2014). (DOI: 10.1002/hfm.20503)

[von Zitzeeitz 07] von Zitzewitz J., Bernhardt M., Riener R., A novel method for automatic treadmill speed adaptation, IEEE Transactions on Neural Systems and Rehabilitation Engineering, 15 (3), pp.401-409, (2007).

[Wang 09] Wang J. M., Fleet D. J., and Hertzmann A., Optimizing walking controllers, ACM Transaction on Graphics, 28 (5), Article #168, (2009). (DOI: 10.1145/1618452.1618514)

[Wang 10] Wang J. M., Fleet D. J., and Hertzmann A., Optimizing walking controllers for uncertain inputs and environments, ACM Transaction on Graphics, 29 (4), Article #73, (2010). (DOI: 10.1145/1778765.1778810)

[Wang 12] Wang J. M., Hamner S. R., Delp S. L., and Koltum V., Optimizing locomotion controllers using biologically-based actuators and objectives, ACM Transaction on Graphics, 31 (4), Article #25, (2012). (DOI: 10.1145/2185520.2185521)

[WHO 07] World Health Organization (WHO), WHO global report on falls prevention in older age, (2007).

[Winter 92] Winter D. A., Foot trajectory in human gait: a precise and multifactorial motor control task. Journal of Physical Therapy, 72 (1), pp.45-53, (1992).

[Xiang 10] Xiang Y., Arora J. S., and Abdel-Malek K., Physics-based modeling and simulation of human walking: a review of optimization-based and other approaches, Journal of Structural and Multidisciplinary Optimization, 42 (1), pp.1-23, (2010). (DOI: 10.1007/s00158-010-0496-8)

[Xiao 14] Xiao J., and Furukawa Y., Reconstructing the world's museums, International Journal of Computer Vision, 110 (1), pp.243-258, (2014). (DOI: 10.1007/s11263-014-0711-y)

[Xie 07] Xie H., Filippidis L., Gwynne S., Galea E. R., Blackshields D., Lawrence P. J., Signage legibility distances as a function of observation angle, Journal of Fire Protection Engineering, 17 (1), pp.41-64, (2007). (DOI: 10.1177/1042391507064025)

[Xiong 13] Xiong X., Adan A., Akinci B., and Huber D., Automatic creation of semantically rich 3D building models from laser scanned data, Journal of Automation in Construction, 31, pp.325-337, (2013). (DOI: 10.1016/j.autcon.2012.10.006)

[Yamada 05] Yamada H., Ooyatsu Y., Ishihara Y., Shuto T., and Tsuchiya M., Research and development of the computer manikin as a conformity evaluation tool of industrial products to human, Japanese Journal of Mitsubishi Research Institute, 44, pp.118-137, (2005). (In Japanese)

[Yanagihara 14a] Yanagihara T., Takahashi F., and Ishimi R., Falls in the elderly and accessibility traffic environment in neighborhood districts, Proceedings of the International Conference on Universal Design (UD 2014), pp. 427-428, (2014).

[Yanagihara 14b] Yanagihara T., Takahashi F., koreisha no tento, tenraku jittai kara mita jukyochiku naino barrier-free seibi ni kansuru kenkyu, Japanease conference of 50th Committee of Infrastructure Planning and Management, #64, (2014).

[Yang 16] Yang K., Ahn C. R., Vuran M. C., and Aria S. S., Semi-supervised near-miss fall detection for ironworkers with a wearable inertial measurement unit, Journal of Automation in Construction, 68, pp.194-202, (2016). (DOI: 10.1016/j.autcon.2016.04.007)

[Yin 07] Yin K. K., Loken K., Panne M., SIMBICON: Simple Biped Locomotion Control, ACM Transaction on Graphics, 26 (3), Article #105, (2007). (DOI: 10.1145/1276377.1276509)

[Yin 08] Yin K., Coros S., Beaudoin P., and van de Panne M., Continuation methods for adapting simulated skills, ACM Transaction on Graphics, 27 (3), Article #81, (2008). (DOI: 10.1145/1360612.1360680)

[Zhang 12] Zhang S., Qu X., Ma S., and Kong L., A dense stereo matching algorithm based on triangulation, Journal of Computational Information Systems, 8 (1), pp. 283-292, (2012).

[Zhou 02] Zhou X., Draganich L. F., and Amirouche F., A dynamic model for simulating a trip and fall during gait, Journal of Medical Engineering & Physics, 24 (2), pp.121-127, (2002). (DOI: 10.1016/S1350-4533(01)00125-4)

Acknowledgement

First, my deepest appreciation goes to my academic supervisor, Professor Satoshi Kanai, who has supported me throughout my research over these five years. This thesis relates to several research fields, so his exact guidance and precious comments based on his comprehensive knowledge have been always supportive. He also provided me many opportunities for attending conference, discussing my researches with researchers and people in companies, and visiting overseas labs. Without his support, this thesis would not have materialized.

I would like to express my gratitude to committee members of this thesis, Professor Atsushi Konno, Associate Professor Hiroaki Date, Professor Masahiko Onosato, and Visiting Associate Professor Mitsunori Tada, for their insightful comments and suggestions.

I would also like to thank Associate Professor Hiroaki Date for his invaluable comments and support over these five years.

I have had the support from Midori Takahashi, and the members of Digital Geometry Processing Laboratory. I also would like to thank them.

I appreciate the all participants and cooperators in experiments in this thesis.

RIEGL JAPAN Corporation provided the outdoor environment point clouds. Kokusai Kogyo Co. Ltd. provided the point clouds of urban environments. I would like to express our gratitude to S. Matsuda of the RIEGL JAPAN Corporation, and G. Takahashi and U. Rin of Kokusai Kogyo Co. Ltd. for their support.

A part of this work was supported by JSPS KAKENHI Grant No. 15J01552 and JSPS Grant-in-Aid for Challenging Exploratory Research under Project No.26560168.

Lastly, I wish my regards and blessings to all of those who helped me in any respect during the completion of this thesis.

Tsubasa Maruyama

2017, Feb. 15

Sapporo, Hokkaido, Japan

Publication list

1. Publications (related to this thesis)

I. Publications

(1) T. Maruyama, S. Kanai, H. Date, and M. Tada, "Motion-capture-based walking simulation of digital human adapted to laser-scanned 3D as-is environments for accessibility evaluation", Journal of Computational Design and Engineering, 3 (3), pp.250-265, (2016)

(2) T. Maruyama, S. Kanai, and H. Date, "A development of a basic walking simulation in as-built environments by combining digital human model with large-scale 3-dimensional laser scan", Journal of the Japan Society for Precision Engineering, 80 (8), pp.755-762, (2014) (In Japanese)

II. Peer-reviewed Proceedings

(1) T. Maruyama, S. Kanai, H. Date, "Vision-based wayfinding simulation of digital human model in three dimensional as-is Environment models and its application to accessibility evaluation", Proceedings of the American Society of Mechanical Engineers 2016 International Design Engineering Technical Conference and Computers and Information Engineering Conference, IDETC2016-59170, (2016)

(2) T. Maruyama, S. Kanai, and H. Date, "MoCap-Based adaptive human-like walking simulation in laser-scanned large-scale as-built environments", Digital Human Modeling and Applications in Health, Safety, Ergonomics, and Risk Management, Human Body Modeling and Ergonomics – Lecture Note in Computer Science, Springer Berlin Heidelberg, Vol.9185, pp.193-204, (2015) (peer-reviewed by the extended abstract)

(3) T. Maruyama, S. Kanai, and H. Date, "Efficient large-scale as-built environment modeling based on 3D laser-scanning for human walking simulation", Digital Human Modeling Symposium 2014, Paper #38, (2014)

(4) T. Maruyama, S. Kanai, and H. Date, "Making a digital human walk directly in the 3D Laser-scanned point clouds of indoor environments", International Conference on Civil and Building Engineering Informatics 2013, pp.69-76, (2013)

(5) T. Maruyama, S. Kanai, and H. Date, "Accessibility evaluation of the as-built two-storey large-scale indoor environments by combining digital human model and terrestrial laser scanners", Asian Conference on Design and Digital Engineering 2013, pp.362-372, (2013)

(6) T. Maruyama, S. Kanai, and H. Date, "Simulating a walk of digital human model directly in massive 3D laser-scanned point cloud of indoor environments", Digital Human Modeling and

Applications in Health, Safety, Ergonomics, and Risk Management, Human Body Modeling and Ergonomics –Lecture Note in Computer Science, Springer Berlin Heidelberg, Vol.8026, pp.366-375, (2013) (peer-reviewed by the extended abstract)

2. Presentations (related to this thesis)

(1) T. Maruyama, S. Kanai, and H. Date, M. Tada, "Motion-capture-based walking simulation adapted to laser-scanned large-scale complex as-built environments for accessibility evaluation", Eighth Asian-Pacific Conference on Biomechanics, PS3-15, (2015) (poster presentation only)

(2) T. Maruyama, S. Kanai, and H. Date, M. Tada, "Enabling human-like walking of digital human model in laser-scanned large-scale as-built environment", Asian Conference on Design and Digital Engineering 2014, (2014) (oral presentation only)

(3) T. Maruyama, S. Kanai, and H. Date, "Walking simulation of digital human in laser-scanned point clouds of as-built large-scale indoor environments", Indoor 3D Conference, (2013) (oral presentation only)

(4) T. Maruyama, S. Kanai, and H. Date, "Human behavior simulation in large-scale 3-dimensional as-is environment models and its application to accessibility evaluation - Estimating potential region of tripping risk from 3-dimensional laser-scanned point clouds -", Proceedings of 2016 JSPE Autumn Conference, pp.495-496, (2016)

(5) T. Maruyama, S. Kanai, and H. Date, "Human behavior simulation in large-scale 3-dimensional as-is environment models and its application to accessibility evaluation – Quantitative tripping risk estimation by Monte Carlo simulation and its validation, Proceedings of 2016 JSPE Hokkaido Branch conference, pp.47-48, (2016)

(6) T. Maruyama, S. Kanai, and H. Date, "Human behavior simulation in large-scale 3-dimensional as-is environment models and its application to accessibility evaluation - Estimating visibility and legibility of signage based on visual perception of digital human - ", Proceedings of 2016 JSPE Spring Conference, pp.775-776, (2016)

(7) T. Maruyama, S. Kanai, and H. Date, "Human behavior simulation in laser-scanned point clouds of real environment and its application to the accessibility evaluation (9th report) - Estimating and displaying toe clearance of digital human model during walking simulation -", Proceedings of 2015 JSPE Autumn Conference, pp.47-48, (2015)

(8) T. Maruyama, S. Kanai, and H. Date, "Human behavior simulation in laser-scanned point clouds of real environment and its application to the accessibility evaluation (10th report) – Development of

tread boundary estimation method for walking simulation on stairs -, Proceedings of 2015 JSPE Hokkaido Branch conference, pp.11-12, (2015)

(9) T. Maruyama, S. Kanai, and H. Date, "Development of walking simulation of digital human model for accessibility evaluation of large-scale as-built environment", Proceedings of 2014 JSDE Hokkaido Branch conference, pp.5-6, (2015)

(10) T. Maruyama, S. Kanai, H. Date, "Human behavior simulation in laser-scanned point clouds of real environment and its application to the accessibility evaluation (8th report) - MoCap-based walking simulation of the digital human model on stairs and slopes - ", Proceedings of 2015 JSPE Spring Conference, pp.513-514, (2015)

(11) T. Maruyama, S. Kanai, and H. Date, "Human behavior simulation in laser-scanned point clouds of real environment and its application to the accessibility evaluation (6th report) - An improvement of walking simulation of the digital human model based on MoCap data -", Proceedings of 2014 JSPE Autumn Conference, pp.383-384, (2014)

(12) T. Maruyama, S. Kanai, and H. Date, "Human behavior simulation in laser-scanned point clouds of real environment and its application to the accessibility evaluation (7th report) – Enabling digital human model to walk with turning motion -, Proceedings of 2014 JSPE Hokkaido Branch conference, pp.49-50, (2014)

(13) T. Maruyama, S. Kanai, H. Date, "Human behavior simulation in laser-scanned point clouds of real environment and its application to the accessibility evaluation (4th report) - A development of an algorithm to extract walk surface points from low-dense point clouds - ", Proceedings of 2014 JSPE Spring Conference, pp.375-376, (2014)

(14) T. Maruyama, S. Kanai, and H. Date, "Human behavior simulation in laser-scanned point clouds of real environment and its application to the accessibility evaluation (4th report) - A development of a walking simulation in large-scale indoor and outdoor environment with caracoles and slopes -", Proceedings of 2013 JSPE Autumn Conference, pp.645-646, (2013)

(15) T. Maruyama, S. Kanai, H. Date, "Human behavior simulation in laser-scanned point clouds of real environment and its application to the accessibility evaluation (3rd report) - A development of a path findings algorithm for human behavior simulation from a 3D laser-scanned point cloud - ", Proceedings of 2013 JSPE Spring Conference, pp.885-886, (2013)

(16) T. Maruyama, S. Kanai, H. Date, "Accessibility evaluation based on human behavior simulation in laser-scanned point clouds", Proceedings of 31th JSPRS Hokkaido Branch Conference, pp.11-15, (2013)

(17) T. Maruyama, S. Kanai, H. Date, "A human behavior simulation in a laser-scanned point cloud for the accessibility evaluation of large-scale real environment", Proceedings of ViEW 2012, pp.236-237, (2012)

(18) T. Maruyama, S. Kanai, and H. Date, "Human behavior simulation in laser-scanned point clouds of real environment and its application to the accessibility evaluation (1st report) - A development of basic walking simulation in a point cloud -", Proceedings of 2012 JSPE Autumn Conference, pp.303-304, (2012)

(19) T. Maruyama, S. Kanai, and H. Date, "Human behavior simulation in laser-scanned point clouds of real environment and its application to the accessibility evaluation (2nd report) – Implementation of local collision avoidance algorithm on basis walking simulation -, Proceedings of 2012 JSPE Hokkaido Branch conference, pp.77-78, (2012)